STUDIA

UNIVERSITATIS BABEŞ-BOLYAI

Chemia

CLUJ-NAPOCA 2006

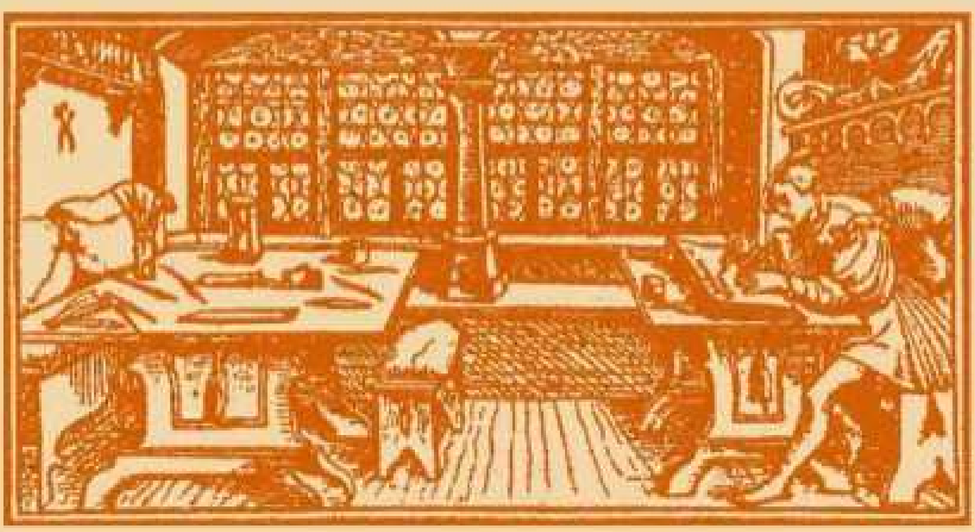

Cluj University Press

2

2/2006

EDITORIAL BOARD OF
STUDIA UNIVERSITATIS BABEŞ-BOLYAI, CHEMIA

EDITORIAL OFFICE: Arany Janos no. 11, 400028 Cluj-Napoca ♦ Phone 0264-59.38.33

ANUL LI **2006**

S T U D I A
UNIVERSITATIS BABEŞ-BOLYAI

CHEMIA

2

EDITORIAL OFFICE: Republicii no. 24, 400015 Cluj-Napoca ♦ Phone 0264-40.53.52

CUPRINS - CONTENTS - SOMMAIRE

STUDIA UNIVERSITATIS BABES - BOLYAI, CHEMIA, LI, 2, 2006

Dedicated to professor Gh. Marcu at his 80th anniversary

ELECTROCHEMICAL CHARACTERIZATION OF SANDWICH-TYPE PHOSPHOTUNGSTOCERATE (IV) AND ARSENOTUNGSTOCERATE (IV) IN AQUEOUS AND NON-AQUEOUS SOLUTION

ADRIAN-RAUL TOMSA[ab], AGLAIA KOUTSODIMOU,[b] POLYCARPOS FALARAS,[b] MARIANA RUSU[c]*

ABSTRACT. The electrochemical properties of two sandwich-type polyoxotungstocerate (IV) $[(CeO)_3(H_2O)_2(PW_9O_{34})_2]^{12-}$ and $[(CeO)_3(H_2O)_2(AsW_9O_{34})_2]^{12-}$ have been studied by cyclic voltammetry in aqueous and acetonitrile solutions. Voltammograms recorded in aqueous solutions showed the existence of two waves for the Ce(III)/Ce(IV) redox couple. These could be explained by a nonequivalence of the Ce atoms in the polyoxotungstate molecule, where one Ce atom is six coordinated and the other two, are seven coordinated. The presence of only one peak pair for Ce(III)/Ce(IV) suggests the equivalence of these metal ions in the polyoxometalate complexes when isolated as tetrabutylammonium salts. When increasing amounts of $LiClO_4$ have been added to the acetonitrile solutions of the polyoxotungstocerate while keeping the ionic strength constant with 1M $[Bu_4N]ClO_4$ a dramatic change of the electrochemical behavior was observed, which was assigned to the association of Li^+ ions with the reduced forms of the polyoxometalates.

Introduction

The interest regarding the polyoxometalates chemistry has increased enormously in last decades when a very large number of different structures as well as new potential applications of such compounds have been reported [1-8]. On this context, it is recognized that the different coordination geometries of the lanthanide cations and the vacant sites afforded by the polyoxometalates usually result in large oxometalate clusters [4-24], showing very interesting electroluminiscence and photoluminiscence activity [4, 11-14, 16, 22] as well as enhanced efficiency against HIV [25, 26].

One example of such compound, in which lanthanides act as linkers between trilacunary Keggin polyoxometalates was described for the first time by Knoth et al. in 1986 [27]. Its structure consists on a belt of three Ce alternating with three oxygens, sandwiched between two trilacunary 9-phosphotungstate units. In the belt, two of the cerium (IV) ions are 7 coordinated, and the third one is only 6 coordinated (Fig. 1).

[a] Department of Inorganic Chemistry, “Raluca Ripan” Institute for Research in Chemistry, 30 Fântânele St., 400294 Cluj-Napoca, Romania
[b] Institute of Physical Chemistry, NCSR “Demokritos”, 15310 Aghia Paraskevi Attikis, Greece
[c] Department of Chemistry, “Babeş-Bolyai” University, 400028 Cluj-Napoca, Romania

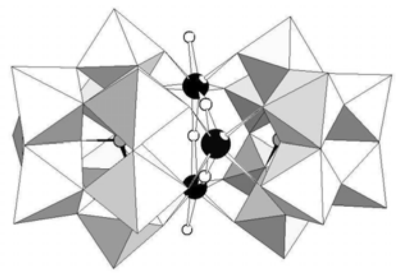

Fig.1. The polyhedral representation of the sandwich polyoxotungstocerates (WO_6 white octahedral; Ce – black spheres; P – grey spheres; O- white spheres).

Herein we report a detailed investigation of electrochemical behavior of $[(CeO)_3(H_2O)_2(PW_9O_{34})_2]^{12-}$ and its arsenic (V) derivative, in aqueous and non-aqueous solutions.

Experimental

1. Methods

Inductively Coupled Plasma Spectroscopy (I.C.P.) was used for the elemental analysis of tin and tungsten, and flamephotometry for sodium and potassium. The water content was thermogravimetrically determined, by means of a Paulik Erdely OD-102 type derivatograph at a temperature range of 20-600°C, using a heating rate of 5°C min^{-1}.

A Nicolet 5DX spectrophotometer was used to record the IR spectra of samples pelleted in KBr.

Cyclic voltammetry measurements were performed using a Vinci Technologies P/G STAT Z1 potentiostat, operating in conjunction with a 33120 A Hewlett Packard function /arbitrary waveform generator and with a Linseis LY 18100 X-Y recorder. A conventional (single-compartment) three electrode electrochemical cell was used, with a Metrohm planar platinum counter electrode and a reference electrode. For the aqueous solutions a Metrohm saturated calomel (Hg/Hg_2Cl_2) (SCE) was used as reference electrode, while for non-aqueous solution, a Metrohm Ag/AgCl electrode (a silver wire covered by AgCl, immersed in a saturated LiCl solution in acetonitrile, which was separated from the studied solution by a salt bridge of 0.1 M $[Bu_4N]ClO_4$ in acetonitrile). Pyrolytic graphite (Union Carbide, Φ~ 3mm) was used as a working electrode (WE). This was polished with emery paper 4000 and cleaned in an ultrasonicator, prior to use.

For aqueous solutions, the WE was polarized in a 10^{-3} M solution of the complex under study in phosphate buffer (pH = 4.0 - 5.5) with a scan rate between 50 and 400 mV s^{-1}.

For non-aqueous solutions, the WE was polarized in 10^{-3} M acetonitrile solution of the complex in the presence of 0.1 M $[Bu_4N]ClO_4$.

Solutions were deoxygenated using purified Ar gas (99.9%). While recording the voltammograms, Ar was passed over the solution surface.

2. Materials

Reagent grade chemicals were used and all syntheses and studies were carried out in distilled water.

The potassium salts $K_{10}H_2[(CeO)_3(H_2O)_2(PW_9O_{34})_2]\cdot 18H_2O$ and $K_{10}H_2[(CeO)_3(H_2O)_2(AsW_9O_{34})_2]\cdot 21H_2O$ have been prepared by the reported procedures [27, 28] and their purity have been proved by chemical analysis and IR spectra.

Synthesis of $[Bu_4N]_{10}H_2[(CeO)_3(PW_9O_{34})_2]$

To a solution of 1.0 g $K_{10}H_2[(CeO)_3(H_2O)_2(PW_9O_{34})_2]$ $18H_2O$ (0.176 mmol) in 30 mL hot water at pH= 4.5-5.0, 2.0 g $[Bu_4N]Br$ (6.204 mmol) were added under vigorous stirring. A pale yellow precipitate was formed, which was removed by vacuum filtration on G_3 frite, washed with 10 mL distilled water, dried under suction for 2 h and then over P_2O_5 for 24h. Yield: 1.23 g (95.45%).

Calcd. for: $[(C_4H_9)_4N]_{10}H_2[(CeO)_3(PW_9O_{34})_2]$ P: 0.84; W: 45.00; Ce: 5.71.

Found: P: 0.77; W: 45.22; Ce: 5.62.

Synthesis of $[Bu_4N]_{10}H_2[(CeO)_3(AsW_9O_{34})_2]$

To a solution of 1.0 g $K_{10}H_2[(CeO)_3(H_2O)_2(AsW_9O_{34})_2]$ $21H_2O$ (0.171 mmol) in 50 mL hot water at pH= 4.5-5.0, 2.0 g $[Bu_4N]Br$ (6.204 mmol) were added under vigorous stirring. A pale yellow precipitate was formed. which was removed by vacuum filtration on G_3 frite, washed with 10 mL distilled water, dried under suction for 2 h and then over P_2O_5 for 24h. Yield: 1.22 g (95.84%).

Calcd. for: $[(C_4H_9)_4N]_{10}H_2[(CeO)_3(AsW_9O_{34})_2]$ As: 2.01; W: 44.46; Ce: 5.65.

Found: As: 1.89; W: 44.61; Ce: 5.58.

Results and Discussions

The cyclic voltammograms of the $[(CeO)_3(H_2O)_2(XW_9O_{34})_2]^{12-}$ (X= P, As) complexes recorded in aqueous solutions at pH= 4.0 are depicted in Fig. 2.

Both complexes showed two successive redox peak pairs in the negative potential range, which were attributed to two single electron tungsten centered processes [29]. In this range, the cyclic voltammograms were very similar to that of the parent anion, indicating a lack of influence by the Ce(IV) present in the polyoxometalate framework. However a negative shift of the peaks provides proof for the coordination of the Ce(IV) to the trilacunary polyanions.

Two additional successive redox peak pairs appear in the positive range, which were assigned to two single electron cerium-centered processes [5]. The existence of two waves for the Ce(III)/Ce(IV) redox couple could be explained by the nonequivalence of the Ce atoms in the polyoxotungstate framework, where one Ce atom is six coordinated and the other two are seven coordinated [30].

The formal standard potentials $\varepsilon^{0'}$ (estimated as the average of anodic and cathodic peak potentials) of the tungstophosphate complex are negatively shifted by comparing with its tungstoarsenate analog (Table 1) which is in agreement with previous reports [31].

The positive shift of the formal standard potentials $\varepsilon^{0'}$ observed in Ce(IV) complexes when compared to the Ce(III) analogs [30], could be due to the lower negative charge of the Ce(IV) polyoxometalate complexes.

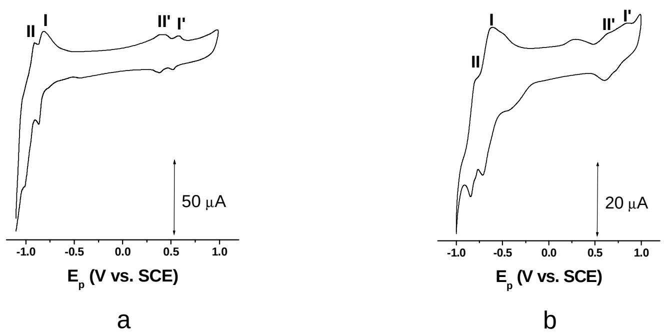

Fig. 2. Cyclic voltammograms of $K_{10}H_2[(CeO)_3(OH_2)_2(PW_9O_{34})_2]\cdot18H_2O$ (a) and $K_{10}H_2[(CeO)_3(OH_2)_2(AsW_9O_{34})_2]\cdot21H_2O$ (b) recorded in aqueous solutions (pH= 4.0, v= 50 mV s^{-1}).

Table 1.

CV data for the $[(CeO)_3(H_2O)_2(XW_9O_{34})_2]^{12-}$ in aqueous solutions.

Process	$E_{p,a}$ (V)	$E_{p,c}$ (V)	$\varepsilon^{0'}$ (V)	ΔE_p (V)
$K_{10}H_2[(CeO)_3(OH_2)_2(PW_9O_{34})_2]\cdot18H_2O$				
I'	0.575	0.510	0.542	0.065
II'	0.399	0.379	0.389	0.020
I	-0.800	-0.852	-0.826	0.052
II	-0.921	-0.999	-0.960	0.078
$K_{10}H_2[(CeO)_3(OH_2)_2(AsW_9O_{34})_2]\cdot21H_2O$				
I'	0.812	0.738	0.775	0.074
II'	0.631	0.610	0.620	0.021
I	-0.619	-0.710	-0.664	0.091
II	-0.801	-0.836	-0.818	0.035

[a] E_{pa}, oxidation potential; E_{pc}, reduction potential; $\varepsilon^{0'}$ formal standard potential estimated as the average of anodic and cathodic peak potentials, ΔE_p the difference between the redox peak potentials. Experimental conditions: H_3PO_4-Na_2HPO_4 buffer solution; pH 4.0, 25℃; graphite working electrode; scan rate 100 mV·s^{-1}; c= 10^{-3}M, potentials recorded *vs* SCE.

The linear relationships between peak currents and the square root of the scan rates for redox waves I (Fig. 3) suggest the diffusion control of the electrochemical processes [32].

Changes in the pH resulted only in minor variations of the formal standard potential $\varepsilon^{0'}$, which imply that protons were not involved in the redox processes [30].

In order to investigate the influence of the different cations on the electrochemical behavior of the polyoxotungstocerate (IV) complexes, their tetrabutylammonium salts have been studied in acetonitrile solutions.

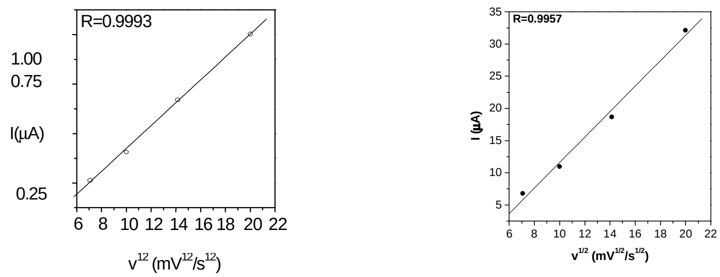

a b

Fig. 3. Dependence of the cathodic peak I current on the scan rate for: $K_{10}H_2[(CeO)_3(OH_2)_2(PW_9O_{34})_2]\cdot18H_2O$ (a) and $K_{10}H_2[(CeO)_3(OH_2)_2(AsW_9O_{34})_2]\cdot21H_2O$ (b) (pH=4.0).

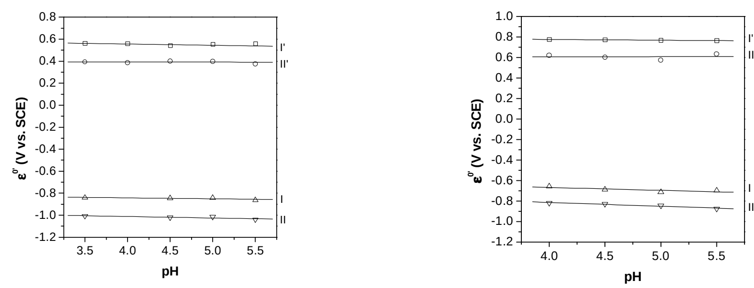

a b

Fig. 4. Dependence of the formal standard potentials on the pH for: $K_{10}H_2[(CeO)_3(OH_2)_2(PW_9O_{34})_2]\cdot18H_2O$ (a) and $K_{10}H_2[(CeO)_3(OH_2)_2(AsW_9O_{34})_2]\cdot21H_2O$ (b) (v= 100 mV s^{-1}).

When 0.1 M $[Bu_4N]ClO_4$ was used as supporting electrolyte, only one pair of waves were observed in the negative potential range for 9-tungstophosphate derivative, while the 9-tungstoarsenate analog exhibited two pair of peaks (Fig. 5). These were assigned to W(VI)/W(V) processes in the polyoxometalate framework. Both complexes, in acetonitrile solution showed only one peak pair in the positive potential range, due to the Ce(III)/Ce(IV) processes, suggesting equivalence of all the cerium ions present in the structure.

When increasing $LiClO_4$ quantities were added to the acetonitrile solutions of the polyoxometalates, while keeping the ionic strength constant at 0.1 by adding $[Bu_4N]ClO_4$, dramatic changes were observed in the voltammograms (Fig. 6). At high Li^+ concentrations, two additional peaks (II and III) appeared in the negative potential range, while the peaks I and I' shifted to more positive values.

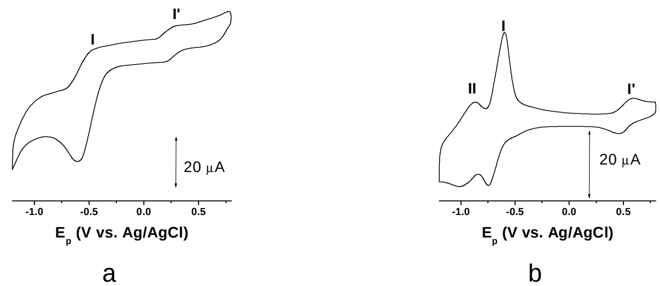

Fig. 5. Cyclic voltammograms of $[Bu_4N]_{10}H_2[(CeO)_3(PW_9O_{34})_2]$ (a) and $[Bu_4N]_{10}H_2[(CeO)_3(AsW_9O_{34})_2]$ (b) (0.1 M $[Bu_4N]ClO_4$ in acetonitrile, v= 100 mV s^{-1}).

The positive shift of the peaks observed upon increasing the Li^+ concentration could be attributed to the association of Li^+ ions with the reduced forms of the polyoxometalates [33, 34].

Table 2.

CV data for the $[(CeO)_3(XW_9O_{34})_2]^{12-}$ in acetonitrile solutions.

Process	$E_{p,a}$ (V)	$E_{p,c}$ (V)	$\varepsilon^{0'}$ (V)	ΔE_p (V)
$[Bu_4N]_{10}H_2[(CeO)_3(PW_9O_{34})_2]$				
I'	0.212	0.268	0.265	0.056
I	-0.582	-0.470	-0.526	0.112
$[Bu_4N]_{10}H_2[(CeO)_3(AsW_9O_{34})_2]$				
I'	0.461	0.584	0.522	0.123
I	-0.744	-0.593	-0.668	0.151
II	-1.009	-0.865	-0.937	0.144

E_{pa}, oxidation potential; E_{pc}, reduction potential; $\varepsilon^{0'}$ formal standard potential estimated as the average of anodic and cathodic peak potentials, ΔE_p the difference between the redox peak potentials. Experimental conditions: 0.1 M $[Bu_4N]ClO_4$ acetonitrile solution; 25℃; graphite working electrode; scan rate 100 mV·s^{-1}; c= 10^{-3}M, potentials recorded *vs* Ag/AgCl.

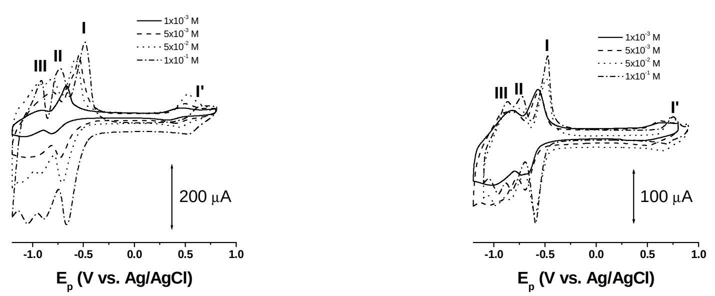

Fig. 6. Cyclic voltammograms of $[Bu_4N]_{10}H_2[(CeO)_3(PW_9O_{34})_2]$ (a) and $[Bu_4N]_{10}H_2[(CeO)_3(AsW_9O_{34})_2]$ (b) at different concentrations of $LiClO_4$ (0.1 M $[Bu_4N]ClO_4$ in acetonitrile, v= 100 mV s^{-1}).

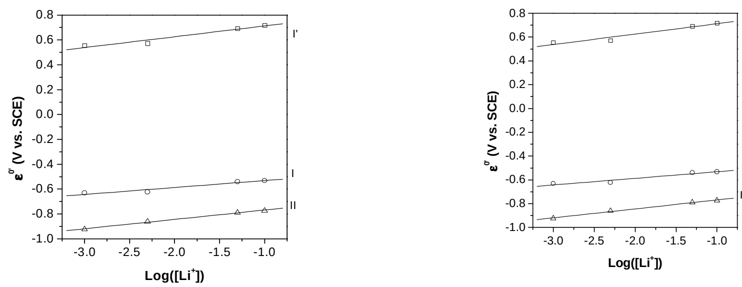

a

b

Fig. 7. Dependence of the formal standard potentials on the Li^+ concentration for: $[Bu_4N]_{10}H_2[(CeO)_3(PW_9O_{34})_2]$ (a) and $[Bu_4N]_{10}H_2[(CeO)_3(AsW_9O_{34})_2]$ (b) (v= 100 mV s^{-1}).

The liniar relationships between the Log([Li^+]) and the formal standard potential $\varepsilon^{0'}$, with slopes of 0.078 (I'), 0.064 (I) and 0.096 (II) for the phosphotungstate derivative, and 0.087 (I'), 0.056 (I) and 0.075 (II) for its arsenotungstate analog, sugest that one Li^+ cation is envolved in each redox process, according to the following equations:

I': $[(Ce^{IV}O)_3(XW_9O_{34})_2]^{12-} + e^- + Li^+ \leftrightarrow Li[(Ce^{III}O)(Ce^{IV}O)_3(XW_9O_{34})_2]^{12-}$
I: $Li[(Ce^{III}O)(Ce^{IV}O)_3(XW_9O_{34})_2]^{12-} + e^- + Li^+ \leftrightarrow Li_2[(Ce^{III}O)(Ce^{IV}O)_3(XW_9O_{34})_2]^{12-}$
II: $Li_2[(Ce^{III}O)(Ce^{IV}O)_3(XW_9O_{34})_2]^{12-} + e^- + Li^+ \leftrightarrow Li_3[(Ce^{III}O)(Ce^{IV}O)_3(XW_9O_{34})_2]^{12-}$

Conclusions

The results of the performed investigations revealed that the electrochemical properties of the sandwich-type polyoxotungstocerate (IV) $[(CeO)_3(H_2O)_2(PW_9O_{34})_2]^{12-}$ and $[(CeO)_3(H_2O)_2(AsW_9O_{34})_2]^{12-}$ are different in aqueous and non-aqueous solution, suggesting different coordination of the cerium (IV) in aqueous and non-aqueous media. The addition of increasing amounts of the Li^+ cations results in a positive shift of the peaks which could be explained by the association of lithium ions with the reduced form of the polyoxotungstocerate.

REFERENCES

1. M.T. Pope, "Heteropoly and Isopoly Oxometalates", Springer-Verlag: Berlin, 1983.
2. M. T. Pope, A. Müller (Eds.), "Polyoxometalates: From Platonic solid to Anti-RetroViral ActiVity", Kluwer: Dordrecht, 1994.
3. G. Marcu, M. Rusu, "Polyoxometalates Chemistry", Ed. Tehnică: Bucureşti, 1997.
4. T. Yamase, *Chemical Review*, **1998**, *98*, 307-326.
5. A. Müller, F. Peters, M. T. Pope, D. Gatteschi, *Chemical Review*, **1998**, *98*, 239– 272.
6. M. T. Pope, A. Müller, A. (Eds.) "Polyoxometalate Chemistry: From Topology Via Self-Assembly to Applications", Kluwer: Dordrecht, 2001.

7. Yamase, T.; Pope, M. T. (Eds.), "Polyoxometalate Chemistry for Nanocomposite Design", Kluwer Academic/Plenum Publishers, 2002.
8. J. J. Borrás-Alamenar, E. Coronado, A. Müller, M. T. Pope (Eds.), "Polyoxometalate Molecular Science, NATO Science series"; Kluwer Academic Publishers, 2003.
9. R. D. Peacock, T. J. R. Weakley, *Journal of the Chemical Society A: Inorganic, Physical, Theoretical*, **1971**, 1836-1839.
10. R. D. Peacock, T. J. R. Weakley, Journal of the Chemical Society A: Inorganic, Physical, Theoretical, **1971**, 1937-1940
11. M. Sugeta, T. Yamase, *Bulletin of the Chemical Society of Japan*, **1993**, *66*, 444-449.
12. T. Yamase, K. Uheda, *Journal of The Electrochemical Society*, **1993**, *140*, 2378-2384.
13. T. Yamase, M. Sugeta, *Journal of the Chemical Society, Dalton Transactions*, **1993**, 759-765.
14. T. Yamase, T. Ozeki, I. Kawashima, *Acta Crystallographica Section C*, **1995**, *51*, 545-547.
15. H. Naruke, T. Yamase, *Acta Crystallographica Section C*, **1996**, *52*, 2655-2660.
16. T. Yamase, T. Kobayashi, M. Sugeta, H. Naruke, *Journal of Physical Chemistry A*, **1997**, *101*, 5046-5053.
17. M. Sugeta, T. Yamase, Acta Crystallographica Section C, **1997**, *53*, 1166-1170.
18. K. Wassermann, M.H. Dickman, M.T. Pope, *Angewandte Chemie International Edition in English*, **1997**, *36*, 1445-1448.
19. H. Naruke, T. Yamase, *Journal of Alloys and Compounds*, **1997**, *255*, 183-189.
20. H. Naruke, T. Yamase, *Journal of Alloys and Compounds*, **1998**, *268*, 100-106.
21. X. Wei, K. Wasserman, M.H. Dickman, M.T. Pope, *Comptes rendus de l'Académie des sciences. Series IIC, Chemistry*, **1998**, *1*, 297-304.
22. T. Yamase, H. Naruke, *Journal of Physical Chemistry B*, **1999**, *103*, 8850-8857.
23. Ostuni, M.T. Pope, *Comptes rendus de l'Académie des sciences. Series IIC, Chemistry*, **2000**, *3*, 199-204.
24. H. Naruke, T. Yamase, *Bulletin of the Chemical Society of Japan*, **2000**, *73*, 375-382.
25. N. Yamamoto, D. Schols, E. De Clercq, Z. Debyser, R. Pauwels, J. Balzarini, H. Nakashima, M. Baba, M. Hosoya, R. Snoeck, J. Neyts, G. Andrei, B.A. Murrer, B. Theobald, G. Bossard, G. Henson, M. Abrams, D. Picker, *Molecular Pharmacology*, **1992**, *42*, 1109-1117.
26. Y. Inouye, Y. Tokutake, T. Yoshida, T. Seto, H. Fujita, K. Dan, A. Yamamoto, S. Nishiya, T. Yamase, S. Nakamura, *Antiviral Research*, **1993**, 20, 317-331.
27. W. H. Knoth, P. J. Domaille, R. L. Harlow, *Inorganic Chemistry*, **1986**, *25*, 1577-1584.
28. Li-Hua Bi, Wei-Hong Zhou, Feng-Tian Mu, *Synthesis and Reactivity in Inorganic, Metal-Organic, and Nano-Metal Chemistry*, **2002**, *32*, 1127-1140.
29. M. Sadakane, E. Steckhan, *Chemical Review*, **1998**, *98*, 219-238.
30. A. R. Tomşa, L. Mureşan, A. Koutsodimou, P. Falaras, M. Rusu, *Polyhedron*, **2003**, *22*, 2901-2909.
31. K. Maeda, S. Himeno, T. Osakai, A. Saito, T. Hori, *Journal of Electroanalytical Chemistry*, **1994**, *364*, 149-154.
32. X. Xi, G. Wang, B. Liu, S. Dong, *Electrochimica Acta*, **1995**, *40*, 1025-1029.
33. S. Himeno, M. Takamoto, *Journal of Electroanalytical Chemistry*, **2000**, *492*, 63-69.
34. S. Himeno, M. Takamoto, T. Ueda, *Journal of Electroanalytical Chemistry*, **2000**, *485*, 49-54.

STUDIA UNIVERSITATIS BABES - BOLYAI, CHEMIA, LI, 2, 2006

Dedicated to professor Gh. Marcu at his 80th anniversary

SYNTHESIS, SPECTRAL AND THERMAL STUDIES OF {[2-[(2,6-DICHLOROPHENYL)AMINO]PHENYL} ACETATE OF RUTHENIUM (III) AND RHODIUM (III)

L. GHIZDAVU*

ABSTRACT. The reactions of $RuCl_3$ and $RhCl_3$ with deprotonated diclofenac (**L**) were studied in aqueous solution. Coordination compounds of the formulae $[Ru(L)_3 (H_2O)_3]3H_2O$ and $[Rh(L)_3{\cdot}(H_2O)_3]{\cdot}2H_2O$ were isolated as solid products and characterized by elemental analyses and spectroscopic (IR, UV-VIS) and thermal studies. In all studied compounds, {2-[(2,6-dichlorophenyl)amino]-phenyl}acetate acts as monodentate ligand with coordinate involving the carboxylate oxygen atom.

INTRODUCTION

Diclofenac, sodium {2-[(2,6-dichlorophenyl)amino]phenyl}acetate is a potent non-steroidal antiinflammatory drug (NSAID), therapeutically used in inflammatory and painful diseases of rheumatic and non-rheumatic origin. The anti-inflammatory activity of diclofenac and most of its other pharmacological effects are thougth to be related to the inhibition of the conversion of arachidonic acid to prostaglandins, which are the mediators of the inflammatory processes [1,2]. Like other NSAIDs, diclofenac is highly (>95%) protein bound. [1]

The interaction of metal ions with drugs administered for therapeutic reasons is a subject of considerable interest. It is known that the drugs act via chelation or by inhibiting the activity of metalloenzymes, but for most of the drugs such as diclofenac little is known about how metal binding inflences their activity.

As part of our research on understanding drug-metal interaction, we have studied the coordination ability of diclofenac with trasition metal ions.

EXPERIMENTAL

Spectrophotometric titration

Electronic absorption spectroscopy is frequentely used to study metal binding to the ligand. [3-8]

Spectrophotometric titration of ruthenium (III) and rhodium (III) with sodium {[2-(2,6 dichlorophenyl) amino] phenyl}acetate is presented.

Preparation of compounds

The coordination compounds were prepared by mixing hot aqueous solutions of the ligand diclofenac (sodium salt tetrahydrate) (pH~5,5-6,5) and aqueous solutions of metal salts (3:1 ligand to metal molar ratio). The reaction mixture was stirred for 5h at 323K. The resulting powders were filtered, washed with hot water to remove Na^+ and Cl^- ions, dried at 303K to a constant mass. The yields and the elemental analyses are presented in Table 1.

Table 1.

Analytical data of compounds.

Compound	GM	Yield	Elemental analysis, [%] found, (calcd.)				
		[%]	C	H	N	Cl	M
$[Na(H_2O)_4]^+L^-$ **1**	390,07		43,15 (43,06)	4,64 (4,61)	3,55 (3,59)	17,40 (18,17)	5,57 (5,89)
$[Ru(L)_3(H_2O)_3]\cdot 3H_2O$ **2**	1093,87	91,6	46,15 (46,07)	3,96 (3,84)	3,50 (3,84)	19,40 (19,44)	9,61 (9,24)
$[Rh(L)_3(H_2O)_3]\cdot 2H_2O$ **3**	1077,42	92,4	46,59 (46,77)	4,10 (3,90)	3,52 (3,90)	19,21 (19,64)	9,50 (9,55)

Where $L = (C_{14}H_{12}O_2NCl_2)^-$.

Measurements

The carbon, hydrogen and nitrogen content in the coordination compounds were determined by elemental analyses using a Perkin Elmer CAN 2000 analyzer. The chlorine content was measured by the Schöninger method. The Ru(III) and Rh(III), contents was determined by AAS method using an Atomic Absorbtion Spectrometer AAS-3 (Carl Zeiss, Jena). The experimental results are concordant with the calculated data (Table 1).

Thermal analysis were performed with an OD-103 MOM Derivatograph using a sample weight of 100±1-2 mg, at a heating rate of 10 K min^{-1}, with Al_2O_3 as reference material in static air atmosphere.

IR spectra were recorded over the range of 4000-400 cm^{-1} using a FT-IR JASCO 600 spectrophotometer, in KBr pellets. UV-VIS spectra were recorded with an UV-VIS Specord Spectrophotometer Carl Zeiss Jena [1].

RESULTS AND DISCUSSION

The coordination compounds: $[Ru(L)_3(H_2O)_3]\cdot 3H_2O$ (**2**), and $[Rh\ (L)_3(H_2O)_3]\cdot 2H_2O$ (**3**), were formed according to egs:

$$MCl_3 + 3NaL + nH_2O \longrightarrow [M(L)_3(H_2O)_3]^{\cdot}\ nH_2O + 3NaCl$$

were M=Ru(III), Rh(III) and n=3,2.

The compounds are brown, microcrystaline powdery solids, that appear to be air- and moisture-stable. They are soluble in methanol, ethanol, acetone, benzene, DMF, DMSO and insoluble in water. The colour of the coordination compounds is typical of the particular ion salts, i.e. Ru (III) and Rh (III), having their origin in the lowest energy of **d** – **d** electronic transitions of the central ions [7]. The structure of coordination compounds 2 and 3 is supported by thermal analysis, IR and UV-VIS spectroscopic data.

UV-VIS spectra

The sodium diclofenac, is a colorless compound with an intense ultraviolet absorbtion band in the 214nm region, due to the allowed intraligand π-π^* transitions and an additional band in the 270 nm region, assigned to the n-π^* transition [24,25]. The binding of metal ions to the carboxylate group of the diclofenac leads to the production of two new absoption bands at ca 236 nm and 285 nm in the UV-difference spectra.

Table 2.

Electronic spectral data (nm) of the ligand and their coordination compounds in aqueous solution

Compound	λ (nm (ε)			
1	214 (6000)	270 (8000)		
2	230 (6500)	288 (8200)	500 (800)	604 (780)
3	239 (6550)	285 (8250)	515 (805)	608 (790)

The isobestic point situated at 236 nm (Fig.1) point out the formation of the metal coordination compound.

IR –spectra

The vibration modes of coordinated ligands in the complexes have been investigated by means of infrared absorbtion spectra. The most important infrared frequencies attributed to the vibrations of the compounds 1 – 3 are reported in Table 3.

The absorption bands ν_{OH} and ν_{HOH} which occur in the range 3482 - 3495 cm^{-1}, confirm the presence of water of crystallization. The absorbtion bands νM-O_{H_2O} which occur in the range 425 – 418 cm^{-1} confirm the presence of coordinated water in the complexes[12]. The presence of water as water of crystallization and as coordinated water in the compounds is confirmed by the thermal decomposition data.

As the carboxylic hydrogen is more acidic than the amino hydrogen, the deprotonation occurs in the carboxylate group. This is characteristic bands for the secondary amino groups and for the coordinated carboxylate group [5,13–15]. The strong band at 3388 cm^{-1}, which appears in diclofenac, is assigned to the stretching motion and the broad band at 3260 cm^{-1} is taken to represent the $\nu_{NH...O}$ mode, due to intramolecular hydrogen bonding [5].The absence of large systematic shifts of the ν_{NH} and δ_{NH} bands in the spectra of the coordination compounds **2,3** compared with those of the ligand indicates that there is not interaction between the NH group and the metal ions.

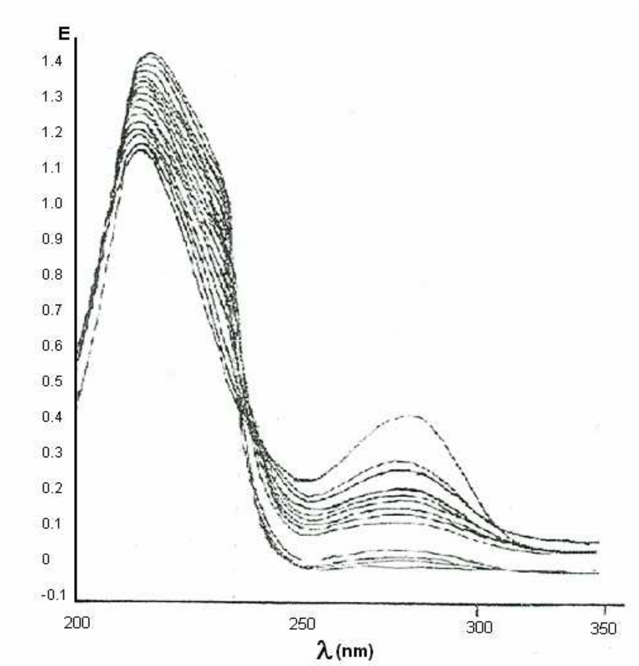

Fig.1. Titration curves of ruthenium (III) chloratum with Sodium diclofenac

Table 3.
Frequences of characteristic absorbtion bands in IR spectra of sodium {2–(2,6-diclorophenyl)amino]phenyl}acetate tetrahydrate and its coordination compounds (cm^{-1}).

Compound	ν OH; ν OHO	ν_{as} COO^-	ν_{sCOO^-}	$\Delta\nu_{COO^-}$	$\nu M-O_{H_2O}$	$\nu M-O_{COO^-}$
1	3560 br	1572 s	1402 s	170	410 mw	-
2	3482 br	1670 s	1346 s	324	425 mw	403 m
3	3495 br	1683 s	1350 s	333	418 w	-402 m

∗ s = strong, m = medium, w = weak, br = broad

The IR spectra bring evidence of the carboxylate ions modus/type to metal ions such as unidentate, bidentate (chelating) or bridging and there is an evidence of that fact in the IR spectrum. The analysis of COO^- group bands frequencies allowed the determination of parameter $\Delta COO^- = \nu\ COO^-$ (as) - $\nu\ COO^-$ (s).

The separations between ν_{as} and ν_s, $\Delta\nu$, in a bidentate (chelate) complex will be significantly smaller than in the free ion; in the bridging complex the $\Delta\nu$ value is that of the to the free ion, while in the monodentate complex it will be higher[13,14]. For complexes **2** and **3** the difference $\Delta\nu > 170\ cm^{-1}$ is higher than that of the free ion (sodium diclofenac salt) and is assigned to the stretching mode for the monodentate carboxylate ligation. Calculated from the examined spectra, the values of $\Delta\nu$ of the coordination compounds **2** and **3** occur in the range domain 324 – 333 cm^{-1}. These values of two bands (COO^- deformation) in coordination compounds **2** and **3** are in good agreement with the literature data for unidentate bonded acetates structures [24]. The absorbtion bands which occur in the range 402– 405 cm^{-1} ν(M-O) confirm the coordination of diclofenac to metallic ions through the oxigen atom of the carboxylate group.

Thermal behavior

The thermal behavior of the ligand and of the synthesized coordination compounds **2** and **3** is presented in Table 4. Thermal stability domains, decomposition phenomena (endo and exo effects in the DTA curves and mass losses, calculated from the TG and DGT cuves) and their assignment are presented.

Between 293-473 K an endo peak at 403 K in the TDA curve of $[Na(H_2O)_4]^+L^-$ indicates the loss of four water molecules. X-ray scattering studies[17] show that in various criystalline salts, Na^+ forms tetrahedral $[Na(H_2O)_4]^+$ ions, with the $4H_2O$ molecules directly coordinated. These results are in agreement with structure and thermal behaviour of sodium diclofenac salts studied by [18-21].

Table 4.

Thermal data of the synthesized coordination compounds

Compound	Temp. Range, K	DTA peak, K Endo	Exo	TG data, % Calc.	Exp	Assignment
1	293 – 473	403	-	18,45	18,21	$4H_2O$
	473 – 1273	555	-	-	-	Melting
		-	558	11,28	11,15	CO_2
		-	673	55,22	55,46	Pyrolysis of organic rest
		1048	-	14,98	14,71	NaCl residue
2	293 – 473	371	-	2,73	2,66	$3H_2O$
		450	-	2,73	2,68	$3H_2O$
	473 – 1273	-	511	2,22	2,31	CO_2
		-	685	83,08	83,03	Pyrolysis of organic rest
		-	1053	15,22	15,75	Ru_2O_3 residue
3	293 – 473	378	-	3,34	3,20	$2H_2O$
		435	-	5,02	5,08	$3 H_2O$
	473 – 1273	-	508	4,08	4,03	CO_2
		-	692	79,01	79,22	Pyrolysis of organic rest
		-	1060	11,78	11,34	Rh_2O_3 residue

The anhydrous sodium diclofenac, NaL is stable up to 555 K where an endo peak marks its melting. The decomposing starts with the shoulder at 558 K which was assigned to the lose of one carboxylate group. In the temperature range 473-1273 K an exothermic peak situated at 673 K marks the pyrolysis of the organic residue. At 1048 K the formation of NaCl residue is observed. The coordination compounds synthesized, **2** and **3** are stable in air and can be stored without change. When heated in air, the coordination compounds decompose in various ways (Table 4). According to literature data[12,22-25] water released below 423 K can be considered as crystallization water, whereas that eliminated above 423 K, as chemically bounded to the central ion through weak coordination bonds.

The decomposition of the coordination compounds **2** and **3** occurs in the 435-450K temperature range, when the coordination water separate from each molecule. The stepped dehydration reaction is observed, the two endo peaks at 371K, 378K and 450K, 435K corresponding to the loss of three and two molecules of hydrating water and three molecules of coordination water, respectively.

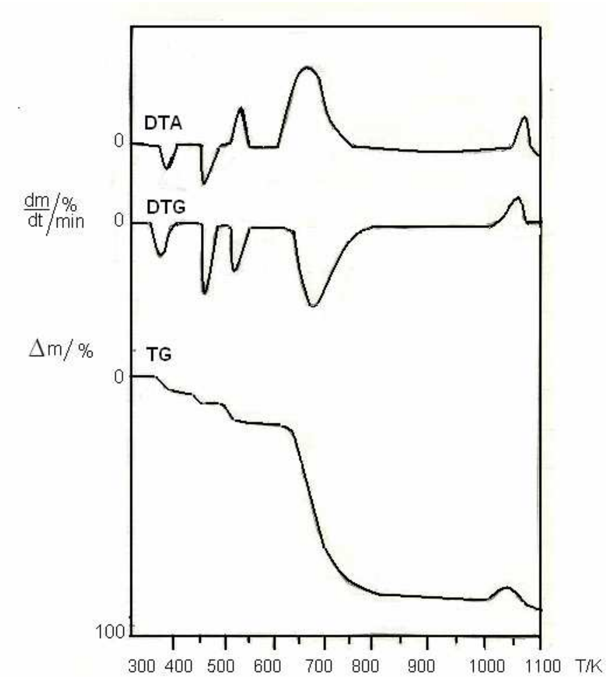

Fig.2. TG, DTG and DTA curves of the coordination compound **2**

The thermal decomposition with the shoulder at 511K and 508 K indicate the destabilization of the ligand due to the weakening of the carboxylate bound as a consequence of M-O bond formation in the coordination compounds.

An exothermic peak situated at 685K and 692K, marks the pyrolysis of the organic residue. In the 720K-1273K temperature range, the formation of intermediated is observed, followed by the thermal decomposition to oxides: Ru_2O_3 , Rh_2O_3 respectively.

The thermal analyses results of the investigated compounds confirm the atom ratio M:L:O = 1:3:3.

CONCLUSIONS

The coordination compounds **2** and **3** are stable in air and soluble in methanol, ethanol and benzene. Heating the compounds first results in a release of crystallization water molecules in complexes **2** and **3**. The decompozition of the compounds **2** and **3** occurs with the loss of the coordination water and is continued with thermal decompozition of the ligand (L). The results reveal that metallic oxides are left as residues. Infrared data are in accordance with the literature data for unidentate bonded acetates structures of complexes **2** and **3** [23,24]. Diclofenac is coordinated to metal (III) through the oxygen atom of its carboxylate group.

REFERENCE

1. P.A.Todd, E.M.Sorkin, *Drugs*., **1988**, *35*, 244
2. P.Moser, A.Sallmann, I.Wiesenberg, *J.Med.Chem*., **1990**, 33, 2358
3. D.P.Kessisoglou, G.E.Manoussakis, A.G.Hatjidimitrion, M.G.Kanatzidis, *Inorg. Chem*., **1987**, *26*, 1395.
4. I.Konstantidinou, D.Kovala-Demertzi, M.A.Demertzi, *J.Inorg. Biochem*., **1998**, *70*, 63.
5. D.Kovala-Demertzi, S.K.Hadjikakon, M.A.Demertzi, *J.Jnorg. Biochem*., **1998**, *64*, 223.
6. A.B.P.Lever, *Inorganic Electronic Spectroscopy*, Second edition, Elsevier Publishing Company, Amsterdam, **1984**
7. C.N.Rao, *Ultraviolet and Visible Spectroscopy*, Butterworts, London, **1961**
8. J.Kracmar, J.Kracmarova, *Pharmazie*, **1966,** 15 (68), 121.
9. J.Kracmar, J.Kracmarova, Pharmazie, **1966,** 16 (21), 460.
10. J.Kracmar, A.Sotolongo, J.Kracmarova, J.Petranova, *Pharmazie*, **1976**, 31 (9), 614.
11. G.Deveto, G.Ponticelli, C.Preti, *J.Inorg.Nucl.Chem*., **1975**, 37, 1635.
12. S.C.Mojumdar, M.Melnik, E.Jona, *J.Therm. Anal.Cal*., **2000**, 61, 915
13. G.Maistralis, N.Katsaros, S.P.Perlepes, D.Kovala-Demertzi, *J.Inorg, Biochem*., **1992**, 45
14. G.B.Deacon, R.J.Phillips, *Coord. Chem. Rev*., **1980**, 33, 227.
15. K.Nakamoto, *Infrared Spectra of Inorganic and Coordination Compounds*, 2nd edn Wiley Interscience, New York, **1970**.
16. D.Stoilova, G.Nikolov, K.Balarev, Izv.Akad.Nauk SSSR, Ser.Khim., **1976**, 9, 371
17. F.A.Cotton, G.Wilkinson, *Advanced Inorganic Chemistry*, Fifth Ed., John Wiley & Sons, New York, **1988**
18. G.Reck, G.Faust, G.Dietz*, Die Pharmazie*, **1988**, 43 (11), 771.
19. P.W.Borthwich, *Acta Cryst*., **1980**, B36, 628.
20. R.Mattes, G.Uckelmann, *Acta Cryst*., **1981**, B37, 207
21. V.Barrans, M.Alleaume, G.Jeminet, *Acta Cryst*., **1892**, 338, 1144.
22. A.V.Nikolaev, V.A.Lodviengo, L.J.Myachina, *Thermal Analysis*, vol.2, Academic Press, New York, **1969**
23. B.Singh, B.A.Agarwala, P.L.Mourya, A.K.Dey, *J.Indian Chem.Soc*., **1992**, 59, 1130.
24. R.C.Mehotra, R.Bohra, *Metal Complexes*, Academic Press, Oxford, **1998**
25. W.Brzyska, W.Ozga, *J.Therm.Anal.Cal*., **2002**, 70, 467.

STUDIA UNIVERSITATIS BABES - BOLYAI, CHEMIA, LI, 2, 2006

Dedicated to professor Gh. Marcu at his 80th anniversary

THE USE OF ORGANODITHIOPHOSPHORIC ACIDS FOR SEPARATION AND DETERMINATION OF SOME METAL IONS FROM RESIDUAL WATERS

MARIA-LOREDANA SORAN[1], MARIA CURTUI[2], IOVANCA HAIDUC[3], DIANA GHERMAN[2]

ABSTRACT. The U(VI), Cu(II) and Ni(II) separation was performed by thin layer chromatography on silica gel H, using o,m,p-xylene, methyl-ethyl-ketone (MEK) and N,N-dimethylformamide (DMF) (16: 2: 1, v/v) mixture as mobile phase. The di(n-pentyl)dithiophosphoric acid was used as complexing agent introduced in the mobile phase. This method was applied for quantitative determination of studied metal ions from waste waters.

Key words: thin layer chromatography, metal ions, di(n-pentyl)dithio- phosphoric, quantitative determination

INTRODUCTION

In the last years many studies are devoted to the identification, separation and determination of trace metal ions in particular samples, because of their strong environment impact. Uranium, natural occurring actinide, is found at a trace level in the environment or associated with other metal ions in complex mixtures, nuclear fission products, and geological materials. Many methods have been proposed for the separation and determination of uranium and other metals. One of these techniques, more suitable due to the simplicity in handling radioactive elements is chromatography. In particular, extraction chromatography which combines the selectivity of organic extractants with multistage feature of chromatographic process has been extensively applied in the analysis of the radioactive materials [1-3].

In recent years thin layer chromatography (TLC), widely applied in pharmaceutical and food industries, biochemistry, and has been used in metal ions analysis because of their simplicity, low cost of qualitative analysis and short time of separation. TLC technique has been employed using different complexants fixed on silica gel or another supports or included in organic solvents used as eluents [4-9].

Organophosphorus compounds have been intensively investigated as complexants in separation of metal ions [8, 9]. Their analogues when one or more oxygen atoms have been replaced by sulphur atoms have been used in lesser extent.

[1] National Institute of Research & Development for Isotopic and Molecular Technology, 72-103 Donath Street, RO-400293 Cluj-Napoca, Romania; E-mail: *loredana_soran@yahoo.com*
[2] Faculty of Chemistry and Chemical Engineering, 11 Arany János, RO-400028, Cluj-Napoca, Romania
[3] Faculty of Environmental Science, 4 Stefan cel Mare, Cluj-Napoca, Romania

Dialkyldithiophosphoric acids are well known as good complexing agents for metal ions [10-12]. The metal chelates formed with organodithiophosphate anions are soluble in organic solvent which make these ligands useful in liquid-liquid extraction [13-18].

Dialkyldithiophosphoric complexants containing different alkyl chains were also investigated as extractants in the chromatographic technique. In our earlier work we have been investigated the extraction of U(VI), Th(IV) and lanthanides with various dialkyldithiophosphoric acids [19-23] and later we extended our investigations on the separation of metal ions by electrophoresis [24] and TLC [25-29].

The work discussed in this paper continues our investigations on the separation of the metal ions by TLC using dialkyldithiophosphoric acids. The work is undertaken to obtain information about TLC behavior of U(VI), Cu(II) and Ni(II) on silica gel H using di(n-pentyl)dithiophosphoric acid (HDPDTP) in mobile phase, in order to establish the optimum conditions for separation and quantitative determination of these elements in different water samples.

EXPERIMENTAL DATA

Apparatus

Normal chromatographic chambers, Brand micropipettes (5 μL), densitometer (DESAGA CD 60), Varian Tectron A 66 Spectrometer and Spekol Zeiss Yena were used.

Materials

TLC plates coated with silica gel H ("Raluca Ripan" Institute for Research in Chemistry), Arsenazo III and uranium nitrates (Sigma-Aldrich Chemie, Steinheim, Germany) were used. Copper and nickel nitrates and all other reagents were of analytical grade supplied by "Chimopar" Bucharest, Romania. HDPDTP were synthesized according to published procedure [30] and its purity was higher than 95%. Test solutions of metal nitrates were standardized gravimetrically and concentrations were obtained by successive dilutions.

Procedure

Silica gel H was used as stationary phase for separation of U(VI), Cu(II), Ni(II). The mixture of o,m,p-xylene, methyl-ethyl-ketone (MEK) and N,N-dimethylformamide (DMF) (16 : 2 : 1, v/v), containing HDPDTP was chosen as mobile phase after preliminary experiments. Standard solutions of metal ions were spotted on the plates using Brand micropipettes (5 μL). The plates were developed on 10 cm distance in unsaturated normal chromatographic chamber. After development the plate were dried for 15 min in a hood and visualized with 0.05% Arsenazo III aqueous solution for U(VI) and 0.1% rubeanic acid in ethanol for Cu(II) and Ni(II). All operations were performed at the room temperature.

Calibration curves for U(VI), Cu(II) and Ni(II) determination were plotted using spots area determined by two methods, for chromatographic system containing HDPDTP in o,m,p-xylene – MEK – DMF mixture as mobile phase.

Unknown concentration samples were collected from Roşia Montana (Alba), Baia Mare (Maramureş) and Ştei (Bihor) mining exploitations.

RESULTS AND DISCUSSION

The study of the chromatographic behavior of U(VI), Cu(II) and Ni(II) on silica gel H using HDPDTP as complexing agent in organic mobile phase show that R_F values depend on the HDPDTP concentration. From Figure 1 it can be observed the increasing of the retention factor until almost constant value with the increase of complexing agent concentration especially for U(VI).

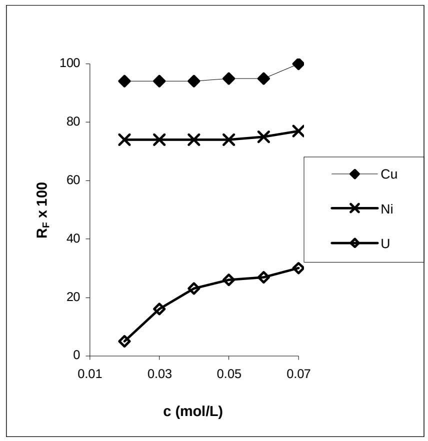

Figure 1. The influence of the HDPDTP concentration in mobile phase upon the R_F values of the metal ions studied

It can be seen also that the separation of U(VI) from Cu(II) – Ni(II) and the separation of Cu(II) – Ni(II) from each other can be achieved in all range of concentration investigated, 0.02 – 0.07M HDPDTP. The best separation with well defined zones is obtained with 0.05M HDPDTP in a mixture of o,m,p-xylene – MEK - DMF (16 : 2 : 1, v/v). In consequence this mobile phase system was used for TLC quantitative determination of U(VI), Cu(II) and Ni(II).

The calibration curve for Cu(II) and Ni(II) determination were obtained by two methods: a) densitometric determination using DESAGA CD 60 densitometer at 505 nm for Cu(II) and 600 nm for Ni(II), and b) scanning TLC plates with a classic scanner linked to a computer. UTHSCSA Image Tool PC based software was used for area determination. Detection limits were determined using the software Statistical Method in Analytical Chemistry [31]. In both cases the shape of the curve is similar.

Figures 2a and 2b show the calibration curves for Cu(II) and Ni(II), respectively.

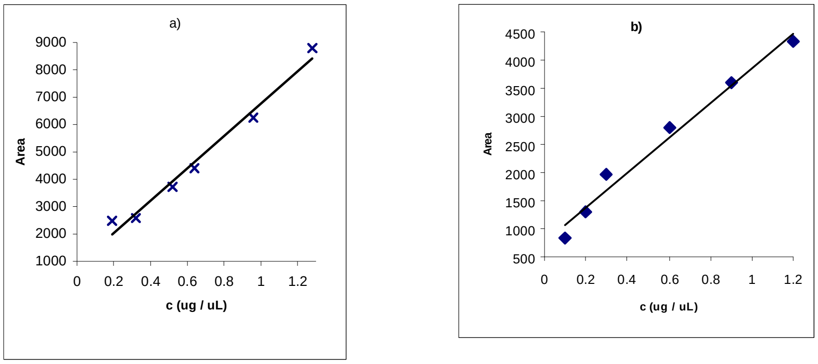

Figure 2. Calibration curve for the determination of: a) Cu(II), b) Ni(II); Stationary phase: silica gel H; mobile phase: o,m,p-xylene – MEK – DMF (16 : 2 : 1, v/v) with HDPDTP 0.05 M

Good linearity is obtained in the concentration range 0.20 – 1.28 μg/μL for Cu(II) and 0.3 – 1.2 μg/μL for Ni(II). The statistic parameters a (intercept), b (slope of the regression lines, y = ax + b), and r (regression factor) are included. The regression factor, detection limit (LD) and quantitative limit (QL) are presented in Table 1.

Table 1

Regression factor, DL and QL values for Cu(II) and Ni(II)

Cation	Method	r	LD (μg/μL)	LQ (μg/μL)
Cu(II)	Photodensitometry	0.9931	0.132	0.244
	UTHSCSA Image Tool software	0.9872	0.176	0.322
Ni(II)	Photodensitometry	0.9864	0.170	0.310
	UTHSCSA Image Tool software	0.9929	0.118	0.215

The calibration curve for U(VI) was obtained only by scanning TLC plates with classic scanner, because of the strong signal noise. Figure 3 show that good linearity is obtained in the concentration range 0.24 – 24 μg / μL and r is 0.9973. DL and QL determined by SMAC software are 1.102 and 2.130 respectively.

Calibration curves (Fig. 1-3) were used for the determination of studied metal ions from mining exploitation waters and the results obtained are presented in Table 2. Cu(II), Ni(II) and U(VI) were also determined by other methods: Flame Atomic Absorbtion Spectrometry (FAAS) (Cu(II), Ni(II)) and spectrophotometric method (U(VI)) [32-34].

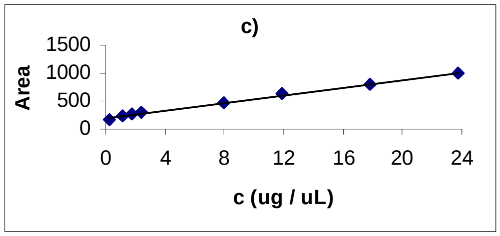

Figure 3. Calibration curve for U(VI); Stationary phase: silica gel H; mobile phase: o,m,p-xylene – MEC – DMF (16 : 2 : 1, v/v) with HDPDTP 0.05 M

Table 2

Analysis of Cu(II). Ni(II) and U(VI) content from water samples

Observed cation	Sample origin	Method/Found concentration (mg / L)		
		FAAS	TLC	e_r(%)
Cu(II)	Ore processing waste water (Baia Mare)	1.50	1.49	-0.67
Ni(II)		2.09	2.12	+1.44
U(VI)	Natural running mine water (Băița)	Spectrophot	TLC	e_r(%)
		1.50	1.48	-1.33

It can be seen a good agreement between TLC data and those obtained by FAAS and spectrophotometric method. Determination by TLC analysis requires preconcentration of the sample, but TLC method has some advantages: short time of analysis, inexpensive and easy getting equipment, rapid qualitative results with no necessary treatment of the sample.

CONCLUSIONS

It was found that U(VI), Cu(II) and Ni(II) can be separated by TLC using HDPDTP as complexing agent in the mobile phase, a mixture of organic solvents: o,m,p-xylene – MEK – DMF (16 : 2 :1, v/v). The mobile phase containing 0.05 M HDPDTP was chosen for TLC quantitative determination of the studied metal ions. Calibration curves plotted for Cu(II), Ni(II) and U(VI) were used for the analysis of unknown samples collected from waste water (Cu(II), Ni(II)) and mine water (U(VI)). The results obtained by TLC method are in a good agreement with those obtained by FAAS and spectrophotometric method.

REFERENCES

1. C.H. Lee, M.Y. Suh, K.S. Choi, J.S. Kim, Y.J. Park and W.H. Kim, Anal. Chim. Acta 475 (2003) 171-179.
2. C.H. Lee, M.Y. Suh, K.S. Choi, J.S. Kim, B.C. Song, K.Y. Jee and W.H. Kim, Anal. Chim. Acta 428 (2001) 133-142.

3. T. Braun and G. Ghersini, Extraction Chromatography, Akadémiai Kiado, Budapest, (1975).
4. Kh.S. Babayan, G.M. Varshal and V.I. Vernadskii, Zhur. Anal. Khim. 28 (1973) 921-927.
5. M.P. Volynets and M.S. Milyukova, Radiokhimiya 13 (1971) 72-78.
6. H. Specker, Chemie fur Labor und Betried 32 (1981) 519-520.
7. R. Kuroda, M. Adachi and K. Oguma, Chromatographia 25 (1988) 989-992.
8. K. Jung and H. Specker, Fresenius' Z. Anal. Chem. 300 (1980) 15-17.
9. J. Wang and Z. Hu, Fenxi Huaxue 16 (1988) 740-742. Chem. Abstr. 110 (1989) 204690.
10. J.R. Wasson, G.M. Watermann and H.J. Stoklosa, Fortschr. Chem. Forsch. (Current Topics Chem.) 35 (1973) 65.
11. I. Haiduc and M. Curtui, Syn. React. Inorg. Metalorg. Chem. 6 (1976) 125-131.
12. I. Haiduc, J. Organomet. Chem. 623 (2001) 29-42.
13. I.P. Alimarin, T.V. Radionova and V.M. Ivanov, Russian Chem. Rev. 58 (1989) 863-877.
14. G. Cote and D. Bauer, Rev. Inorg. Chem. 10 (1989) 121-144.
15. R. Fitousi and C. Musikas, Sep. Sci. Techn. 15 (1980) 845-853.
16. I. Haiduc and M. Curtui, J. Radioanal. Nucl. Chem. 99 (1986) 257-263.
17. I. Haiduc, M. Curtui, Iovanca Haiduc and I. Silaghi-Dumitrescu, Chemical Aspects of Nuclear Methods and Analysis, Proceedings of the Final Research Co-Ordination Meeting organized by International Atomic Energy Agency, Hamanatsu Japan, Oct. 2-5, 1984, IAEA-TECDOC-350, Viena (1985) 101-172.
18. M. Curtui, J. Radioanal. Nucl. Chem., Letters 186 (1994) 273-280.
19. M. Curtui, I. Haiduc and L. Ghizdavu, J. Radioanal. Nucl. Chem. 250 (2001) 359-362.
20. L. Bromberg, J. Phys. Chem. 100 (1996) 1767-1770.
21. A. G. Strikovsky, A. Warshawsky, L. Hankova and K. Jerabek, Acta Polym. 49 (1998) 600-605.
22. S.P. Quináia, J.B.B. da Silva, M.C.E. Rollemberg and A.J. Curtius, Talanta 54 (2001) 687-696.
23. I. Haiduc and M. Curtui, Studia Univ. „Babeş-Bolyai”, Chemia 19 (1974) 71-75.
24. M. Curtui, I. Haiduc and L. Ghizdavu, J. Radioanal. Nucl. Chem. 251 (2002) 163-166.
25. T. Hodişan, M. Curtui and I. Haiduc, J. Radioanal. Nucl. Chem. 238 (1998) 129-133.
26. T. Hodişan, M. Curtui, S. Cobzac, C. Cimpoiu and I. Haiduc, J. Radioanal. Nucl. Chem. 238 (1998) 179-182.
27. M.L. Soran, C. Măruțoiu, M. Curtui and M. Dascălu, Chem. Environ. Res. 12 (2003) 135-139.
28. M.L. Soran, C. Măruțoiu, M. Curtui, T. Hodişan and R. Oprean, Acta Univ. Cibiniensis, Seria F, Chemia 5 (2002) 69-73.
29. L. Soran, T. Hodişan, M. Curtui and D. Casoni, J. Planar Chromatogr.-Mod. TLC 18 (2005) 164-167.
30. K. Sasse, Methoden der Organischen Chemie (Houben-Weyl) Band XII, Teil 2, G. Thieme Verlag, Stuttgart, 1964.
31. P.C., Meier, R.E. Zünd, Statistical Methods in Analytical Chemistry, Ed. John Wiley & Sons, Inc., 1993.
32. S.B. Savin, Talanta, 1961, 8, 673-685.
33. STAS 7795-80: Ape de suprafață şi ape uzate. Determinarea cuprului, 1980.
34. STAS 7987-67: Ape de suprafață şi ape uzate. Determinarea nichelului, 1968.

STUDIA UNIVERSITATIS BABES - BOLYAI, CHEMIA, LI, 2, 2006

Dedicated to professor Gh. Marcu at his 80th anniversary

A QUANTUM CHEMICAL CONFORMATIONAL ANALYSIS OF P-TERT-BUTYL/PENTYL/OCTYL-CALIX[8]ARENES

ALEXANDRU LUPAN[1], ALINA SAPONAR[1], IOAN SILAGHI-DUMITRESCU[1,3], ATTILA KUN[1], LUMINITA SILAGHI-DUMITRESCU[1] and ELISABETH JEANNE POPOVICI[2]

ABSTRACT. A conformational analysis of *p-tert*-butyl/*tert*-pentyl/ *tert*-octyl-calix[8]arenes has been performed by semiempirical calculations. The results are in agreement with the available experimental data, as predicted for the pleated-loop conformation. The relative stability of the conformers depends on the substituents located in the *para* position, however the energy difference between the most stable and the next conformations is low.

Keywords: *p-tert*-butyl-calix[8]arene, *p-tert*-pentyl-calix[8]arene, *p-tert*-octyl-calix[8]arene, conformations, PM3 semiempiric.

Introduction

Calixarenes are [1n]-metacyclophanes, obtained from the condensation of formaldehyde with *p*-alkylphenols, thus resulting structures in which phenol fragments are connected by methylene bridges[1]. They have received a special interest as their calix crater is suitable for accommodating guest molecules.

As the calix[8]arenes have many torsion possibilities they are much more flexible than smaller-cycle representatives: there are sixteen up-down conformations plus others in which phenolic fragments adopt an out arrangement[2].

The goal of this research is to identify and characterize the most stable *para*-substituted calix[8]arene conformations by means of semiempirical methods.

Computational procedure

The starting structures have been built using the graphical interface of Spartan 04 [3] and preoptimized by molecular mechanics. Optimizations were continued at the semiempirical level employing the PM3 model of Stewart[4,5] using Gaussian 98 package of programs[6]. Frequency analysis followed all optimizations in order to establish the nature of the stationary points found, so that all the structures reported in this study are genuine minima on the potential energy surface at this level of theory, without any imaginary frequencies. Only the lowest energy conformers (within 15 kcal/mol) have been retained for discussion.

[1] Faculty of Chemistry and Chemical Engineering, Babeş-Bolyai University, Cluj-Napoca, Romania
[2] Institute of Chemical Research 'Raluca Ripan', Cluj-Napoca, Romania
[3] To whom the correspondence should be addressed: isi@chem.ubbcluj.ro

Results and discussion

The solid state structure of *p-tert*-butyl-calix[8]arene, determined by X-ray diffractometry[7,8] consists of four pleated fragments joined together. Indeed the global minimum structure found for the *p-tert*-butyl-calix[8]arene is the conformer having this pleated-loop shape, of an average D_{4d} symmetry, an arrangement that favors an internal circular hydrogen bonding stabilizing this conformation[9] (figure 1). The calculated average O·O distance of 2.74 Å is very close to the 2.71 Å average determined by Gutsche for an empty *p-tert*-butyl-calix[8]arene and the 2.70 Å average reported by Schatz et.al.[10] for the calix:chloroform 1:8 clathrate, thus proving the strong hydrogen bonds maintaining this conformation. The computed value of interplanar angle between two adjacent phenolic units is 111.6º comparable with the ~112º average reported for the chloroform clathrate.

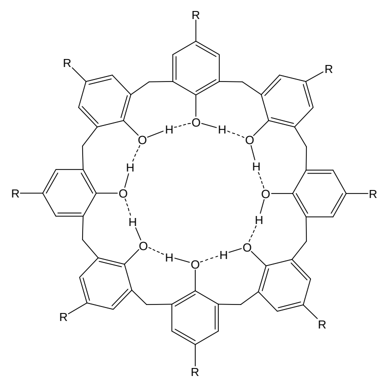

Figure 1. The internal circular hydrogen bonding in the calix[8]arene pleated loop conformer.

The next structure (*tert*-butyl-calix[8] **2** in figure 2) only 0.8 kcal/mole higher in energy may be described as consisting of two trimeric craters with the remaining two phenolic units ensuring a good linking through a "pleated motif" the result being again a stabilising internal circular hydrogen bonding.

The following two structures (*tert*-butyl-calix[8] **3** and **4**) consist of two calix[4] units joined together in an anti C_2 arrangement. Both calix[4] fragments adopt a cone conformation, which has already been proved to be the most stable one among the four possible conformations for a calix[4]arene[11,12]. Conformations **1**, **2**, **3** and **4** were identified in the case of rare earth (Eu and Lu) dinuclear calix[8]arenes complexes[13].

Conformer no. **5** at +4.18 kcal/mole above the global minimum is also based on two calix[4]arene fragments but this time having the same orientation although with a certain degree of crater distortion as the two connecting phenols have a parallel orientation. This conformer has been identified in the crystal structure of a tungsten complex trapping a WO group inside each of the calix[4] units[14]. This structure is also related to conformer no. **7**, the so-called 'pinched' conformer[15], whose calix[4] cones are more circular due to the lower distance between the connecting groups, but this definitely makes it less stable so its energy is higher than that of the other one.

This conformation was also found experimentally in the case of oligonuclear europium(III) derivatives of *p-tert*-butyl-calix[8]arene crystallized with DMSO[16,17].

The presence of pseudoconic calix[4] units should not be surprising: researchers noticed the remarkable similarity between the temperature dependent ^{1}H-NMR spectra of *p-tert*-butyl-calix[8]arene and *p-tert*-butyl calix[4]arene[15].

Tert-butyl-calix[8] **6** originates from the lowest energy pleated loop conformer but in this case one of the pleatings has an anti orientation as compared to all the other ones leading to a non-planar structure which makes hydrogen bonding more difficult although the circular shape is well-maintained.

Tert-butyl-calix[8] **8** is also based on two calix conic units joined together, but this time a calix[3] with a calix[5]. The calix[3] unit is slightly tensioned making this conformer less stable but the general orientation of the hydroxyl groups at the lower rim is almost circular, stabilizing this conformation.

Structure *tert*-butyl-calix[8] **9** may be depicted as a distorted two calix[4] structure with the units' connecting fragments adopting an almost out orientation, while the last remaining structure *tert*-butyl-calix[8] **10** may be described as reunion of a large opened calix[4]arene unit connected to a pleated motif by two phenolic fragments having an out orientation.

Interestingly, the global minimum conformer for the *tert*-pentyl-calix[8]arene is the one based on two calix[4]arene cone units joined together in an anti orientation and not the pleated loop conformer found for the *tert*-butyl-calix[8]arene. This arrangement provides enough space for the bulky upper rim substituents and also preserves the stabilizing hydrogen bonding at the lower rim. It is related to *tert*-pentyl-calix[8] **4** which has a similar conformation but with larger calix cavities.

The pleated loop conformer is the next structure at 4.3 kcal/mole above the global minimum, and at the same energy a structure based on two calix[3] units plus a pleated connection fragment is located. All the other structures found for *tert*-pentyl-calix[8]arene have practically the same geometries as the conformers already reported for the *tert*-butyl species respecting the same stability order.

For each class of compounds the corresponding structures are ordered upon their stability, with the corresponding relative energy towards the global minimum conformer indicated (in kcal/mole).

The lowest energy conformer found for the *tert*-octyl-calix[8]arene is the one based on two calix[3] fragments and a V-shaped cleft. Although it shouldn't be so stable from the calix crater point of view, watching the structure not from above but from the calix "plane" side, offers the image of a half-circle geometry, this arrangement providing the necessary space for these large substituents.

The following structure is based on two calix[4] *anti*-oriented units with the calix craters wide opened so that an internal hydrogen bonding can be established between these two units. The space requirement for the bulky octyl fragments is also satisfied, leading to a conformation of only 0.8 kcal/mole above the global minimum structure.

Other two conformers (*tert*-octyl-calix[8] **3** and **7** at 3.0 and 6.8 kcal/mole, respectively) are also based on calix[4] fragments but as they are not so opened the upper rim ligands are more sterically hindered so that these conformers are less stable. The pleated loop conformer is only the sixth one in terms of energy. This is due to the fact that the pleated structure although stabilized in the interior, can not easily accommodate voluminous ligands at the external V-shaped cleft area.

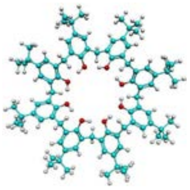

tert-butyl-calix[8] **1** (0.0)

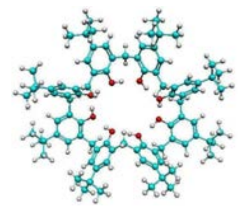

tert-butyl-calix[8] **2** (+0.8)

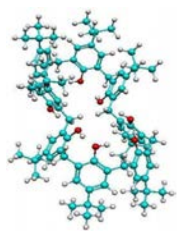

tert-butyl-calix[8] **3** (+2.3)

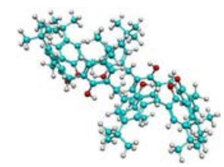

tert-butyl-calix[8] **4** (+3.3)

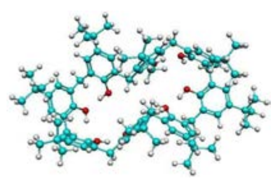

tert-butyl-calix[8] **5** (+4.2)

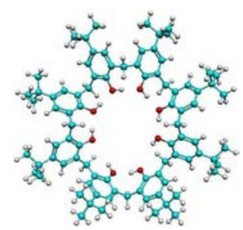

tert-butyl-calix[8] **6** (+4.4)

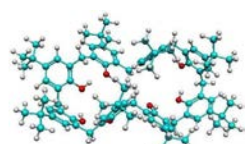

tert-butyl-calix[8] **7** (+6.0)

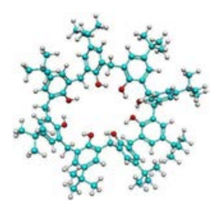

tert-butyl-calix[8] **8** (+6.9)

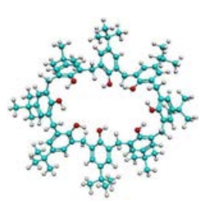

tert-butyl-calix[8] **9** (+7.5)

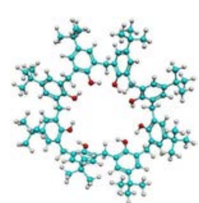

tert-butyl-calix[8] **10** (+10.5)

Figure 2. The ten lowest energy conformers found for *p*-*tert*-butyl-calix[8]arene.

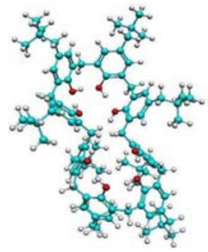

tert-pentyl-calix[8] **1** (0.0)

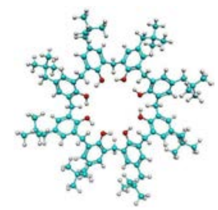

tert-pentyl-calix[8] **2** (+4.3)

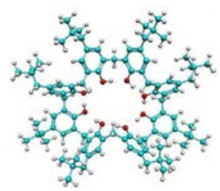

tert-pentyl-calix[8] **3** (+4.3)

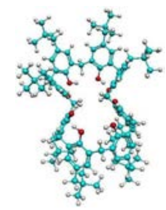

tert-pentyl-calix[8] **4** (+5.8)

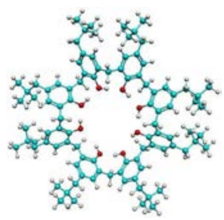

tert-pentyl-calix[8] **5** (+6.4)

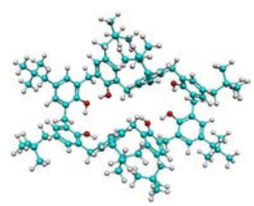

tert-pentyl-calix[8] **6** (+7.3)

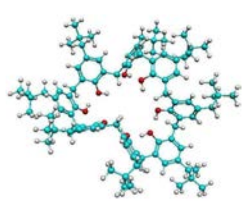

tert-pentyl-calix[8]] **7** (+8.2)

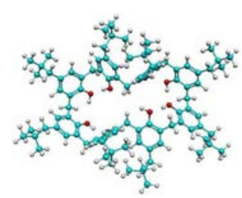

tert-pentyl-calix[8] **8** (+10.8)

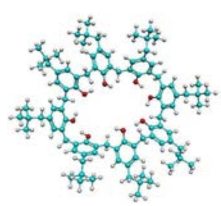

tert-pentyl-calix[8] **9** (+12.2)

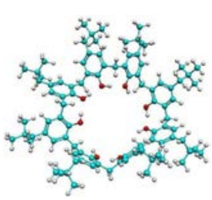

tert-pentyl-calix[8] **10** (+15.2)

Figure 3. The ten lowest energy conformers found for *p*-*tert*-pentyl-calix[8]arene.

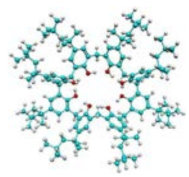

tert-octyl-calix[8] **1** (0.0)

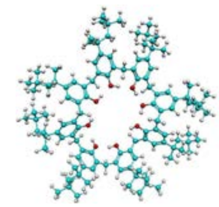

tert-octyl-calix[8] **2** (+0.8)

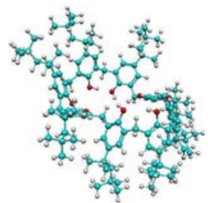

tert-octyl-calix[8] **3** (+3.0)

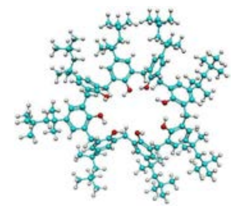

tert-octyl-calix[8] **4** (+4.4)

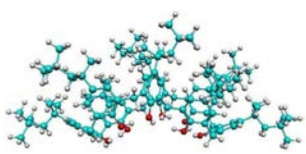

tert-octyl-calix[8] **5** (+4.5)

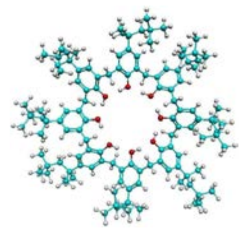

tert-octyl-calix[8] **6** (+5.5)

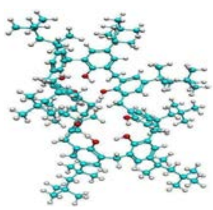

tert-octyl-calix[8] **7** (+6.8)

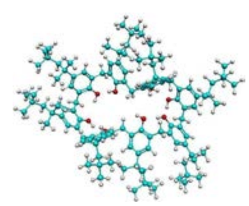

tert-octyl-calix[8] **8** (+6.9)

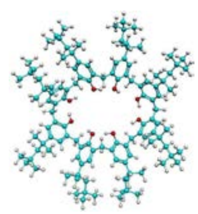

tert-octyl-calix[8] **9** (+7.8)

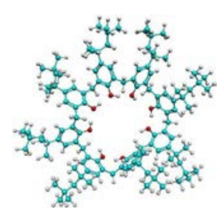

tert-octyl-calix[8] **10** (+10.5)

Figure 4. The ten lowest energy conformers found for *p*-*tert*-octyl-calix[8]arene.

Conclusions

Thirty conformers of *p-tert*-butyl/pentyl/octyl-calix[8]arenes have been investigated by PM3 semiempirical method. Their stability is influenced by the hydrogen bonding established at the lower rim and also depends on the volume of the para substituents: thus the most stable geometry for the *p-tert*-butyl-calix[8]arene corresponds to a pleated-loop shape, as exepected from the experimental data. For the *p-tert*-pentyl analogue however the lowest energy conformer is the one consisting of two calix[4] pseudoconic units with an opposed orientation. Their stability is in agreement with the NMR data, as the calix[8]arenes' spectra are similar to those of calix[4]arenes. The most stable conformer for the *p-tert*-octyl-calix[8]arene is the one composed of three fragments including two calix[3] units, an arrangement providing the necessary space for the bulky *tert*-octyl substituents.

Aknowledgements

This work was financially supported by CNCSIS Romania under grant CALIXCOM.

REFERENCES

1. C.D. Gutsche, "Calixarenes revisited", RSC **1998**.
2. C.D. Gutsche, L.J. Bauer, *J. Am. Chem. Soc.*, **1985**, *107*, 6052-6059.
3. Spartan '04, Wavefunction Inc., 18401 Von Karman Avenue, Suite 370 Irvine, CA 92612.
4. J.J.P. Stewart, *J. Comput. Chem.*, **1989**, *10*, 209-220.
5. J.J.P. Stewart, *J. Comput. Chem.*, **1989**, *10*, 221-264.
6. Gaussian 98, Revision A.11.3, M.J. Frisch, G.W. Trucks, H.B. Schlegel, G.E. Scuseria, M.A. Robb, J.R. Cheeseman, V.G. Zakrzewski, J.A. Montgomery, Jr., R.E. Stratmann, J. C. Burant, S. Dapprich, J. M. Millam, A.D. Daniels, K.N. Kudin, M.C. Strain, O. Farkas, J. Tomasi, V. Barone, M. Cossi, R. Cammi, B. Mennucci, C. Pomelli, C. Adamo, S. Clifford, J. Ochterski, G.A. Petersson, P.Y. Ayala, Q. Cui, K. Morokuma, N. Rega, P. Salvador, J. J. Dannenberg, D.K. Malick, A. D. Rabuck, K. Raghavachari, J.B. Foresman, J. Cioslowski, J. V. Ortiz, A.G. Baboul, B.B. Stefanov, G. Liu, A. Liashenko, P. Piskorz, I. Komaromi, R. Gomperts, R.L. Martin, D.J. Fox, T. Keith, M.A. Al-Laham, C.Y. Peng, A. Nanayakkara, M. Challacombe, P. M. W. Gill, B. Johnson, W. Chen, M. W. Wong, J. L. Andres, C. Gonzalez, M. Head-Gordon, E.S. Replogle, and J. A. Pople, Gaussian, Inc., Pittsburgh PA, **2002**.
7. C.D. Gutsche, A.E. Gutsche, A.I.J. Karoulov, *J. Inclusion Phenom.*, **1985**, *3*, 447-451.
8. K.H. Ahn, S.-G. Kim, J.S. U, *Bull. Korean Chem. Soc.*, **2000**, *21*, 813-816.
9. S.H. Dale, M.R.J., Elsegood, C. Redshaw, *CrystEngComm*, **2003**, *5*, 368-373.
10. J. Schatz, F. Schildbach, A. Lentz, S. Rastätter, T. Debaerdemaeker, *Z. Kristallogr*., **2001**, *216*, 182-186.
11. T.-N. Ursaleş, A. Ursaleş, I. Silaghi-Dumitrescu, *Rev. Chim.*, **2003**, *54*, 229-231.
12. T.-N. Ursaleş, I. Silaghi-Dumitrescu, *Rev. Roum. Chim.*, **2004**, *49*, 143-147.

13. J.-C. G. Bünzli, F. Ihringer, P. Dumy, C. Sager, R.D. Rogers, *Dalton Trans.*, **1998**, 497-503.
14. C. Redshaw, M.R.J. Elsegood, *Eur. J. Inorg. Chem.*, **2003**, 2071-2074.
15. C.D. Gutsche, L.J. Bauer, *Tetrahedron Lett.*, **1981**, *22*, 4763-4766.
16. S. Fleming, C.D. Gutsche, J.M. Harrowfield, M.I. Ogden, B.W. Skelton, D.F. Stewart, A.H. White, *Dalton Trans.*, **2003**, 3319-3327.
17. J.M. Harrowfield, M.I. Ogden, A.H. White, *Austr. J. Chem.*, **1991**, *44*, 1237-1247.

STUDIA UNIVERSITATIS BABES - BOLYAI, CHEMIA, LI, 2, 2006

Dedicated to professor Gh. Marcu at his 80th anniversary

SYNTHESIS OF NEW BROMO-STANNANES: TOWARD UNSATURATED TIN DERIVATIVES

PETRONELA MARIA PETRAR, GABRIELA NEMEŞ, IOAN SILAGHI-DUMITRESCU*, LUMINITA SILAGHI-DUMITRESCU

ABSTRACT. Two novel organometallic tin derivatives, bis-dibromomethyl-bis-(2,4,6-tri*iso*propyl-phenyl)-stannane **1** and tribromomethyl--bis-(2,4,6-tri*iso*propyl-phenyl)-bromo-stannane **2** have been obtained by the reaction of Tip_2SnF_2 (Tip = 2,4,6-*tri*-*i*Pr-C_6H_2) with bromoform in the presence of *n*BuLi. The compounds were characterized through NMR spectroscopy and the solid state structure of **2** was determined by X-ray diffraction. Compound **2** is a potential precursor of novel stannaalkenes and 1,3-distannaallenes.

Keywords: stannaalkenes, stannaallenes, double bonded derivatives.

Introduction

Chemists have always shown a big interest in the similarity of carbon with other elements from the same group. The quest for analogue derivatives of alkenes, allenes and even cumulenes containing heavier group 14 elements like silicon, germanium or tin has resulted in an increasing number of publications over the last decades [1]. Alkene derivatives of the type >E=C< (E = heavy group 14 elements) are known [2] and in the last five years, heteronuclear unsaturated compounds of the type >E=E'< have been obtained [3].

Stannaalkenes seem to be more difficult to synthesize than their Si and Ge analogues, as shown by the number of such derivatives known to date: five silenes, eight germenes and only four stannenes [2a] are described in the literature. Allenic compounds >Sn=C=C< are also unknown. Only one tin derivative containing cumulated double bonds, a stannaketenimine, has been reported [4].

In this paper, we describe the synthesis and characterization of two potential precursors of stanna-alkenes and -allenes, starting from a sterricaly hindered organometallic tin derivative, Tip_2SnF_2.

For the synthesis of double bonded tin derivatives, the choice of the starting material is important, because of the protective role played by the organic groups on the tin atom in the Sn=C bond. Bulky radicals, like Tip (2,4,6-*i*Pr-C_6H_2), afford sterricaly stabilization of the very reactive tin-carbon bond. The efficiency of Tip as a protection group has already been proved [5]. Scheme 1 summarizes a possible synthetic route which might lead to stanaallenes and stannaalkenes, starting from Tip_2SnF_2:

* Universitatea Babeş-Bolyai, Facultatea de Chimie şi Inginerie Chimică, Str. Kogălniceanu, Nr. 1, RO-400084 Cluj-Napoca, România.isi@chem.ubbcluj.ro

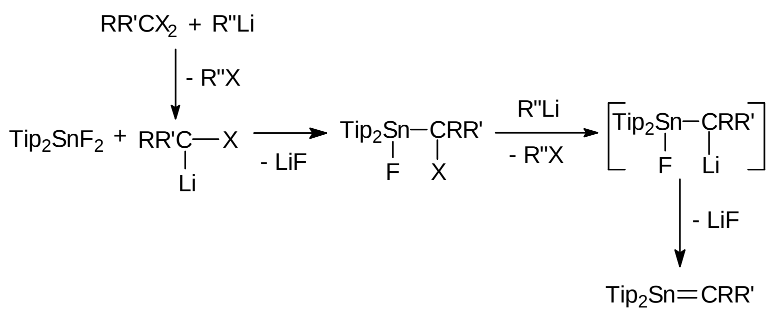

Scheme 1

The reaction of REX_2 derivatives (E = group 15 elements) with chloroform or bromoform in the presence of lithium derivatives always leads to the formation of $RE{=}CX_2$ compounds [6]. The reaction of supermesithyldichlorophosphane Mes*PCl_2 (Mes* = 2,4,6-*t*Bu-C_4H_2) with haloforms results in the formation of phosphaalkenes Mes*$P{=}CX_2$, by means of a lithium carbenoid. Replacement of a halogen atom is possible in the case of bromine and iodine, as shown in Scheme 2.

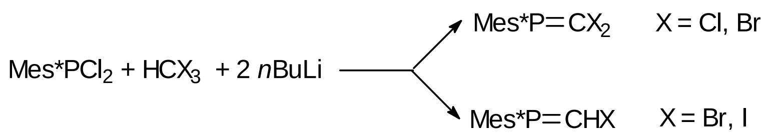

Scheme 2

Similar behavior was recorded for Mes*AsF_2 [7].

It was therefore interesting to explore the reactivity of halostannanes towards bromoform, in the hope of obtaining the corresponding stanaalkenes RR'$Sn{=}CBr_2$. However, the behavior of dihalosubstituted group 14 derivatives in such reactions is quite different from that of similar group 15 compounds. Thus, when Tip_2SnF_2 was reacted with one equivalent of $CHBr_3$ followed by 2 equivalents of *n*BuLi, several unidentified products were obtained with a very poor yield. In order to improve the yield of the formation of the lithium carbenoids $CLiHBr_2$ and $CLiBr_3$, the reaction of the dihalostannane with two equivalents of bromoform was attempted.

Results and discussion

The reaction of Tip_2SnF_2 with two equivalents of $CHBr_2$ and *n*BuLi was performed at -90℃, in THF and leads to the formation of two main compounds **1** and **2** in a 4:1 ratio (Scheme 3).

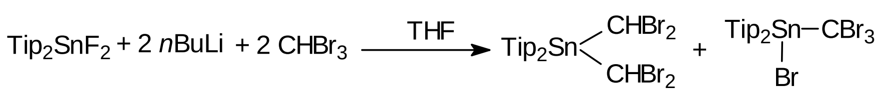

1 **2**

Scheme 3

As reported in the literature [6], both $CLiHBr_2$ and $CLiBr_3$ may be formed by the reaction of lithium derivatives with bromoform. The action of the $CLiHBr_2$ carbenoid on Tip_2SnF_2 leads to compound **1**, while $Tip_2Sn(F)CBr_3$ is formed with $CLiBr_3$. A fluorine-bromine exchange is supposed to take place between $Tip_2Sn(F)CBr_3$ and the LiBr formed *in situ*, leading to compound **2**.

Compounds **1** and **2** have been characterized by multinuclear NMR spectroscopy. The relevant NMR data for **1** are given in Table 1.

Table 1

NMR data for $Tip_2Sn(CHBr)_2$

^{1}H NMR	^{119}Sn NMR	^{13}C NMR
1.50 ppm (d, $^{3}J_{HH}$ = 6.4 Hz, 24H, C<u>H</u>$_3$, orto-*i*Pr) 1.18 ppm (d, $^{3}J_{HH}$ = 6.4 Hz, 12H, C<u>H</u>$_3$, para- *i*Pr) 2.58 (m, $^{3}J_{HH}$ = 6.4Hz, 4H, C<u>H</u>, orto-*i*Pr) 2.82 (m, $^{3}J_{HH}$ = 6.4 Hz, 2H, C<u>H</u>, para-*i*Pr) 5.80 (s, 2H, C<u>H</u>Br$_2$) 6.96 (s, 4H, meta-C<u>H</u> Tip).	-134.2 ppm ($^{2}J_{SnBr}$ = 11.8 Hz)	23.9 ppm (<u>C</u>H$_3$, orto-*i*Pr) 24.7 ppm (<u>C</u>H$_3$, para-*i*Pr) 32.5 ppm (<u>C</u>H, orto-*i*Pr) 34.3 ppm (<u>C</u>H, para-*i*Pr) 40.1 ppm (<u>C</u>HBr$_2$) 122.6 (meta-<u>C</u>H Tip), 150.9 and 151.6 ppm (orto and para-C Tip).

The ^{119}Sn NMR spectrum of compound **1** shows the multiplet resulted from the coupling with the four bromine atoms (Figure 1). Such signals are usually broad and the coupling constant is not observed; to our best knowledge, it is the first time that coupling of tin with such an important number of bromine atoms resulted in an observed hyperfine splitting of the signal and not just in its widening.

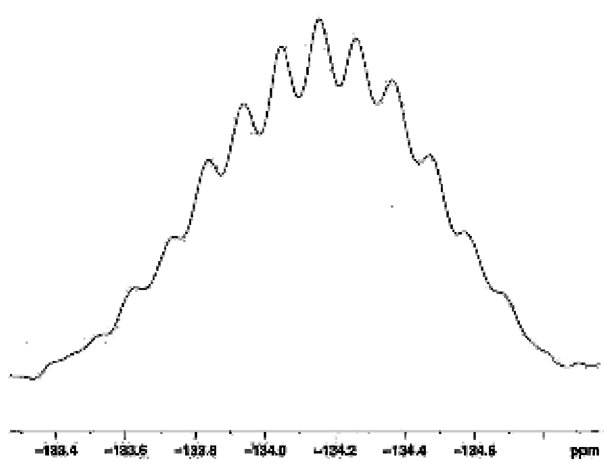

Figure 1. ^{119}Sn NMR signal for $Tip_2Sn(CHBr_2)_2$

The ^{1}H-NMR chemical shifts for compound **2** are within the expected range; the position of all signals is given in the Experimental section. Two different signals were recorded for the two methyl groups in the *o-iso*propyl groups (1.050 ppm, 1.080 ppm respectively). This indicates that the free rotation around the Sn-C bond is significantly hindered, no doubt due to the presence of the sterricaly challenging groups on the tin atom.

Compound **2,** $Tip_2Sn(Br)CBr_3$, was characterized in solid state through X-ray diffraction on single crystal. An ORTEP rendering of the molecular structure is shown in Figure 2. Some geometrical data are also given in Table 2. The presence of the heavy bromine atoms makes the refinement of the structure more difficult. Two equivalent positions atom are possible for the CBr_3 groups, as well as for the Br1 atom, with respect to an axis containing the central tin and acting as a two-fold symmetry axis for the Tip groups. The Sn-Br distance (2.714 Ǻ) is remarkably larger than those found in similar compounds (2.50 - 2.60 Ǻ) [8, 9]. As expected, the geometry about the tin atom is distorted tetrahedral, with wider angles with atoms belonging to the CBr_3 group.

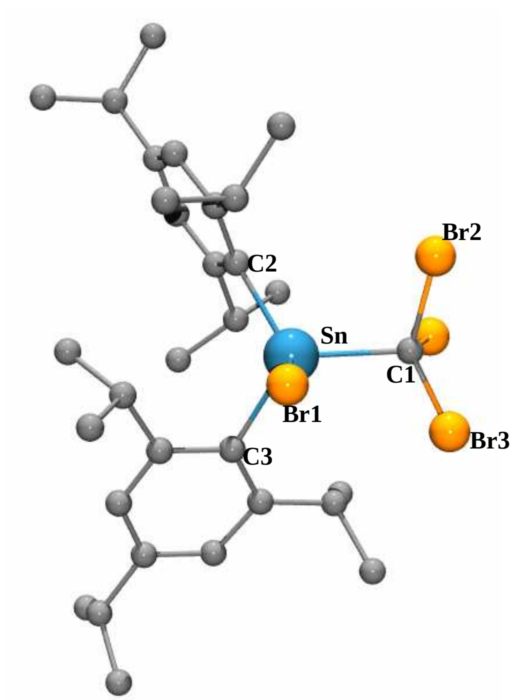

Figure 2. Molecular structure of $Tip_2Sn(Br)CBr_3$ (hydrogen atoms were omitted for clarity)

Table 2

Geometrical data for $Tip_2Sn(Br)CBr_3$

Bond lengths (Å)		Bond angles (°)	
Sn-C1	2.227	Br1-Sn-C1	94.19
Sn-C2	2.156	C2-Sn-C3	110.81
Sn-Br1	2.714	C1-Sn-C3	122.70
C1-Br2	1.932	Br2-C1-Sn	104.52
C1-Br3	1.940	Br1-C1-Br2	114.98

Conclusions and perspectives

Two novel organometallic tin derivatives have been obtained. Their structure in solution was elucidated by NMR spectroscopy. The solid-state structure of $Tip_2Sn(Br)CBr_3$ was also determined.

Even though the reaction of Tip_2SnF_2 with bromoform did not lead to the expected stannaalkene, it afforded a potential precursor of double bonded derivatives of tin. Scheme 4 shows the possible use of $Tip_2Sn(Br)CBr_3$ in the synthesis of stannaalkenes and 1,3-distannaallenes.

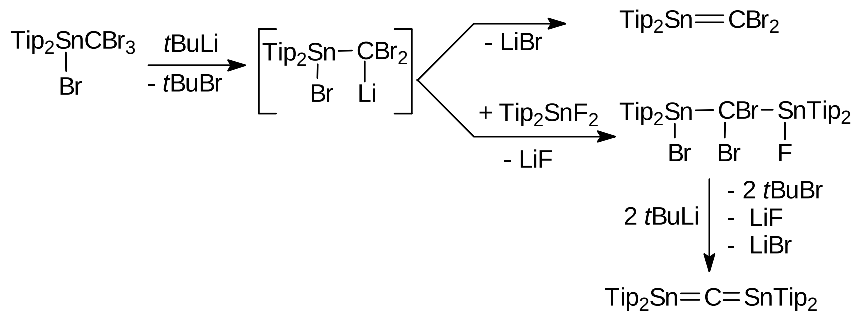

Scheme 4

The distaannallene $Tip_2Sn{=}C{=}SnTip_2$ would be the first compound of this type obtained to date. The proposed synthetic routes are currently under experimental investigation.

Acknowledgment. Dr. Jean Escudie from Paul Sabatier University Toulouse, is thanked for his hospitality and for useful discussion on this manuscript, as well as Dr. Heinz Gornitzka for collecting the X-Ray diffraction data. We thank the Ministry of Education and Research Bucharest (CEEX project) and CNCSIS Agency for partial financial support of this work.

Experimental procedure

All manipulations were carried out under N_2 or Ar using standard Schlenk techniques with solvents freshly distilled from sodium benzophenone. Mass spectra were measured on a Hewlett-Packard 5989 A spectrometer by EI at 70 eV. Melting points were determined on a Leitz microscope heating stage 250. NMR Spectra were recorded on a Bruckner Varian 200 MHz for ^{1}H and ^{31}P and 300 MHz for ^{13}C and ^{119}Sn nucleus. $CDCl_3$ was used as a solvent.

Crystal Data for **2** were collected at room temperatures using an oil-coated shock-cooled crystal on a Bruker-AXS CCD 1000 diffractometer with MoKα radiation (λ =

0.71073 Å). The structure was solved by direct methods (SHELXS-97) [10] and all non hydrogen atoms were refined anisotropically using the least-squares method on F^2 [11].

Synthesis of bis-dibromomethyl-bis-(2,4,6-triisopropyl-phenyl)-stannane **1** *and tribromomethyl--bis-(2,4,6-triisopropyl-phenyl)-bromo-stannane* **2:**

A mixture of 2 g (0.0035 mols) Tip_2SnF_2 and 1.77 g $CHBr_3$ (0.007 mols) in 70 ml THF was cooled at -90℃ and 4.5 ml *n*BuLi 1.6 M (0.0072 mols) were added dropwise. The reaction mixture was stirred for half an hour at -90℃ and then it was allowed to warm up at room temperature. The solvent was removed under vacuum and replaced with 20 ml pentane. Lithium salts were removed by filtration and the filtrate was stored at -25℃. After 24 hours, compo und **1** was isolated by filtration as a white powder with a 45% yield. The remaining solution was further concentrated under vacuum and stored at -25℃. Tran sparent crystals of **2** were isolated after a few hours with a 11% yield.

1: NMR data are given in Table 1;

MS (Z/e): 697 (M-$CHBr_2$), m.p. = 177℃

2: ^{1}H-NMR: 1.050 ppm (d, $^3J_{HH}$=6.2 Hz, 6H, C<u>H</u>$_3$, orto-*i*Pr); 1.080 ppm (d, $^3J_{HH}$=5.8 Hz, 6H, C<u>H</u>$_3$, orto-*i*Pr); 1.194 ppm (d, $^3J_{HH}$=7 Hz, 6H, C<u>H</u>$_3$, para-*i*Pr); 2.567 ppm (m, 1H, C<u>H</u>, para-*i*Pr); 3.35 ppm (m, 2H, C<u>H</u>, orto-*i*Pr), 7.080 ppm (s, 4H, meta-C<u>H</u> Tip).

REFERENCES

1. J. Escudié, H. Ranaivonjatovo, L. Rigon, *Chem. Rev.*, **2000**, *100*, 3639-3696**.**

2. a) P.P. Power, *Chem. Rev*., **1999**, *99*, 3463-3503; b) J. Escudié, C. Couret, H. Ranaivonjatovo, *Coord. Chem. Rev*., **1998**, *178–180*, 565-592.

3. V. Ya. Lee, A. Sekiguchi, *Organometallics,* **2004,** *23,* 2822-2834.

4. H. Grützmacher, S. Freitag, R. Herbst-Irmer, G. S. Sheldrick, *Angew. Chem. , Int. Ed. Engl.*, **1992**, *31*, 437-438.

5. M. A. Chaubon, B. Dittrich, J. Escudié, H. Ramdane, H. Ranaivonjatovo, J. Satgé, *Synth. React. Inorg. Met.-Org. Chem*., **1997**, *27*, 519-533.

6. S. J. Goede, F. Bickelhaupt, *Chem. Ber.*, 124, **1991**, 2677-2684.

7. H. Ramdane, H. Ranaivonjatovo, J. Escudié, N. Knouzi, *Organometallics* **1996**, *15*, 2683-2684.

8. a) H. Preut, F.Huber, *Acta Crystallogr., Sect.B: Struct. Crystallogr .Cryst. Chem.* **1979**, *35*, 744-746; b) M. Saito, R. Haga, M. Yoshioka, *Heteroat. Chem*., **2001**, *12*, 349-353; c) N.W. Alcock, J. F. Sawyer, *J. Soc.,Dalton Trans.*, **1977**, 1090-1095; d) P. Brown, M. F. Mahon, K. C. Molloy, *J. Organomet. Chem.,* **1992** *,435*, 265-273.

9. **a**) U. C. Konig, M. Berkei, F. Neikes, H. Preut, T.N. Mitchell; *Acta Crystallogr., Sect.C: Cryst. Struct .Commun.*, **2000**, *56*, 53-55;

b) S. A. Bajue, F. B. Bramwell, M. Charles, F. Cervantes-Lee, K. Pannell, *Inorg. Chim. Acta* , **1992**, *197*, 83-87;

c) L. F. Tang, Z.H. Wang, W.L. Jia, Y.M. Xu, J.T. Wang, *Polyhedron*, **2000**, *19*, 381-387.

10. G. M. Sheldrick, *Acta Crystallogr.,* **1990**, *A46*, 467-473.

11. SHELXL-97, Program for Crystal Structure Refinement, G. M. Sheldrick, University of Göttingen **1997**.

STUDIA UNIVERSITATIS BABES - BOLYAI, CHEMIA, LI, 2, 2006

Dedicated to professor Gh. Marcu at his 80th anniversary

NEW ORGANOTIN(IV) AND – LEAD(IV) *N*,*N*-DIMETHYLDITHIOCARBAMATES: SYNTHESIS, SOLUTION NMR CHARACTERIZATION AND SINGLE-CRYSTAL X- RAY STRUCTURE OF $Ph_2MCl(S_2CNMe_2)$ (M = Sn, Pb) AND $Ph_2Sn(S_2CNMe_2)_2$

CARMEN COMSA, ADINA CRISTEA, ANCA SILVESTRU AND CRISTIAN SILVESTRU*

ABSTRACT. New *N*,*N*-dimethyldithiocarbamato derivatives of organotin(IV) and –lead(IV), $R_2MCl(S_2CNMe_2)$ (R = Bu, M = Sn; R = Ph, M = Sn, Pb), $R_2M(S_2CNMe_2)_2$ (R = Bu, Ph, M = Sn) and $R_3M(S_2CNMe_2)$ (R = Ph, M = Sn, Pb; R = Me, M = Pb), were prepared and characterized by multinuclear (^{1}H, ^{13}C, 2D) NMR spectroscopy in solution. The molecular structures of $Ph_2SnCl(S_2CNMe_2)$ (**3**), $Ph_2Sn(S_2CNMe_2)_2$ (**4**) and $Ph_2PbCl(S_2CNMe_2)$ (**6**) were established by single-crystal X-ray diffraction. In all cases the dithio ligand acts as an asymmetric monometallic biconnective moiety. The mixed chloro-dithiocarbamato derivatives **3** and **6** exhibit distorted trigonal bipyramidal C_2MClS_2 cores, with a sulfur and chlorine atoms in axial positions. For $Ph_2Sn(S_2CNMe_2)_2$ (**4**) a distorted octahedral environment is achieved, with *cis* organic groups attached to tin atom.

Key-words: organotin, organolead, dithiocarbamato ligands, solution NMR studies, X-ray diffraction

INTRODUCTION

Main group dithiocarbamato complexes find various applications in materials and separation science, and have potential use as chemotherapeutics, pesticides, and fungicides. In addition, the dithiocarbamato moiety is a highly versatile ligand towards main group metals, they can stabilize a variety of oxidation states and coordination geometries and small modifications to the ligand can often lead to significant changes in the structure of the complexes formed. The literature on the structural aspects of tin and lead dithiocarbamates was recently reviewed [1], and a search of the Cambridge Structure Database revealed many gaps concerning the structure investigations of organotin(IV) dimethyldithiocarbamates, while no structure of an organolead(IV) analog was so far established by single-crystal X-ray diffractometry.

We report here on the synthesis and solution behavior of several diorgano- and triorganometal(IV) (M = Sn, Pb) dimethyldithiocarbamates, the molecular structures of $Ph_2SnCl_x(S_2CNMe_2)_{2-x}$ (x = 0, 1) as well as the first molecular structure of a diorganolead(IV) dithiocarbamate, *i.e.* $Ph_2PbCl(S_2CNMe_2)$.

* *Faculty of Chemistry & Chemical Engineering, "Babes-Bolyai" University, RO-400028 Cluj-Napoca, Romania. Fax: 0040-264-590818; Tel: 0040-264-593833; E-mail: cristi@chem.ubbcluj.ro*

EXPERIMENTAL

The starting materials, *i.e.* organotin(IV)- and organolead(IV)- chlorides and $Me_2NCS_2Na{\cdot}2H_2O$, were commercially available (Aldrich) and were used without further purification. Room-temperature ^1H and ^{13}C NMR spectra, including 2D experiments, were recorded in dried $CDCl_3$ on a BRUKER AVANCE DRX 400 instrument operating at 400.16 and 100.62 MHz, respectively. The chemical shifts are reported in ppm relative to the residual peak of solvent (ref. $CDCl_3$: ^1H 7.26 ppm, ^{13}C 77.0 ppm).

*Preparation of $Bu_2SnCl(S_2CNMe_2)$ (**1**)*

$Me_2NCS_2Na{\cdot}2H_2O$ (0.460 g, 2.567 mmol) was added to a solution of Bu_2SnCl_2 (0.782 g, 2.574 mmol) in CH_2Cl_2. A white precipitate of NaCl formed in short time. After removing the NaCl, the solvent was evaporated and the title compound was isolated as viscous yellowish oil. ^1H NMR: δ 0.93t [6H, CH_3-$(CH_2)_3$-Sn, $^3J_{HH}$ 5.8 Hz], 1.41m,br [4H, CH_3-CH_2-$(CH_2)_2$-Sn], 1.83m,br [8H, CH_3-CH_2-$(CH_2)_2$-Sn], 3.40s (6H, CH_3-N). ^{13}C NMR: δ 13.58s (C_δ), 26.21s (C_γ, $^3J_{SnC}$ 98 Hz), 27.75s (C_β, $^2J_{SnC}$ 34 Hz), 29.08s (C_α, $^1J_{SnC}$ 501 / 522 Hz), 45.10s (CH_3-N), 198.04 (N-CS_2).

*Preparation of $Bu_2Sn(S_2CNMe_2)_2$ (**2**)*

$Me_2NCS_2Na{\cdot}2H_2O$ (0.922 g, 5.146 mmol) was added to a solution of Bu_2SnCl_2 (0.782 g, 2.574 mmol) in CH_2Cl_2. A white precipitate of NaCl formed in short time. After removing the NaCl, the solvent was evaporated and the title compound was isolated as yellowish solid. Yield: 0.95 g (78%), m.p. 137-140°C. ^1H NMR: δ 0.91t [6H, CH_3-$(CH_2)_3$-Sn, $^3J_{HH}$ 7.3 Hz], 1.41tq [4H, CH_3-CH_2-$(CH_2)_2$-Sn, $^3J_{H\text{-}H}$ 7.2 Hz], 1.88m [4H, CH_3-CH_2-CH_2-CH_2-Sn], 2.01m [4H, CH_3-$(CH_2)_2$-CH_2-Sn], 3.42s (12H, CH_3-N). ^{13}C NMR: δ 13.70s (C_δ), 26.36s (C_γ, $^3J_{SnC}$ 124 Hz), 28.46s (C_β), 34.18s (C_α, $^1J_{SnC}$ 576 / 598 Hz), 44.58s (CH_3-N), 200.93 (N-CS_2).

The following compounds were prepared similarly:

*$Ph_2SnCl(S_2CNMe_2)$ (**3**)*, from Ph_2SnCl_2 (1.605 g, 4.668 mmol) and $Me_2NCS_2Na{\cdot}2H_2O$ (0.837 g, 4.668 mmol) in CH_2Cl_2. Yield: 1.30 g (65%), m.p. 240-241°C. ^1H NMR: δ 3.40s (6H, CH_3-N), 7.47m (6H, C_6H_5-*meta+para*), 8.07d (4H, C_6H_5-*ortho*, $^3J_{HH}$ 7.8, $^3J_{SnH}$ 88 Hz). ^{13}C NMR: δ 45.83s (CH_3-N), 128.77s (C_m, $^3J_{SnC}$ 88 Hz), 130.16s (C_p, $^4J_{Sn\text{-}C}$ 18 Hz), 135.66s (C_o, $^2J_{SnC}$ 64 Hz), 141.85s (C_i), 196.81 (N-CS_2).

*$Ph_2Sn(S_2CNMe_2)_2$ (**4**)*, from Ph_2SnCl_2 (1.605 g, 4.668 mmol) and $Me_2NCS_2Na{\cdot}2H_2O$ (1.673 g, 9.336 mmol) in CH_2Cl_2. Yield: 1.68 g (70%), m.p. 160-165°C. ^1H NMR: δ 3.30s (12H, CH_3-N), 7.42m (6H, C_6H_5-*meta+para*), 8.06m (4H, C_6H_5-*ortho*, $^3J_{SnH}$ 88 Hz). ^{13}C NMR: δ 45.80s (CH_3-N), 128.75s (C_m, $^3J_{SnC}$ 88 Hz), 130.15s (C_p), 135.64s (C_o, $^2J_{SnC}$ 63 Hz), 141.83s (C_i), 196.75 (N-CS_2).

*$Ph_3Sn(S_2CNMe_2)$ (**5**)*, from Ph_3SnCl (0.82 g, 2.127 mmol) and $Me_2NCS_2Na{\cdot}2H_2O$ (0.38 g, 2.120 mmol) in CH_2Cl_2. Yield: 0.31 g (31%), m.p. 275-280°C. ^1H NMR: δ 3.46s (6H, CH_3-N), 7.42m (9H, C_6H_5-*meta+para*), 7.76m (6H, C_6H_5-*ortho*, $^3J_{SnH}$ 61 Hz). ^{13}C NMR: δ 45.95s (CH_3-N), 128.47s (C_m, $^3J_{SnC}$ 61 Hz), 129.08s (C_p, $^4J_{Sn\text{-}C}$ 13 Hz), 136.67s (C_o, $^2J_{SnC}$ 46 Hz), 142.16s (C_i, $^1J_{SnC}$ 579 / 606 Hz), 196.76 (N-CS_2).

*$Ph_2PbCl(S_2CNMe_2)$ (**6**)*, from Ph_2PbCl_2 (1.561 g, 3.61 mmol) and $Me_2NCS_2Na{\cdot}2H_2O$ (0.647 g, 3.61 mmol) in CH_2Cl_2. Yield: 1.57 g (84%), m.p. 190-192°C. ^1H NMR: δ 3.35s (6H, CH_3-N), 7.41t (2H, C_6H_5-*para*, $^3J_{HH}$ 7.4 Hz), 7.56dd (4H, C_6H_5-*meta*, $^3J_{HH}$ 7.6 Hz), 8.26d (4H, C_6H_5-*ortho*, $^3J_{HH}$ 7.9, $^3J_{PbH}$ 175 Hz). ^{13}C

NMR: δ 45.29s (CH_3-N), 129.93s (C_p), 130.28s (C_m, $^3J_{PbC}$ 43 Hz), 134.83s (C_o, $^2J_{PbC}$ 115 Hz), 137.92s (C_i), 200.87 (N-CS_2).

$Ph_3Pb(S_2CNMe_2)$ (***7***), from Ph_3PbCl (0.793 g, 1.674 mmol) and $Me_2NCS_2Na{\cdot}2H_2O$ (0.30 g, 1.674 mmol) in CH_2Cl_2. Yield: 0.53 g (57%), m.p. 199-200°C. ^{1}H NMR: δ 3.48s (6H, CH_3-N), 7.38t (3H, C_6H_5-*para*, $^3J_{HH}$ 7.4 Hz), 7.50dd (6H, C_6H_5-*meta*, $^3J_{HH}$ 7.4 Hz), 7.86d (4H, C_6H_5-*ortho*, $^3J_{HH}$ 6.8, $^3J_{PbH}$ 105 Hz). ^{13}C NMR: δ 46.21s (CH_3-N), 128.96s (C_p, $^4J_{PbC}$ 22 Hz), 129.79s (C_m, $^3J_{PbC}$ 100 Hz), 136.89s (C_o, $^2J_{PbC}$ 83 Hz), 158.18s (C_i, $^1J_{PbC}$ 563 Hz), 199.14 (N-CS_2).

$Me_3Pb(S_2CNMe_2)$ (***8***), from Me_3PbCl (0.70 g, 2.433 mmol) and $Me_2NCS_2Na{\cdot}2H_2O$ (0.438 g, 2.444 mmol) in CH_2Cl_2. Yield: 0.54 g (60%), m.p. 235-237°C. ^{1}H NMR: δ 1.44s (9H, CH_3-Pb, $^2J_{PbH}$ 64 Hz), 3.47s (6H, CH_3-N). ^{13}C NMR: δ 13.30s (CH_3-Pb, $^1J_{PbC}$ 282 Hz), 45.30s (CH_3-N), 201.24 (N-CS_2).

X-ray Crystallographic Study

Data were collected with a SMART APEX diffractometer (*National Center for X-Ray Diffractometry*, "Babes-Boyai" University, Cluj-Napoca, Romania) at 297 K. In all cases a graphite monochromator was used to produce a wavelength (Mo-$K\alpha$) of 0.71073 Å. The crystal structure measurement and refinement data for compounds **3, 4** and **6** are given in Table 1. Absorption corrections were applied using the multi-scan (Bruker SAINT) method [2]. The structures were solved by direct methods (full-matrix least-squares on F^2). All non hydrogen atoms were refined with anisotropic thermal parameters. For structure solving and refinement a software package SHELX-97 was used [3]. The drawings were created using the Diamond program by Crystal Impact GbR [4].

CCDC-601481 (**3**), CCDC-601483 (**4**) and CCDC-601482 (**6**) contain the supplementary crystallographic data for this paper. These data can be obtained free of charge at www.ccdc.cam.ac.uk/conts/retrieving.html [or from the Cambridge Crystallographic Data Centre, 12, Union Road, Cambridge CB2 1EZ, UK; fax: (internat.) +44-1223/336-033; E-mail: deposit@ccdc.cam.ac.uk].

Table 1.

Crystallographic data for compounds **3**, **4** and **6**.

	3	4	6
Empirical formula	$C_{15}H_{16}ClNS_2Sn$	$C_{18}H_{22}N_2S_4Sn$	$C_{15}H_{16}ClNPbS_2$
Formula mass	428.55	513.31	517.05
Crystal system	Triclinic	Tetragonal	Triclinic
Space group	*P-1*	I4(1)/a	*P-1*
a [Å]	9.1505(13)	16.532(2)	6.68(3)
b [Å]	9.7273(14)	16.532(2)	9.36(4)
c [Å]	11.8051(17)	15.533(4)	14.97(6)
α [°]	79.367(2)	90	79.06(6)
β [°]	67.558(2)	90	81.35(7)
γ [°]	62.500(2)	90	69.98(6)
V [Å^3]	861.4(2)	4245.1(13)	859(6)
Z	2	8	2
$D_{calcd.}$ [g/cm^3]	1.652	1.606	1.999
F(000)	424	2064	488
Crystal size [mm]	0.22x0.16x0.16	0.26x0.13x0.10	0.23x0.20x0.15
μ(Mo-Kα) [mm^{-1}]	1.870	1.601	10.209
θ range [°]	1.87-26.37	1.80-26.36	2.34-25.35

No. of reflections collected	9227	16801	8144
No. of independent reflections	3507 (R_{int} = 0.0265)	2171 (R_{int} = 0.0565)	3107 (R_{int} = 0.0376)
No. of parameters	183	116	183
R_1 [$I > 2\sigma(I)$]	0.0334	0.0560	0.0287
wR_2	0.0723	0.0635	0.0675
GOF on F^2	1.144	1.271	1.150
Largest difference electron density [e/Å^3]	0.714/-0.784	0.803/--0.946	1.006/-1.244

RESULTS AND DISCUSSION

Synthesis

The new compounds were obtained by reacting R_2MCl_2 and R_3MCl with sodium dimethyldithiocarbamate in 1:1 and 1:2 molar ratios, in CH_2Cl_2, at room temperature, according to the following equations:

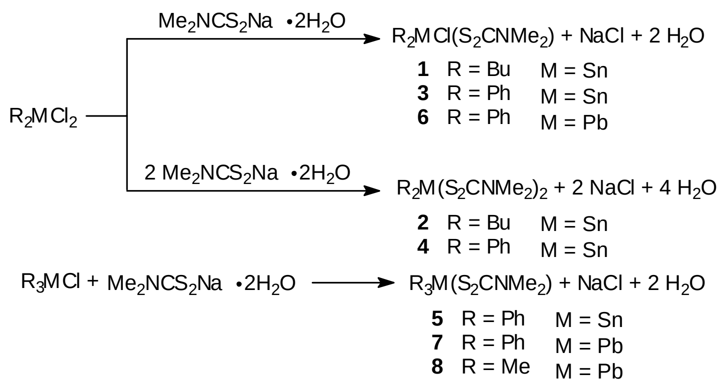

Most of the organotin(IV)- and organolead(IV) dithiocarbamates were isolated in good yield as yellowish solids. Compound **1** was obtained as viscous yellowish oil. They are air-stable compounds, soluble in common organic solvents. All compounds were investigated by NMR spectroscopy (^{1}H, ^{13}C, 2D) in $CDCl_3$ solutions and for compounds **3, 4** and **6** the molecular structures were established using single-crystal X-ray diffraction.

NMR Spectroscopy

For both the organoSn(IV) and -Pb(IV) complexes the spectra contain characteristic resonance signals for equivalent organic groups bonded to the metal centre as well as for the dimethyldithiocarbamato ligand, thus providing evidences for the identity of the obtained compounds. The ^{1}H resonances assigned to the *ortho* protons in the phenyl groups attached to the metal and to the methyl protons in the trimethyllead(IV) derivative, as well as most of the ^{13}C resonances for the organic groups bound to tin or lead, show satellites due to metal-proton or metal-carbon couplings.

The coordination geometry of organotin(IV) derivatives is reflected in the NMR parameters [5]. Thus, based on the reported dependence on the $^1J(^{119}Sn^{13}C)$ coupling constants in butyltin(IV) derivatives [$|^1J(^{119}Sn^{13}C)| = 9.99\theta$-746] [6], the estimated values for the C-Sn-C angle (θ) are 126.9^o [$^1J(^{119}Sn^{13}C$ 522 Hz] in **1** and 134.5^o [$^1J(^{119}Sn^{13}C$ 598 Hz] in **2**. This suggests a distorted trigonal bipyramidal structure for the chloro(dithiocarbamato)tin(IV) derivative **1** and a skew-trapezoidal bipyramid (or highly distorted octahedron) for the bis(dithiocarbamato)tin(IV) derivative **2**. Similar coordination geometries were previously reported for several related organotin(IV) derivatives [1].

The magnitude of the lead-proton and lead-carbon coupling constants is consistent with the presence of diphenyllead(IV) moiety in compound **6** [$^{3}J(^{207}Pb^{1}H)$ 175 Hz, $^{2}J(^{207}Pb^{13}C)$ 115 Hz] and triorganolead(IV) fragments in compounds **7** [R = Ph, $^{3}J(^{207}Pb^{1}H)$ 105 Hz, $^{2}J(^{207}Pb^{13}C)$ 183 Hz, $^{1}J(^{207}Pb^{13}C)$ 563 Hz] and **8** [R = Me, $^{3}J(^{207}Pb^{1}H)$ 64 Hz, $^{1}J(^{207}Pb^{13}C)$ 282 Hz], respectively [7,8].

The ^{1}H and ^{13}C NMR spectra of compounds **1** – **8** are very similar with respect to the dimethyldithiocarbamato moiety. The presence of sharp singlets for the methyl protons in the ^{1}H NMR spectra and for the methyl carbons in the ^{13}C NMR spectra, respectively, indicates the equivalence of the methyl groups on nitrogen. Taking into account the restricted rotation about the $(S_2)C$-N partial double bond of the dithiocarbamato group, this behavior is consistent with a fast fluxional behavior on the NMR chemical shift time scale which alternatively brings the two sulfur atoms in the same position of the primary coordination sphere of the metal centre.

Single-crystal X-ray diffraction studies

Single-crystals suitable for X-ray diffraction studies were obtained by slow diffusion from a mixture of chloroform and hexane (1/4, v/v) for compounds $Ph_2SnCl(S_2CNMe_2)$ (**3**) and $Ph_2PbCl(S_2CNMe_2)$ (**6**). The crystal of **3** consists of discrete monomers separated by normal van der Waals distances, while in the crystal of **6** dimeric associations might be considered (see subsequent discussion). The ORTEP diagrams of the molecular structures of compounds **3** and **6**, with the atom numbering scheme, are shown in Figures 1 and 2. Selected interatomic distances and angles are listed in Table 2.

The molecular structure of compounds **3** and **6** exhibits some common structural features. The dimethyldithiocarbamato moiety behaves as *asymmetric monometallic biconnective units*, with short [Sn(1)-S(1) 2.4718(10) Å in **3**, and Pb(1)-S(1) 2.607(8) Å in **6**] and long [Sn(1)-S(2) 2.6834(10) Å in **3**, and Pb(1)-S(2) 2.821(8) Å in **6**] metal-sulfur distances.

The length of the Sn(1)-S(1) primary bond in **3** is typical for a covalent bond, while the secondary Sn(1)-S(2) bond is stronger than that observed in the related $Me_2SnCl(S_2CNMe_2)$ [Sn-S 2.48(1) Å, Sn···S 2.79(1) Å] [9] or $(PhCH_2)_2SnCl(S_2CNMe_2)$ [Sn-S 2.464(2) Å, Sn···S 2.707(2) Å] [10].

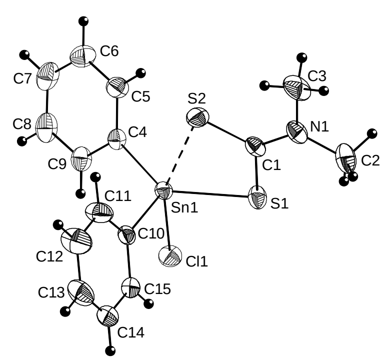

Figure 1. ORTEP representation at 30% probability and atom numbering scheme for $Ph_2SnCl(S_2CNMe_2)$ (**3**).

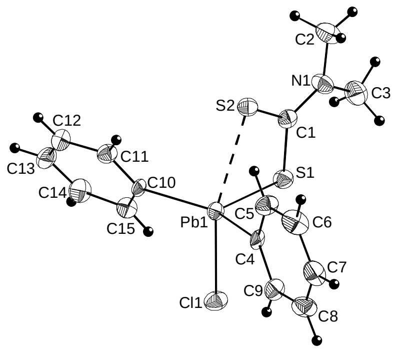

Figure 2. ORTEP representation at 30% probability and atom numbering scheme for $Ph_2PbCl(S_2CNMe_2)$ (**6**).

Table 2.

Interatomic bond distances (Å) and angles (°) for compounds **3** and **6**.

3		**6**	
Sn(1)-C(4)	2.137(3)	Pb(1)-C(4)	2.195(8)
Sn(1)-C(10)	2.140(3)	Pb(1)-C(10)	2.232(10)
Sn(1)-Cl(1)	2.4486(9)	Pb(1)-Cl(1)	2.617(10)
Sn(1)-S(1)	2.4718(10)	Pb(1)-S(1)	2.607(8)
Sn(1)-S(2)	2.6834(10)	Pb(1)-S(2)	2.821(8)
C(1)-S(1)	1.739(4)	C(1)-S(1)	1.754(9)
C(1)-S(2)	1.713(4)	C(1)-S(2)	1.704(8)
C(1)-N(1)	1.317(4)	C(1)-N(1)	1.339(10)
C(2)-N(1)	1.457(5)	C(2)-N(1)	1.466(11)
C(3)-N(1)	1.460(5)	C(3)-N(1)	1.467(11)
C(4)-Sn(1)-C(10)	116.93(13)	C(4)-Pb(1)-C(10)	146.5(3)
S(1)-Sn(1)-C(4)	132.35(10)	S(1)-Pb(1)-C(4)	109.0(3)
S(1)-Sn(1)-C(10)	109.10(9)	S(1)-Pb(1)-C(10)	103.8(3)
Cl(1)-Sn(1)-C(4)	96.77(10)	Cl(1)-Pb(1)-C(4)	95.0(3)
Cl(1)-Sn(1)-C(10)	98.25(10)	Cl(1)-Pb(1)-C(10)	93.09(18)
Cl(1)-Sn(1)-S(1)	87.99(4)	Cl(1)-Pb(1)-S(1)	87.4(2)
S(2)-Sn(1)-C(4)	92.91(10)	S(2)-Pb(1)-C(4)	93.7(3)
S(2)-Sn(1)-C(10)	96.47(10)	S(2)-Pb(1)-C(10)	93.2(2)
S(2)-Sn(1)-S(1)	69.70(3)	S(2)-Pb(1)-S(1)	66.4(3)
Cl(1)-Sn(1)-S(2)	156.36(4)	Cl(1)-Pb(1)-S(2)	153.84(9)
Sn(1)-S(1)-C(1)	89.42(12)	Pb(1)-S(1)-C(1)	90.2(3)
Sn(1)-S(2)-C(1)	83.21(12)	Pb(1)-S(2)-C(1)	84.3(4)

Table 2.

(continued).

N(1)-C(1)-S(1)	120.4(3)	N(1)-C(1)-S(1)	119.1(5)
N(1)-C(1)-S(2)	122.1(3)	N(1)-C(1)-S(2)	122.1(6)
S(1)-C(1)-S(2)	117.5(2)	S(1)-C(1)-S(2)	118.8(5)
C(1)-N(1)-C(2)	122.8(3)	C(1)-N(1)-C(2)	121.3(7)
C(1)-N(1)-C(3)	121.5(4)	C(1)-N(1)-C(3)	122.4(7)
C(2)-N(1)-C(3)	115.7(3)	C(2)-N(1)-C(3)	116.2(7)

The Pb(1)-S(1) primary bond [2.607(8) Å] in **6** is considerably stronger, while the secondary Pb(1)-S(2) bond [2.821(8) Å] is similar with respect to those found for lead(II) dithiocarbamates *e.g.* $Pb(S_2CNMe_2)_2$ [Pb-S 2.779(5) Å; Pb···S 2.873(6) Å] [11], $Pb(S_2CNEt_2)_2$ [Pb-S 2.744(9), 2.786(9) Å; Pb···S 2.885(11), 2.940(10) Å] [12], or $Pb(S_2CNPr^i{}_2)_2$ [Pb-S 2.673(4), 2.681(4) Å; Pb···S 2.843(5), 2.859(5) Å] [13].

The tin-chlorine distance in **3** [Sn(1)-Cl(1) 2.4486(9) Å] compares well with those observed in $Me_2SnCl(S_2CNMe_2)$ [Sn-Cl 2.465(9) Å] [9] or $(PhCH_2)_2SnCl(S_2CNMe_2)$ [Sn-Cl 2.482(2) Å] [10]. The lead-chlorine bond in **6** [Pb(1)-Cl(1) 2.617(10) Å] is shorter than that observed in the polymeric Ph_2PbCl_2 starting material [Pb-Cl 2.795(1) Å in the Pb-Cl-Pb bridges] [14], but of the same magnitude as found in the related $Ph_2PbCl[S(S)CPPh_2(O)]$ [Pb-Cl 2.62(1) Å] [15], respectively.

The resulting coordination geometry at the metal centre is best described as highly distorted trigonal bipyramidal, with the dithiocarbamato ligand spanning axial–equatorial positions. The long metal-S(2) bond is axial, in *trans* to the chlorine atom [Cl(1)-Sn(1)-S(2) 156.36(4)^o in **3**, and Cl(1)-Pb(1)-S(2) 153.84(9)^o in **6**]. The equatorial plane is described by the C(4), C(10) and S(1) atoms, with the metal atom displaced from this plane towards the chlorine atom with 0.163 and 0.104 Å in **3** and **6**, respectively. The S(1)Sn(1)S(2) plane is almost perpendicular to the C(4)C(10)S(1) basal plane (dihedral angle 84.1^o and 89.3^o in **3** and **6**, respectively). The distortion is mainly due to the small bite of the ligand [S(1)···S(2) 2.951(2) and 2.98(1) Å in **3** and **6**, respectively].

The main difference between these two molecular structures is the opened equatorial C(4)-Pb(1)-C(10) angle [146.5(3)^o] in **6** compared to the corresponding C(4)-Sn(1)-C(10) angle [116.93(13)^o] in **3**. A closer check of the crystal structure of the lead derivative revealed the presence of a weak intermolecular π-Pb–phenyl interaction [Pb(1)···$C_{6,7,8}$ 3.77(1)-4.23(2) Å] which involves one of the aromatic rings attached to the metal centre. The vector of this π-Pb–phenyl interaction bisects the C(4)-Pb(1)-C(10) angle, in *trans* to the S(1) atom, and might be the cause of enlargement of this equatorial angle. Based on these interactions dimer associations might be considered to be formed, in which the coordination geometry around the lead can be described as distorted octahedral (Figure 3). Similar intra- or intermolecular π-Pb–phenyl interactions were previously described in the monomeric $Pb[(SPPh_2)_2N]_2$ [Pb(1)···$C_{1,2,6}$ 3.31(1)-3.70(2) Å] [16] and the dimeric $[Pb\{(OPPh_2)(SPPh_2)N\}_2]_2$ [Pb(1)···$C_{1,2,6}$ 3.424-3.579 Å] [17].

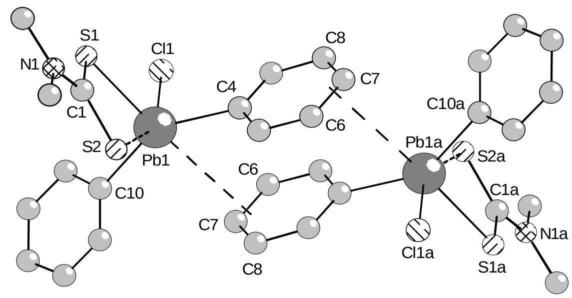

Figure 3. Dimeric association in the crystal of $Ph_2PbCl(S_2CNMe_2)$ (**6**).

The molecular structure of $Ph_2Sn(S_2CNMe_2)_2$ (**4**) was also established by single-crystals X-ray diffraction studies [the crystals were obtained from a chloroform and hexane (1/4, v/v) mixture]. The crystal of **4** consists of discrete monomers separated by normal van der Waals distances. The ORTEP diagram of the molecular structure of compound **4**, with the atom numbering scheme, is shown in Figure 4. Selected interatomic distances and angles are listed in Table 3.

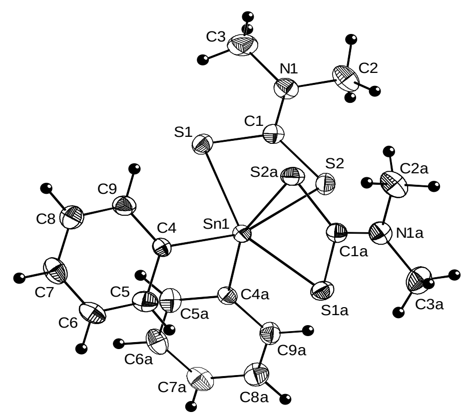

Figure 4. ORTEP representation at 30% probability and atom numbering scheme for $Ph_2Sn(S_2CNMe_2)_2$ (**4**).

Table 3.

Interatomic bond distances (Å) and angles (^{o}) for compound **4**.

Sn(1)-C(4)	2.165(5)	C(4)-Sn(1)-C(4a)	98.2(3)
Sn(1)-S(1)	2.5860(14)	S(1)-Sn(1)-S(2)	68.34(5)
Sn(1)-S(2)	2.6632(15)	S(1)-Sn(1)-S(1a)	152.83(7)
		S(1)-Sn(1)-S(2a)	90.90(5)
C(1)-S(1)	1.728(5)	S(2)-Sn(1)-S(1a)	90.90(5)
C(1)-S(2)	1.702(5)	S(2)-Sn(1)-S(2a)	82.45(7)
C(1)-N(1)	1.329(7)	S(1a)-Sn(1)-S(2a)	68.34(5)
C(2)-N(1)	1.467(7)		

C(3)-N(1)	1.450(8)	C(4)-Sn(1)-S(1)	93.81(14)
		C(4)-Sn(1)-S(2)	161.15(14)
N(1)-C(1)-S(1)	120.2(4)	C(4)-Sn(1)-S(1a)	103.94(14)
N(1)-C(1)-S(2)	121.3(4)	C(4)-Sn(1)-S(2a)	92.18(14)
S(1)-C(1)-S(2)	118.6(3)		
		C(4a)-Sn(1)-S(1)	103.94(14)
C(1)-N(1)-C(2)	121.4(5)	C(4a)-Sn(1)-S(2)	92.18(14)
C(1)-N(1)-C(3)	122.1(5)	C(4a)-Sn(1)-S(1a)	93.81(14)
C(2)-N(1)-C(3)	116.5(5)	C(4a)-Sn(1)-S(2a)	161.15(14)
		Sn(1)-S(1)-C(1)	87.39(18)
		Sn(1)-S(2)-C(1)	85.44(18)

As in compound **3**, both dimethyldithiocarbamato moieties in a molecular unit of **4** act as *asymmetric monometallic biconnective units*, with short [Sn(1)-S(1) 2.5860(14) Å] and long [Sn(1)-S(2) 2.6632(15) Å] tin-sulfur distances. However, the Sn(1)-S(1) primary bonds are much longer than in **3** [2.4718(10) Å] and thus the extent of asymmetry is considerably reduced (Δ = [Sn(1)-S(2)] - [Sn(1)-S(1)] is 0.077 Å in **4** *vs.* 0.212 Å in **3**).

The resulting coordination geometry around the tin atom is highly distorted octahedral, with *cis* phenyl groups [C(4)-Sn(1)-C(4a) 98.2(3)^o] and axial shorter tin-sulfur bonds [S(1)-Sn(1)-S(1a) 152.83(7)^o]. The distortion is mainly due to the small bite of the ligand [S(1)···S(2) 2.949(2)] and is reflected by the dihedral angles: C(4)Sn(1)C(4a) / S(1)Sn(1)S(1a) 83.2^o; S(1)Sn(1)S(2) / S(1a)Sn(1)S(2a) 72.5^o. Similar coordination geometries were reported for other related diphenyltin(IV) derivatives, *i.e.* $Ph_2Sn(S_2CNEt_2)_2$ (regardless the monoclinic [18,19] or tetragonal [20] forms) or $Ph_2Sn(S_2CNCy_2)_2$ [21]. By contrast, for the $Me_2Sn(S_2CNMe_2)_2$ the geometry at tin was found to be a highly distorted skew-trapezoidal bipyramid, with angular C-Sn-C angle [136.45(1)^o] and a planar equatorial SnS_4 system [22].

With respect to the dimethyldithiocarbamato ligand in compounds **3**, **4** and **6** some common features should be noted. The MS_2CNC_2 skeleton is basically planar. Although, consistent with the *asymmetric monometallic biconnective* pattern, short and long metal-sulfur distances are established, in the dithio ligand unit the sulfur-carbon distances are almost equivalent on the basis of the 3σ criteria [C(1)-S(1) 1.739(4) Å in **3**, 1.754(9) Å in **6** and 1.728(5) Å in **4** *versus* C(1)-S(2) 1.713(4) Å in **3**, 1.704(8) Å in **6** and 1.702(5) Å in **4**, respectively]. The carbon-nitrogen bond distance and the planarity of the NC_3 fragment reflect the double bond character and the sp^2 hybridization of the nitrogen atom, respectively.

ACKNOWLEDGEMENTS

This work was supported by the National University Research Council of Romania (CNCSIS grant, A_T-23/552/2004) and CERES Project, Contract No 32/12.11.2002). We thank the *National Center for X-Ray Diffraction* (“Babes-Bolyai” University, Cluj-Napoca) for support of the single-crystal X-ray diffraction studies.

REFERENCES

1. P. J. Heard, in *Progress in Inorganic Chemistry*, **2006**, *53* (K.D. Karlin, Ed.), 1.
2. G. M. Sheldrick, *SADABS, Program for area detector adsorption correction*, Institute for Inorganic Chemistry, University of Göttingen, Germany, **1996**.
3. Sheldrick GM, *SHELXTL-97*, University of Göttingen, Germany, **1997**.
4. DIAMOND – Visual Crystal Structure Information System, CRYSTAL IMPACT: Postfach 1251, D-53002 Bonn, Germany, **2001**.
5. A.G. Davies, P.J. Smith, in: G. Wilkinson, F.G.A. Stone, E.W. Abel (Eds.), *Comprehensive Organometallic Chemistry*, Vol. 2, Pergamon Press, Oxford, **1982**, pp. 529–530.
6. J. Holecek, A. Lycka, *Inorg. Chim. Acta*, **1986**, *118*, L15.
7. R. A. Varga, C. Silvestru, I. Haiduc, *Synth. React. Inorg. Met.-Org. Chem.*, **2000**, *30*, 485.
8. R. A. Varga, J. E. Drake, C. Silvestru, *J. Organomet. Chem.*, **2003**, *675*, 48.
9. K. Furue, T. Kimura, N. Yasuoka, N. Kasai, M. Kakudo, *Bull. Chem. Soc. Jpn.*, **1970**, *43*, 1661.
10. H.-D. Yin, C.-L. Ma, Y. Wang, *Indian J. Chem., Sect. A*, 2002, **41,**342.
11. H. Iwasaki, *Acta Crystallogr., Sect. B*, **1980**, *36*, 2138.
12. H. Iwasaki, H. Hagihara, *Acta Crystallogr., Sect. B*, **1972**, *28*, 507.
13. M. Ito, H. Iwasaki, *Acta Crystallogr., Sect. B*, **1980**, *36*, 443.
14. M. Mammi, V. Busetti, A. Del Pra, *Inorg. Chim. Acta*, **1967**, *1*, 419.
15. S. N. Olafsson, C. Flensburg, P. Andersen, *J. Chem. Soc., Dalton Trans.*, **2000**, 4360.
16. J. S. Casas, A. Castineiras, I. Haiduc, A. Sanchez, J. Sordo, E. M. Vazquez-Lopez, *Polyhedron*, **1994**, *13*, 2873.
17. V. Garcia-Montalvo, R. Cea-Olivares, G. Espinosa-Perez, *Polyhedron*, **1996**, *15*, 829.
18. P. F. Lindley, P. Carr, *J. Cryst. Mol. Struct.*, **1974**, *4*, 173.
19. N. W.Alcock, J. Culver, S. M. Roe, *J. Chem. Soc., Dalton Trans.*, **1992**, 1477.
20. J. M. Hook, B. M. Linahan, R. L. Taylor, E. R. T. Tiekink, L. van Gorkom, L. K. Webster, *Main Group Metal Chem.*, **1994**, *17*, 293.
21. V. J. Hall, E. R. T. Tiekink, *Main Group Metal Chem.*, **1995**, *18*, 611.
22. T. Kimura, N. Yasuoka, N. Kasai, M. Kakudo, *Bull. Chem. Soc. Jpn.*, **1972**, *45*, 1649.

STUDIA UNIVERSITATIS BABES - BOLYAI, CHEMIA, LI, 2, 2006

Dedicated to professor Gh. Marcu at his 80th anniversary

CHEMICALLY MODIFIED BASIC ALUMINA N FOR TLC. SYNTHESIS, CHARACTERIZATION AND APPLICATIONS

MIUȚA FILIP[1], VIRGINIA COMAN[1], RODICA GRECU[1], CHRISTOPH MEYER[2], ZAHARIE MOLDOVAN[3] AND GHEORGHE MARCU[4]

ABSTRACT. The synthesis of chemically modified basic alumina N has been performed by organosilylation reaction of hydroxylated alumina surface with trifunctional modifiers: *n*-octadecyltrichlorosilane and 3-mercaptopropyltrimethoxysilane.

These chemically modified aluminas were characterized by elemental analysis, specific surface area, FTIR and ^{13}C-CP/MAS NMR spectroscopy, mass spectrometry and thermoanalytical methods.

Chromatographic behaviour of unmodified and chemically modified aluminas were tested by the separation and identification of some dyes and benzo[a]pyrene derivatives.

Keywords: Chemically modified basic alumina N, Thin layer chromatography, FTIR spectroscopy, ^{13}C-CP/MAS NMR spectroscopy, Mass spectrometry, Thermal analysis.

The progress of chemically modified stationary phases with applicability in liquid chromatography have been permitted the use of the inorganic oxides, such as alumina, titania and zirconia, as supports due to their specific properties or as an alternative for silica gel. Alumina is a stationary phase widely used in liquid chromatography due to its special chromatographic properties and of inherent higher pH stability [1-3].

The sort of alumina frequently used in thin layer chromatography (TLC) is γ–Al_2O_3 which has on its surface three types of active centers: oxygen anions, surface hydroxyl groups and aluminium cations [4].

In order to increase the selectivity and the efficiency of the chromatographic separation, the chemical modification with a high variety of organic compounds attached to the hydroxylated surface of adsorbent is a very useful method [1,4,5].

The characterization and the applications of reversed phases based on alumina are presented in literature [2,3,6,7].

[1] „Raluca Ripan" Institute for Research in Chemistry, 30 Fântânele St., RO-400294, Cluj-Napoca, Romania, E-mail: mfilip@iccrr.ro; v.coman@iccrr.ro
[2] University of Tübingen, Institute of Organic Chemistry, Auf der Morgenstelle 18, D-72076 Tübingen, Germany
[3] National Institute for Research and Development of Isotopic and Molecular Technologies, 71-103 Donath St., RO-400293, Cluj-Napoca, Romania, E-mail: zaha@oc1.itim-cj.ro
[4] „Babes-Bolyai" University, Department of Inorganic Chemistry, 11 Arany Janos St., RO-400028 Cluj-Napoca, Romania.

Infrared studies on chromatographic aluminas have been mainly focused on the hydroxyl groups and Al–O–Al linkages created during the dehydration process [3]. Diffuse reflectance infrared Fourier transform (DRIFT) spectra have been used to the characterization of chemically modified aluminas [8-10]. The study of chemically modified stationary phases by mass spectrometry is not frequently met in literature [11-15].

The TG (thermogravimetry), DTG (derivative thermogravimetry) and DTA (differential thermal analysis) thermoanalytical methods are not usually used for the study of modified stationary phases. However, these methods are suitable for the characterization of chromatographic adsorbents. The shape of thermoanalytical curves gives information about the mass losses of the material and the effects that occur [7,16,17].

EXPERIMENTAL

REAGENTS:

Basic alumina N was supplied by Macherey-Nagel (Düren, Germany).

n-Octadecyltrichlorosilane, 3-mercaptopropyltrimethoxysilane, hexane and the dyes: Toluidine blue, Bromothymol blue, Sudan black B, Sudan III, were purchased from Merck (Darmstadt, Germany).

Xylene, dichloromethane, diethyl ether, acetone, benzene, ethanol, methanol, carbon tetrachloride were purchased from Chimopar Bucharest (Romania).

The benzo[a]pyrene derivatives: benzo[a]pyrene-*trans*-7,8-diol-9,10-epoxy, benzo[a]pyrene-*trans*-9,10-dihydrodiol, benzo[a]pyrene-*trans*-7,8-dihydrodiol, benzo[a]pyrene-8-hydroxy, benzo[a]pyrene-7-hydroxy were purchased from Fluka (Switzerland).

SYNTHESIS OF CHEMICALLY MODIFIED BASIC ALUMINA N:

The chemically modified aluminas were prepared by the silylation reaction of basic alumina N with the modifiers: *n*-octadecyltrichlorosilane and 3-mercaptopropyltrimethoxysilane in the mass ratio of 2.5:1 (w/w) [7].

The obtained product was filtered and washed successively with xylene, dichloromethane and diethyl ether until the complete removal of the modifier traces.

CHARACTERIZATION OF CHEMICALLY MODIFIED BASIC ALUMINA N (Abbreviations of the studied samples are given in TABLE 1) has been performed by:

The *elemental analysis* (carbon, hydrogen and sulphur) of samples was performed by means of VARIO EL Elemental Analysis System.

The *specific surface area* of samples was determined using the BET method (krypton adsorption at the temperature of liquid nitrogen).

The *infrared spectra* of alumina samples were registered on a JASCO-610-FTIR spectrometer, using the KBr pellet technique. To improve the sensitivity of the IR method the difference and second derivative spectra were also analyzed.

^{13}C *CP/MAS NMR spectra* were recorded on a BRUKER DSX 200 spectrometer with samples of 200-300 mg in a double bearing 7 mm rotors of ZrO_2. Magic Angle Spinning (MAS) was carried out at 3500 Hz. The spectra were recorded with a proton pulse of 6.5 µs, a recycle delay of 1 s and a contact time of 1 ms.

The *mass spectra* (EI-MS) were registered on a FINIGAN MAT 311 spectrometer with double focusing in the following conditions: 70 eV electron energy, 100 µA emission current, 180°C ion source temperature. The sample has been introduced directly in the ion source and heated up to 320°C in 10^{-6} torr vacuum. The mass spectra of all samples have been continuously registered.

The *thermal analysis* was performed by means of an OD 102 Derivatograph (MOM, Hungary) in the conditions: 200 mg sample quantity, 10°C/min rate of increase of oven temperature and TG - 100 mg; DTA - 1/5; DTG - 1/5 sensitivities respectively. The measurements were conducted in air atmosphere in the temperature range of 20-1000°C.

The *chromatographic testing* was performed on 10x14 cm glass plates prepared both from unmodified and from chemically modified alumina N. The plates were coated with 0.25 mm layers by the application of an ethanolic slurry of a mixture of the stationary phase and an organic binder [6,7].

The standard solutions (0.1%) of dyes singly or as a mixture prepared in ethanol, both singly and as a mixture, were applied as 5 μL spots on the chromatographic plates by means of Brand micropipettes. Standard solutions (0.05%) of benzo[a]pyrene derivatives were prepared in benzene and spotted on the chromatographic plates in the same mode. Ascending development to a distance of 10 cm was performed at room temperature in an unsaturated Stahl chamber for all studied compounds. The dyes were developed using the dichloromethane - diethyl ether - acetone (20 + 70 + 10, v/v) mixture as mobile phase. The benzo[a]pyrene derivatives were developed using the benzene - acetone (70 + 30, v/v) mixture as mobile phase and the visualization was performed at 365 nm by a Camag lamp.

RESULTS AND DISCUSSIONS

The ideal representation of the ***synthetized chemically modified aluminas*** is shown in FIGURE 1.

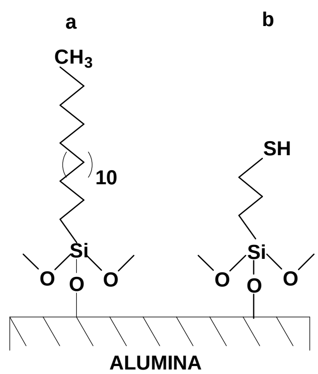

Figure 1. Chemically modified alumina: **a**, alumina-C18; **b**, alumina-SH

The obtained chemically modified aluminas were characterized by elemental analysis, specific surface area, coverage density, FTIR spectroscopy, ^{13}C CP/MAS NMR spectroscopy, mass spectrometry, thermal analysis and chromatographic behaviour by TLC separation of some dyes on unmodified and chemically modified alumina layers.

Elemental analysis data (combustion method), ***specific surface area*** (BET method) and ***coverage density*** (calculus) for unmodified and chemically modified aluminas, are presented in TABLE 1.

TABLE 1

Coverage density of unmodified and chemically modified aluminas
(% C; % H; %S; specific surface area – S_{BET}; coverage density– α)

Alumina	**Abbreviation**	**C (%)**	**H (%)**	**S (%)**	**S_{BET} (m^2/g)**	**α ($\mu mol/m^2$)**
basic alumina N	alumina	–	–	–	114.2	–
n-octadecyl basic alumina N	alumina-C18	3.22	1.66	–	89.0	1.37
3-mercaptopropyl basic alumina N	alumina-SH	2.78	0.67	1.27	96.9	7.6

The data in this table show the presence of carbon, hydrogen and sulphur and the decreasing of specific surface area of the chemically modified aluminas.

Using ***FTIR spectroscopy***, the presence of the modifier on alumina surface is well evidenced by the new bands observed in the 2800–3000 cm^{-1} range.

Due to the low concentration of the organic part of modifier on the surface, the intensity of the new bands is weak (FIGURE 2).

The bands with maximum at ~ 2923 cm^{-1} and at ~ 2853 cm^{-1} are assigned to stretching vibrations of *n*-alkyl chain: $\nu_{as}(CH_2)$ and $\nu_{sym}(CH_2)$ respectively.

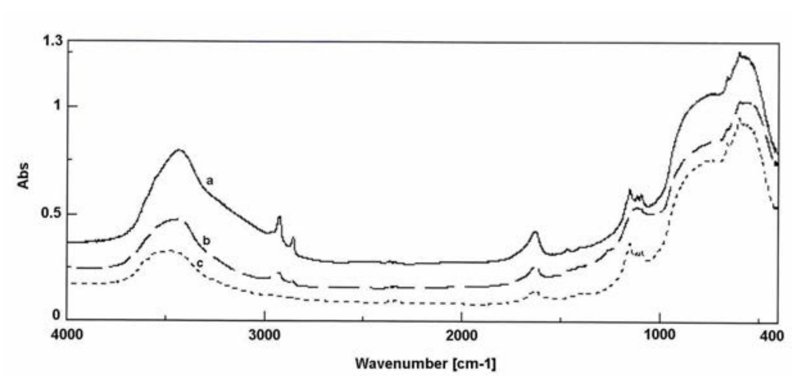

Figure 2. FTIR spectra of: **a**, alumina-C18; **b**, alumina-SH, **c**, alumina

In the difference FTIR spectrum (FIGURE 3) of unmodified and chemically modified alumina N the band observed at ~ 1468 cm^{-1} is due to the $\delta(CH_2)$ vibration. The bands observed in the range of 900-1200 cm^{-1} are assigned to ν(Al-O) and ν(Si-O) vibrations, showing the formation of Al-O-Si bridges.

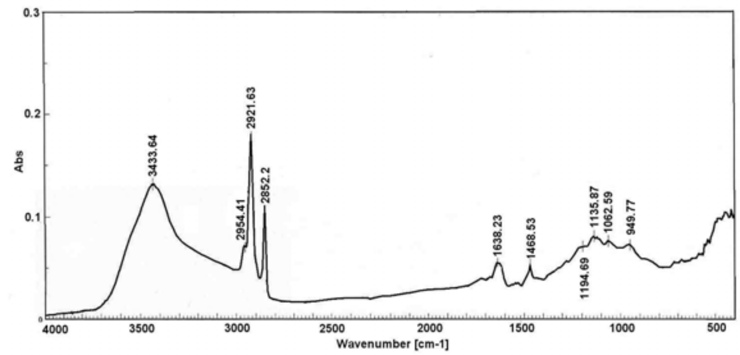

FIGURE 3. Difference FTIR spectrum of alumina-C18 and alumina

To improve the sensitivity of the infrared method, the second derivative spectra were also analysed in order to show that there are differences in the envelope of the infrared spectrum of unmodified and chemically modified alumina N (see FIGURE 4 for 3-mercaptopropyl alumina N).

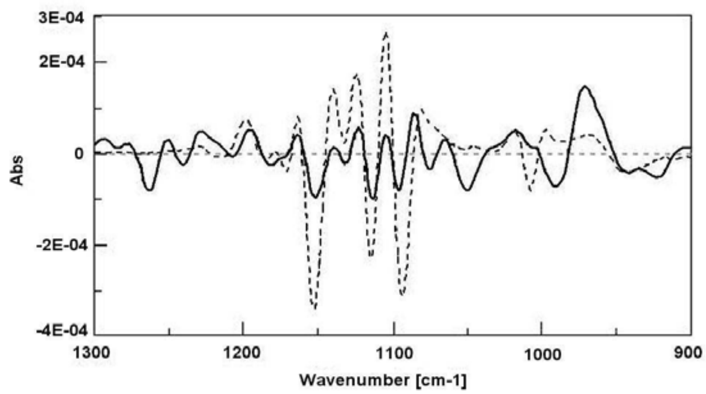

Figure 4. Second derivative spectrum of alumina-SH (–) and alumina (…)

The ***^{13}C-CP/MAS NMR spectroscopy*** was used to study the conformational properties of immobilized ligands.

The observed signals in the NMR spectrum (FIGURE 5) were assigned to the corresponding carbon atoms as it is indicated. The high field shifted signal belongs to the C-1 atom, in the neighbourhood of the silicon (12.832 ppm). The low field shifted signals are characteristic for the carbon atoms C-2 (23.07 ppm, as a shoulder) and C-3 (27.859 ppm) of the mercapto grups.

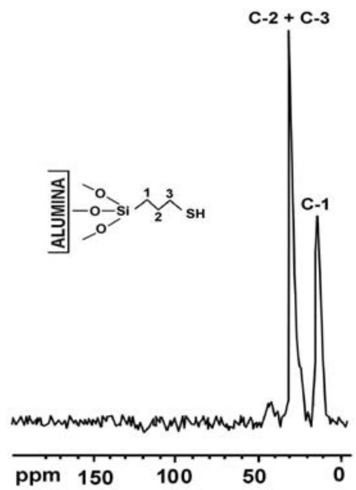

Figure 5. ^{13}C-CP/MAS NMR spectrum of alumina-SH

The comparative ***mass spectrometry*** study of unmodified and chemically modified alumina N puts in evidence the presence of the adequate chains on the modified alumina surface.

The mass spectrum (FIGURE 6) of *n*-octadecyl alumina N is dominated by the series of ions C_nH_{2n+1} (29, 43, 57, 71, …, M-15) characteristic for the long normal hydrocarbon chain [14,15]. These ions are accompanied by those of C_nH_{2n-1} (27, 41, 55, 69,…) series. The formation of both ion series can be explained based on the fragmentation rules of hydrocarbons with normal chain. The periodicity of the main ions with a mass difference of Δm 14 (CH_2) must be mentioned. The characteristic ions appear around 200°C (FIGURE 7).

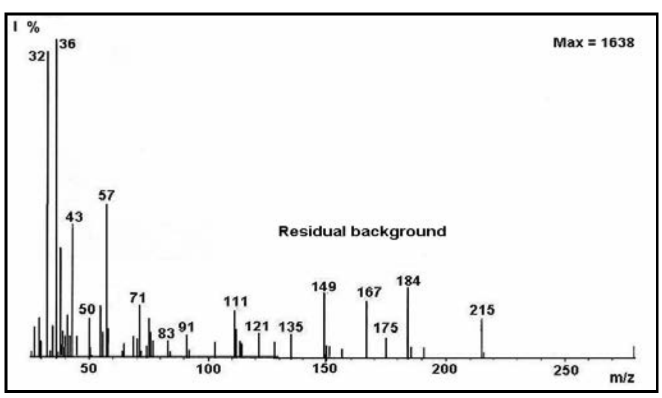

Figure 6. Mass spectrum (EI-MS) in the maximum intensity point for alumina-C18

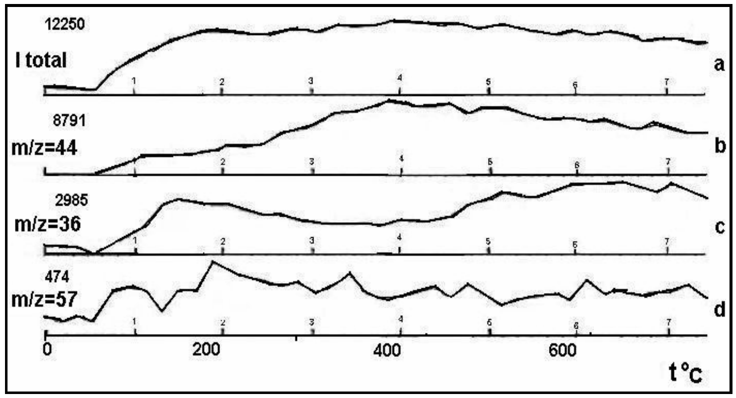

Figure 7. Intensity of characteristic ions *versus* temperature for alumina-C18: **a**) I total, **b**) m/z = 44 $[CO_2]^+$, **c**) m/z = 36 $[HCl]^+$ ion, **d**) m/z = 57 (organic part) ion

Over 100°C the characteristic ions for HCl (*m/z* 36 and 38) are visible, that confirms the fact that some initial radicals –Cl remain on the modified alumina surface.

FIGURE 8 and FIGURE 9 show the mass spectrum in the maximum intensity point and the intensity of characteristic ions *versus* temperature, for 3-mercaptopropyl alumina N, respectively.

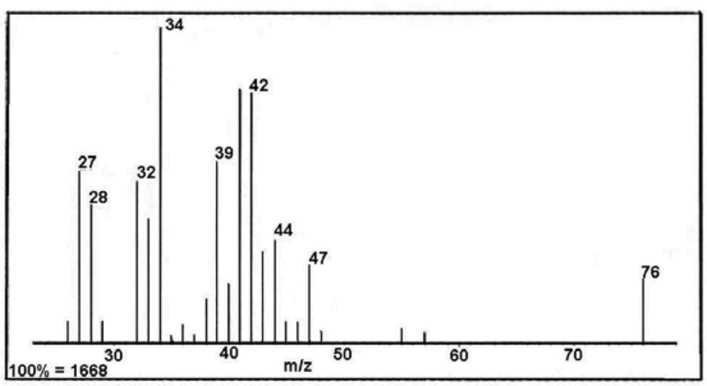

FIGURE 8. Mass spectrum in the maximum intensity point for alumina-SH

In the mass spectrum the main ions observed with: *m/z* 34, 47 and 76 correspond to SH_2, HS-CH_2 and HS-CH_2-CH_2-CH_3 structures and start around of 220°C. The characteristic ions appear around 250°C.

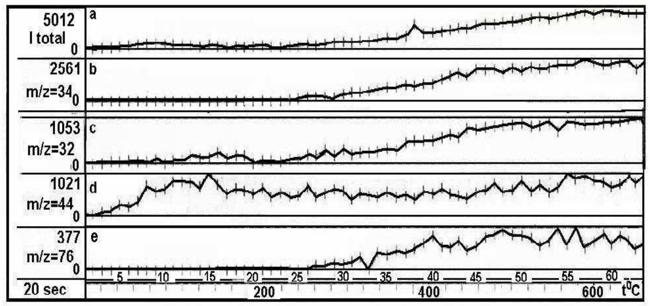

FIGURE 9. Intensity of characteristic ions *versus* temperature for alumina-SH:
a) I total, **b**) m/z = 34 $[SH_2]^+$ ion, **c**) m/z = 32 $[CH_3\text{-}OH]^+$ ion,
d) m/z = 44 $[CO_2]^+$ ion, **e**) m/z =76 $[C_3H_8S]^+$ ion

Over 180°C are visible the characteristic ions for CH_3-OH (*m/z* 32) too, confirming the remaining of some initial radicals –O–CH_3. Thus the 2,3 functionality of trifunctional modifier is explained.

The comparative study of mass spectra of unmodified aluminas *versus* chemically modified alumina, puts in evidence the modifications of alumina surface with the corresponding *n*-octadecyl and 3-mercaptopropyl chains.

The ***thermoanalytical (TG, DTG, DTA)*** method gives quantitative information about the water removed by the desorption and dehydration processes (endothermal effect) and the elimination process of organic part (exothermal effect) of the studied stationary phases and data referring to the temperature ranges where the thermal effects take place.

Thermoanalysis results for aluminas (unmodified and chemically modified) are presented in TABLE 2 and FIGURE 10.

TABLE 2

Thermoanalysis results for unmodified and chemically modified aluminas

Stationary phase	***Endothermal effect t°C***	***Δm %***	***Exothermal effects***				***ΔM %***
			Effect I, t°C	***Δm_I %***	***Effect II, t°C***	***Δm_{II} %***	
alumina	**80** (35–90)	1.0	**165, 350** (90–700)	11.5	–	–	12.5
alumina -C18	**95** (35–160)	1.8	**360** (160–480)	24.2	**560** (480–700)	5.5	31.5
alumina -SH	**80** (100–240)	8.5	**340** (240–410)	11.0	**520** (410–800)	12.0	31.5

The TG data indicate a continuous mass loss which depends on the nature and length of the chain bonded to alumina surface. The mass loss is less for unmodified alumina than for the modified material.

The DTA data show two types of thermal effects. The endothermal effect was attributed to the desorption and dehydration processes of superficial water. For the modified alumina N, the observed exothermal effects are assigned to the removal of species from the surface and to the elimination process of the organic part (see TABLE 2).

The different thermal behaviour of unmodified and modified alumina revealed the differences among these compounds as a result of the organosilanization reaction.

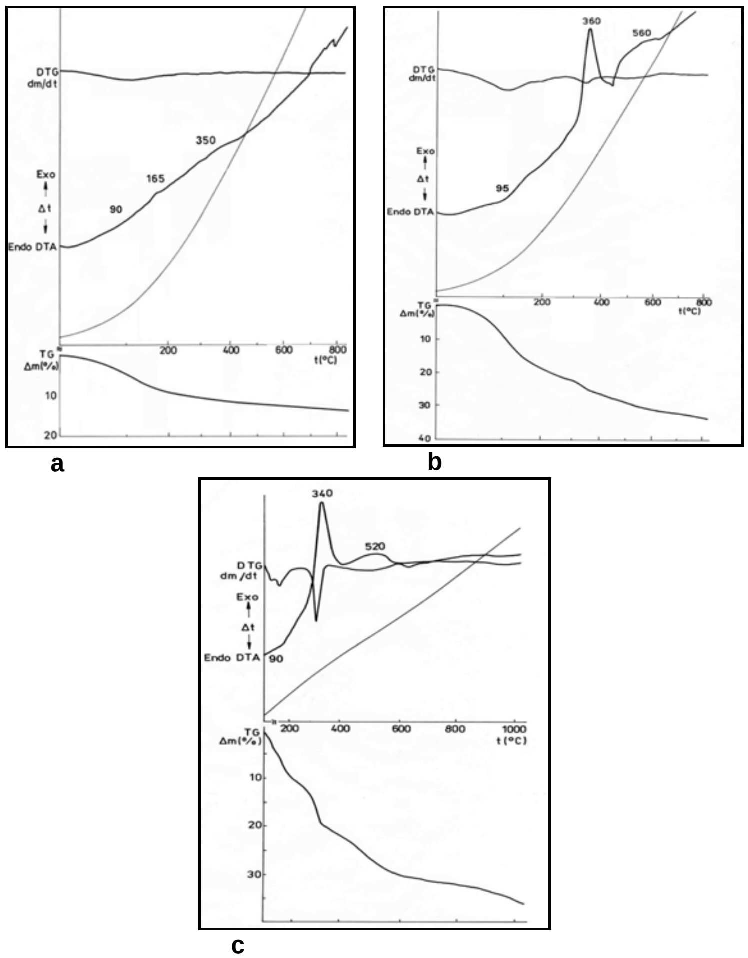

Figure 10. Thermoanalytical (TG, DTG, DTA) diagrams for:
a) alumina, **b**) alumina-C18; **c**) alumina-SH

The ***chromatographic testing*** of unmodified and chemically modified alumina N has been studied for the separation of some dyes and benzo[a]pyrene derivatives.

The parameters that define the TLC behaviour of the separated compounds on the unmodified and chemically modified aluminas [selectivity (β), efficiency (E) and resolution (R_S)] were calculated according to Equations 1-3 [18], for two neighbouring spots of studied compounds.

$$\beta = \frac{R_{f2} - R_{f1} \times R_{f2}}{R_{f1} - R_{f1} \times R_{f2}} \quad (1)$$

$$E = \frac{(\beta - 1)^2}{4\beta} \times (1 - R_{f2}) \times (1 - R_{f1}) \frac{1}{\sqrt{H_2 H_1}} \quad (2)$$

$$R_S = \frac{\Delta R_f \sqrt{Z_f - Z_0}}{2(\sqrt{R_{f1} H_1} + \sqrt{R_{f2} H_2})} \quad (3)$$

where:

$H = \frac{Z_f - Z_0}{N}$, is the theoretical plate height and $N = 16\left(R_f \frac{Z_f - Z_0}{\delta_x}\right)^2$, the theoretical plate number. R_{f1}, R_{f2}, represent the retention factors of a neighbouring pair of substances, Z_f-Z_0, the distance between origin and the mobile phase front and δ_x, the spot diameter.

The experimental average values for δ_x are 0.5 cm for unmodified alumina and 0.4 cm for chemically modified aluminas.

In FIGURE 11 are presented the chromatographic results obtained at the separation of some dyes on thin layers of unmodified and chemically modified alumina N using the dichloromethane : diethyl ether : acetone, (20 / 70 / 10, v/v) mixture as mobile phase.

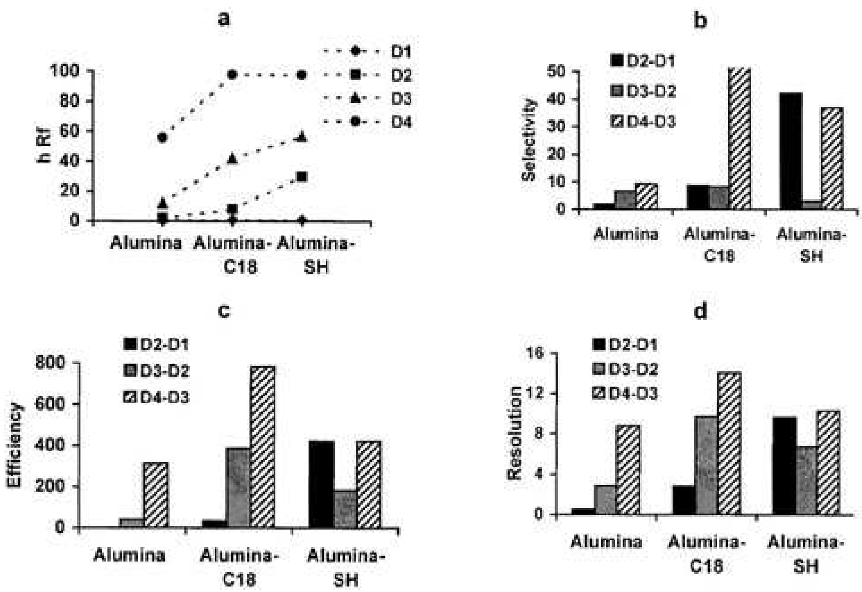

Figure 11. TLC separation of some dyes on unmodified and chemically modified basic alumina N: **a** –hR_f values **b** – Selectivity, **c** – Efficiency, **d** – Resolution
Mobile phase: dichloromethane:diethyl ether:acetone, (20 / 70 / 10, *v/v*);
Dyes: Toluidine Blue (D1), Bromothymol Blue (D2), Sudan Black (D3), Sudan III (D4)

The chromatographic results obtained at the separation of benzo[a]pyrene derivatives on unmodified and chemically modified aluminas are presented in FIGURE 12.

The results show that the values of the chromatographic parameters depend on the retention factors of two neighbouring compounds, the migration distance of mobile phase, the diameter of spots and the type of mobile and stationary phases, respectively.

Analysing the results presented in FIGURE 12 we can conclude:

- for $\boldsymbol{R_f}$ values from the 0.2-0.8 range, the selectivity has a small variation;
- the separation degree of two neighbouring compounds is given by the value of resolution;
- the efficiency of separation of two neighbouring compounds depends on the selectivity, $\boldsymbol{R_f}$ values and spot diameter.

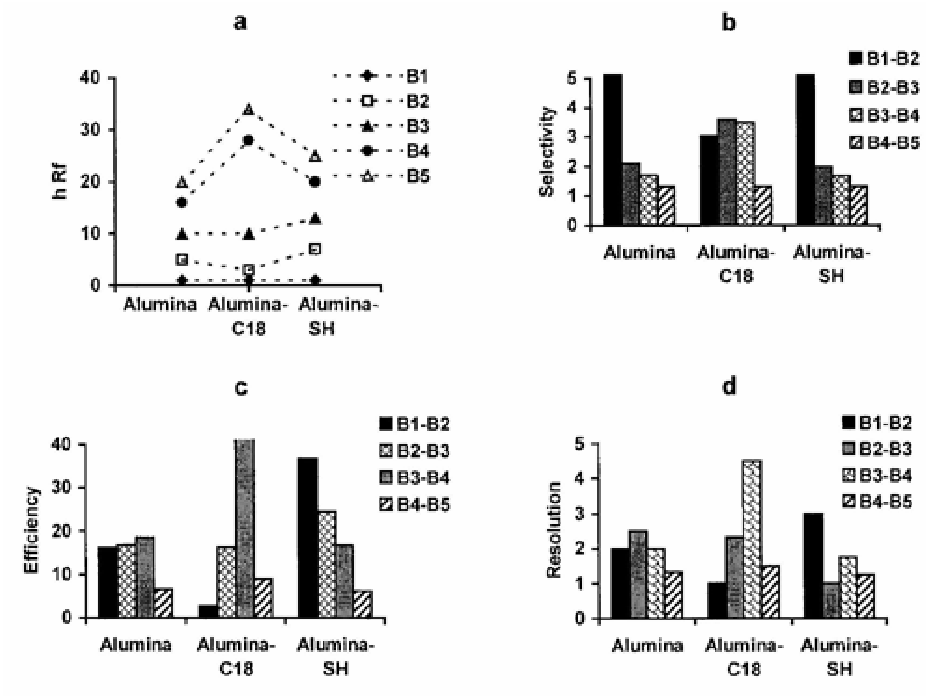

Figure 12. TLC separation of benzo[a]pyrene derivatives on unmodified and chemically modified alumina N: **a** – hR_f values; **b** – Selectivity; **c** – Efficiency; **d** – Resolution.
Mobile phase: benzene:acetone (70 / 30, *v/v*);
Benzo[a]pyrenes: Benzo[a]pyrene-*trans*-7,8-diol-9,10-epoxy (*syn*) (B1), Benzo[a]pyrene-*trans*-9,10-dihydrodiol (B2), Benzo[a]pyrene-*trans*-7,8-dihydrodiol (B3), Benzo[a]pyrene-8-hydroxy (B4), Benzo[a]pyrene-7-hydroxy (B5

The best values of the chromatographic parameters at the separation of some dyes and benzo[a]pyrenes derivatives have been obtained on *n*-octadecyl alumina N thin layers.

The chromatographic results demonstrated new retention properties for the chemically modified aluminas and the possibility to use them at different chromatographic applications.

CONCLUSIONS

Chemically modified alumina N samples have been obtained by the silylation reaction of basic alumina N with trifunctional modifiers, namely *n*-octadecyltrichlorosilane and 3-mercaptopropyltrimethoxysilane.

Elemental analysis and FTIR spectra of modified alumina show the presence of organic modifier on the alumina surface. An important change of specific surface area is obtained.

The comparative mass spectrometry and ^{13}C CP/MAS NMR spectroscopy study of unmodified and chemically modified alumina put in evidence the presence of the adequate chains on the modified alumina surface.

Thermoanalytical diagrams permitt to find out the type of thermal effects and the temperature ranges where they take place, as well as the corresponding mass loss values.

The chromatographic behaviour of chemically modified alumina proves their new retention properties at the separation of some dyes and benzo[a]pyrene derivatives.

ACKNOWLEDGEMENTS

This work was supported by CNCSIS GRANT No. 318/2000-2002.

REFERENCES

1. F. Geiss, "Fundamentals of TLC (Planar Chromatography)", Hüthig, Heidelberg, 1987.
2. J. Nawrocki, C. Dunlap, J. Li. J. Zhao, C.V. McNeff, A. McCormick, P.W. Carr, *J. Chromatogr. A*, **2004**, 1028(1), 31-62.
3. J.J. Pesek, M.T. Matyska, *J. Chromatogr. A*, **2002**, 952(1-2), 1-11.
4. T. Kowalska, Adsorbents in Thin Layer Chromatography, in: Sz. Nyiredy (Ed.) "Planar Chromatography. A Retrospective View for the Third Millennium", Springer Scientific Publisher, Budapest, 2001, 33-46.
5. S. Héron, and A. Tchapla, *Analusis*, **1993**, 21**,** 327-347.
6. C. Măruţoiu, M. Filip, C.Tigae, V. Coman, R. Grecu, Gh. Marcu, *J. Planar Chromatogr*., **2003**, 16, 183-185.
7. M. Filip, V. Coman, R. Grecu, K. Albert, Z. Moldovan, *J. Planar Chromatogr.*, **2004**, 17, 424-430.
8. H. Azour, J. Derouault, P. Lauroua, G. Vezon, *Spectrochimica Acta. Part A*, **2000**, 56**,** 1627-1635.
9. J.J. Pesek, H.-D. Lin, *Chromatographia*, **1989**, 28, 565-568.
10. J.J. Pesek, J.E. Sandoval, M. Su, *J. Chromatogr*., **1993**, 630, 95-103.
11. R.E. Aries, C.S.Gutteridge, R. Macrae*, J. Chromatogr.,* **1985**, 319, 285-297.
12. V. Coman, Z. Moldovan, C. Măruţoiu, *Acta Universitatis Cibiniensis- Seria F Chemia*, **2001**, 4, 51-58.
13. Z. Moldovan, V. Coman, M. Filip, *Studia Universitatis Babes-Bolyai, Physica, Special Issue 2,* **2003**, XLVIII, 420-423.
14. F.V. McLafferty, F. Turecek, „Interpretation of Mass Spectra", University Science Books, Mill Valley, 1993.
15. B.S. Middleditch, „Practical Mass Spectrometry-A Contemporary Introduction", Middleditch,B.S.(Editor), Plenum Press, New York- London, 1979, 1-55.
16. K. Kovács-Hadady, É. Balázs, *J. Planar Chromatogr.*, **1993**, 6**,** 463-466.
17. I. Dranca, V. Coman, R. Constantinescu, F. Dogar, C. Măruţoiu, T. Lupaşcu, *J. Planar Chromatogr*., **2000**,13, 48-51.
18. C. Liteanu, S. Gocan, T. Hodişan, H. Naşcu, "Cromatografia de lichide (Liquid Chromatography)", Scientific Publishing House, Bucharest 1974, 424-429.

STUDIA UNIVERSITATIS BABES - BOLYAI, CHEMIA, LI, 2, 2006

Dedicated to professor Gh. Marcu at his 80th anniversary

SYNTHESIS AND VIBRATIONAL STUDIES ON NEW COMPLEXES OF MONODEPROTONATED (4*H*-5-MERCAPTO-1,3,4-THIADIAZOL-2-YL)THIOACETIC ACID

M.M. VENTER[a*], V. CHIŞ[b], S. CÎNTĂ PÎNZARU[b], V.N. BERCEAN[c], M. ILICI[c] AND I. HAIDUC[a]

ABSTRACT. Partial neutralisation of (4*H*-5-mercapto-1,3,4-thiadiazol-2-yl)thioacetic acid with 1 eq. of sodium bicarbonate produced the sodium carboxylate salt. This salt was further used in the preparation of the title compounds as four d metal complexes, Co, Ni, Cu and Zn. Preliminary vibrational studies on this new series are discussed in terms of FT-IR and FT-Raman spectroscopy. The spectral data are consistent with the coordination of the deprotonated carboxylic groups to the metal centers. In all cases, the occurrence of the thione tautomeric form of the heterocycle was found.

Key-words: (4*H*-5-mercapto-1,3,4-thiadiazol-2-yl)thioacetic acid, metal complexes, FT-IR and Raman spectroscopy.

INTRODUCTION

We have an on-going interest in the chemistry of mercapto-aza type heterocyclic derivatives mainly from the aspect of their coordination and supramolecular chemistry, and also because of their various applications in analytical chemistry, materials science, etc.[1-11] Previous structural studies performed on well known analytical reagents revealed their extraordinary potential in this field. For example, 1,3,5-triazine-2,4,6-trithione, $C_3N_3S_3H_3$ (also known as trimercaptotriazine or trithiocyanuric acid) and 4-phenyl-2-mercapto-1,3,4-thiadiazole-5-thione (also known as *Bismuthiol II*) have been intensively used in removing heavy metals from waste waters and also as industrial precursors.[1-6] Recently, the co-crystallization of trithiocyanuric acid with melamine, tricyanuric acid, 4,4'-bipyridine, etc. generated supramolecular structures with nanometric cavities and channels. Many of these compounds have proved excellent zeolitic properties.[7-9] Furthermore, crystallographic investigations on (organo)metallic complexes of such ligands revealed interesting 1D, 2D and 3D supramolecular architectures build up *via* intermolecular covalent and/or secondary interactions.[10,11]

[a] Faculty of Chemistry and Chemical Engineering, "Babeş-Bolyai" University, RO-400028 Cluj-Napoca, Romania. Fax: 0040-264-590818; Tel: 0040-264-593833; E-mail: monica@chem.ubbcluj.ro.
[b] Faculty of Physics, "Babeş-Bolyai" University, RO-400084 Cluj-Napoca, Romania.
[c] Faculty of Industrial Chemistry and Environment Engineering,"Politehnica" University, RO-300006 Timişoara, Romania.

It was concluded that the flat, rigid molecular geometry of the ligands, along with their increased number of heteroatoms E and EH groups (E: O, N, S, etc.), encourage the self-assembly of these molecules into layered channel-type crystal structures. Moreover, the involvement of the NCS groups into the building pattern is crucial.[10,11] For example, the presence of exo- and endocyclic sulfur atoms may give rise to S···S interactions, which have been found of great importance in the supramolecular construction of molecular electronics.[12]

We have recently initiated the vibrational investigation of a new range of π-excessive heterocyclic systems based on dimercapto-thiadiazole, $C_2H_2N_2S_3$ (also known as *Bismuthiol I*).[13,14]

We decided to use one of these compounds, the (4*H*-5-mercapto-1,3,4-thiadiazol-2-yl)thioacetic acid, $C_2HN_2S_3$-CH_2COOH **1** (Scheme 1), in the syntheses of five new metallic derivatives: $M(C_2HN_2S_3\text{-}CH_2COO)_n$, n = 1, M = Na, **2**; n = 2, M = Co, **3**; Ni, **4**; Cu, **5**; Zn, **6**.

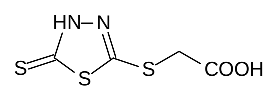

Scheme 1

Hence, the aim of this work is the synthesis of the above series of derivatives together with their preliminary IR and Raman characterization. It could infer us about i) the occurrence of the thione *vs.* thiol tautomeric form of the heterocyclic moiety in solid state and ii) to suggest the most probable coordination sites in the series 2-6.

EXPERIMENTAL

FT-IR and FT-Raman spectra on solid samples were recorded using a Bruker FT-IR Equinox 55 Spectrometer equipped with an integrated FRA 106 S Raman module. The excitation of the Raman spectra was performed using the 1064 nm line from a Nd:YAG laser with an output power of 250 mW. An InGaAs detector operating at room temperature was used. The spectral resolution was 2 cm^{-1}.

The starting materials were purchased from commercial sources as analytical pure reagents and were used with no further purification. Compound **1** was prepared following a literature protocol.[13]

The pure monosodium salt of **1**, $C_2HN_2S_3$-CH_2COONa **2** was obtained by reacting stoechiometric amounts of acid **1** and sodium bicarbonate in aqueous solution, at room temperature and subsequent recrystallization of crude **2** from hot distilled water.

The transition metal complexes of **1** as monodeprotonated forms **3-6**, $[M(C_2HN_2S_3\text{-}CH_2COO)_2]$, M = Co, **3**; Ni, **4**; Cu, **5** and Zn, **6** were synthetised by reacting stoechiometric amounts of **2** with the corresponding metal salt $Co(NO_3)_2{\cdot}6H_2O$, $NiCl_2{\cdot}6H_2O$, $CuSO_4{\cdot}5H_2O$ and $ZnCl_2$, respectively, in aqueous solution, at room temperature. In all cases, the complexes precipitated at once. After stirring the reaction mixtures for 1 – 2 hours, the crude products were filtered and purified by recrystallization from warm distilled water (**3** and **5**) or by washing with warm water (**5** and **6**). Preparation details and brief characterization of compounds **2** – **6** are given in Table 1.

Table 1

Preparation details and characterization of compounds **2** – **6.**

No.	Compound	Yield (%)	mp (°C)	Aspect
2	$C_2HN_2S_3$-CH_2COONa	86	268 - 270	colorless, crystalline
3	$[Co(C_2HN_2S_3$-$CH_2COO)_2]$	52	151 - 153	pink , crystalline
4	$[Ni(C_2HN_2S_3$-$CH_2COO)_2]$	57	183 - 185	pale green, crystalline
5	$[Cu(C_2HN_2S_3$-$CH_2COO)_2]$	58	199 - 201	green, powder
6	$[Zn(C_2HN_2S_3$-$CH_2COO)_2]$	52	218 - 220	white, powder

RESULTS AND DISCUSSION

Partial neutralisation of (4*H*-5-mercapto-1,3,4-thiadiazol-2-yl)thioacetic acid, $C_2HN_2S_3$-CH_2COOH **1** with sodium bicarbonate produced the monosodium salt, $C_2HN_2S_3$-CH_2COONa **2**. Compound **2** was further used in the preparation of four d metal complexes, $[M(C_2HN_2S_3$-$CH_2COO)_2]$, M = Co, **3**; Ni, **4**; Cu, **5** and Zn, **6** (Scheme 2). All the reactions worked in aqueous media, at room temperature. Compounds **2** – **4** are soluble in water and were isolated as crystalline solids. Compounds **5** and **6** are not soluble in common solvents and were isolated as powders. All metal derivatives are air and light stable in solid state.

$$\underset{\mathbf{1}}{\mathbf{2\ C_2HN_2S_3\text{-}CH_2COOH}} \xrightarrow[-\ 2\ H_2O\ \ -\ 2\ CO_2]{+\ 2\ NaHCO_3} \underset{\mathbf{2}}{\mathbf{2\ C_2HN_2S_3\text{-}CH_2COONa}} \xrightarrow[-\ 2\ Na^+]{+\ M^{2+}} \mathbf{[M(C_2HN_2S_3\text{-}CH_2COO)_2]}$$

M = Co, **3;** Ni, **4;** Cu, **5;** Zn, **6.**

Scheme 2

The FT-IR and Raman spectra of **2** – **6** were recorded in the 4000 – 400 and 3500 – 200 cm^{-1} spectral ranges, respectively. For the copper(II) complex **5**, the Raman spectrum could not be recorded. The most relevant spectral data are listed in Table 2. The following discussion is based on the comparison between our spectral data recorded for **2** – **6** and the known literature data for **1** and *Bismuthiol I*.[13,14]

The 4000 – 2000 cm^{-1} spectral range was relevant for the characterization of NH, OH, SH and CH groups in IR and/or Raman spectra.

However, the presence of the carboxylic OH group in the starting acid **1** gave rise to a large and complex IR band (approx. 3100 - 2500 cm^{-1}) which overlapped the other expected fundamentals and makes their assignation less accurate. In the IR spectra of **2** - **6**, the title band disappeared as a result of carboxylic group deprotonation. On the other hand, the same spectra show broad bands at 3487 - 3385 cm^{-1} which may be assigned to the $\nu(H_2O)$ mode, as well as weak to medium bands at 3106 – 3090 cm^{-1} which are tentatively assigned to the ν(NH) fundamental.

The Raman spectra of **1** – **6** were more suitable for the interpretation of the tautomeric form of the heterocycle and the characterization of the alkyl fragment. Thus, all spectra lack the characteristic ν(SH) bands, usually assigned in the 2600 – 2400 cm^{-1}. In addition, the $\nu_{as}(CH_2)$ and $\nu_s(CH_2)$ stretching vibrations may be clearly assigned at 3022 – 2953 and 2944 – 2905 cm^{-1}, respectively.

It can be concluded that the deprotonation of the acid **1** took place at the COOH group and the ligand participates in coordination as carboxylato anion. In addition, we tentatively suggest that the remaining proton was located at an aza-atom, which gave option to the thione tautomer form of the heterocyclic unit.

The 2000 – 1000 cm^{-1} spectral range was relevant for both heterocyclic and alkyl-carboxylic units of the coordinated ligand. The most important as characteristic bands for the heterocyclic fragment fall in the 1541 – 1433, 1120 – 1103 and 1059 – 1045 cm^{-1} regions and are assigned to the ν(C=N), ν(N-N) and ν_{as}(S-C=S) modes, respectively. The first stretching mode consists of two components, which are assigned in the spectra of **2** - **6** at 1541 – 1515 and 1457 – 1433 cm^{-1}. These components are comparable with the two corresponding fundamentals found for **1** (1494 and 1448 cm^{-1}) and related mercapto-thiadiazoles (e.g. 1510 –1506 and 1452 -1450 cm^{-1} for *Bismuthiol I*). Similarly, the assignment of the other two stretching modes is consistent with the literature data for **1** and *Bismuthiol I*.

As it concerns the alkylcarboxylic substituent, the title spectral range offers consistent information about both CH_2 and COOH groups but the most outstanding behavior was revealed by the COOH / COO^- groups. According to literature,[13-15] the COOH group is defined by two major modes: ν(C=O) and ν(C-OH); the later may be represented by two bands. As the deprotonation occurs, the resulting COO^- group is expected to adopt a C_{2v} symmetry and to reveal the ν_{as}(COO) and ν_s(COO) fundamentals. In the case of compounds **1** – **6**, the first mode of both groups was easily assigned. Thus, for compound **1** the band corresponding to ν(C=O) falls at 1693 cm^{-1} in both IR and Raman spectra while in the spectra of the metal derivatives the same mode is shifted dramatically to lower wave numbers (1641 – 1558 cm^{-1}) and can be related to the ν_{as}(COO) fundamental. The assignment of the ν(C-OH) / ν_s(COO) modes in the expected region (1400 – 1200 cm^{-1}) proved very difficult due to the overlap with a significant number of bands. Despite this ambiguity, we propose a tentative assignment of these fundamentals at 1303 in **1** and 1333 – 1293 cm^{-1} in the series **2** – **6**.

The 1000 – 200 cm^{-1} spectral range shows no unusual features. The plethora of bands located in this region was assigned to group bending and other skeleton vibrational modes (i.e. $\nu_{as}(CSC)_{endo}$ 738 – 717 and $\nu_s(CSC)_{endo}$ 678 – 657 cm^{-1}).

CONCLUSIONS

In the explored series of metal complexes, the ligand (4*H*-5-mercapto-1,3,4-thiadiazol-2-yl)thioacetate is present as carboxylato anion, saving the thione tautomer form. The coordination of the ligand to the metal centers M^{2+} (M = Co, Ni, Cu and Zn) is suspected to occur through the carboxylato group. We avoid, however, to evaluate its coordination behavior by comparing the $\Delta\nu = \nu_{as}(COO) - \nu_s(COO)$ values until more spectral and structural investigations will be completed on the title metal complexes.

AKNOWLEDGEMENTS

M.M.V. thanks The National Council of Academic Research (CNCSIS) for financial support during the course of this work.

REFERENCES

1. A. K. Majunidar, M. M. Chabrabarthy, *Anal. Chim. Acta*, **1958**, *19*, 372.
2. A. Kumar, *Z. Anal. Chem*., **1957**, *156*, 265.
3. A. K. Majunidar, M. M. Chabrabarthy, *Z. Anal. Chem*., **1957**, *154*, 262.
4. A. K. Majunidar, M. M. Chabrabarthy, *Z. Anal. Chem*., **1959**, *165*, 100.
5. M. M. Osman, M. A. Makhyoun, A. B. Tadros, *Bull. Soc. Chim. Fr*., **1980**, *11-12*, 1.
6. K. Henke, D. A. Atwood, *Inorg. Chem*., **1998**, *37*, 224.
7. V. R. Pedireddi, S. Chatterjee, A. Ranganathan, C. N. R. Rao, *J. Am. Chem. Soc.,* **1997**, *119*, 10867.
8. A. Ranganathan, V. R. Pedireddi, S. Chatterjee, C. N. R. Rao, *J. Mater. Chem*., **1999**, *9*, 2407.
9. A. Ranganathan, V. R. Pedireddi, C. N. R. Rao, *J. Am. Chem. Soc.,***1999**, *121*, 1752.
10. V. Bercean, C. Crainic, I. Haiduc, M. F. Mahon, K. C. Molloy, M. M. Venter, P. J. Wilson, *J. Chem. Soc., Dalton Trans*, **2002**, 1036.
11. M. F. Mahon, K. C. Molloy, M. M. Venter, I. Haiduc, *Inorg. Chim. Acta.*, **2003**, *348*, 75.
12. D. W. Bruce, D. O'Hare (eds.), "Inorganic Materials", John Wiley & Sons, New York, 1999.
13. M. M. Venter, S. Cinta Pinzaru, I. Haiduc, V. Bercean, *Studia Univ. Babes-Bolyai, Physica*, **2004**, *XLYX(3)*, 285.
14. M. M. Venter, V. Chis, S. Cinta Pinzaru, V. Bercean, I. Haiduc in V. Rastogi (ed.), *"Progresses in Vibrational Spectroscopy"*, 2006, in press.
15. K. Nakamoto, "Infrared Spectra and Raman Spectra of Inorganic and Coordination Compounds", John Wiley & Sons, New York, 1986.

Dedicated to professor Gh. Marcu at his 80th anniversary

ACCELERATOR MASS SPECTROMETRY RADIOCARBON DATING OF AN OLD TROPICAL TREE: PRELIMINARY REPORT. 1. RADIOCARBON DATES.

ADRIAN PATRUT[a], KARL F. VON REDEN[b], DANIEL A. LOWY[c], PAULINE LINDEQUE[d], ANDRIES H. ALBERTS[e], RUDOLF WITTMANN[f], EDITH FORIZS [a], DRAGOS MARGINEANU [a], JOHN W. POHLMANN[g], LI XU [b], DANA GERLACH [b] AND CLARK S. MITCHELL [g]

ABSTRACT. A number of 11 samples collected from the remains of a very large African baobab (*Adansonia digitata*) were processed and investigated by AMS radiocarbon dating. Radiocarbon dates of several samples, collected from different areas of the collapsed trunk, were found to be greater than 1000 yr BP. Several additional samples are under investigation.

KEY WORDS: radiocarbon dating, AMS, tropical trees, age determination, dendrochronology, dendroclimatology.

INTRODUCTION

In present, a number of 16 “millenarian” tree species with accurate dating, i.e. species with individuals that had lived over 1000 years (yr), are known [1, 2]. All these tree species are gymnosperms/conifers. The champion species is the bristlecone pine *(Pinus longaeva)*, with an age of 4844 yr for the cross-dated WPN-114 or Currey (Prometheus) tree [3].

Somewhat surprisingly, no angiosperm tree with a confirmed age of over 1000 yr has been identified, so far. The oldest angiosperm tree reported in the literature is an African baobab *(Adansonia digitata)*, felled in 1960 at Lake Cariba (in former Rhodesia, today Zimbabwe). This specimen, with a girth of 14.4 m (at a height of ca. 0.6 m above ground level), was far from being one of the largest trees of the species. It was dated by Swart via radiocarbon dating (using the beta decay counting method), who reported

[a] “Babes-Bolyai” University, Faculty of Chemistry and Chemical Engineering, 11 Arany Janos Str., 400028 Cluj-Napoca, Romania.
[b] Woods Hole Oceanographic Institution, Geology & Geophysics Department, NOSAMS Facility, Woods Hole, MA 02543, U.S.A.
[c] Nova Research Inc., Alexandria, VA 22308, U.S.A.
[d] Ministry of Environment and Tourism, Scientific Services, Windhoek, Namibia.
[e] Ministry of Environment and Tourism, Directorate Parks and Wildlife Management, Nyae Nyae Conservancy, Tsumkwe, Namibia.
[f] Tree Research Office, 85051 Ingolstadt, Germany.
[g] U.S. Naval Research Laboratory, Chemistry Division, Washington D.C.20375, U.S.A.

a radiocarbon age of 1010 ± 100 yr BP for a sample collected from the core of the stump [4]. After calibration, this value corresponds to a calendar age of 925 ± 105 yr (in 1960, when the tree died).

One should mention a singular study, which claimed incredible age values of over 1000 years, determined by radiocarbon dating, for two tropical trees of the Amazonian rainforest (i.e. 1370 yr for *Cariniana micrantha* and 1170 yr for *Dipteryx odorata*) [5]. These values contradict dramatically other results concerning the age limit of similar tree species from the Amazonian rainforest and have been questioned by several researchers [6-8]. It was mentioned that the respective results were outliers to all other findings in the dating of tropical trees. Criticism was raised due to the fact that results were based on single samples of each tree and on single radiocarbon measurements, without any corroborating data or replicated analyses [8].

According to a number of researchers, the species of the genus *Adansonia* are the main angiosperm candidates to become "millenarian". The genus *Adansonia*, which belongs to the Bombacacee family, comprises eight species of deciduous trees: six are endemic to Madagascar, one to Australia and one is widespread in continental Africa [9].

The African baobab (*Adansonia digitata* L.), which can be considered a tropical tree, is the largest and best-known of the eight *Adansonia* species. It is widespread south of the Sahara, especially in savanna regions. The familiar picture of the African baobab is of an almost grotesque tree, with a girth out of proportion to its height. Therefore, the African baobab is often named the upside-down tree. Although the baobab is a relatively short tree, with an usual height around 20 m, some individuals can reach an exceptionally large girth of over 25 m [10-12]. The African baobab is a very special tree. Baobabs are more similar to succulents than they are to woody trees. Thus, as they die, they might best be described as rotting, rather than slowly decaying. The trunk and the branches are constructed in concentric layers of succulent tissue, reminiscent of the layers of an onion. The wood is soft, spongy, fibrous and light; between each layer of xylem cells there is a layer of parenchyma cells that store water [10]. Thus, the African baobab can be considered a stem-succulent tree species. In the rainy season, baobabs store enormous quantities of water in their bulbous trunks, which they use to survive during the dry season.

The tremendous size of certain individuals has led many observers to state that the baobab lives to a long age. However, the age of the oldest baobab trees, i.e. the age limit of the African baobab, remains a controversial topic, which has generated two competing hypotheses:

(i)*The long lived baobab hypothesis* (baobabs as millenarian trees) is based on local traditions, the statements of pioneer explorers and the study of several large and old specimens. Early African explorers, such as Adanson and Livingstone, ventured to extrapolate the very slow growth rate of old baobabs over their entire life cycle, without any corrections, thus claiming incredible age values of several thousands years (up to 5150 yr) for the largest individuals [13, 14]. Modern measurements of several huge individuals from Botswana and Mozambique, performed by Guy, when compared to historic records of the same trees, evinced a very small increase or even a decrease in girth during a time span of ca. 110 yr, namely from ca. 1850–60 to1966 [15]. The studies of Guy and Swart evinced very small growth rates (i. e. annual increase in radius) for old baobabs of Southern

Africa (South Africa, Zimbabwe, Botswana, Mozambique) [15, 16, 4]. The singular result of Swart also suggests that much larger individuals than the radiocarbon dated tree could be well over 1000 yr old. [10, 12, 16].

(ii)*The short lived baobab hypothesis* (baobabs as centenary trees), promoted by many contemporary researchers, is based on several relatively recent studies that reveal very fast growth rates, especially for young baobab trees of Central Africa (Zambia, Sudan, Mali, Kenya, Tanzania) and of South Africa, as well [18-23]. These researchers, who discount or question the dating result of Swart, claim that the age limit of the African baobab is around 500–800 yr, perhaps reaching values close to 1000 yr, in the case of the largest trees [22-25]. Several additional remarks should be made. Even if an enormous girth would suggest a very old tree, the largest baobabs are not necessarily the oldest ones. As in the case of other tree species, the size of the baobab depends not only on its age, but also on the genetic variability and on its location, especially its access to moisture [26]. Consequently, there is a big problem to estimate the age of baobabs via girth measurements, due to the impact of the hydrostatic conditions within the tree and to the large variation in growth rates between individuals. In addition, most baobab researchers consider that the growth rate decreases severely with age.

Given that the trunk of the baobab is a water-storing organ, it swells and shrinks periodically, in direct relation to the water content. Seasonal, annual and long period girth variations have been reported; they may sometimes mask the radial increase du to cambial activity.

The baobab stops growing during the dry season and produces a sort of rings. These faint rings are believed by modern researchers to be annual rings, even if this has not been yet demonstrated conclusively [24]. The majority of researchers agree, however, that in areas with a distinct dry season, the baobab exhibits annual rings. Ring counting of young trees of known age have been shown to be within 2 % of the real age [10]. However, ring counting cannot be used to aging large baobabs, because of the presence of large hollows in the trunk.

Further, large baobabs have sometimes multiple stems, more or less fused in a single trunk. This could either be ascribed to multiple sprouting from the same rootstock or to the simultaneous germination of several seeds [24]. A baobab tree with two or more fused stems at an earlier stage of its life can be younger than its girth would suggest [12].

It should also be noticed that, when they die, baobabs collapse into a huge fibrous mass. The wood fibers dry out rapidly and the heat of the desert during the dry season may ignite them. It is also possible that the dehydrated, dry and friable wood fibers may be washed away by heavy rains over the rainy season or that they may crumble and be blown away by winds. Hence, a huge collapsed tree may disappear in a relatively short time, with no trace left behind. This fact may be at the origin of the popular myth which states that, after they die, baobabs catch fire spontaneously [24].

Hence, the sole technique for determining the age of old baobabs is radiocarbon dating of wood samples collected from a recently fallen tree, namely by measuring their ^{14}C content relative to the content of stable carbon.

In 1949, Libby pioneered the first radiocarbon measurements by monitoring the beta radioactive decay of individual ^{14}C atoms with modified Geiger counters. He used samples of several grams of carbon-black powder. In the 1950's period, when atmospheric nuclear bomb tests were performed, this method was relatively insensitive and subject to statistical errors due to the absorption of nuclear contaminant [27].

More accurate methods in the decay counting technology had been developed by the conversion of sample solid carbon to CO_2 for measurement in gas-proportional counters and liquid-scintillation counters. Both methods rely on observing the decay of the radioactive ^{14}C atoms. When a ^{14}C atom decays, it emits a beta particle, which can be counted in a gas by the electrical pulse it generates. In a liquid-scintillation counter, the beta particle excites the emission of light from the molecules of an organic solvent, which acts as a "scintillant". Because only ca. 13.5 decays per minute occur in 1 g of modern carbon, it is necessary to use fairy large samples, up to several grams of carbon. Today, the majority of radiocarbon laboratories utilize these two dating methods [27].

It was recognized that direct counting of ^{14}C atoms in the sample would greatly enhance the sensitivity and accuracy of the dating. Some unsuccessful attempts were made by using conventional mass spectrometry. In 1977, a new development added a particle accelerator into a mass spectrometer to produce an accelerator mass spectrometer [28]. The technique uses a very high performance particle accelerator to accelerate sample atoms as ions to high energies. After a first attempt which utilized positive ion acceleration [29], the superior approach with negative ion acceleration was developed [30-31]. This so-called Accelerator Mass Spectrometry (AMS) method allows the determination with high accuracy of tiny amounts of isotopes with a small relative abundance. The dating with radiocarbon by AMS is of very high sensitivity, up to $1:10^{15}$ atoms for carbon, which is 10^3 to 10^5 higher than the older decay counting methods. Thus, it allows for the analysis of very small samples, well below 1 mg, in a much shorter time. The higher costs are justified by the value of results. Over the past years, new concepts and technologies have been brought into the field of AMS radiocarbon dating and new types of accelerators and ion sources have been developed [32].

Grootboom, an exceptionally large African baobab (Photo 1), collapsed unexpectedly in north-eastern Namibia, at the end of 2004. The huge dimensions of the tree, associated with the unusual fact that it did not have very large hollow parts, offered an unique opportunity to clarify certain aspects concerning the controversial age of large baobabs.

An international joint research project was initiated, with the following aims: 1) to determine accurately the true age of the tree; 2) to establish whether Grootboom's trunk was a single unit or was made up of several fused stems; 3) to learn about the dynamics of Grootboom's growth rate during its life cycle.

Several samples were collected from the remains of the collapsed tree and were processed and analyzed by AMS radiocarbon dating.

EXPERIMENTAL SECTION

Collection of samples. Grootboom collapsed stepwise and very chaotically into six stems. Several sets of wood samples have been collected from two fallen stems (samples Nos. 5–10), as well as from the remaining stumps of two other stems (Nos. 1–4), that broke at a variable height from the ground and collapsed. Two stems were not available for sampling, one being already severely decayed, while the other was covered and partially crushed by a larger stem. Another sample (No. 11) was collected from towards the upper part of the tallest unbroken fallen branch.

Several additional samples collected from the remaining stumps, from the fallen stems and from the thickest exposed root, as well, are being currently dated.

Photo 1. The image (facing north) shows the heavy trunk of Grootboom and its rich crown full of leaves, at the beginning of the rainy season 2001–2002.

The sampling of Grootboom was recorded on videotape, a number of photographs were taken and several measurements of the remains of the collapsed tree were undertaken. This allowed the subsequent establishment of the position of each sample in the trunk of the tree prior to its collapse.

Sample preparation. The preparation of the samples for AMS radiocarbon dating involved the standard steps: i) pretreatment of the wood samples to isolate cellulose from the bulk tissue; ii) combustion of the separated cellulose to CO_2; iii) reduction of CO_2 to graphite.

Pretreatment of samples. Wood samples (with a mass of 0.7–2.0 g) were subsampled by cutting with a clean razor blade. The wood shavings were weighed and placed into a pre-combusted glass centrifuge tube to undergo numerous wet chemistry pretreatment steps. The woody tissues of trees, involved in water transport, contain several hydrolizable and mobile organic substances. Pretreatment intends to remove non-structural mobile carbon and to isolate only structural non-mobile carbon components, mainly cellulose, which had been synthesized at the original formation of the respective woody tissue.

The pretreatment method used was, with the exception of one sample, the so-called Acid-Base-Acid (ABA), which is widely employed in the case of wood samples prepared for AMS analysis. This classic method consists of a sequential washes of weak acids and bases and yields a residue consisting primarily of cellulose [33].

First, wood samples were treated with HCl solution (10% v/v), and then placed in a water bath at 60º C, for 1 h, to remove any inorganic carbon. The acid solution was discarded by means of a pipette and the sample rinsed with organic-free water to neutral pH. NaOH solution (2% w/v) was added to the centrifuge tube, which was placed in the water bath for 1 h. The samples were treated with multiple base rinses until the solution was clear and free of humic or fulvic acid discoloration. The base solution was removed with a pipette and the sample was rinsed to neutral pH with organic free water. HCl solution (10% v/v) was added to drive off any CO_2 gas that may have adsorbed onto the sample during processing. After being heated in the water bath for 1 h, the final acid solution was removed by pipette and the sample was rinsed again to neutral pH. Subsequently, the remaining residues of each sample were filtered on pre-combusted quartz fiber filters, which were dried overnight in a drying oven at 60ºC. All samples were stored in a dessicator, to await combustion.

One sample (No. 7) had the wood fibers quasi-totally destroyed, due to severe decay caused by microorganisms. Because in such cases the ABA method can produce large errors, the α-Cellulose (Jayme-Wise) method was used for pretreatment of this sample. The method involves an organic solvent extraction, followed by a bleach delignification process, which leaves only α-cellulose as residue.

α-Cellulose was extracted according to the method described by Jayme and Wise [34] and modified by Loader et al. [35]. Briefly, dried wood shaving was extracted with 9:1 (v/v) dichloromethane and methanol, using an accelerated solvent extractor (ASE 200, Dionex Corp., Sunnyvale, USA) at 100 ℃ a nd 1000 psi. The resulting sample was dried in an oven at 50 ℃. Then, the sample was introduced in a glass centrifuge tube and a bleaching solution of sodium chlorite (0.19 mol dm^{-3}) and HCl (0.07 mol dm^{-3}) was added. The centrifuge tube was placed in an ultrasonic bath at about 75℃ for 2 h, after which the acid solution was removed with a pipette. Three further additions of the bleaching solution were made, one after each hour. The resulting sample was thoroughly rinsed with pure water.

Next, a solution of NaOH (10% w/v) was added to the tube. The tube was placed in the ultrasonic bath for 45 min at 75 ℃. The sample was washed with pure water and treated with a solution of NaOH (17% w/v) in the ultrasonic bath at room temperature. The sample was washed with water and then with a diluted solution of H_3PO_4 (3% v/v). Finally, a large volume of cold pure water was used to wash the sample to neutral. The remaining α-cellulose residue was dried at 50 ℃.

Combustion to CO_2. **.** The combustion method used for the resulted cellulose samples was the Closed Tube Combustion (CTC) method [36]. Samples were weighed and placed into pre-combusted quartz combustion tubes with 2 g copper oxide wires (to provide oxygen for the combustion) and 100 mg of silver powder (to scavenge sulfur and chlorine gases). The combustion tubes were then placed in a vacuum line where they were evacuated, leak-checked and flame-sealed. They were combusted in a muffle furnace at 850ºC, for 5 h. The generated CO_2 was cryogenically purified, quantified and transferred to a graphite reactor.

Reduction to graphite. In the graphite reactor, the generated CO_2 was converted to graphite by Fe catalysed reaction in a H_2 atmosphere. The graphite samples were submitted to AMS analysis.

AMS radiocarbon analysis. The radiocarbon (^{14}C) content of the graphite samples was determined at the National Ocean Sciences Accelerator Mass Spectrometry (NOSAMS) Facility of the Woods Hole Oceanographic Institution.

Graphite derived from each sample was compressed into a small cavity in an aluminum "target", which acted as a cathode in the ion source. The surface of the graphite was sputtered with heated cesium and the ions produced were extracted and accelerated in the 3 MV Tandetron (TM) AMS system. After acceleration and removal of electrons, the emerging positive ions were magnetically separated by mass and the ^{12}C and ^{13}C ions were measured in Faraday Cups, where a ratio of their currents was recorded. Simultaneously, the ^{14}C ions were recorded in a gas ionization counter, so that instantaneous ratios of ^{14}C to ^{13}C and ^{12}C were recorded. These are the raw signals that were ultimately converted to a radiocarbon age [37].

The AMS analysis of the samples was performed relative to an array of primary and secondary standard samples. Two primary standards were used: NIST Certified Oxalic Acid I (NIST-SRM-4990) and the derived Oxalic Acid II (NIST-SRM-4990C). The ^{14}C activity ratio of Oxalic Acid II (Fm = 1.3605; $\delta^{13}C$ = –17.3 $^{0}/_{00}$) to Oxalic Acid I (Fm = 1.0520; $\delta^{13}C$ = –19.0 $^{0}/_{00}$) is taken to be 1.293. Three secondary standards were also used, namely FIRI B (Old Wood, Consensus Fm = 0.0033, NOSAMS Fm = 0.003), FIRI F (Dendro-dated Wood, Consensus Fm = 0.5705, NOSAMS Fm = 0.5668) and FIRI H (Dendro-dated Wood, Consensus Fm = 0.7574, NOSAMS Fm = 0.7450). System background measurements were performed with petroleum-derived Johnson-Matthey 99.9999% graphite powder (no chemical preparation, Fm < 0.002) and IAEA C-1 hydrolyzed Carrara marble (Fm < 0.002). The measurement of the secondary standards was used to assess the accuracy of the sample analysis. The overall system error is a function of the average deviation of the secondary standard results from their respective consensus values [38-40].

Radiocarbon date/age and auxiliary quantities/values. The quantities/values calculated from the experimental results of the AMS analysis are the following:

Fraction modern (carbon). Fraction modern (carbon) is a measurement of the deviation of the $^{14}C/^{12}C$ ratio of a sample from "modern." Modern is defined as 95% of the radiocarbon concentration (in AD 1950) of a NIST

Oxalic Acid I normalized to $\delta^{13}C_{VPDB}$ = –19 $^{0}/_{00}$ [E7]. AMS results are calculated using the internationally accepted modern $^{14}C/^{12}C$ ratio of 1.176 ± 0.010 x 10^{-12} [38]; all results are normalized to -25 $^{0}/_{00}$ using the $\delta^{13}C_{VPDB}$ of the sample.The value used for this correction is specified in the report of final results. Fraction modern (Fm) is basically computed from the expression: Fm = (S – B) / (M – B) , where B, S and M represent the $^{14}C/^{12}C$ ratios of the blank, the sample and the modern reference, respectively. ***$\delta^{13}C$** Correction*. In addition to loss through decay of radiocarbon, ^{14}C is affected by natural isotopic fractionation. Fractionation is the term used to describe the differential uptake of one isotope with respect to another. While the three carbon isotopes are chemically indistinguishable, lighter ^{12}C atoms are preferentially taken up before the ^{13}C atoms in biological pathways. Similarly, ^{13}C atoms are taken up before ^{14}C. The assumption is that the fractionation of ^{14}C relative to ^{12}C is twice that of ^{13}C, reflecting the difference in mass. Fractionation must be corrected for in order to make use of radiocarbon measurements as a chronometrical tool for all parts of the biosphere. In order to remove the effects of isotopic fractionation, the Fraction Modern is then corrected to the value it would have if its original $\delta^{13}C$ were –25 $^{0}/_{00}$ (the $\delta^{13}C$ value to which all radiocarbon measurements are normalized).

The Fraction modern corrected for $\delta^{13}C$, noticed by $Fm_{\delta^{13}C}$, is calculated by: $Fm_{\delta^{13}C} = Fm\,[(1 - 25\cdot 10^{-3}) / (1 + 10^{-3}\,\delta^{13}C)]^2$.

Errors. Atoms of ^{14}C contained in a sample are directly counted using the AMS method of radiocarbon analysis. Accordingly, an internal statistical error is calculated using the total number of ^{14}C counts measured for each target, $\pm(n)^{1/2}$. An external error is calculated from the reproducibility of multiple exposures for a given target. The final error is the largest of the internal or external errors.

Aside from the normal statistical errors intrinsic to the counting of ^{14}C events, there are additional statistical errors associated with the corrections applied to the Fm value.

The error associated with $\delta^{13}C$ is described by :

$\delta^{13}C$ error = $4 \cdot 10^{-8} / (1 + 10^{-3}\ \delta^{13}C)^2$.

This component of the Fm error is added in quadrature as follows:

$Fm_{\delta^{13}C}$ error = $Fm_{\delta^{13}C}$ [(Fm error^2 / Fm^2) + $\delta^{13}C$ error^2]$^{1/2}$.

Radiocarbon date/age (^{14}C age). Conventional radiocarbon age, the main result of radiocarbon measurements, is calculated according to the formula:

$$^{14}C \text{ age} = -\tau \ln (Fm_{\delta^{13}C}) ,$$

where $\tau = T / \ln 2 = 8033$ yr is the Libby mean life and T = 5568 yr is the Libby half-life.

Radiocarbon ages are calculated using the Libby half-life of ^{14}C.

The ^{14}C age is expressed in yr BP (radiocarbon years before present, i.e. before AD 1950).

The ^{14}C age error is given by:

^{14}C age error = τ ($Fm_{\delta^{13}C}$ error).

According to the convention outlined by Stuiver and Pollach [41] and Stuiver [42], radiocarbon dates are reported as follows: ^{14}C age values < 1000 yr BP are rounded to the nearest 5 yr, ^{14}C age values > 1000 yr BP are rounded to the nearest 10 yr and the ^{14}C age errors < 100 yr are rounded to the nearest 5 yr etc. However, not all laboratories subscribe to this convention.

In our report, the radiocarbon age of the samples and the corresponding error values were rounded to the nearest 5 yr

RESULTS

General research on Grootboom. The area of Northeastern Namibia, located between the village of Tsumkwe and the border with Botswana, which belongs to the Tsumkwe Constituency, traditionally known as Bushmanland, has several large African baobab trees. Three of these baobabs, known under the names of *Dorslandboom, Grootboom* and *Holboom*, are of outstanding size.

Die Grootboom (*The Big Tree* in Afrikaans) site is situated at 15 km (as the crow flies) east of Tsumkwe, in close proximity of the Makuri and Djokhoe campsites. The position of *Grootboom* is defined by the following parameters: GPS coordinates 19.649317 S-lat, 020.657583 E-long (19º38'57.5'' lat S, 20º39'23.7'' long E); altitude 1149 m. Geographically, the region belongs to the Northern Kalahari Woodland basin and the corresponding vegetation type is known as woodland savanna. The semi-arid climate has a distinct dry season (April-October) and a rainy season (November-March) with ca. 60–100 rainy days. Average annual rainfall is 451 mm (measured from 1965 to 2005).

Grootboom was the largest tree of a so-called "Group of Seven", composed initially of seven baobabs spread over an area of ca. 2 hectares, under the protection of the Nyae Nyae Conservancy.

The first records of *Grootboom* are found in the writings of the "Dorslandtrekkers" (Thurstland trekkers), that moved from South Africa in 1875 through Namibia onwards to Angola. They were Afrikaan Boers oppressed by the English in South Africa in those years. In their writings, the Dorslandtrekkers state that they moved through the "Tebra veld" (Bushmanland), where they encountered large numbers of wildlife and big "kremetartbooms" (baobab trees). Around 1890, they visited a huge baobab, known as *Homasi* by the San people (Bushmen), after the name of the respective place in the Juhoansi tongue (San dialect). The Dorslandtrekkers, which renamed the tree *Grootboom*, were impressed not only by its extraordinary dimensions, but also by its excellent condition.

The heavy trunk of *Grootboom* was accurately measured by the German researcher Rudolf Wittmann [43]. The measurements done in November 2001, at the beginning of the rainy season, when the tree was in leaf, indicated a cbh (circumference/ girth at breast height, i.e. at 1.30 m above ground) of 30.6 m. This value (that might have been even larger by the end of the rainy season) corresponds in a very illusory circular approximation to a dbh (diameter at breast height) of 9.74 m. The basal circumference of *Grootboom* was of ca. 36 m and the largest base diameter (west to east) was found to be 12.1 m.

The bark was very thin, measuring only 1-2 cm and its color was elephant gray with reddish spots. The trunk of Grootboom divided at a height of 2-6 m in seven branches, out of which the tallest four were pointed straight upwards. The height of these branches, estimated from the largest unbroken fallen branch, from other broken branches and from several photographs of the tree were (from west to east and than to northeast, facing north) the followings: 14.0, 26.5, 30.5, 32.0, 27.0, 20.5 and 17.0 m (estimated error: ± 0.5 m). The maximum height of 32.0 m is also exceptional for an African baobab. The estimated mean crown spread was of ca. 32 m.

Taking into account the 3 standard dimensions (height, circumference and crown spread), Grootboom can be considered the biggest known African baobab.

As for many other large baobabs, the shape of the trunk was very irregular. Several deep incisions and some obvious fissures determined certain researchers to consider that the huge trunk of *Grootboom* was possibly composed of 3-5 fused stems. Other researchers considered that the incisions and fissures were generated by the twisting movement of branches in time and that the trunk of *Grootboom* was in fact a single entity.

At the end of the 2003/2004 rainy season, Grootboom was full of leaves and looked very healthy. In late June 2004, however, it started dying suddenly. Several branches fell first, approximately two months before the trunk began to collapse. The huge trunk collapsed successively into no less than six stems. The last stem fell around New Year's eve of 2005. Grootboom was probably killed by the mysterious baobab disease, which has affected many baobabs in Southern Africa since 1960.

The fallen stems are labeled (from west to east and than to northeast, facing north) as: A, B, C, D, E, F, in the reverse order of collapse (Photos 2–4). The largest stem (D) fell with roots exposed, three stems (C, E and F) collapsed totally with no roots exposed, while two stems (A, B) broke at irregular heights from the ground (between 1–2 m), also leaving behind stumps.

The original positions of the collected samples in the trunk prior to its collapse are shown in Photo 5.

Growth rings. Growth rings could be identified on only one single sample out of the collected. This is quite surprising, as one considers that in addition to the dated samples, some other large samples (with sizes up to 30 x 30 x 10 cm) have been collected

Sample No. 3 exhibited two obvious growth rings and the external contour of a third ring, as well. The width values of the three consecutive rings, each composed of several wood layers, were the following: 4.8, 4.6 and 2.5 x 10^{-3} m (mm).

The alternation of two larger rings and one thinner ring is in agreement with the sequence of rainy seasons rich or scarce in precipitation, which have been recently recorded in the area. However, one cannot unmistakably state that the observed growth rings are true annual rings.

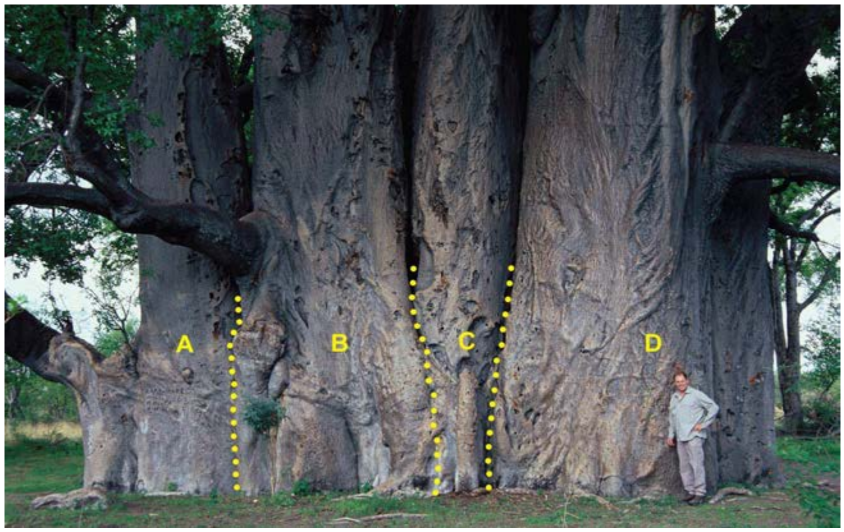

Photo 2. Location of stems on the southern flank.

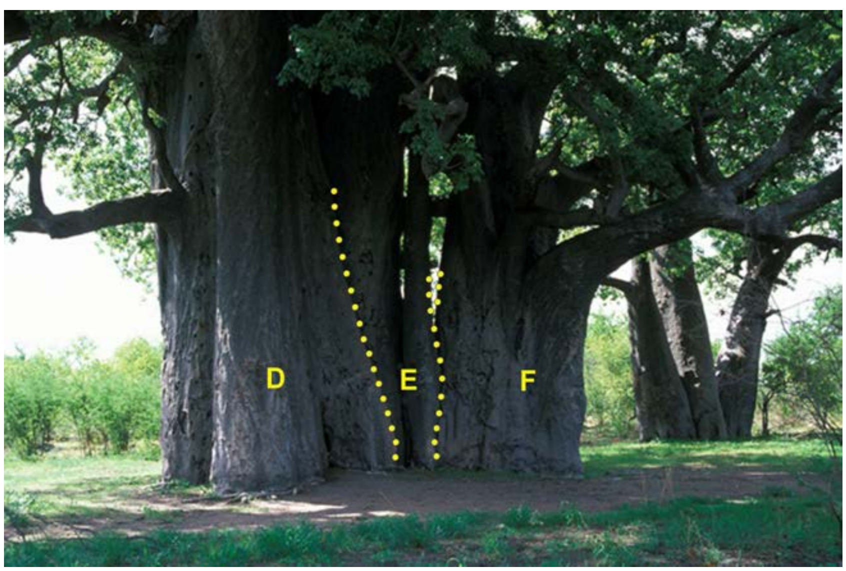

Photo 3. Location of stems on the eastern flank.

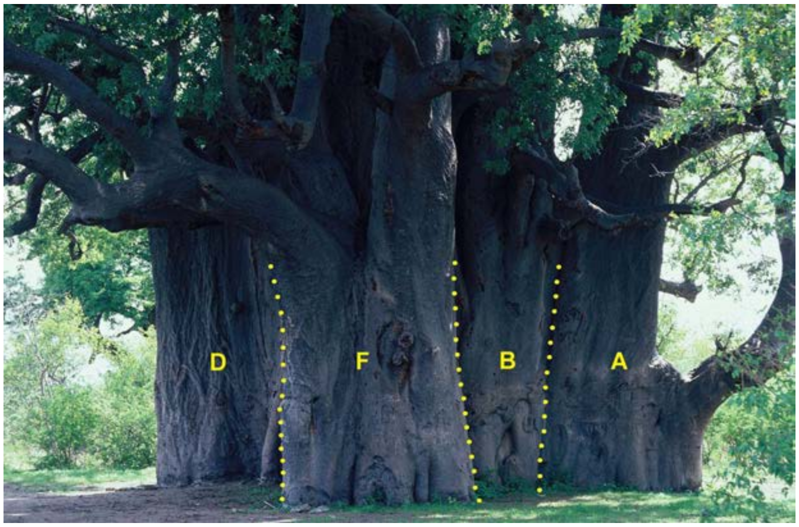

Photo 4. Location of stems on the northern and northeastern flanks.

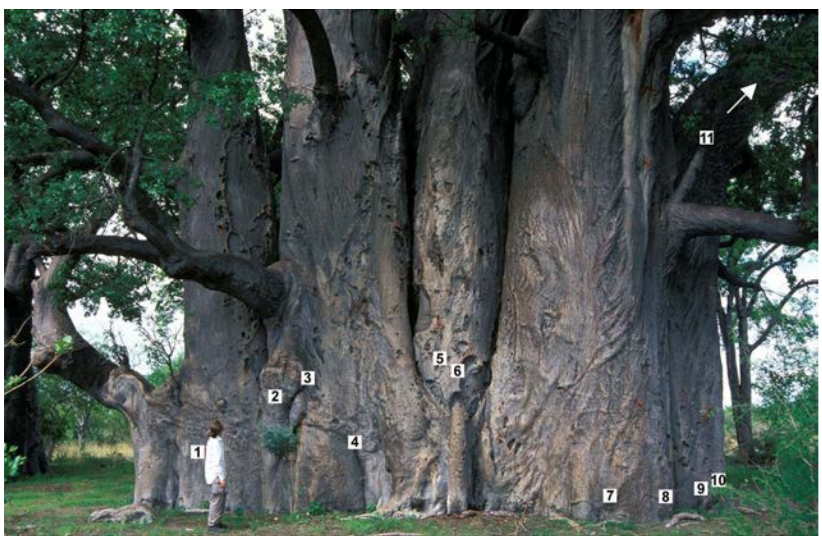

Photo 5. Original position of the samples prior to Grootboom's collapse.

AMS dating results. The NOSAMS dating results are displayed in Table 1. The radiocarbon dates/ages of 3 samples (Nos. 1, 4 and 8), collected from three different stems, was found to be greater than 1000 yr BP, i. e. 1255 ± 35, 1045 ± 20 and 1090 ± 55 yr BP, evidence for Grootboom's old age.

The calibration of radiocarbon dates to calendar ages is presented in part two of the report.

Credits:
Photos 1–5 were taken by Rudolf Wittmann on November 14, 2001 and are copyrighted: © Rudolf Wittmann (www.baumsachverstaendiger.de).

REFERENCES

1. Brown P. M., Rocky Mountain Tree-Ring Research, Oldlist, 2006 (www.rmtrr.org/oldlist.htm).
2. Grissino-Mayer H. D., Ultimate Tree-Ring Web Pages, 2006 (www.utk.edu/~grissino/gallery.htm).
3. Currey D. R., "An ancient bristlecone pine stand in eastern Nevada", *Ecology*, 1965, 46, 564-566.
4. Swart E. R., "Age of the Baobab Tree", *Nature*, 1963, 198, 708-709.
5. Chambers J. Q., Higuchi N., Schimel J. P., "Ancient trees in Amazonia", *Nature*, 1998, 39, 135-136.
6. Worbes M., Junk W. H., "How old are tropical trees? The persistence of a myth", *IAWA J.*, 1999, 20, 255-260.
7. Williamson G. B., Eldik T. V., Delamonica P., Laurance V. F., "How many millenarians in Amazonia? Sizing the ages of large trees", *Trends Plant Sci.*, 1999, 4, 387.
8. Fichtler E., Clark D. A., Worbes, M., "Age and Long-term Growth of Trees in an Old-Growth Tropical Rain-Forest, Based on Analyses of Tree Rings and ^{14}C", *Biotropica*, 2003, 35, 306-317.
9. Baum D. A., "A systematic revision of *Adansonia* (Bombacaceae)", *Ann. Mo. Bot. Gard.*, 1995, 82, 440-471.
10. Wickens G. E. „The Baobab: Africa's Upside-Down Tree", *Kew Bull.*, 1983, 47, 173-209.
11. Mullin L., „Baobabs in my soup (1)", *Tree Life*, 2002, 264, 5-17.
12. Mullin L., *Historic Trees of Zimbabwe*, CBS, Bath, 2003.
13. Adanson M., "Déscription d'un arbre d'un genre nouveau appelé Baobab observé au Sénégal", *Hist. Act. Roy. Sci.*, 1771, 1791, 77-85, 218-243.
14. Livingstone D., *"A Popular Account of Missionary Travels and Researches in South Africa"*, Murray, London, 1857.
15. Guy G. L., "*Adansonia digitata* and its rate of growth in relation to rainfall in South Central Africa", *Proc. & Trans. Rhod. Sci. Assoc.*, 1970, 54, 68-84.
16. Coates Palgrave M., Coates Palgrave K., *Trees of Southern Africa*, ed. 3, Struik, Cape Town, 2002.
17. Guy G. L., "Baobabs and elephants", *Afr. J. Ecol.*, 1982, 82, 215-220.
18. Caughley G., "The elefant problem – an alternative hypothesis", *E. Afr. Wldl. J.*, 1976, 14, 256-283.
19. Barnes R. F. W., "The decline of the Baobab tree in Ruaha National Park, Tanzania", *Afr. J. Ecol.*, 1980, 18, 234-252.

20. Barnes R. F. W., "Woodland changes in Ruaha National Park (Tanzania) between 1976 and 1982", *Afr. J. Ecol.*, 1985, 23, 215-221.
21. Barnes R. F. W., Barnes K. L., Kapela E. B., "The long-term impact of elephant browsing on Baobab trees at Msembe, Ruaha National Park, Tanzania", *Afr. J. Ecol.*, 1994, 32, 177-184.
22. Wilson R. T., "Vital statistics of the Baobab *(Adansonia digitata)*, *Afr. J. Ecol.*, 1988, 26, 197-206.
23. von Breitenbach F., "Aantekeninge oor die groeitempo van aangeplante kremeteartbome (Adansonia digitata) en opmerkinge ten opsigte van lewenstyd, groeifases en genetiese variasie van die spesie", *J. Dendrology*, 1985, 5, 1-21.
24. Esterhuyse N., von Breitenbach J., Sőhnge H., *Remarkable Trees of South Africa*, Briza, Pretoria, 2001.
25. Pakenham T., *The Remarkable Baobab*, Norton, New York, London, 2004.
26. Fenner M., "Some measurements on the water relations of Baobab trees", *Biotropica*, 1980, 12, 205-209.
27. Taylor R. E., Long A., Kra R. S. (eds.), *Radiocarbon after four decades*, Springer, New York, 1998.
28. Tuniz C., Bird R. D., Fink D., Herzog G. R., *Accelerator Mass Spectrometry: Ultrasensitive Analysis for Global Science*, CRC Press LLC, 1998.
29. Muller R. A., "Radioisotope Dating with a Cyclotron", *Science*, 1977, 196, 489-494.
30. Nelson D. E., Korteling R. G., Stott W. R., "Carbon-14: Direct Detection at Natural Concentrations", *Science*, 1977, 198, 507-508.
31. Bennett C. L., Beukens R. P., Clover M. R., Gove H. E., Liebert R. B., Litherland A. E., Purser K. H., Sondheim W. E., "Radiocarbon Dating Using Electrostatic Accelerators: Negative Ions Provide the Key", *Science,* 1977, 198, 508-510.
32. Suter M., "25 years of AMS – a review of recent developments", *Nucl. Instr. Meth.*, 2004, B 223-224, 139-148.
33. Olsson I. U., "Radiometric Methods", in *Handbook of Holocene palaeoecolgy and palaeohydrology*, (Berglund B., ed.), Wiley, Chichester, 1986, pp. 273-312.
34. Green J. W., "Wood cellulose", in *Methods in carbohydrate chemistry*, Vol. 2, (Whistler R. L., ed), Academic Press, New York, 1963, pp. 9-21.
35. Loader N. J., Robertson I., Baker A. C., Switsur V. R., Waterhouse J. S., "An improved technique for the batch processing of small wholewood samples to α-cellulose", *Chem. Geol.*, 1997, 136, 313-317.
36. Sofer Z., "Preparation of carbon dioxide for stable carbon isotope analysis of petroleum fractions", *Anal. Chem.*, 1980, 52, 1389-1391.
37. * * *, "General Statements of ^{14}C Procedures at the National Ocean Sciences Facility", Woods Hole Oceanographic Institution, 1999. 38. Karlen I., Olsson I. U., Kallburg P., Kilici S., "Absolute determination of the activity of two ^{14}C dating standards", *Ark. Geofys.*, 1968, 4, 465-471.
39. Olsson I. U., "The use of Oxalic acid as a Standard", in *Radiocarbon Variations and Absolute Chronology, Nobel symposium, 12th Proc.* (Olsson, I. U., ed.), Wiley, New York, 1970, p. 17.
40. Boaretto E., Bryant C., Carmi I., Cook G., Gulliksen S., Harkness D., Heinenmeier J., McClure J., McGee E., Naysmith P., Possnert G., Scott. M., van der Plicht H., van Strydonck M., " How reliable are radiocarbon laboratories?: A report on the Fourth International Radiocarbon Inter-comparison (FIRI) (1998-2001)", *Antiquity*, 2003, 77 (295),146-154.
41. Stuiver M., Polach H. A., "Discussion: Reporting of ^{14}C data", *Radiocarbon*, 1977, 19, 465-483.
42. Stuiver M., "Workshop on ^{14}C data reporting", *Radiocarbon,* 1980, 22, 964-966.
43. Wittmann R., *Die Welt der Bäume*, Ulmer, Essen, 2003.

STUDIA UNIVERSITATIS BABES-BOLYAI, CHEMIA, LI, 2, 2006

Dedicated to professor Gh. Marcu at his 80th anniversary

ACCELERATOR MASS SPECTROMETRY RADIOCARBON DATING OF AN OLD TROPICAL TREE: PRELIMINARY REPORT 2. CALIBRATED RESULTS

ADRIAN PATRUT[a], KARL F. VON REDEN[b], DANIEL A. LOWY[c], EDITH FORIZS[a], DRAGOS MARGINEANU[a], ANDRIES H. ALBERTS[d], PAULINE LINDEQUE[e], JOHN W. POHLMANN[f], RUDOLF WITTMANN[g], DANA GERLACH[b], LI XU[b] AND CLARK S. MITCHELL[f]

ABSTRACT. Calibration of radiocarbon dates of 11 samples collected from a recently collapsed African baobab is discussed. The 1-σ calibrated calendar ages of several old samples are over 1000 yr.
The obtained results also suggest that the investigated baobab was morphologically a multiple tree, with several fused stems, while genetically it was a single individual.

KEY WORDS: radiocarbon dating, AMS, tropical trees, age determination, dendrochronology, dendroclimatology.

Part one presented the AMS radiocarbon dating results of 11 samples collected from Grootboom, the world's largest African baobab, which had collapsed recently in Namibia [1].

Part two is dedicated to calibration of radiocarbon dates to calendar ages and to the discussion and interpretation of the resulting age values.

[a] "Babes-Bolyai" University, Faculty of Chemistry and Chemical Engineering, 11 Arany Janos Str., 400028 Cluj-Napoca, Romania.
[b] Woods Hole Oceanographic Institution, Geology & Geophysics Department, NOSAMS Facility, Woods Hole, MA 02543, U.S.A
[c] Nova Research Inc., Alexandria, VA 22308, U.S.A.
[d] Ministry of Environment and Tourism, Directorate Parks and Wildlife Management, Nyae Nyae Conservancy, Tsumkwe, Namibia.
[e] Ministry of Environment and Tourism, Scientific Services, Windhoek, Namibia.
[f] U.S. Naval Research Laboratory, Chemistry Division, Washington D.C.20375, U.S.A.
[g] Tree Research Office, 85051 Ingolstadt, Germany.

EXPERIMENTAL SECTION

Calibration. The calculation of the radiocarbon age (^{14}C age) of a sample assumes that the rate of production of ^{14}C and consequently the specific activity/ concentration of the ^{14}C in the atmospheric CO_2 is constant. This assumption is now known to be incorrect, meaning that radiocarbon years are not equivalent to calendar years. Long-term variations in the rate of production correspond to fluctuations in the strength of the Earth's magnetic field. Short-term variations, i.e. "wiggles," are known as the de Vries effect and may be related to variations in sunspot activity.

Radiocarbon ages are always reported as yr BP (before present, where 0 BP = AD 1950), assuming that the atmospheric ^{14}C concentration has always been the same as it was in AD 1950 and that the half-life of ^{14}C is T = 5568 yr (Libby half-life). Consequently, a calibration dataset is necessary to convert uncalibrated conventional radiocarbon dates/ages into calibrated calendar ages. Calibration curves also include the correction factor for conversion to the Cambridge half-life (T = 5730 yr). Calibrated ages are reported as calBP, calBC or calAD, as they are expressed in calendar yr BP, calendar yr BC or calendar yr AD.

Practically, calibration programs calculate, via a calibration dataset, probability distributions of the calibrated calendar age for a certain radiocarbon age (with a certain standard deviation). Probabilities are ranked and summed to find the 68.3% (1-σ; one sigma) and 95.4% (2-σ; two sigma) confidence intervals and the relative areas under the probability curves for the two standard intervals. Each 1-σ or 2-σ probability distribution corresponds, by the selected areas, to one or several ranges of calendar years.

The radiocarbon ages of samples were calibrated with the OxCal version 3.10 for Windows software/program [2-6] and also with the CALIB version 5.0 software/program [7-9], using the atmospheric data from Reimer et al., i. e. the IntCal04 terrestrial calibration dataset [10]. For one sample (No. 11), the atmospheric data from McCormac et al., i.e. the SHCal04 calibration dataset [11] was used .

All calibrated calendar ages and the corresponding errors were rounded to the nearest 5 yr (excepting the calAD ages calculated with the CALIB program, which were rounded to the nearest year).

RESULTS

Calibrated ages. The calibration of radiocarbon dates/ages (^{14}C ages) to calendar ages are listed in Table 1 (as calibrated with the OxCal v3.10 program) and Table 2 (as calibrated with the CALIB. 5.0 program). The 1-σ (68.2%) and 2-σ (95.4%) probability distributions, which define calAD age ranges of the dated samples, were obtained (calAD ages are rounded to the nearest 5 yr by the OxCal program and to the nearest year by the CALIB program).

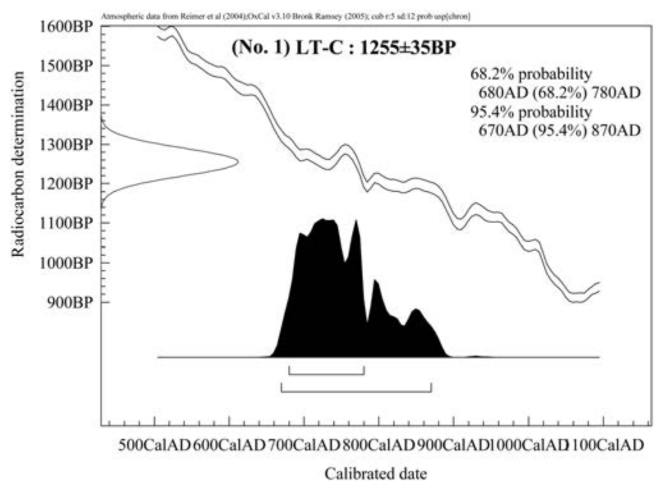

Fig. 1. The plotted OxCal calibration for sample No. 1.

From these values, we chose as the calAD age of each sample the corresponding 1-σ range (when only one range exists) or the corresponding 1-σ range with the highest probability (when there is more than one range). The selected calAD range of each sample is marked in bold.

Tables 1 and 2 also include the mean calBP age values and the corresponding errors of the samples (each rounded to the nearest 5 yr), calculated form the selected calAD range.

Shown are also calendar ages of the samples at the death of the tree. They were calculated from the corresponding mean calBP ages extrapolated (from AD 1950) to AD 2005. AD 2005 was chosen as the reference year for calculating sample ages, as the stems of Grootboom, where the samples originated from, collapsed between September 2004 and New Year 2005. Also rounding reasons pleaded for this year. In the case of sample No. 11, no calAD age interval was selected, for reasons to be explained later in this paper.

Results obtained with the two different programs, using both the same calibration datasets, are very similar. The 3 samples with high radiocarbon date were found to be millenarian, with ages of 1275 (No. 1), 1000 (No. 4) and 1050–1060 (No. 8) cal yr.

The plotted OxCal calibration results for the 3 millenarian samples are presented in Figs. 1–3.

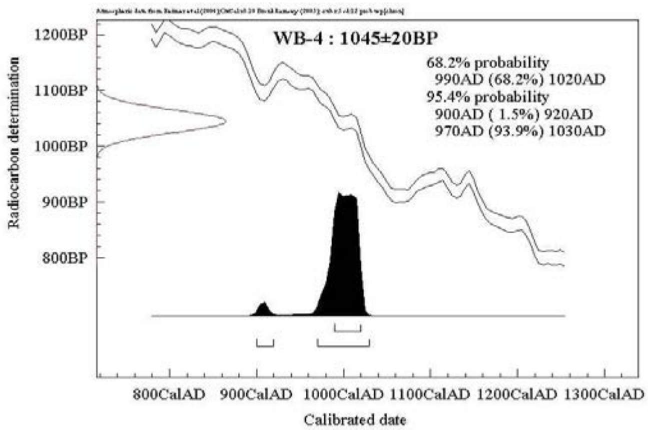

Fig. 2. The plotted OxCal calibration for sample No. 4.

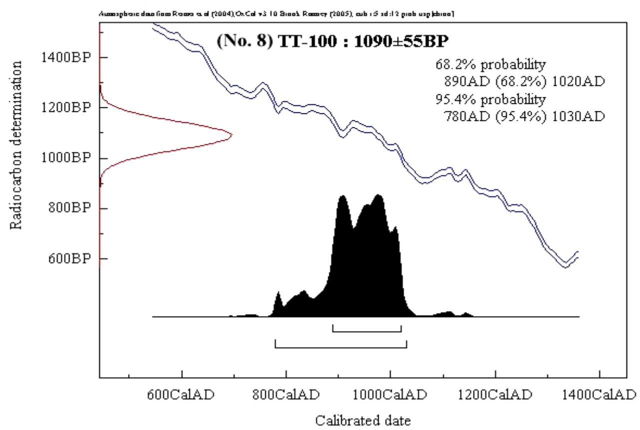

Fig. 3. The plotted OxCal calibration for sample No. 8.

DISCUSSION

Northern vs. Southern Hemisphere calibration. The radiocarbon calibration dataset is the result of committed work and significant joint efforts of numerous researchers over several decades. It is based on dating results of samples with known age collected almost exclusively form the Northern Hemisphere, especially dendro-dated wood and marine records.

Several studies have revealed, however, regional radiocarbon offsets. The most important is the so-called interhemispheric offset. Certain comparative studies evinced that trees from the Southern Hemisphere dated older than identically aged trees from the Northern Hemisphere. Such results suggest hemispheric differences in the distribution of ^{14}C throughout the troposphere. These differences are attributed to the larger expanse of ocean in the Southern Hemisphere and the atmosphere–ocean exchange [12-17].

The very first Southern Hemisphere calibration dataset was developed in 2002, based on several research on dated wood samples from New Zealand, Tasmania, Chile and South Africa, covering the period AD 1955–955. The SHCal02 calibration [18] is based on the IntCal 98 dataset for the Northern Hemisphere [19], corrected with a number of results from the Southern Hemisphere. The SHCal02 dataset indicates older ^{14}C ages by ca. 8–80 yr in the Southern Hemisphere, with a mean offset of 41 ± 14 yr for the period cal AD 1850–950 and also shows a periodicity in the offset of about 130 yr.

The International Radiocarbon Conference in Wellington, New Zealand recommended the use of the SHCal02 dataset for samples with cal AD 1850–950 (0–1000 cal yr BP) ages from the Southern Hemisphere [11]. The Southern Hemisphere is defined as south of the thermal equator or south of the Intertropical Convergence Zone (ITCZ). The ITCZ is the region that circles the Earth and extends from about 5º N to 5º S, where the northeast and southeast trade winds converge in a low pressure zone.

There are, however, seasonal shifts in the ITCZ that may bring atmospheric CO_2 from the Northern Hemisphere to a site for part of the year and from the Southern Hemisphere for another part. This seasonal migration of the ITCZ, combined with multi-decadal and millennial migrations in the past, poses some uncertainties for calibration of dated samples from tropical and neo-tropical sites [11].

The SHCal02 dataset, corrected and completed with new research data, determined in 2004 the development of the SHCal04 calibration dataset, which covers a much longer period, between 0–11 cal kyr BP [11]. The SHCal04 Southern Hemisphere calibration is associated with the new developed IntCal04 Northern Hemisphere calibration for the period 0-26 cal kyr BP [10] (Fig. 4). SHCal04 shows a larger interhemispheric offset than the previous SHCal02 that varies only slightly from 55 to 58 yr.

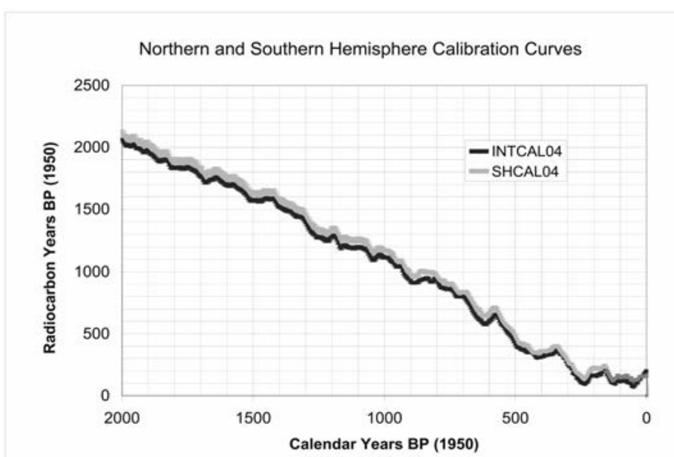

Fig. 4. Plotted IntCal04 and SHCal04 calibration datasets for the period 0–2000 cal yr BP. The difference (for a certain calendar year BP value) between the SHCal04 and IntCal04 curves (expressed in radiocarbon years BP) corresponds to the offset.

Nevertheless, the calibration of the dated samples collected from Grootboom was performed by using the atmospheric data from Reimer et al., i. e. the very large and well documented IntCal04 terrestrial calibration dataset [10]. The reasons for this choice are the following:

i) The SHCal Southern Hemisphere calibration is based on a relatively scarce number of dating results of wood samples from mid-latitude areas, which suggest a mean interhemispheric offset of several decades. On the other hand, alternative studies show no or very small interhemispheric offset values [20-22]. A very recent extended research done on Tasmania huon pine (*Lagarostrobus franklinii*) decadal samples do not document a distinguishable offset from the Northern Hemisphere for the time period 1550–2100 cal yr BP [23].

ii) The Grootboom site is located at relatively small latitude, ca. 19º S, right in the intertropical area, for which there are some uncertainties concerning calibration. We outline that all results used for the Southern Hemisphere calibration originates from wood samples collected from greater latitudes. It should be also noticed that some research suggests intrahemispheric offsets between samples collected form different latitudes of the same hemisphere [24-28, 14-15].

Only the youngest sample (No. 11), with a ^{14}C age of 30 ± 40 yr BP, was calibrated using the atmospheric data from McCormac et al., i. e. the SHCal04 calibration dataset [11], because this recent period is much better documented and a small interhemispheric offset was demonstrated.

One should notice that the calibration of the samples using the SHCal04 dataset leads to lower calendar age values, with an offset of several decades.

Age of samples. Trees take up atmospheric CO_2 by photosynthesis. CO_2 is being used in part for the quasi-continuous building of the wood texture of the trunk and branches. As other trees, the African baobab grows due to cambial activity which, during the rainy season, adds every year new layers of woody tissue. Dead wood does no longer exchange CO_2 with the environment.

Beside structural non-mobile carbon components, mainly cellulose, which have been synthesized at the very moment of the original formation of the respective woody tissue, the wood (xylem) also contains non-structural mobile carbon components, which are formed earlier or later and are removed by pretreatment of samples

While the stable isotope (i.e. ^{12}C and ^{13}C) content of the wood remains constant over time, the amount of the unstable ^{14}C isotope, also called radiocarbon, gradually decreases via radioactive beta minus decay. Thus, ^{14}C emits continuously electrons and is converted to nitrogen, according to reaction:

$$^{14}C \rightarrow {}^{14}N + e^- \ .$$

By determining the ^{14}C content, relative to the content of stable carbon, of a pretreated wood sample, one can date that particular sample.

The age of a certain position in the trunk or branches is calculated starting with the moment of the original formation of the respective woody tissue. Theoretically, the true age of a certain position is equal to the age of a pretreated wood sample collected from the respective location, which was dated and calibrated.

However, in certain cases, especially of tree species with soft and spongy wood, the age of one particular sample may differ, more or less, from the true age of the corresponding position.

The age of several samples collected from the remains of Grootboom belong to this category, such as the dating results suggest. One can distinguish the following three cases:

i) Samples collected from the rim of hollow parts. Beside hollows generated by elephants or by fire, hollows are generally formed by twisting movements of large branches, due to their growth and/or excessive weight, which may rotate and break the soft wood of the baobab trunk. Thus, at the moment when a hollow forms, woody tissues are displaced from their original position. On the other hand, certain tree species, including the African baobab, show the tendency to partially repair over time the hollows with amounts of new wood, especially for hollows relatively close to the external surface of the trunk. In special cases, such as the Livingstone baobab of Chiramba (Mozambique) or Holboom, another huge Namibian baobab located at only 8 km from the Grootboom site, it was reported that rims of an internal hollow can be covered over time with new bark.

ii) Samples collected in the vicinity of contact or fusion areas between neighboring stems. For trees with multiple stems, the neighboring stems may eventually get in contact and may even fuse together. Production of woody tissue can continue in contact and in fusion areas, even when no free place would be available for growth. Thus, a wood sample collected from such a location may contain woody tissues of different ages, which are mixed together.

ii) Samples collected from collapsed stems. In the case of tree species with soft and spongy wood, the collapsed stems are damaged and get bent due to their own weight. Thus, woody tissues from different positions may mix together. Samples collected along the central axis, parallel to the ground, may also contain younger wood, which originates from positions located towards the upper part of the fallen stem.

Consequently, samples collected from the rim of hollows, in the vicinity of contact or fusion areas between stems or from collapsed and damaged stems may date younger than the true age of the position from where they are collected. On the other hand, such samples may even be non-homogenous, containing woody tissues of different ages in variable proportions.

In the light of these remarks, the only samples whose dated and calibrated age is identical or very close to the true age of their corresponding position in the trunk are those which were collected from a remaining stump of a fallen stem, from a location away from the rim of a hollow and also not very close to a contact or fusion area between two neighboring stems. These conditions are met only by one of the samples collected from Grootboom, namely No. 3.

Discussed below are calibrated ages of the dated samples (Tables 1 and 2). The samples collected from four different stems are numbered (from No. 1 to No. 10) from west to east, facing north, considering their original position in the trunk prior to collapse [1].

Sample No. 1, ca. 1275 yr. This is the oldest sample of the tree, collected at a height of ca. 1.20 m and at a distance of ca. 0.40 m from the center of the remaining stump of stem A, the last to collapse around New Year's eve 2005.

Sample No. 2, ca. 510 yr. The sample originates from the stump of stem B and it was collected at a height of ca. 1.90 m and a distance of only ca. 0.20 m from the contact and partial fusion line between stems A and B. Its age is suspected to be younger than the true age of the corresponding position. In addition, the wood of the sample is much more compact and dense relative to other samples, suggesting that a large number of woody tissues had been added to this location and had been pressed together over time.

Sample No. 3, ca. 515–520 yr. This is an extreme lateral sample, collected at a height of ca. 2.30 m and at only 0.10 m from the southern edge of the remaining stump of stem B.

Sample No. 4, ca. 1000 yr. It is another millenarian sample, collected from the stump of stem B, at a height of ca. 1.40 m and also from the rim of the largest internal hollow of Grootboom. The corresponding position was shifted towards the southern flank.

Sample No. 5, ca. 600 yr. This sample was collected from the collapsed stem C. In the standing stem, the corresponding position was located close to the rim of a large hollow, at a height of ca. 2.60 m above ground level.

Sample No. 6, ca. 560 yr. It was collected, like sample No. 5, from the fallen stem C, from a position located at the rim of the same very large hollow and a height of ca. 2.40 m above ground level.

Sample No. 7, ca. 815–820 yr. This sample was collected from the rim of a small hollow, located just in the core/center of the fallen stem D, the largest of the tree. It had a rather sandy aspect, being severely decayed due to microorganisms which destroyed the fibrous structure of the wood. Its age is suspected to be considerably younger than the true age of the corresponding position. All samples originating from stem D were located near ground level in the standing trunk.

Sample No. 8, ca. 1050–1060 yr. It is the second oldest sample of the tree, which was collected from the rim of a hollow of the collapsed stem D, from a position located initially at 1.00 m towards east, relative to sample No. 7.

Sample No. 9, ca. 590 yr. The sample was collected from the fallen stem D, from a position situated at 1.20 m towards east, as compared to sample No. 8.

Sample No. 10, ca. 575 yr. This is another extreme lateral sample, collected from the fallen large stem D. Prior to collapse, it was located at only 0.25 m from the eastern extremity of the stem and of the whole trunk.

Sample No. 11, no selected age. This sample was collected at 1.60 m from the top of the unbroken fallen high branch, with a measured length of 26.31 m, following its contour.

The calibration and interpretation of radiocarbon dating for samples formed after AD 1640 is problematic and is characterized by low accuracy. This is mainly due to industrial fossil fuel burning, which involved large emissions of million-year old practically ^{14}C-free carbon in atmosphere. The high variations of ^{14}C concentration in the atmosphere over the industrial period, known as the Suess effect, affected to a larger extent the Northern Hemisphere, which was more advanced [29]. The incorporation in living tissues, including those which became shortly thereafter dead wood, of CO_2 from the period of the Suess effect produces generally an overestimation of the ^{14}C age of the corresponding samples. This determines that a calibration of a sample from this period results in up to five cal age ranges for one ^{14}C age [30].

The ^{14}C age of sample No. 11, i. e. 30 ± 40 yr BP, corresponds to three 1-σ ranges (calibrated with OxCal and CALIB), respectively to three 2-σ ranges (calibrated with OxCal) and even to six 2-σ ranges (calibrated with CALIB) (Tables 2-3). The 1-σ range and also the 2-σ range with the highest probability correspond, with both calibration programs, to the period AD 1950–1960 (rounded values).

The 1950–1960 decade is also known for the beginning of the dramatic period of troposphere bomb tests. Due to the 404 atmospheric nuclear detonations between 1953–1963, a large amount of artificial ^{14}C was injected into the stratosphere. Consequently, the ^{14}C concentration in the troposphere almost doubled from 1950 to 1964 [31-33]. Again, the Northern Hemisphere, where the large majority of nuclear weapon tests took place, was affected earlier and to a more significant extent than the Southern Hemisphere. Incorporation in living tissues of CO_2 from the bomb tests period, which contains modern carbon very rich in ^{14}C, determines generally an underestimation of the ^{14}C age of the respective sample. The calibration of a sample from this period also results in three or more cal age ranges for one ^{14}C age.

Given that both the Suess effect and the bomb tests affected to different extents the two hemispheres, these differences being relatively well documented, determined us to use the SHCal04 dataset to calibrate the ^{14}C age of sample No. 11.

Selection of a reliable/accurate cal age range is, however, almost impossible. The range AD 1950–1960, which has the highest probability, is practically excluded, even if the ^{14}C age is probably underestimated. This is due to a large number of testimonies that state that Grootboom practically had not changed at all from its discovery in ca. 1890 until its sudden death. What is certain is that sample No. 11 was formed after AD 1640, thus having an age of less than 365 cal yr. In our opinion, the age of sample No. 11 is probably between 200–300 yr.

Structure of Grootboom. The enormous trunk of Grootboom collapsed very chaotically in all directions, so that six fallen stems have been eventually identified. After the fall of the last stem to the ground, the remains of Grootboom looked as if the tree would had been bombed or blasted with dynamite.

The six stems were marked (from west to east and than to northeast, facing north) by: A, B, C, D, E and F, in the reverse order of collapse [1].

The dated samples were collected from four stems, namely A, B, C and D. The fluctuation of the age of samples and the presence of 3 millenarian samples in three different stems strongly indicate that the trunk of Grootboom was made up of several (the more or the less) fused stems.

Considering the dating results and other information, we will try to answer the following question: How many and which of the six fallen stems had been independent, i. e. belonged to the original structure of Grootboom?

Discussed and analyzed below are the six stems, which were all of oval shape. The estimated values of the largest dbh (diameter at breast height) and of the dbh in perpendicular direction are presented in brackets.

Stem A (ca. 2.5 m x 1.2 m). This stem, which collapsed the last, was located at the western extremity of the trunk (facing north). It was located next to trunk B towards east, the two stems being partially fused up to a height of ca. 1 m above ground level. Its small dimensions are somewhat surprisingly, especially because it had enough free room to grow towards west. The oldest dated sample (No. 1) was collected exactly from stem A.

Stem B (ca. 3.1 m x 1.8 m). Stem B was located in between stems A and C and had no free room for additional growth. The third oldest sample (No. 4) was collected form this stem, more precisely from the rim of the largest hollow of the tree.

Stem C (ca. 1.6 m x 0.8 m). This small stem was fused up to a height of ca. 2 m with other three stems: B (towards west), D (towards east) and E (towards northeast). Its reduced dimensions and the relatively young age of the samples collected from it (Nos. 5 and 6) reveal that stem C must have been only a fusion product of the three stems, that continued to produce woody tissue after fusion.

Stem D (ca. 5.5 m x 3.2 m). Stem D, obviously the largest of the tree, was located at the eastern extremity of the trunk. It was the only stem which fell with roots exposed. Stem D was partially fused with stems C (towards west) and E (towards north). After breakdown, its base diameter parallel to the ground was measured and found to be 5.90 m. The second oldest sample (No. 8) was collected from this stem.

Stem E (ca. 3.0 m x 2.0 m). Stem E, which originates form the eastern flank of the trunk, was fused with stem D (towards south) and was in contact with stem F (towards north). It was unavailable for sampling, as it was partially hollow and also almost entirely covered and crushed by other fallen stems.

Stem F (ca. 3.5 m x 3.2 m). This stem, the first which collapsed, was almost isolated at the northeastern extremity of the trunk. It had only a connection area near ground level with stem E. The partially hollow stem F had already been severely decayed at the moment of the first sampling and no sample was collected from it.

These data suggests that five stems (A, B, D, E and F) may be considered independent and they are likely to belong to the original structure of Grootboom. The sixth stem (C) was much younger, being the result of fusion of three vicinal independent stems.

As already mentioned, there are two possibilities for the genesis of a baobab with multiple stems [34]. The first possibility is multiple sprouting from the same rootstock of a fallen parent tree. Hence, the stems are clones of the parent tree and they look very similar, because they are genetically identical. The second possibility is the simultaneous germination of several seeds. In this case, the stems are genetically different and they look somewhat different, for instance they may break into leaf at a different time and the tint of leaves and bark may also be somewhat different.

No such differences have been observed for Grootboom. This fact supports the hypothesis that the five independent stems sprouted simultaneously and fused into a single trunk at some later time. Consequently, one can state that morphologically Grotboom was a quintuple tree, while genetically it was a single individual.

The moment of complete fusion can be estimated by means of the age of samples collected from the fusion stem C (Nos. 5 and 6) and near the fusion area in between stems A and B (No. 2). Considering some corrections, we estimate that the five independent stems fused into a single trunk ca. 600–800 yr ago.

It should be also noticed that other very large African baobabs obviously have or are suspected of having multiple stems. We mention here the following trees: Chapman baobab at Gootsa pan (in Botswana), Dorslandboom in Bushmanland (in Namibia), Platland baobab near Duiwelskloof (in South Africa), Big tree at Victoria Falls and Big baobab at Devuli/Mokore ranch (in Zimbabwe), Big baobab near Joal (in Senegal).

Age of Grootboom. The 3 oldest dated samples with ages of at least 1000 yr, collected from three different stems, evince beyond doubts that Grootboom was a millenarian tree. Grootboom's true age can be estimated from the age of the oldest sample and its position in the respective stem. Sample No. 1, with a calendar age of 1,275 ± 50 yr, was collected from the stump of the relatively small stem A, located at the western extremity of the trunk, at a height of 1.20 m above ground and a distance of 0.40 m from the calculated position of its core which was hollow. These results reveal that the age of Grootboom was of +1,275 yr, i.e. the tree was older than 1,275 yr (our estimate is 1,350–1,500 yr).

Growth rate. The classic concept of growth rate of the whole trunk is meaningless for trees with multiple stems. One can only evaluate growth rates of independent stems and their dynamics, taking into account that the growth of each stem is limited by other stems in at least one direction.

In the particular case of Grootboom, one should notice that all stems had a clearly oval shape. Thus, the west-east diameter of the first three independent stems (A, B and D), from which samples were collected, was almost twice larger than their north-south diameter. This appears to be surprising as these stems had much more available room for growing towards north and south than towards west and east. Consequently, the growth rate in the west-eastern direction was almost twice greater than the growth rate in north-southern direction. For the other two stems (E and F), the west-east growth rate was also greater.

Because in case of multiple sprouting all independent stems are of the same age, i. e. +1275 yr, for each stem one can calculate the mean growth rate in two perpendicular directions. Mean growth rate values at breast height (grbh) for the entire life cycle of Grootboom are shown in Table 3. Given that in these calculations, we used the minimum age value (1275 yr), the growth rate data presented can be considered as representing the upper range values. The presented values for the mean growth rate (expressed in 10^{-3} m·yr^{-1}) correspond to the mean annual increase in radius (expressed in 10^{-3} m or mm).

Table 3.

Mean growth rate values of the independent stems

Stem	Age (cal yr)	Diameter at breast height (m)		Mean growth rate at breast height/ /annual increase in radius (10^{-3} m·yr^{-1})	
		dbh 1 [WE]	dbh 2 [NS]	grbh 1 [WE]	grbh 2 [NS]
A	+1275	2.50	1.20	0.98	0.47
B	+1275	3.10	1.80	1.22	0.71
D	+1275	5.50	3.20	2.16	1.25
E	+1275	3.00	2.00	1.18	0.78
F	+1275	3.50	3.20	1.37	1.25

The largest mean growth rate is the west-east value for stem D (2.16 x 10^{-3} m·yr^{-1}), while the smallest is the north-south value for stem A (0.47 x 10^{-3} m·yr^{-1}).

These mean values do not reflect, however, the growth dynamics of Grootboom's stems. According to published accounts, the growth rate of the African baobab decreases severely with the age [35, 36, 37, 38]. This statement can be also verified in the case of

Grootboom, by the ratio of the position of the extreme lateral samples to their age.Ages of extreme lateral samples (Nos. 3 and 10) show that over the past ~520 yr stem B grew by only 0.10 m towards south, while stem D grew by 0.25 m towards east in ~575 yr, even though there was enough room in both directions (no neighbouring stem). The calculated growth rate values are very small: 0.19 and 0.43×10^{-3} m yr^{-1} (corresponding to a mean annual increase in radius by only 0.19 and 0.43 mm). Such values reveal that over the past 500–600 yr Grootbooom almost ceased growing.

When compared to historic records of the same trees, measurements of several huge individuals from Botswana and Mozambique showed a very small increase or even a decrease in girth during a time span of ~110 yr, from 1850–60 to 1966 [39]. These results were attributed to an obvious decrease of rainfall in Central Southern Africa. Our dating results of Grootboom suggest that the period of prolonged drought may have begun several centuries earlier, probably around AD 1400–1500.

Age limit of the African baobab. Preliminary dating results of the samples collected from Grootboom strongly support the long lived baobab hypothesis or at least that certain individuals of the species may become millenarians. The oldest sample indicates an age of +1275 yr for Grootboom, while our estimates augment the age up to 1350–1500 yr. One should consider that shortly before its demise Grootboom looked healthy and seemed not to be a very old and decrepit tree, nearing its end. It is very likely that it was attacked and killed by the poorly studied baobab disease. Had this unfortunate event not happened, Grootboom might have probably lived for additional years. Therefore, we estimate that the age limit of the African baobab, which is probably identical to the age limit of angiosperms, is around 1,500 yr.

History of Grootboom. The acquired data suggests the following scenario for the history of Grootboom. Over 1275 yr ago (prior to AD 730), maybe 1350–1500 yr ago (around AD 500–650), a very large African baobab collapsed somewhere in Central Southern Africa, in a semi-arid area habited only by San people or Bushmen. Five sprouts/shoots developed from the prostrate parent, which could be named Ur-Grootboom.

The five young baobabs, which were clones of the parent tree, grew gradually, until 600–800 yr ago (around AD 1200–1400), when they fused together into a single huge trunk, which came to be known much later as the Grootboom baobab. About 500–600 yr ago (around AD 1400–1500), the trunk of Grootboom was almost as large as at the time of its death. Presumably, climate changes in the area, especially shift towards conditions of prolonged drought, almost stopped its growth.

In AD 1890, Grootboom was discovered by the modern world, namely by the Dorslandtrekkers, a group of Boers who withdrew from South Africa to Angola. The tree, which looked very healthy, had not changed its physical appearance until AD 2004, when it unexpectedly died, being probably killed by the still mysterious baobab disease. Grootboom begun to collapse stepwise, until the last stem fell around New Year AD 2005. At the beginning of AD 2006, the last traces of Grootboom disappeared completely, leaving behind only the memories of what once was a mighty baobab tree.

CONCLUSIONS

Grootboom, the world's largest African baobab tree, dies and collapsed unexpectedly in Bushmanland, Namibia, in late 2004. Six fallen stems have been identified on the ground.

The international research project started on this occasion had the following aims: 1) to determine accurately the true age of the tree; 2) to establish whether Grootboom's trunk was a single unit or was composed of several fused stems; 3) to learn about the dynamics of Grootboom's growth rate during its life cycle.

11 samples collected from the remains of the collapsed tree were processed and analyzed by AMS radiocarbon dating. Several additional samples are under investigation.

The presented results and conclusions of the research can be summed up as follows:

1) The radiocarbon age (^{14}C age) values of 3 samples (Nos. 1, 4 and 8), collected from three different stems, was greater than 1000 yr BP, i. e. 1255, 1045 and 1090 yr BP. These are the first samples of an angiosperm tree, with accurate dating results, older than 1000 yr.

The radiocarbon age of the oldest sample (No. 1) was found to be 1255 ± 35 yr BP, which corresponds to a 1-σ calendar age of 1275 yr, at the moment of the tree's demise.

Grootboom becomes the first millenarian angiosperm tree, with an age of +1275 yr. Our estimate of the age is around 1350–1500 yr, according to the position of the oldest sample in the corresponding stem prior to collapse.

2) The acquired results indicate that five stems may be considered independent, belonging to the original structure of Grootboom, while the sixth stem was the result of fusion of three vicinal independent stems.

The five (genetically identical) independent stems sprouted simultaneously from a parent tree and they fused into a single trunk at some later time. The age of samples collected from the fusion stem (Nos. 5 and 6) and near the fusion area of two neighboring stems (No. 2) suggest that the five stems fused into a single trunk around 600–800 yr ago.

One can state that morphologically Grootboom was a multiple tree, but genetically it was a single individual.

3) The age of the extreme lateral samples (Nos. 3 and 10) reveals that Grootboom grew by only ca. 0.10 m towards the southern edge and 0.25 m towards the eastern extremity over the past ca. 500–600 yr. The severe decrease of the growth rate could be ascribed to climate changes in Central Southern Africa, i.e. a shift towards conditions of prolonged drought.

Acknoledgements:

We thank Mike Elliott, Stacey Main, Gunther Friedrich, Ken Grabowski, David Knies, Edward Fletcher and Eugene Gergely for help and useful discussions. Special thanks are due to the Ministry of Environment and Tourism of Namibia for facilitating the research and providing export permits for the samples, as well as to Russel Jeffries from Nova Research, Inc. (Alexandria, VA) for supporting this project.

Special thanks are due to the Ministry of Environment and Tourism of Namibia for facilitating the research and providing the export permits for the samples.

NOSAMS is supported by U.S. National Science Foundation Cooperative Agreements 82899608 and 82899613.

REFERENCES

1. A. Patrut, K. von Reden, D. A. Lowy, P. Lindeque, A. H. Alberts, R. Wittmann, E. Forizs, D. Margineanu, J. Pohlmann, D. Gerlach, L. Xu, C. S. Mitchell, "Accelerator mass spectrometry dating of a very old tropical tree: Preliminary report. I. Radiocarbon dates", *Studia Univ. Babes-Bolyai, Chem.*, 2006, this issue.
2. Bronk Ramsey C., "Analysis of chronological information and radiocarbon calibration: The program OxCal", *Arch. Comput. Newslett.*, 1994, 41, 11-16.
3. Bronk Ramsey C., "Radiocarbon calibration and analysis of stratigraphy: The OxCal Program", *Radiocarbon*, 1995, 37, 425-430.
4. Bronk Ramsey C., "Probability and dating", *Radiocarbon*, 1998, 40, 461-474.
5. Bronk Ramsey C., "Development of the radiocarbon calibration program", *Radiocarbon*, 2001, 43, 353-363.
6. Bronk Ramsey C., "OxCal Program, v3.10", University of Oxford, Radiocarbon Accelerator Unit, 2005 (www. rlaha.ox.ac.uk/oxcal/oxcal.html).
7. Stuiver R., Reimer P. J., "A computer program for radiocarbon age calibration", *Radiocarbon*, 1986, 28, 1022-1030.
8. Stuiver R., Reimer P. J., "Extended ^{14}C database and revised CALIB 3.0 ^{14}C age calibration program", *Radiocarbon*, 1993, 35, 215-230.
9. Stuiver R., Reimer P. J., Reimer M., CALIB Radiocarbon Calibration Program, University of Washington, Queens University of Belfast, 2005 (www.calib.qub.ac.uk/crev50/manual/ reference.html).
10. Reimer P. J., Baillie M. G. L., Bard E., Bayliss A., Beck J. W., Bertrand C. J. H., Blackwell P. G., Buck C. E., Burr G. S., Cutler K. B., Damon P. E., Edwards R. L., Fairbanks R. G., Friedrich M., Guilderson T. P., Hogg A. G., Hughen K. A., Kromer B., McCormac G., Manning S., Bronk Ramsey C., Reimer R. W., Remmele S., Southon J. R., Stuiver M., Talamo S., Taylor F. W., van der Plicht J., Weyhenmeyer C. E., "IntCal04 terrestrial radiocarbon age calibration, 0-26 cal kyr BP", *Radiocarbon*, 2004, 46,1029-1058.
11. McCormack F. G., Hogg A. G., Blackwell P. G., Buck C. E., Higham T. F. G., Reimer P. J., "SHCal 04 Southern Hemisphere calibration, 0-11.0 cal kyr BP", *Radiocarbon*, 2004, 46, 1087-1092.
12. Vogel J. C., Fuls A., Visser E., Becker B., "Radiocarbon fluctuations during the third millennium BC, *Radiocarbon*, 1986, 28, 935-938.
13. Vogel J. C., Fuls A., Visser E., Becker B., "Pretoria calibration curve for short-lived samples", *Radiocarbon*, 1993, 35, 73-85.
14. Stuiver M., Braziunas T., "Anthropogenic and solar components of hemispheric ^{14}C", *Geophys. Res. Lett.*, 1998, 25, 329-332.
15. McCormac F. G., Hogg A. G., Higham T. F. G., Lynch-Stieglitz J., Broecker W. S., Baillie M. G. L., Palmer J., Xiong L., Pilcher J. R., Brown D., Hoper S. T., "Temporal variation in the interhemispheric ^{14}C offset", *Geophys. Res. Lett.*, 1998, 25, 1321-1324.
16. McCormac F. G., Hogg A. G., Higham T. F. G., Baillie M. G. L., Palmer J., Xiong L., Pilcher J. R., Brown D., Hoper S. T., "Variations of radiocarbon in tree rings: Southern Hemisphere offset preliminary results", *Radiocarbon*, 1998, 40, 1153-1159.
17. Hogg A. G., McCormac F. G., Higham T. F. G., Reimer P. J., Baillie M. G. L., Palmer J. G., "High-precision radiocarbon measurements of contemporaneous tree-ring dated wood form the British Isles and New Zealand, *Radiocarbon*, 2002, 44, 633-640.

18. McCormack F. G., Reimer P. J., Hogg A. G., Higham T. F. G., Baillie M. G. L., Palmer J., Stuiver M., "Calibration of the radiocarbon time scale for the Southern Hemisphere: AD 1850-950, *Radiocarbon*, 2002, 44, 641-651.
19. Stuiver M., Reimer P. J., Bard E., Beck J. W., Burr G. S., Hughen K. A., Kromer B., McCormac F. G., van der Plicht J., Spurk M., "IntCal98 radiocarbon age calibration, 24,000-0 cal BP", *Radiocarbon*, 1998, 40,1041-1083.
20. Sparks R. J., Melhuish W. H., McKee J. W. A., Ogden J., Palmer J. G., Mollloy B. P. J., "^{14}C calibration in the Southern Hemisphere and the date of the last Taupo eruption: evidence for tree ring sequences", *Radiocarbon*, 1995, 37, 155-163.
21. Barbetti M., Bird T., Dolezal G., Taylor G., Francey R., Cook E, Peterson M., "Radiocarbon variations from Tasmanian conifers: First results from late Pleistocene and Holocene logs", *Radiocarbon*, 1992, 34, 806-817.
22. Barbetti M., Bird T., Dolezal G., Taylor G., Francey R., Cook E, Peterson M., "Radiocarbon variations from Tasmanian conifers Results from three Holocene logs", *Radiocarbon*, 1995, 37, 361-369.
23. Guilderson T. P., Cook E., Buckley B. M., "Huon pine extension of the Southern Hemisphere ^{14}C-calendar calibration dataset", 19th International ^{14}C Conference, Oxford, April 3-7, 2006.
24. Damon P. E., Cheng S., Linick T. W., "Fine and hyperfine structure in the spectrum of secular variations of atmospheric ^{14}C", *Radiocarbon*, 1989, 31, 955-959.
25. Damon P. E., Burr G., Cain W. J., Donahue D. J., "Anomalous 11-year Δ^{14}C cycle at high latitudes", *Radiocarbon*, 1992, 34, 235-238.
26. Damon P. E., "A note concerning Location-dependent differences in the ^{14}C content of wood", *Radiocarbon*, 1995, 37, 829-830.
27. Damon P. E., "Note concerning Inter-comparison of high precision ^{14}C measurements at the University of Arizona and Queen's University of Belfast Radiocarbon Laboratories", *Radiocarbon*, 1995, 37, 955-959.
28. McCormac F. G., Baillie M. G. L., Pilcher J. R., Kalin R. M., "Location-dependent differences in the ^{14}C content of wood", *Radiocarbon*, 1995, 37, 395-407.
29. Tans P. R., de Yong A. F. M., Mook W. G., "Natural atmospheric ^{14}C variations and the SUESS-effect", *Nature*, 1979, 280, 826-828.
30. Stuiver M., Becker B., "High-precision decadal calibration of the radiocarbon time-scale, AD 1950 – 2500 BC", *Radiocarbon*, 1986, 28, 863-910.
31. Hua Q., Barbetti M., Worbes M., Head J., Levchenko V. A., "Review of Radiocarbon Data from Atmospheric and Tree Ring Samples for the Period 1950 – 1977 AD", *IAWA J.*, 1999, 20, 261-284.
32. Worbes M., Junk W. J., "Dating Tropical Trees by Means of ^{14}C From Bomb Tests", *Ecology*, 1989, 70, 503-507.
33. Hua Q., Barbetti M., "Review of tropospheric bomb ^{14}C data for carbon cycle modeling and age calibration purposes", *Radiocarbon*, 2004, 46, 1273-1298.
34. Esterhuyse N., von Breitenbach J., Sőhnge H., *Remarkable Trees of South Africa*, Briza, Pretoria, 2001.
35. von Breitenbach F., "Aantekeninge oor die groeitempo van aangeplante kremeteartbome (Adansonia digitata) en opmerkinge ten opsigte van lewenstyd, groeifases en genetiese variasie van die spesie", *J. Dendrology*, 1985, 5, 1-21.
36. Guy G. L., "*Adansonia digitata* and its rate of growth in relation to rainfall in South Central Africa", *Proc. & Trans. Rhod. Sci. Assoc.*, 1970, 54, 68-84.
37. Coates Palgrave M., Coates Palgrave K., *Trees of Southern Africa*, ed. 3, Struik, Cape Town, 2002.
38. Swart E. R., "Age of the Baobab Tree", *Nature*, 1963, 198, 708-709.

STUDIA UNIVERSITATIS BABES - BOLYAI, CHEMIA, LI, 2, 2006

Dedicated to professor Gh. Marcu at his 80th anniversary

VOLTAMPEROMETRIC DATA ON THE BIOLOGICAL ACTIVE SYSTEMS CU(II), PD(II) AND NI(II) – SALICYLIC ALDEHIDE THIOSEMICARBAZONE

MARIA JITARU[1], MARIA BIRCA[*] AND HURDUCAS MIHAELA

ABSTRACT. The voltamperometric behavior of the systems Cu(II), Ni(II) and Pd(II) – thiosemicabazone of salicylic aldehyde (TSCSA) has been investigated on glassy carbon electrodes (cyclic voltametry) in DMF/$LiClO_4$ 0,2 M medium, using computer aided electrochemical systems BAS 100W and AUTOLAB – ECOCHEMIE.

In the case of all complexes can be seen that the peak related with the sulphur oxidation was moved towards positive higher values, which confirm the involving of sulphur in the coordination. From the point of view of the donor – acceptor interaction between metallic ion and sulphur atom as donor, it can be affirmed that, in these conditions, the Cu(II) complex is more stable than the Ni(II) and Pd(II) complexes. This conclusion is in accordance with the especial affinity of the Cu(II) ion against sulphur.

Based on the shifts of reduction potentials of the metals, ΔЄ = 215 mV for Cu complex, ΔЄ = 162 mV for Ni complex and ΔЄ = 180 mV for Pd complex, various degrees of interaction have been identified. They are qualitatively correlated with the stability of the complexes.

Key words: thiosemicarbazones, metal complexes, cyclic voltammetry.

Introduction

Thiosemicarbazones and related compounds, as well as their metal complexes have been the subject of great interest of many researchers, the first of all because they are active from the biological point of view, some having antitumoral activity. The statement is supported by a large number of papers, some of them in the last years [1,2]. Because in the human body there are redox processes it is important to have the information about the electrochemical behavior of the systems metal ions, Cu(II), Pd(II) and Ni(II) - thiosemicabazone of salicylic aldehide in solution. Apart from their diverse chemical and structural characteristics, the significance of these compounds, especially related to thiosemicarbazones and theirs metal complexes, the relation between structure and biological activity has

[1] Associated Francophone Laboratory, "Babeş-Bolyai" University, Faculty of Chemistry and Chemical Engineering, 11, Arany Janos Street, 400028, Cluj-Napoca, Romania, *E-mail : mjitaru@chem.ubbcluj.ro*

[*] State University of Moldova, Faculty of Chemistry, 60, Matveevici Street, Chisinau, Moldova

been covered in papers by West et al.[3,4]. The complexes have been prepared using the interaction of Ni(II) and Cu(II) sulphates, respectively $[PdCl_4]^{2-}$ with the thiosemicarbazone of salicylic aldehide (TSCSA) in aqueous solutions of ethylic alcohol, in echimolar amounts, resulting 1/1 type ligand thiosemicarbazone metal complexes [5].

In order to characterize the redox processes of these systems, which may occur on the ligands and complexes, as well as to compare the stability of the complexes and the coordinating ligand position involved in complex formation in solution, electrochemical investigations are usually performed, in suitable solvents. Although the thiosemicarbazone – based ligands were investigated by electrochemical methods [6,7], for the system (TSCSA) – Me(II) there are not the data in the literature.

The investigations have been made in organic media (DMF, THF, AC), in the presence of several supporting electrolytes, usually at glassy carbon electrode. The most important conclusion of these voltamperometric determinations was the complexity of the electrochemical answer, involving both the redox processes on the level of ligand moiety and metal ion [8].

Experimental

The tests were performed in a classical cell having three electrodes. All the samples were deaerated 20-30 minutes before each test. Because of low solubility of the complex in the protic medium, the non aqueous medium of DMF was chosen.

Cyclic voltammograms were recorded in a dried cell purged with argon. DMF used as electrolyte solvent was purified according to standard procedures [9]. $LiClO_4$ dried in an oil pump vacuum at 100°C was added as supporting electrolyte at a concentration of 0.2 M. Compounds under investigation were added at 1 mM concentration. The working electrode (GC, Hg and Pt) and platinum wire counter-electrode were used. An Ag/Ag^+, AgCl electrode, in a separate compartment served as reference electrode. CVs were recorded both in negative and positive-going direction at the starting potentials, at different scan rate using a Autolab potentiostat (Ecochemie) equipped with PGSTAT 12 soft. All experiments were run at room temperature (22°C).

Results and discussion

The ligand (TSCSA), produced from the condensing salicylic aldehide with thioureea (TU), has basically three electroactive positions: hydroxyl oxygen, the sulphur from the remaining thiourea and the azometin grouping. From these, the last two unsaturated groups can be reduced and the OH can be easily oxidized.

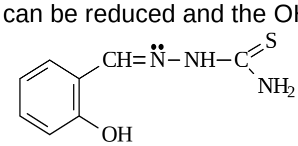

The electronic interaction between datively bonded ligand (TSCSA) and divalent metal ions has been studied with cyclic voltammetry and polarography, both in reduction and oxidation potential range.

Typical CVs of complexation in Cu(II)-TSCSA system, in DMF, in negative – going direction are displayed in Fig. 1.

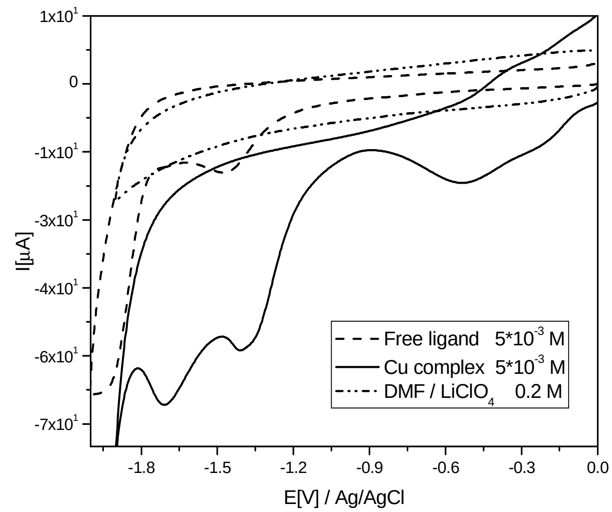

Figure 1. Comparison between the electrochemical behavior of (TSCSA) and Cu (II) complex in negative – going direction.

In DMF medium, on glassy carbon, the ligand presents two oxidation peaks, the first in the 700-850 mV range *vs* Ag/AgCl,KCl, which can be related to phenolic group [10, 11], Fig.2a.

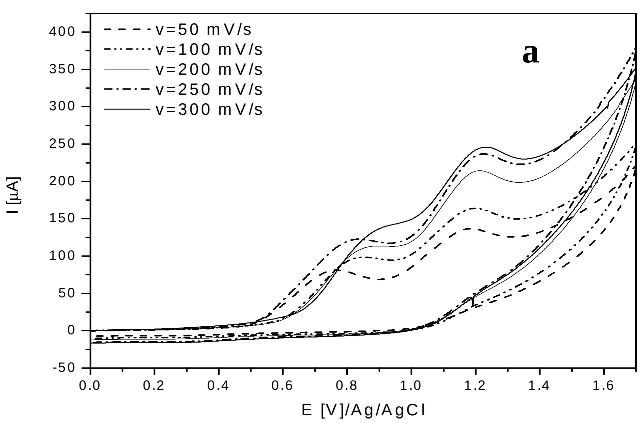

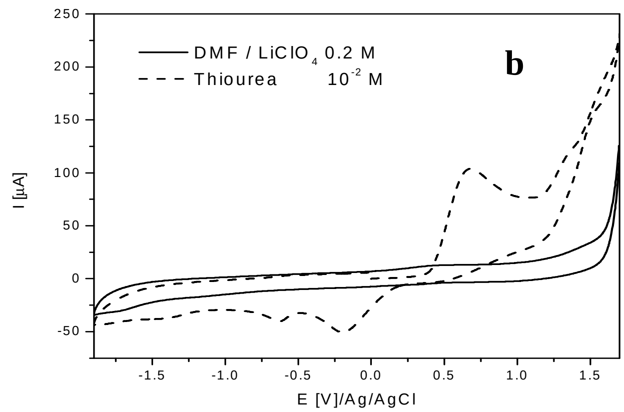

Figure 2. CVs for the oxidation of ligand and (TU) on GC electrode in DMF/ 0.2 M $LiClO_4$ for :
a – oxidation of 10^{-3} M (TSCSA)
b – oxidation of 10^{-3} M (TU)

and the second in the high and positive range (>1 V *vs* Ag/AgCl) which is specific to π carbon-sulphur oxidation; this last peak's attribution was confirmed by the voltamperometric response of (TU), Fig 2b.

To spot the entail the complexation of metal ions, respectively the processes of reduction of the azometin group of ligand, it was followed in the same parameters the voltamperometric response of the components and of the system in an extended range of negative voltages, allowed by the use of non-aqueous electrolyte, ($Є_0$= -0.4 V/ Ag/AgCl, KCl and $Є_f$=-2.2V/).

The irreversible reduction of azometin group in (TSCAS) might occur at the negative electrode potential, to $Є_{-C=N-}$> - 1.8 V/ Ag/AgCl, KCl, Fig.3.

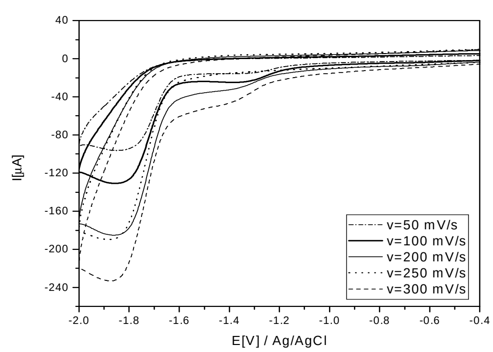

Figure 3. Reduction of azometin group in (TSCAS).

By comparing VCs of the free ligands (TSCSA) and TU, and for the complexed metalic ions can be seen differences of the peak voltages and for the peak currents because of complexation, Table 1.

According to other authors, confirmed for related compounds in solid state [8], usually thiosemicarbazones act such tridentate ligand (O, S, N):

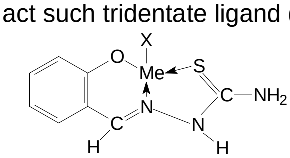

Me: Ni(II), Cu(II), Pd(II)

but in some cases, M=Ru(II),Os(II) the phenolic oxygen is not included in the coordination [14] and the dimer structures have been demonstrated for Tl complexes with related ligands.

Table 1.

The influence of complexation on the peak potentials in DMF [V/ Ag/AgCl, KCl].

Compound	Oxidation		Reduction	
	ϵ_{OH}	$\epsilon_{C=S}$	$-\ \epsilon_{-CH=N-}$	$-\ \epsilon_{Me(II)}$
TSCAS	0.81	1.09	1.47;1.82	-
Cu (II) - TSCAS	0.86	1.43	1.40; 2.12	0.40; 1.20
Cu(II)	-	-	-	0.30
Ni (II) - TSCAS	0.91	1.18	1.53; 2.02	1.53
Ni(II)	-	-	-	1.28
Pd(II) - TSCAS	0.98	1.28	1.46; 1.98	1.55
Pd(II)	-	-	-	0.55;1.30

Comparing our data in DMF for ligand and complexes, Table 1, we can see that the redox properties of the linkages involving donor atoms were stabilized by complexation, Table 2. These facts are valuable both for OH and C=S, when the oxidation potential is displaced to more positive values. For CH=N, the second reduction step could be easier, at lower negative potentials. We consider that the displacement of peaks potentials is due to the complexation and the value of the shift is in relation with the stability of the complex.

Table 2.

Displacement [mV] of the peak potentials of donors and metal ions, by complexation in DMF/0.2M $LiClO_4$.

Me(II)	Donor group	Δε* [mV]	Δε** [mV]
Cu(II)	–OH	50	215
	=S	340	
	–N=CH–	- 300	
Ni(II)	–OH	100	162
	=S	90	
	–N=CH–	- 200	
Pd(II)	–OH	170	180
	=S	190	
	–N=CH–	- 160	

* Average of 3 determinations.

** For complexed metal ions comparing to metal ion coordinated only with perchlorate.

The explanation of the shifts of oxidation potentials of donors after complexation is easier for the oxidable groups (OH and =S): the density of electrons after complexation becomes lower, so the oxidation becomes more difficult. For the azometin reducible group, the π character of double bond diminishes by complexation, the linkage becomes weaker and its reduction is possible to smaller negative potentials.

Taking the reduction potential of metal ions complexes coordinated with perchlorate anion, even in dissolved state, results in a negative shift, by complexation with (TSCSA), Table 2, corresponding to the stability of the complexes.

Conclusions

The following qualitative remarks were deducted on complexation interactions:

- Powerful engaging of the sulphur donor atom and azometin group in complexation with Cu(II) ions, more comparing to Ni(II) and Pd(II).
- Participation of the hydroxyl oxygen in complexation with Ni(II) and Pd(II) more than for Cu(II).
- Engaging of the π electrons of the azometin linkage in complexation in the following order:

Cu(II) > Ni(II) > Pd(II)

- According to shift of the reduction potentials of metals ions, the relative stability of the complexes is:

Cu(II) >Pd(II) > Ni(II)

Based on the information reported here, future experiments will be realized to establish the quantitative data on the stabilization of these metal ions through complexation.

REFERENCES

1. V. Arion, M. Revenco, J. Gradinaru, Yu. Simonov, V. Kravtsov, N. Gebeleu, E. Saint-Aman, F. Adams, *Rev.Inorg.Chem*., **2001**, *21*, 1.
2. H. Beraldo, *Quim.Nova,* **2004,** *27*, 461.
3. D. X. West, S. B. Padhye, P. B. Sonawane, *Struct.Bond*., **1991,** *76,* 1.
4. D. X. West, A. E. Liberta, S. B. Padhye, R. C. Ghikate, P. B. Sonawane, A. S. Kumbar, R. G. Yerande, *Coord.Chem.Rev*., **1993**, *123*, 49.
5. A. Gulea, M. Birca, V. Tapkov, M. Jitaru, M. Toma. D. Poire "*The XXIst International Conference on Coordinative Chemistry*, 10-13 July, **2003**, Kiev, Ukraina.
6. M. Canadas, E. Loppez-Tores, A. Martinez-Arias, M. A. Mendiola, M. T. Sevilla, *Polyhedron,* **2000**, *19*, 2059.
7. L. J .Bjelica, Lj. S. Jovanovic, V. M. Leovac, *Z.Phys.Chemie* (Leipzig), **1988,** *269,* 768.
8. Lj. S. Jovanovic, C. S. Jevtovic, V. M. Leovac, L. J. Bjelica, *J.Serb.Chem.Soc*., **2005**, *70*, 187.
9. C. K. Mann, in: A. J. Bard (Ed.), *Electroanalytical Chemistry*, **1969**, *3*, 57, Marcel Dekker, New York.
10. M. Jitaru, J. Stroka and Z. Galus, *J. d'Electrochimie*, **1997,** Montreal, Canada, 2-5 iulie.

11. M. Jitaru, A. Katona, N. Dulămiță, M. Stanca and M. Bîrca, *Scientific Annals of State University of Moldavia (biologie-chemistry series)*, **2001**, 282-287.
12. M. Jitaru, C. Moinet, C. Filip and M. Toma, *51th ISE Meeting,* 3-9 September **2000**, Warsaw, Poland.
13. M. Leschke, Dissertation, Technische Universitat Chemnitz, **2002**; *http://archive.tu-chemnitz.de/pub/2003/0031/index.html*
14. V. M. Leovac, Lj. S. Jovanovic, V. I. Cesljevic, L. J. Bjelica, N. J. Evic, *Polyhedron,* **1992,** *11*, 1029.

Acknowledgements: This work was supported by the CNCSIS Grant cod 1323/11.

STUDIA UNIVERSITATIS BABES - BOLYAI, CHEMIA, LI, 2, 2006

Dedicated to professor Gh. Marcu at his 80th anniversary

ADSORPTION AND ELECTROCHEMICAL DATA FOR p-NITROPHENOL REMOVAL FROM SYNTHETIC WASTEWATERS

MARIA JITARU[*], BOGDANA KOUMANOVA[**]

ABSTRACT. There are three main results reported in this paper refer to: (*i*) the equilibrium adsorption experiments of recalcitrant toxic p-nitrophenol (p-NP) on natural zeolites from Balkan area; (*ii*)voltamperommetric data on the electrochemical behavior of p-nitrophenol, depending on the electrode nature and working conditions (pH, electrolyte composition, hydrodynamic parameters (*iii*) and electrochemical oxidation to remove the remaining p-nitrophenol on different electrodes after the adsorption.

The zeolite from Mirsid, Romania (zeolite-2) seems to have the best adsorption properties for p-nitro phenol, comparing to classical sorbent, active carbon powder. The synthetic waste waters containing 0.01p-NP have been treated by adsorption on (zeolite-2) and the decrease of the p-NF concentration up to 0.01 mM has been obtained. The remaining p-NP was treated by electrochemical way (electro-oxidation). Applying the combined adsorptive-electrochemical oxidation procedure we have been obtained the decrease of COT up to 98%, on $SnO_2/IrO_2/Ti$ (Modified Oxides Electrode- MOE). These results could be explained by the catalytic effect of the zeolite for the chemical phenol oxidation.

Key words: nitrophenols, adsorption, zeolites, electrochemical oxidation

Introduction

Due to the recognized toxicity of nitrophenols, the International Programme on Chemical Safety (IPCS), established in 1980, as a joint venture of the United Nations Environment Programme (UNEP) and the World Health Organization (WHO) elaborate the authoritative document, Concise International Chemical Assessment Document (CICAD 20), on the risk assessment of nitrophenols.

During the past decade, extensive research has been conducted to develop innovative, effective, inexpensive and promising adsorbent materials that are regenerated easily for dealing with the problem of the treatment of contaminated wastewater. Organically modified benthonites and zeolites, produced

---

[*] “Babeş-Bolyai” University, Faculty of Chemistry and Chemical Engineering, Associated Francophone Laboratory, 11, Arany Janos Street, 400028 Cluj-Napoca, Romania; *mjitaru@chem.ubbcluj.ro*

[**] Technical University of Chemistry& Metallurgy 8, Kliment Ohridsky, Blvd., 1756 Sophia, Bulgaria; *bogdana@uctm.edu.bg*

by replacing exchangeable inorganic cations with quaternary alkyl ammonium cations, have been reported as strong adsorbents for non-ionic organic pollutants.

The monosubstituted 4-nitrophenol is found in wastewaters discharged from various industrial activities such as pulp and paper industries, textile mills, steel plants, oil refineries, etc. [1]. This compound is also associated with agricultural activities as an intermediate for the production of pesticides, herbicides and insecticides [2].

Attempts have been made to remove mononitrophenols from wastewater by a number of methods: oxidation with strong oxidizing agents as H_2O_2 [3], biodegradation [4], biosorption [5], photocatalytic degradation [6], etc. With respect to adsorption of nitrophenols, activated carbon is one of the most commonly used adsorbents due to its high surface area and well developed pore structure [7-11]. As activated carbon is relatively costly, attempts have been directed to the utilization of low-cost and abundant natural materials as alternative adsorbents for nitrophenols removal from aqueous phase.

Electrochemical processes offer useful possibilities for *in situ* and local treatment of industrial waste-waters at anodes for destructive removal or modification of noxious solutes (especially organics) [9]. For this latter type of impurity solutes, the overall process most desirable is that of so-called “mineralization”, *i.e.*, complete anodic oxidation to CO_2 and H_2O, or additionally to N_2 or NO_3^-, or to SO_4^{2-} in the case of N or S containing organics, respectively. The use of electrode processes has the advantage that no added oxidizing or reducing agent needs to be provided since electrons (at cathodes) or their vacancy states (at anodes) are direct reagents, so that no other undesired exogenous products will arise. The oxidation of phenols on different types of modified oxides anodes, including the DSA commercial anodes has been studied, by cyclic voltammetry, polarization measurements, and electrochemical impedance spectroscopy and potentiostatic transients in different aqueous solutions [11-14]. The formation of a phenoxy radical in a diffusion-controlled irreversible process is the initial step. In the concentrated phenols solution, the polymerization of phenoxy radicals leads to the formation of porous polyoxyphenylene film, strongly adherent to the electrode surface; this film inhibits partially the further oxidation [3].

Continuing our previous research focus on the electrochemical investigation of the phenols and other organic pollutants oxidation [12, 13], this paper presents the results obtained by combining two procedures in order to eliminate the nitrophenols: adsorption of nitrophenols from the quasi concentrated solution (10^{-2}M) and the electrochemical oxidation of the remaining nitrophenols.

Experimental

Nitrophenols are sparingly soluble in water and therefore, both the adsorption and electrochemical properties have been investigated from their hydro alcoholic solutions (1/1 water/n-propyle alcohol mixture). For the electrochemical measurements the 0.1 M Britton-Robinson buffer electrolytes was used. The voltamperommetric and spectrophotometric control of nitrophenols has been achieved using a common three electrodes cell (WE: glassy carbon and; RE: $Ag/Ag^+/AgCl$; AE: Pt wire).

The reactor setup used for adsorption measurement contains magnetic stirred and thermostated saturation vessel equipped with a reflux condenser. In a typical adsorption experiments, 0.5 mg of zeolites were been added to a glass reactor followed by the addition of known quantity of nitrophenols in 1/1 water/i-propanol mixture. Initial sample was taken before starting the experiment. Each experiment was carried out at the constant temperature. The experiment was continued until analysis of two successive samples was constant, which confirmed the adsorption equilibrium stage.

The concentration of the remaining nitrophenols, after their adsorption on zeolites has been reduced by electrochemical way (oxidation or/and reduction), using a modified PRIAM reactor [12]. The intermittent samples were taken out at certain time intervals during both adsorption and electrochemical experiments and analyzed by UV-VIS (Pye UNICAM Heliosβ) and cyclic voltammetry (ECOCHEMIE-BAS100W).

The yellow benthonite used for the investigations was taken from deposits in the southern part of Bulgaria. The zeolites were taken from deposits in different regions in Romania: zeolite 1- from the region Marsid, zeolite 2- from Macicas and zeolite 3- from Sacaramb.

Results and discussion

Adsorptive properties of the investigated sorbents

The chemical composition and physical properties of the zeolite 1, zeolite 2 and yellow benthonite are presented in Table 1. Specific surface area and pore volume of the natural materials were determined using Sorptomatic 1990, Fisons instruments.

The adsorption isotherms, Figure 1 (plots of q - the quantity of adsorbed solute per unit weight of adsorbent, versus C_e- equilibrium concentration):

$$q= V (C_0- C_e)/w$$

suggested that the isotherms of p-nitrophenols on zeolites are similar to Langmuir isotherms.

Table 1

Characteristics of zeolites

Content, %	Zeolite 1	Zeolite 2	Yellow bentonite
SiO_2	65.43	63.905	59-75
TiO_2	0.29	0.385	0.1-0.8
Al_2O_3	13.94	14.455	12-16
Fe_2O_3	1.31	1.74	1-6
CaO	3.98	5.335	1.8-5
MgO	0.41	0.30	0.9-3
Na_2O	0.28	1.02	0.5-1
K_2O	2.06	0.86	0.5-1
Loss at ignition	12.3	12.00	-
Specific surface area $m^2\ g^{-1}$	44.56	27.33	57.99
Pore volume at p/p^0 0.99, $cm^3\ g^{-1}$	0.133	0.132	0.169
Monolayer volume, $cm^3\ g^{-1}$	8.8704	8.5030	13.3204

The Langmuir adsorption isotherm has been successfully applied to many adsorption processes. A basic assumption of the Langmuir theory is that adsorption takes place at specific homogenous sites within the absorbent. It is then assumed that once an organic molecule occupies a site, no further adsorption can taken place at that site. Theoretically, therefore, a situation value is reached beyond which no further sorption can take place. The values of the calculated Langmuir constants (K_L, a_L) and the correlation coefficient (R^2) are listed in Table 2.

The adsorption of p-nitrophenol on zeolites was compared with the data on activated carbon indicating that the adsorption is quite similar, in both cases could be attributed to the physisorption.

The adsorbed quantity of monolayer, q_m was found to vary with temperature. The adsorption equilibrium constant, K, decreased with increase in temperature, which was also consistent with the Langmuir theory.

Form the comparative analysis of the experimentally obtained adsorption capacity of the studied natural materials it was established that zeolite 2 and yellow bentonite exhibited the highest affinity to 4-NP. The values of the equilibrium and monolayer adsorption capacity of the sorbents to 4-NP follow the order:

Yellow bentonite = zeolite 2 > zeolite 1

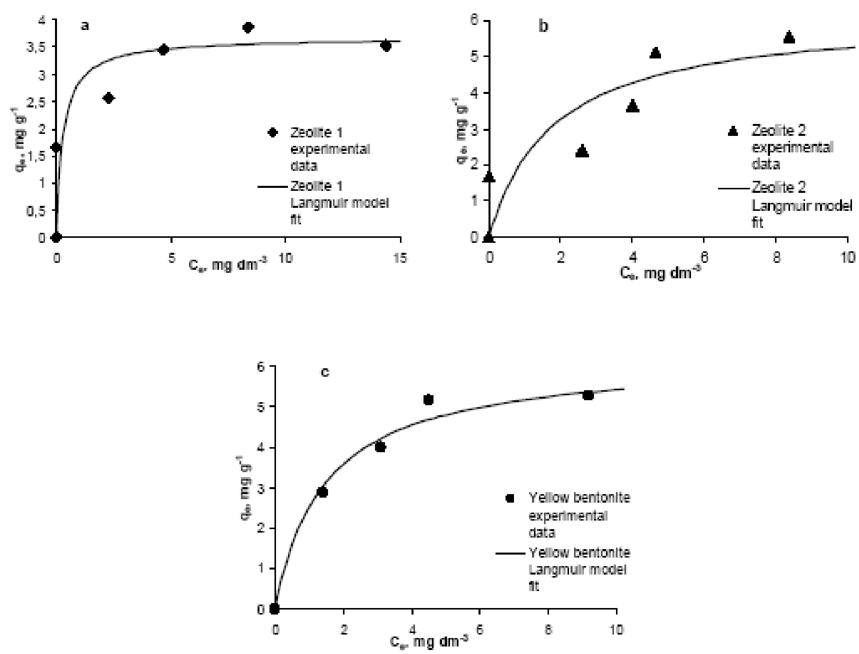

Figure 1. The adsorption isotherms comparing with Langmuir model

Table 2

Value of the calculated constants in the Langmuir and Freundlich models.

Sorbent	Langmuir			Freundlich		
	K_L	a_L	R^2	K_F	n_f	R^2
Zeolite 1	12.5313	3.4097	0.9911	2.3911	0.1827	0.6694
Zeolite 2	3.4435	0.5557	0.7642	1.3270	0.7259	0.8076
Yellow bentonite	4.2212	0.6809	0.9875	2.7077	0.3385	0.8787

Adsorption experiments of p-nitrophenol on Zeolite-2

During the adsorption of p-NP on Zeolite-2 the change of color has been observed, as can see in UV-spectrum, Figure 2 (λ=400nm);

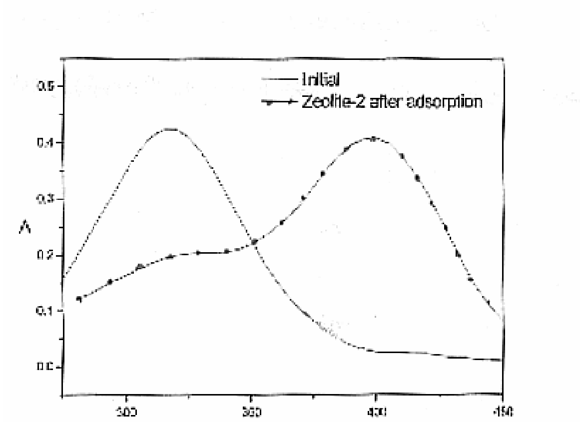

Figure 2. Evidence for p-NF oxidation after the adsorption on Zeolite-2, after 20 min of adsorption (see Fig.3).

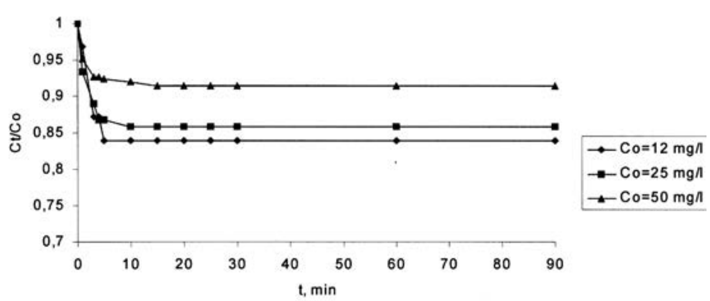

Figure 3. Effect of the initial concentration on adsorption of p-NP on benthonite. P=300 rpm; W=2 g

The surface of sorbent has been totally covered after 10-20 min, depending on the initial concentration.

This behavior (Figure 2) could be explained by the catalytic activity of the Zeolite-2 for p-NP oxidation. The most important results of p-NP adsorption are: decrease of p-NP concentration with (5-18) %, depending on the zeolite nature and conditions and partial oxidation of p-NP to the quinone structure, easier to oxidize by electrochemical way.

Decrease of nitrophenols concentration by electrochemical oxidation

According to our previous results the decrease of p-NF concentration could be realized both by reduction and oxidation [12].

The oxidation potential of 4-nitro phenol slowly decrease at the same time with increasing of phenols concentration, due the increasing of the coverage degree, Fig. 3

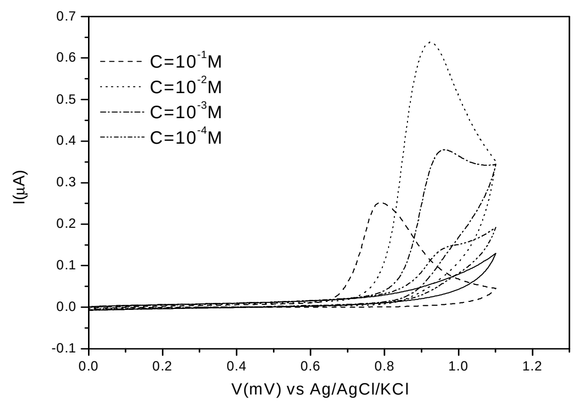

Figure 3. Dependence of oxidation potential of p-NP on concentration on GC.

Because each type of electrode shows a different behavior depending on its superficial characteristics and properties, by electrochemical oxidation on (MOE) and GC (glassy carbon electrode) the total mineralization takes place with different yields.

To make the comparison between these types of electrodes (GC and MOE), the oxidation of aqueous synthetic phenolic water was chosen.

As can be seen in figure 4, on (MOE) [16] an almost complete mineralization of the p-NP achieves and the mineralization rate is higher than those obtained on GC. The electrochemical total oxidation of the remaining p-NP, on (MOE) from about 1 mM to 10–50 μM.

On the other hand the analysis of the answer after multiples scans shows that polymerization is an important secondary reaction pathway on GC, Figure 5.

Preliminary data by the GPC liquid chromatography have demonstrated that the polymeric material developed in the process was a mixture of the various polymers with low molecular weight (ranging from 200 to 500 mg/mmol). Conversely, the oxidation of the phenol waste using (MOE) electrode deals to the sequential formation of aromatic compounds, carboxylic acids and carbon dioxide, Table 3.

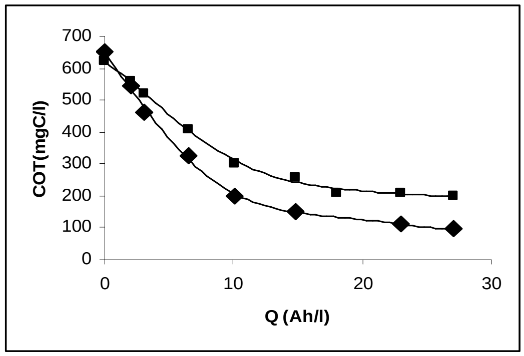

Figure 4. Decrease of COT on GC (■) and on MOE (◆)
$[Phenol]_O$: 1000 ppm; $[Na_2SO_4]$: 5000 ppm; pH: 2; Current density: 10 mA/cm^2

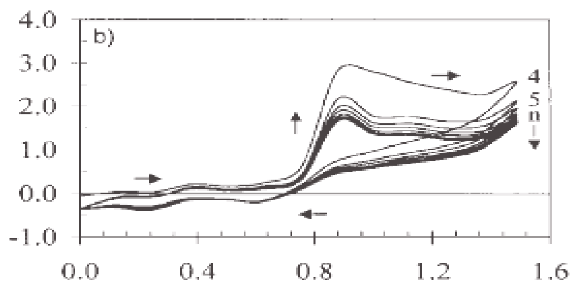

Figure 5. Polymers formation on GC.

Table 3

Preliminary data concerning the intermediates and final products of electro-oxidation (mg/l)

Compound	GC	MOE
Quinones	1.6	1.1
C_4 acids+C_2 acids	2.8	2.5
Polymers	38.5	0.0
Carbon dioxide	30.0	90.3
Unidentified compounds	26.6	6.1

Results obtained in this work could be explained in the terms of the oxidations of phenol to phenoxy radicals (first step of the process). The oxidation performed in (MOE) is stronger dealing whit the quick formation of benzoquinone and to the split of the aromatic ring. On the contrary the softer oxidation performed in GC electrode.

Conclusion

The combined procedure proposed in this paper is the adsorption of p-NP on zeolite in order to reduce the pollutant concentration up to 1 mM, followed by the electrochemical oxidation of remaining p-NP, up to 10–50 μM. The electrochemical mineralization of the remaining p-NP on (MOE) could be realized at accessible temperatures and pH≈2, when the competitive oxygen formation diminishes. The preliminary data on the nature and distribution of the oxidation intermediates and products has to be confirmed by future experiments.

REFERENCES

1. Spectrum Laboratories, Chemical Fact Sheet – CAS # 100027 http://www.speclab.com).
2. The International Programme on Chemical Safety (IPCS), Concise International Chemical Assessment Document 20 (CICAD), Mononitrophenols.
3. Y.S. Li, Y.H. You, E.T. Lien, *Arch. Environ. Contam. Toxicol*., **1999**, *4*, 427-433.
4. J-P. Arcangeli, E. Arvin, *Wat. Sci. Technol*., **1995**, *31*, 117-128.
5. B. Koumanova, Z. Kircheva, *J. Univ. Chem. Technol. Met*. (Sofia), **2003**, *1*, 71-78.
6. M. Salaices, B. Serrano, H.I. de Lasa, *Chem. Eng. J*., **2004**, *59*, 3-15.
7. S. Nouri, F. Haghseresht, G.Q. Max Lu, *Adsorption*, **2002**, *8*, 215-223.
8. J-M. Chern, Y-W. Chien, *Wat. Res*., **2002**, *36*, 647-655.
9. R-S. Juang, R-L. Tseng, F-C. Wu, *Adsorption*, **2001**, *7*, 65-72.
10. A. A.M. Daifullah, B.S. Girgis, *Wat. Res*., **1998**, *4*, 1169-1177.
11. J.F. Garcia-Araya, F.J. Beltran, P. Alvarez, F.J. Masa, *Adsorption*, **2003**, *9*, 107-115.
12. M. Jitaru, L.R. Mandoc, C. Mihai, O.Tudoran, *Studia Universitatis "Babes-Bolyai" Chemia,* **2005**, *L1,*137-142.
13. K. Rajeshwar, J. Ibanez, *Environmental Elecrochemistry Academic Press,* 1997, 89p.
14. A.M. Polcaro, A. Vacca, S. Palmas, M. Mascia, *J. of Appl. Electrochem.*, **2003,** *33*, 885-892
16. F. Kormos, C. Roman, M. Pávai, E. Kálmán et Maria Jitaru, *Table Ronde, Chisinau, Republica Moldova, mai **2005**, Cahier ELCONDES*, Ed. Casa Cartii de Stiinta, Cluj-Napoca, **2005,** p. 195-200, ISBN 973-686-712-9.

STUDIA UNIVERSITATIS BABES - BOLYAI, CHEMIA, LI, 2, 2006

Dedicated to professor Gh. Marcu at his 80th anniversary

ON THE DEPOLLUTION OF SOME RADIOACTIVE EFFLUENTS

K. POPA, D. HUMELNICU, M. RĂILEANU, R. CALMOI, AL. CECAL*

ABSTRACT. In this review, parts of our recent analyses in the depollution of the radioactive wastewaters are reported. The studies were focused in two main directions: (1) laboratory analyses on biodepollution of low radioactive waste waters, both in the absence and in the presence of the ionic competition and (2) chemical treatment of the radioactive waste waters using microporous titanosilicates and calix[4]arene/ *p*–(*tert*–butyl)calix[4]arene. In some cases, different aspects of the chemical reactivity, the kinetic of the reactions and the thermodynamic properties are presented.

1. Introduction

The problems of environmental radioactivity pollution are of crucial concern to state and local authorities responsible for environmental protection and control of nuclear wastes and weapons. In principle, there are two sources of environmental radioactivity, namely natural and manmade [1].

The pathways of radionuclides through the environmental waters are extremely complex. Transportation by water contaminates soils and water sources (rivers, lakes and the sea), many of which are situated far away from the release point. This is why in the Laboratory of Radiochemistry of "Al.I. Cuza" University of Iaşi a reinforced research in this matter started about ten years ago.

2. Recent analyses of bioaccumulation using plant species and microorganisms

Application of bacteria, fungi, algae or even plants to clean up surface and ground water contaminated by radionuclides has been increasingly applied. Hence a large number of studies on bioaccumulation or biosorption of $^{51}Cr^{3+}$, $^{60}Co^{2+}$, $^{90}Sr^{2+}$, $^{137}Cs^{+}$, $^{204}Tl^{+}$, Th(IV), U(VI) from liquid wastes on different biocollectors has been reported.

2.1. Bioaccumulation of uranium using different strains of Saccharomyces cerevisiae

Under conditions of a natural aqueous systems, the insoluble uranium rapidly corrodes forming yellow uranyl compounds, where the linear $[O=U=O]^{2+}$ entity forms the characteristic structural elements. Most notably, the solution chemistry of

* *"Al.I. Cuza" University, Department of Inorganic and Analytical Chemistry, 11–Carol I Blvd., 700506–Iasi, Romania; tel: +40-232-272478, fax: +40-232-201313, e-mail address: cecal@uaic.ro*

U(VI) is relatively complex, with numerous mono– and polynuclear uranyl–hydroxide and uranyl–carbonate complexes being formed.

The possibility of bioaccumulation of uranium species in beer yeast was investigated [2]. The behaviour of the *S. cerevisiae* – UO_2^{2+} system was studied versus contact time, pH and anion nature without ionic competition. Analysis of the obtained data revealed the following optimal working conditions: 1 h contact time, pH = 6.5 and 0.1 M $UO_2(CH_3COO)_2$ solution as uranyl source; as result, the maximum degree of bioaccumulation attends a value nearly 8.75 mmol UO_2^{2+}/g yeast. Both scanning electron microscopy and amino acid determinations lead to the conclusion that the uranyl nitrate solution may devastate the yeast cells provoking membrane damage and the release of the cell constituents (including the bioaccumulated uranium species).

However, in natural contaminated waters, the uranium series decay products and the non-radioactive cations influence uranium bioaccumulation process. Consequently, five different strains of *S. cerevisiae* were tested to analyze the bioaccumulation of U(VI) from waste water containing competitive ions [3]. Samples of water passing out from a previous uranium mill were used. The accumulation capacities of the tested strains were different. The kinetics of bioaccumulation, the leaching degree, the influence of cell density and their origin were analyzed. Under the applied working conditions, more then a half of the total activity could be accumulated after 1 h contact time of 1 ml *S. cerevisiae* suspension and 5 ml of water. The heavy metals effectively competed the uranium accumulation.

2.2. Decontamination of radioactive liquid wastes by hydrophytes vegetal organisms

The bioaccumulation of some radioactive ions from contaminated waste solutions, on hydrophytic vegetal organisms. In order to follow the distribution of radioactive ions $^{51}Cr^{3+}$ [4], $^{60}Co^{2+}$, $^{137}Cs^{+}$ [4,5] and $^{65}Zn^{2+}$ [6] in various cell components extracted from *Spirulina platensis, Porphiridium cruentum, Scenedesmus quadricauda, Lemna minor, Elodea canadensis, Pistia stratiotes*, *Riccia fluitans* and *Azolla caroliniana* the plants were "cultivated" in radioactive solutions.

The formed complexes were extracted with acetone or acetic acid and were chromatographically separated. The results show an intense activity of the polysaccharide and lipoid fractions in the bioaccumulation process. The unusually high removal activity of lipids was probably due to the partial hydrolysis into the fatty acids and triglycerides, with a greater chelating action of the cations. An example of thin layer radiochromatography experiment is presented in Fig. 1.

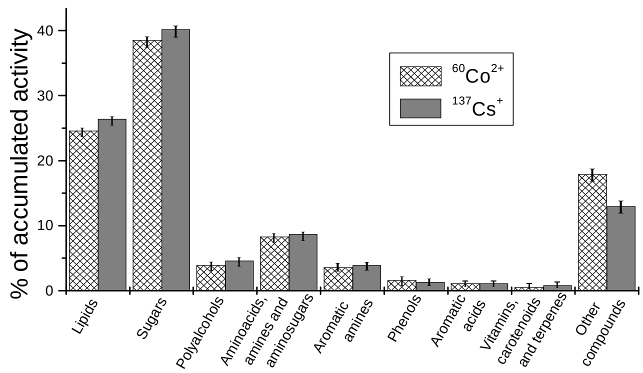

Fig. 1. The amount of $^{137}Cs^{+}$ and $^{60}Co^{2+}$ – radioactive ions localized in different biochemical components of the living fern *Azolla caroliniana* Willd.

3. Chemical treatment of the low radioactive wastewaters

3.1. Sorption of $^{60}Co^{2+}$, $^{115}Cd^{2+}$, $^{137}Cs^{+}$ and $^{204}Hg^{2+}$ on ETS-4 and ETS-10 microporous titanosilicates

ETS-4 (synthesized from gel with following molar composition: 2.0Na_2O: 0.3TiO_2: 0.6KF: 2.56HCl: 1.49SiO_2: 39.5H_2O) and ETS-10 (synthesized from gel with following molar composition: 1.0Na_2O: 1.49SiO_2: 0.2TiO_2: 0.6KF: 1.28HCl: 39.5H_2O) were subjected to sorption of radioactive cations $^{60}Co^{2+}$, $^{115}Cd^{2+}$, $^{137}Cs^{+}$ and $^{204}Hg^{2+}$ from aqueous solution, in the absence of ionic competition [7,8]. The uptake of these radiocations was compared by means of the distribution coefficient (K_d) versus contact time, determining their cationic exchange capacity at equilibrium.

Table 1.

The distribution coefficients of $^{60}Co^{2+}$, $^{115m}Cd^{2+}$ and $^{203}Hg^{2+}$ on ETS-4 and ETS-10 titanosilicates.

Radioactive ion	Temperature, K	K_d, ml/g	R, meq/g
$^{60}Co^{2+}$	277	436	3.03
	293	733	4.23
	313	760	4.31
$^{115}Cd^{2+}$	277	631	3.87
	293	791	4.43
	313	811	4.48
$^{137}Cs^{+}$	277	1258	3.83
	293	1636	4.50
	313	1670	4.55
$^{204}Hg^{2+}$	277	341	2.54
	293	627	3.85
	313	808	4.45

For all sorption systems and the considered radiocations, a rapid increase of K_d in the first minutes of contact can be observed. The higher the exchange temperature, the higher the value of K_d; further, the equilibrium value is established more quickly. The maximum sorption capacity at equilibrium, stated in ml/g (K_d) and meq/g (exchange capacity – R), are summarised in Table 1. The values of ΔH^o, ΔS^o and ΔG^o for the considered sorption systems were given in Table 2.

Table 2.

Thermodynamic parameters for the sorption of $^*M^{n+}$ radiocations on ETS-4 and ETS-10 titanosilicates.

Cation	Titanosilicate	K_d, cm^3/g			
		277 *K*	293 *K*	313 *K*	333 *K*
Co^{2+}	ETS-4	536	593	625	649
	ETS-10	436	733	760	-[b]
Cd^{2+}	ETS-4	583	651	693	750
	ETS-10	631	791	811	-[b]
Hg^{2+}	ETS-4	644	778	801	810
	ETS-10	341	627	808	-[b]

3.2. Use of some calixarenes as cleaning agents for low radioactive waste waters

Calixarenes are products of the condensation of phenol *p*–substituited with formaldehyde in an alkaline medium. One of the most important practical applications of this class of compounds is the environmental decontamination of waters containing ions of the heavy metals like Cs^+, Ag^+, Au^+, Hg^{2+}, Pb^{2+}, Cd^{2+} etc.

In order to clean some low radioactive contaminated waters containing β+γ–active cations ($^{55+59}Fe^{3+}$, $^{60}Co^{2+}$, $^{65}Zn^{2+}$ and $^{137}Cs^+$), calix[4]arene and *p*–(*tert*–butyl)calix[4]arene has been used [9]. Experiments were performed in the absence of ionic competition, at 277, 293 and 313 K. Whatever the temperature and the sorbent used, the capacity of retaining the β+γ–active cations varies as follows: $^{55+59}Fe^{3+} > ^{60}Co^{2+} \geq ^{65}Zn^{2+} > ^{137}Cs^+$ (the capacity of sorption decreases with the increasing ionic radius and decreasing cationic valence).

In the uranium case, the interaction is a chemical one, a new 1:1 UO_2^{2+}: *p*–*tert*–butylcalix[4]arene complex being synthesised [10] in acetone. The combination metal: ligand ratio was determined by mass spectrometry and by the Job method. The chemical binding of uranium was proved by FT–IR spectroscopy and by a leaching study. The mass spectrum of the UO_2^{2+}:*p*–*tert*–butylcalix[4]arene complex (Fig. 2) indicates that the molecular peak appears at m/z = 908 a.m.u. which correspond to a combination ratio M:L = 1:1 (650÷700 K). The most intense peaks appears at m/z = 56 a.m.u. (solvent) and m/z = 648 a.m.u. (p–*tert*–butylcalix[4]arene ligand). Although other significant peaks do not appear in the 648÷908 u.a.m. m/z range, we cannot conclude that the prepared compound is pure, because a part of ligand may be still unreacted.

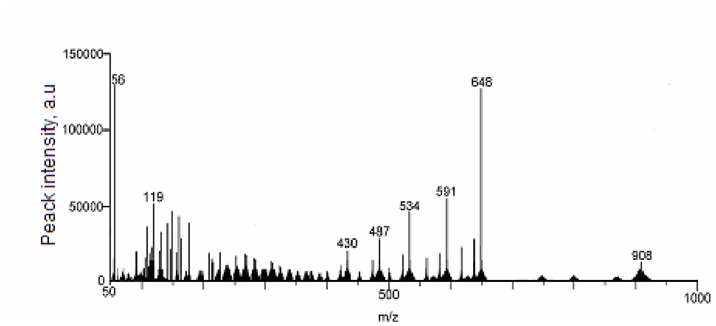

Fig. 2. Mass spectrum of the 1:1 UO_2^{2+}:p–*tert*–butylcalix[4]arene complex.

Acknowledgement

The authors would like to acknowledge MEdC/CNCSIS-Romania for financial support.

REFERENCES

1. R. Tykva, D. Berg, "Man–made and natural radioactivity in environmental pollution and radiochronology, Kluwer, Dordrecht", 2004.
2. K. Popa, Al. Cecal, G. Drochioiu, A. Pui, D. Humelnicu, *Nukleonika,* 2003, **48** 121-125.
3. R. Tykva, *Nukleonika,* 2004, **49**, S3-S6.
4. Al. Cecal, K. Popa, V. Potoroaca, N. Puica-Melniciuc, *J. Radioanal. Nucl. Chem.,* 2002, **251**, 257-261.
5. K. Popa, Al. Cecal, D. Humelnicu, I. Cărăuş, C.L. Drăghici, *Cent. Eur. J. Chem.*, 2004, **2**, 434-445.
6. Al. Cecal, K. Popa, I. Cărăuş, V. Potoroacă, *Isot. Environm. Health S.,* 2002**, 38,** 33-37.
7. C.C. Pavel, K. Popa, N. Bîlbă, Al. Cecal, D.G. Cozma, A. Pui, *J. Radioanal. Nucl. Chem.,* 2003, **258,** 243-248.
8. K. Popa, C.C. Pavel, N. Bîlbă, Al. Cecal, *J. Radioanal. Nucl. Chem.,* 2006, **269,** in print.
9. Al. Cecal, K. Popa, I.I. Crăciun, I. Neda, *Czech. J. Phys.,* 2003, **53**, A557-A562.
10. K. Popa, M. Răileanu, T. Timofte, Al. Cecal, *Anall. St. Univ. Al.I.Cuza – Iasi S. Chem.,* 2003, **11**, 22-27.

Dedicated to professor Gh. Marcu at his 80th anniversary

INHIBITORY EFFECT OF METOPROLOL UPON CATALASE–H_2O_2 DECOMPOSITION, USED AS A POTENTIAL KINETIC METHOD TO DETERMINE THE DRUG CONCENTRATION

FLORINA POGACEAN*, IOAN BALDEA* AND FLORIN TURBAT*

ABSTRACT. The enzyme catalyzed process of decomposition of hydrogen peroxide has been investigated by means of a Clark oxygen sensor, in the presence and absence of various concentrations of Metoprolol – a β-blocker drug - having an inhibiting role. The Michaelis – Menten kinetic parameters of H_2O_2-catalase reaction have been determined from Lineweaver-Burk plots. The inhibition pattern we have deduced, suggested by the Lineweaver - Burk plots, corresponds to a fully mixed inhibition mechanism. Inhibition constants K_I and $K_I^{'}$ were determined. The inhibitory effect can be used to determine metoprolol in low concentrations by a kinetic method.

Keywords: Metoprolol, Catalase, Hydrogen peroxide decomposition, Inhibition mechanism, Kinetic methods of analysis.

INTRODUCTION

Inhibitors of enzymatic reactions have acquired large applications in medical and pharmaceutical research [1]. The catalase mediated decomposition of H_2O_2:

$$2H_2O_2 \xrightarrow{catalase} 2H_2O + O_2 \qquad (1)$$

has been the subject of extensive investigations both with regard to the kinetics and to the mechanism of the reactions.[2, 3, 4, 5]

Similar reactions were also observed for other organic peroxides [6, 7] Well-known inhibitors of these reactions are ions like azide, cyanide and fluoride [8, 9, 10], or some organic compounds like 3-amino-1, 2, 4-triazole [11] atenolol [12] and metoprolol [13].

Catalase is widely distributed in nature. It is found in all aerobic microorganisms, in plant and animal cells [14]. The catalase activity of mammalian tissues varies greatly: it is highest in liver and kidney and low in connective tissues. The enzyme, when located in organelles, acts as a regulator of the H_2O_2 level, while in erythrocytes, catalase provides protection for hemoglobin against the oxidizing agents like H_2O_2 together with gluthathione peroxidase [16].

* *Department of Chemistry and Chemical Engineering, Babes-Bolyai University of Cluj, 11 Arany Janos Str.,Cluj-Napoca 400028*

Inhibitors are compounds that slow down the activity of the enzyme by preventing either the formation of substrate-enzyme or breaking down enzyme-product complexes.

Metoprolol ($C_{34}H_{56}N_2O_{12}$) is a cardioselective β-adrenoceptor blocking agent (β-blocker). Its formula is (±)-1-isopropyl-amino-3-p-(2-methoxyethyl)- phenoxypropan-2-ol(2R,3R)-tartrate with number 56392-17-7, in accordance to British Pharmacopeia[17],

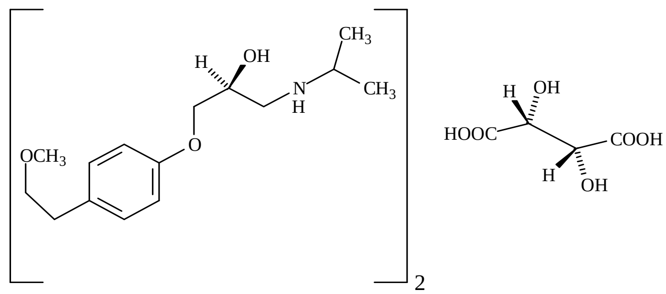

This agent is used in clinical medicine for the treatment of various diseases including hypertension, pectoral angina, cardiac aritmia, and especially ventricular tahicardic and hart attract, [18, 19, 20]

A number of analytical methods have been developed for its determination including spectrophotometrical [21], potentiometrical and amperometric methods [22, 23, 24]. The purpose of this work is to establish the type of inhibition for this reversible inhibitor by it effect on the rate of hydrogen peroxide decompositions catalyzed by catalase.

EXPERIMENTAL

Equipment. The measurements were undertaken with a Clark oxygen sensor, attached to a Multiline P4 multimeter with automatic data acquisition on a PC. The sensors cover a measuring range from 0 up to 19.99 mg/L for the dissolved oxygen, with a resolution of 0.01 mg/L and an accuracy of ±0.5% from 5.30 ℃. All experiments were performed in a vessel provided with a water jacket. To maintain a constant temperature value (20±0.1 ℃) it was connected to a Falc 90 rec irculation water bath. The reaction mixture was stirred during the run with a magnetic stirrer, always with the same frequency.

Reagents and solutions. We used bacterial catalase from *Micrococcus Lysodeikticus* 176340 U/ml (where the enzyme unit 1U is the amount of enzyme needed to transform 1 μmol of the substrate within 1 min, under standard conditions), from FLUKA with a purity index of 0.85, which came from the ratio of absorbance at 405 nm and 280 nm, A_{405}/A_{280}.The molar concentration of catalase was determined spectrophotometrically at 407 nm, where the molar absorptions coefficient is known to be $4x10^5$ mol^{-1} dm^3 cm^{-1} [21].

All the other reagents were of analytical reagent grade. The solutions were prepared with de-ionized, four-times distilled water in order to avoid the interference of heavy metals. Stock solutions of catalase ($9x10^{-10}$ mol/L), H_2O_2 (4.9 x 10^{-2} mol/L) and metoprolol (10^{-5} mol/L) in phosphate buffer of pH=7.0 were freshly prepared before each set of runs. Hydrogen peroxide has been standardized against potassium permanganate in acidic media.

Procedure. The reaction mixture of 10 mL volume was prepared directly in the reaction vessel connected to a thermostat. All the solutions of the reagents were kept in the water bath. Measured volumes of buffer and metoprolol stock solution were placed in the vessel, and the change in the concentration of oxygen was monitored while the mixture was continuously stirred. The oxygen content of the solutions became constant after about 50 s, when a known volume of H_2O_2 stock solution was added. After about 50 s the concentration of oxygen reached a constant value. Now, the catalyzed reaction was started by a quick adding of 2 mL of the enzyme stock solutions by means of syringe. A typical oxygen concentration versus time curve obtained by monitoring the reaction with a Clark sensor is presented in Fig. 1. The rate has been measured after the introduction of the enzyme solution into the mixture as the slope of the oxygen concentration increase with time. Only the starting period, within 25 – 30 % of reaction, with a linear dependence has been considered. The degree of H_2O_2 transformation was calculated from the experimental measured oxygen concentration as

$$X = \frac{2[O_2]_t - [O_2]_0}{[H_2O_2]_0} \qquad (2)$$

where $[O_2]_t$ is the actual concentration of O_2, and $[O_2]_0$ is the constant value of $[O_2]$ obtained after the addition and consumption of the whole amount of H_2O_2.

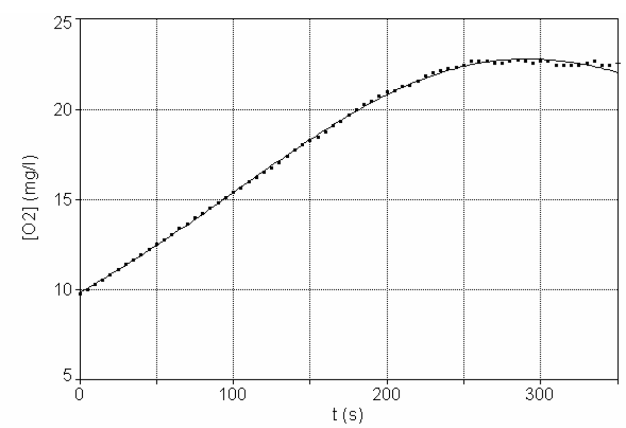

Fig. 1. A typical curve for O_2 evolution, recorded with the Clark sensor in the reaction mixture pH=7 at 20^0C

RESULTS AND DISCUSSION

A large amount of information is available in the literature concerning the kinetics and the mechanism [4, 26, 27, 28] of the reaction in the absence of inhibitor. Although the catalase-H_2O_2 complex formed in the first step of the reaction interacts with another hydrogen peroxide molecule [29] and some exchange of the valence state of iron ion takes place, we obtained a Michaelis behavior of the over-all reaction (1) with the initial rates.

The initial reaction rates were determined from the slopes of the early part of the O_2 evolution curves, after catalase addition. According to the well-known Michaelis-Menten equation [30]

$$r_0 = \frac{k[E_0][S]}{K_M + [S]} = \frac{r_{max}[S]}{K_M + [S]} \quad (3)$$

where $[E]_0$ and [S] stand for the initial concentration of the enzyme and for the substrate concentration respectively, K_M and r_{max} are the Michaelis-Menten parameters, and k is the rate constant of breakdown of the enzyme substrate complex to the product. This equation can be brought into the double-reciprocal form:

$$\frac{1}{r_0} = \frac{1}{r_{max}} + \frac{K_M}{r_{max}} \cdot \frac{1}{[S]} \quad (4)$$

and used to obtain the Lineweaver-Burk plots [31]. The value of the Michaelis-Menten constant K_M= 4.55x10^{-4} mol/L and the maximum velocity r_{max}=5.11x10^{-2} mol L^{-1} s^{-1}, obtained by us, are comparable to those mentioned in literature[32]. And dose to those determined in our previous study. [12]

The influence of metoprolol on the enzyme-catalyzed decomposition of hydrogen peroxide .Several kinetic runs performed in the presence of different concentrations of metoprolol proved the inhibitory effect of this compound. When the concentration of H_2O_2 was varied at several chosen concentrations of metoprolol, Lineweaver-Burk plots for the inhibited reaction

$$\frac{1}{r_{o(I)}} = \frac{1}{r_{max(I)}} + \frac{K_{M(I)}}{r_{max(I)}} \cdot \frac{1}{[S]} \quad (5)$$

resulted in a family of straight lines (Fig. 2), which have a common intersection point on the left side of the ordinate and below the abscissa.

Table 1

Equations of Lineweaver-Burk plots for different concentration of metoprolol

$[Metoprolol]_0$x10^7 (mol/L)	Intercept (L.s/mol)	Slope (s)
0	19.538	0.0089
1	23.147	0.0095
2	27.150	0.0099
3	37.120	0.012

As the slopes of Lineweaver- Burk plots depend on the inhibitor concentration, a systematic study could lead to a kinetic method of determination of this inhibiting agent concentration. The Michaelis-Menten parameters in the presence of the inhibitor were determined from the parameters of the lines in figure 2. Their values are given by the equations (6):

$$r_{max(I)} = r_{max}\frac{1+\beta\frac{[I]}{K'_I}}{1+\frac{[I]}{K'_I}} \quad \text{and} \quad K_{M(I)} = K_M\left(\frac{1+\frac{[I]}{K_I}}{1+\frac{[I]}{K'_I}}\right) \tag{6}$$

where: K'_I and K_I are the dissociation constants of the enzyme – substrate - inhibitor complex, ESI, and the enzyme. inhibitor complex, EI. The constant β is equal to zero for full inhibition, while for partial inhibition 0< β≤1. Lineweaver- Burk plots of Fig. 2 correspond to the inhibition pattern of either full or partial mixed inhibitors [33].

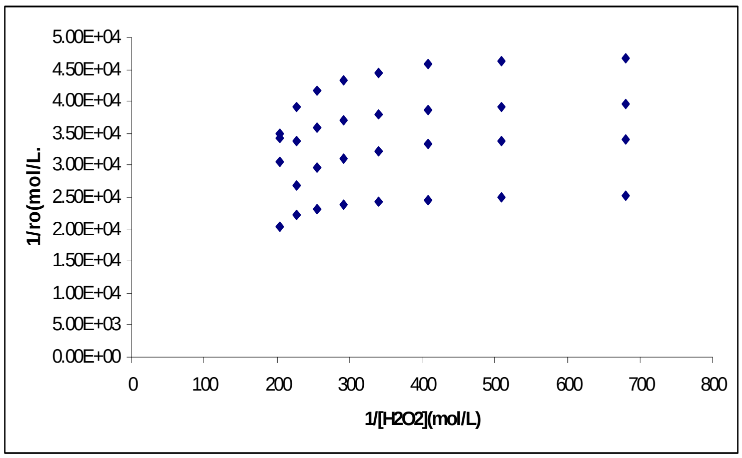

Fig.2. Lineweaver Burk plots obtained for different concentration of metoprolol

In order to distinguish between full and partial inhibition, the slopes and intercepts from the primary Lineweaver- Burk plots were re-plotted against the corresponding inhibitor concentration. They are presented in figure 3. Both plots gave straight lines. This behavior is considered as typical for full inhibition [24]. Considering the possibility of a partial inhibition, a non-linear fit of the intercept $1/r_{max(I)}$=f([I] and the slope $K_{M(I)}/r_{max(I)}$=f [I] gave negative values for β. Therefore it is very likely that metoprolol acts as a reversible full mixed inhibitor according to the reaction scheme 1

The plot (Fig.3) of slopes and intercepts respectively, against the inhibitor concentration were used to determine the dissociation constants mentioned in the scheme above, $K_I=8.86\text{x}10^{-7}$ M for EI complex and $K'_I=3.04\text{x}10^{-7}$ M for ESI complex . The constant K_I was obtained from the slope of the $K_{M(I)}/r_{max(I)}$ versus [Metoprolol] graph:

$$K_I = \frac{K_M}{r_{max}\cdot slope} \tag{7}$$

while the K'_I constant was determined from the slope of the $1/r_{max(I)}$ versus [metoprolol] graph:

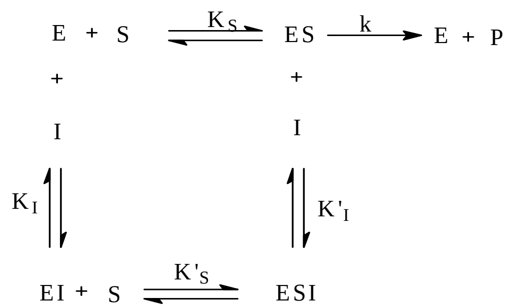

Scheme 1. Mixed inhibition mechanism for metoprolol, where E stands for catalase, S for hydrogen peroxide and I for metoprolol.

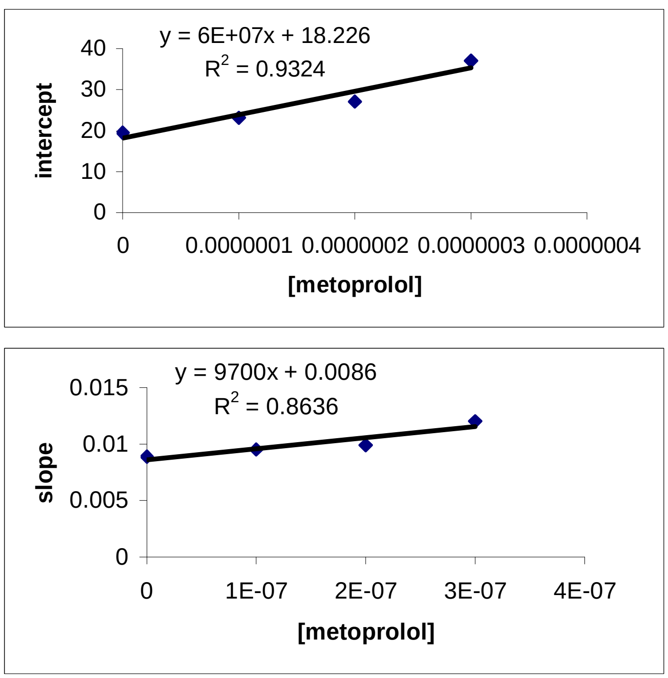

Fig 3. The plot of intercepts and slopes versus the inhibitor concentration

$$K'_I = \frac{1}{r_{max \cdot slope}} \tag{8}$$

Table 2

Mean values of $r_{max(I)}$ and Michaelis constant in the presence of the inhibitor $K_{M(I)}$

$[Metoprolol]_0 \times 10^7$(mol/l)	$r_{max(I)} \times 10^2$(mol/Ls)	$K_{M(I)} \times 10^4$(mol/L)
0.00	5.11	4.55
1.00	4.32	4.10
2.00	3.68	3.64
3.00	2.69	3.23

Kinetic method for the determination of metoprolol

We tried to exploit the inhibitory effect of metoprolol, upon the catalytic reaction of catalase, for the determination of this compound by means a kinetic method.The method consist in the monitoring of the oxygen evolution by means of Clark sensor The results were employed to obtain a calibration graph of initial rate against metoprolol concentration at fixed concentration of H_2O_2 and catalase. The graph exhibit a non linear aspect as described by the equation (9) and presented in figure 4.

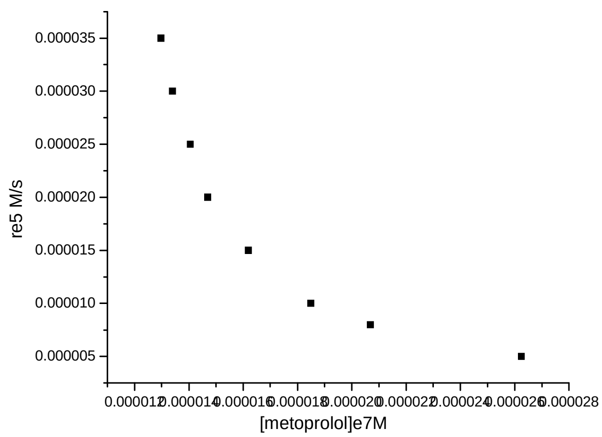

Fig 4. Calibration graph for metoprolol

$$r_{(I)} = \frac{r_{max} \cdot [S]}{\frac{K_M}{K_I} \cdot [(K_I + [I]) + [S \cdot (K'_I) + [I]]]} \qquad (9)$$

Its linear form is presented in figure 5.

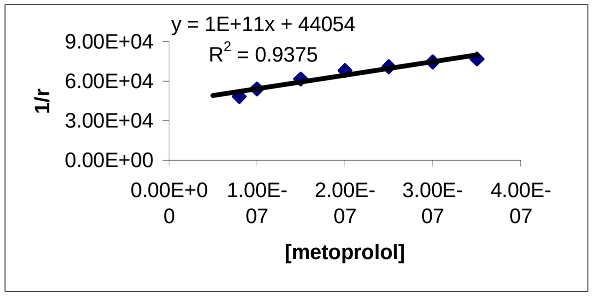

Fig 5. Linear calibration for metoprolol

It is obvious that heavy metals ions (Cu^{2+}, Fe^{3+}, Zn^{2+}, Ni^{2+}) will influence the reaction rate, because they have a catalytic effect on the decompositions of H_2O_2, but according to the literature there are many organic compounds (especially aromatic compounds) that may interfere too, because they act as inhibitors of catalase, including: naphthalene, 2-naphthol, 2- naphthalene-sulfonic acid, benzene, phenol, benzenesulfonic acid, menthol, inositol, biotin, procaine, sulfanilamide, pyridoxine, folic acid, aminopterin,and riboflavine [34]

Further sturdy will elucidate the potential interference on this kinetic method.

CONCLUSIONS

The catalase –catalyzed decomposition of hydrogen peroxide in phosphate buffer was studied in the presence of metoprolol. The metoprolol acts like a fully mixed inhibitor, as observed from Lineweaver-Burk plots.

Michaelis Menten parameters were determined for the decomposition of H_2O_2 in the present of catalase yielding the values of K_M =4.55x10^{-4} mol/L and

$$r_{max}=5.11x10^{-2}mol/L^{-1}s^{-1}$$

Linear dependence of the slope and respectively intercept of Lineweaver-Burk linearisations from metoprolol concentration indicates a fully mixed inhibition mechanism.

A kinetic method was suggested for the determination of metoprolol according to its inhibitory effect.

REFERENCES

1. K.Yoshihiro, S. Yoshiyuki, H. Jingyi, K. Takahiro, J. Chem.Soc. Perkin Trans, **1995**, 2, 1749-1759
2. P.Nicholis, G.R. Schonbaum, P.D. Boyer, H. Lardy, K. Myrback, The Enzymes, Acad. Press. New York, **1963**, 8 , p 147

3. A. S. Brill,Comprehensive Biochemistry, Ed M.Florkin , E . Stotz, Elsevier, Amsterdam, **1966**,14, p 447
4. P. Jones, A Suggett, *Biochem J*., **1968**, 110, 617-620
5. P. Jones, H. B. Dunford, J. Theor. Biol., **1977**, p 457
6. K.Kikuchi, Y. Kawamura-Konishi, H.Suzuki, *Arch. Biochem. Biophys*, **1992**, 296, 88-94.
7. M.L.Kremer, *J.Chem. Soc., Faraday Trans*. **1985**, 1, 81,91-104
8. M.L.Kremer, *J.Phys Chem*. **1981**, 85, 835-839
9. B. Chance, J. Biol., Chem. **1949**, 179, 1299-1309
10. Y. Ogura, Y. Tonomura, S.Hino, H. Tamiya, *J. Biochem*-Tokyo, **1950**, 37, 153-177.
11. E. Margoliash, A. Novogrodsky, *Biochem J*, **1958**, 468-475
12. F. Pogacean, I. Baldea, F Turbat, Studia Univ. BB. Chem. 51(1) **2006**, 67 - 76
13. R. F.Stack, L. D. Paul, D. Springer, T. Kraemer, Biochem. Parmacol., **2004**, 15, 235
14. A. Deisseroth, A.L.Dounce, Physical and Chemical Properties, Mechanism of Catalysis and Physiological Role*, Physiol Rev*. **1970**, 50, 319-375.
15. B. Chance H.Sies, A. Boveris, *Physiol Rev*., **1979**, 59, 527-605
16. G. R. Schonbaum , B. Chance Catalase ,The Enzymes , Third Editions, 13, Acad pres, New York, **1976**, 363-408
17. *** British Pharmacopeia, London, **1992**
18. O. E. Brodde, H. K. Kroemer, Arzneimittelforschung, **2003**, 53, 814
19. A. Sharma, B. A. Hamelin, Curr. Drug. Metab., **2003**, 4, 105
20. J. Robertson, J. L. Fryer, D. L. O'Connerll, A. Spogis, D. A. Henry, Med. J. Aust., **2001**, 175, 407
21. F Dragan, S. Bungau, M. M. Dragan, Rev. Med. Oradeana, **2003**, 10, 31
22. B.G. Milagres, G. Oliveira, L.T. Kubota, H. Yamanaka, Anal.Chim. Acta., **2000**, 347, 35-41
23. R.I.L. Catarino, M.B.Q. Garcia, R.A.S. Lapa, J.L.F.C. Lima, L. Barrado, J.AOAC Int., **2002**, 347, 35-41
24. M.S.M.Quitino D. Corbo, M. Bertotti, L. Angnes, Talanta, 2002, 58, 943-1346
25. P. Jones, A Suggett, *Biochem J*., **1968**, 108, 833-938.
26. DP. Nelson, LA. Kiesow, *Anal. Biochem*, **1972**, 49, 474-478
27. P.Jones, Wynnes-Jones WFK, *T.Faraday Soc*.,**1972**, 49, 474-478
28. ML Kremer, *J. Chem. Soc Farad T* ,**1983**, 79, 2125-2131
29. B. Change Enzyme mechanism in living cell ***A Symposion on Mechanism of Enzyme Action, Ed. W. McElroy and B. Glass, John Hopkins Press Baltimore, **1954,** 399-453.
30. L. Michaelis ,M. Menten, *Biochem.Z*, **1913**, ,49, 33-369
31. H.Lineweaver, D. Burke, J*. Am. Chem. Soc* ,**1934**, 56, 658-666.
32. JL. Gelpi, JJ.Aviles, M. Busguets, S.Imperial, A. Mazo, A. Cortes, *J. Chem Educ*. ,**1993,** 70,805-816.
33. R. Kellner, J.M. Mermet, M.Otto, H. M. Widmer, Anal. Chem., **1998**, 15-17
34. W.H. Vogel, R. Snyder, M.P. Schulman, J. Pharmacol Exp.Ther, **1964**,146, 66-73

STUDIA UNIVERSITATIS BABES - BOLYAI, CHEMIA, LI, 2, 2006

Dedicated to professor Gh. Marcu at his 80th anniversary

STUDIES ON THE INFLUENCE OF FLUX NATURE ON THE PROPERTIES OF NIOBIUM ACTIVATED YTTRIUM TANTALATE PHOSPHOR

AMALIA MESAROS [1,2], ELISABETH - JEANNE POPOVICI[1], LAURA MURESAN[1], MARIA ŞTEFAN[1,2], RODICA GRECU[1] AND MARILENA VASILESCU[3]

ABSTRACT. Niobium activated yttrium tantalate ($YTaO_4$:Nb) presents good X-ray absorption and emits in the blue region of the spectrum. The goal of the paper is to study the influence of flux nature on the crystalline structure, morphology and luminescent characteristics of $YTaO_4$:Nb powders. Phosphors samples were prepared by solid state reaction route and theirs properties were investigated by X-ray diffraction (XRD), Fourier transform infrared spectroscopy (FTIR), photoluminescence (PL) measurements and scanning electron microscopy (SEM).

Keywords: yttrium tantalate, phosphors, luminescence, X-ray imaging

INTRODUCTION

Niobium activated yttrium tantalate, $YTaO_4$:Nb is an efficient luminescent material used in medical X-ray imaging applications[1,2]. The characteristic emission spectra consist in a broad band situated in the UV-blue domain of the electromagnetic spectrum with a maximum at 390-410 nm. Performances of $YTaO_4$:Nb phosphor powder are correlated with the crystalline structure, particle size, morphology and luminescence properties.

It is well known that the emission intensity and colour purity of $YTaO_4$-based phosphor are extremely sensitive to crystalline phase composition of the materials [3-5]. Depending on the synthesis conditions yttrium tantalate present different crystalline structures. There are two polymorphs, i.e. high temperature tetragonal (T-$YTaO_4$ phase, scheelite structure) and low-temperature monoclinic (M-$YTaO_4$ phase, fergusonite structure) forms. There is an additional monoclinic phase, designed as M-prime form (M'-$YTaO_4$) that can be obtained in appropriate conditions,

[1] *"Raluca Ripan" Institute for Research in Chemistry, 30 Fântânele, 400294 Cluj-Napoca, Romania*
[2] *Faculty of Chemistry and Chemical Engineering "Babes-Bolyai" University, 11 Arany Janos, 400028, Cluj Napoca, Romania*
[3] *"I.G. Murgulescu" Institute of Physical Chemistry of the Romanian Academy, 202 Spl. Independentei, Bucureşti, Romania*
Correspondence: amaliahristea@yahoo.com

namely below 1450°C. The high luminescence performances of niobium activated yttrium tantalate phosphor are associated with the monoclinic crystalline structure, where M'-$YTaO_4$ represents the equilibrium phase at room temperature.

The preparation of $YTaO_4$: Nb phosphor is usually achieved by solid state reaction route from synthesis mixtures containing different metallic oxide sources. The monoclinic M' crystalline structure of the $YTaO_4$ host lattice**,** as well as the emission centre formation is substantially improved when the thermal synthesis is flux-assisted by some inorganic salts.

The paper presents several aspects referring to the synthesis of niobium activated yttrium tantalate phosphor ($YTaO_4$: Nb). The influence of the flux nature on the crystalline structure, particle morphology and luminescent characteristics of $YTaO_4$: Nb phosphor is investigated in order to identify an optimal flux reagent that could generate a high performing material.

EXPERIMENTAL PART

Niobium activated yttrium tantalate samples were prepared by solid state reaction route from homogeneous mixtures consisting of raw oxide precursors Y_2O_3 (99.9%), Ta_2O_5 (Optipur), Nb_2O_5 (99%) and Li_2SO_4 (99%) and/or Na_2SO_4 (99%) as flux. The stoichiometric amounts of Y_2O_3, Ta_2O_5, Nb_2O_5 and 30 wt % alkaline sulphates were ball-milled with acetone and dried at 70°C. The powders mixture was calcined in air at 1200°C, for 4 h and slowly cooled to the room temperature. Finally, phosphors samples were water washed, dried and sieved.

The as-prepared phosphors were characterized by fluorescence and FTIR spectroscopy, X-ray diffraction and scanning electronic microscopy.

Photoluminescence (PL) measurements were performed at room temperature, with a Perkin-Elmer 204 Fluorescence Spectrophotometer. The emission spectra were registered under 254 nm excitation and were normalised in comparison with an internal standard. X-ray Diffraction (XRD) analysis was performed on SIEMENS D5000 diffractometer (CuKα radiation). IR absorption spectra were registered on JASCO 610 FTIR Spectrometer (KBr pellets technique). Scanning Electron Microscopy (SEM) analysis was performed using a LEO 1550 microscope.

The interpretation of XRD data was achieved on the basis of powder diffraction files namely, PDF 00-024-1425 for M'-$YTaO_4$, PDF 00-048-0265 for orthorombic-Y_3TaO_7.

RESULTS AND DISCUSSION

Niobium activated yttrium tantalate phosphors ($YTaO_4$:Nb) were obtained by the classic solid state reaction route, from synthesis mixtures containing yttrium oxide and tantalum oxide as generators of the host matrix, niobium oxide as generator of activator ions, and lithium sulphate and/or natrium sulphate as flux. The formation of yttrium tantalate activated with 15 mole % niobium phosphors could be described by the equation (1):

$$Y_2O_3 + (1-x)Ta_2O_5 + xNb_2O_5 \xrightarrow{M_2SO_4, T} 2YTa_{1-x}Nb_xO_4 \quad (1)$$

where: x=0.15

During the thermal synthesis stage, the flux reacts with the mixture of oxides to produce intermediate compounds that are more reactive than the starting oxides. According to the literature, a high calcination temperature facilitates their mutual interaction to give the final product and to regenerate the flux [1,2]. For this reason, the flux compound is considered as catalyst or reactive flux [6].

Photoluminescence (PL) characteristics, crystalline structure, particle morphology and sizes of $YTa_{0,85}Nb_{0.15}O_4$ samples were determined in order to establish the correlation between the phosphors properties and their synthesis conditions.

Luminescence properties

All powder samples are white coloured and exhibit blue luminescence during a 254 nm excitation.

The emission spectra show broad bands with a maximum at around 390 nm (**Fig. 1**). The sample, which was prepared at 12000C with Li2SO4 as flux, presents the highest luminescent intensity. Using a Li_2SO_4 - Na_2SO_4 mixture or Na_2SO_4 as flux, an obvious decrease of the $YTaO_4$: Nb phosphor emission intensity can be observed.

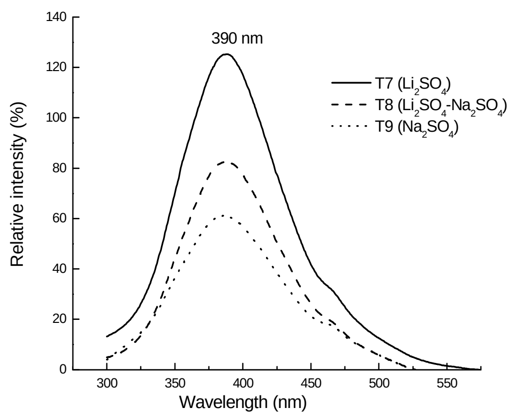

Fig. 1. Emission spectra of $YTa_{0.85}Nb_{0.15}O_4$ samples (λ_{exc}= 254 nm)

The flux-dependence of the luminescence intensity can be partially explained by the crystalline structure or particle morphology and the size of $YTaO_4$-based phosphors obtained in different conditions.

Crystalline structure

The crystalline structure and order degree of phosphors were evaluated on the basis of X-ray diffraction patterns (XRD) and FTIR spectra (**Fig. 2**).

The most homogeneous crystalline phosphor powder was obtained at 1200^0C, by using Li_2SO_4 as flux. Sample T7, $YTaO_4$:Nb [Li_2SO_4; 1200°C] is a single phase material of monoclinic M' polymorph form. Replacing Li_2SO_4 with Na_2SO_4 (sample T9), additional reflections are observed that can be ascribed to some intermediate compounds, such as the orthorhombic Y_3TaO_7. This shows that at 1200ºC, sodium sulphate does not assure the complete conversion of oxides into yttrium tantalate phase.

Mention has to be made that our experimental data for the compounds obtained in the Y_2O_3-Ta_2O_5-Nb_2O_5 system are in good agreement with the literature XRD data for the Y_2O_3-Ta_2O_5 system. This fact evidences that niobium oxide is well dissolved into the $YTaO_4$ crystalline lattice to form the niobium activated yttrium tantalate phosphor, as suggested by the PL spectra.

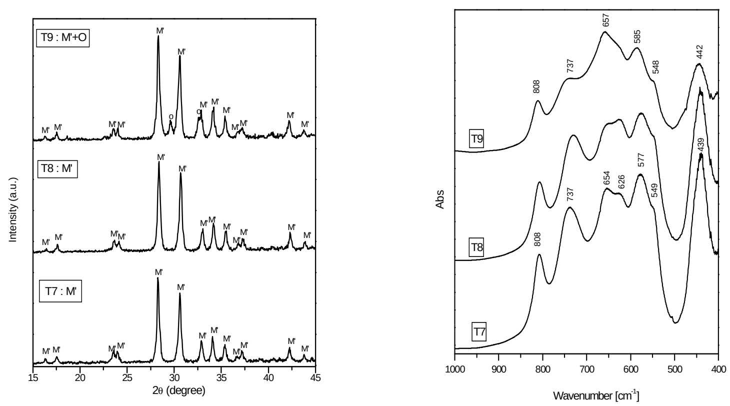

Fig. 2. XRD patterns (left) and FT-IR (right) spectra of $YTa_{0.85}Nb_{0.15}O_4$ samples prepared with different fluxes,T7= Li_2SO_4]; T8= Li_2SO_4+Na_2SO_4; T9= Na_2SO_4 (M'=M'-$YTaO_4$ and O= orthorhombic Y_3TaO_7 structures)

The infrared spectra confirm that flux nature influences the crystalline order degree of phosphors, as it was already illustrated by the XRD patterns. Sample T7 prepared with Li_2SO_4 has a single phase M'- structure, as shown by the well formed 439 and 808 cm^{-1} bands. In sample T9, obtained with Na_2SO_4 as a flux, the M' phase still exists, but the crystalline structure is less organised, as suggested by the FTIR spectra.

For the Y_2O_3-Ta_2O_5-Nb_2O_5 system, Na_2SO_4 shows reduced flux reactivity as compared to Li_2SO_4. This behaviour is responsible for the weakest luminescence emission observed for T9 samples.

Particle morphology and sizes

SEM investigations were performed with the aim to characterize and compare the particle morphology and sizes for $YTaO_4$:Nb powders obtained in different synthesis conditions (**Fig. 3**)

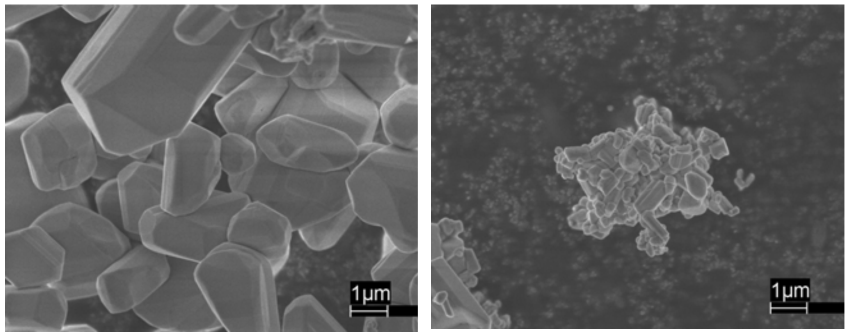

Fig. 3. SEM images of $YTa_{0,85}Nb_{0.15}O_4$ samples prepared with different fluxes: T7 - Li_2SO_4 (left) and T9 - Na_2SO_4 (right)

Using Li_2SO_4 as flux (sample T7), non-agglomerated particles with regular shape are obtained. Most of the polyhedral, elongated crystals are of 2 ÷ 5 μm in length and about 1μm in thickness. The partial or the total replacement of Li_2SO_4 by Na_2SO_4 strongly decreases the particle dimensions. In these conditions, particles with less regulated shape and with aggregation tendency are formed.

The most heterogeneous crystalline powder was prepared with Na_2SO_4, while the most homogeneous powder was obtained with Li_2SO_4 as flux.

Even if Li_2SO_4 (m.p.=884°C) and Na_2SO_4 (m.p.= 860°C) show close melting point values, their behaviour as flux is very different due to the large difference between the two cation sizes. The fact that Li^+ (0.073 nm) is much smaller than Na^+ (0.113 nm) is in the favour of the total conversion of oxides into the M'-$YTaO_4$ crystalline phase.

The general characteristics of $YTa_{0.85}Nb_{0.15}O_4$ phosphors prepared with different fluxes, i.e. the photoluminescence (PL) intensity at peak position, the main crystalline phase and the powder particle dimensions are summarized in Table 1.

Table 1

General characteristics of $YTaO_4$: Nb samples

Phosphor sample	Flux nature (w/w)	General properties		
		PL intensity I_{390} (%)	Crystalline phases	Particle size (μm)
T7	30% Li_2SO_4	125	M'	2.0 ÷ 5.0
T8	15% Li_2SO_4-15% Na_2SO_4	83	M'	0.5÷3.0
T9	30% Na_2SO_4	61	M' + O	0.2÷1.0

where: M' = M'-$YTaO_4$; O = orthorombic-Y_3TaO_7

One can conclude that the highest luminescence intensity of $YTa_{0.85}Nb_{0.15}O_4$ [1200ºC;Li_2SO_4] is associated with the high order degree of the crystalline lattice with M'-$YTaO_4$ structure phase. At 1200ºC, Li_2SO_4 shows the strongest flux reactivity for the Y_2O_3-Ta_2O_5-Nb_2O_5 system.

CONCLUSIONS

The flux nature is an important factor that determines luminescence properties, structural and morphological characteristics of niobium activated yttrium tantalate phosphor. Morphological and structural investigations put in evidence the high crystalline order degree of $YTaO_4$:Nb powders prepared with lithium sulphate as flux. The photoluminescence intensity is strongly affected by the crystalline homogeneity and particle dimensions of the phosphor powders.

REFERENCES

1. L. H. Brixner, *Mater. Chem. Phys*. ***16**,* 253-281, (1987).
2. S. L. Issler and C. C. Torardi, *J. Alloys Comp*. **229**, 54-65, (1995)
3. G. M. Wolten, *Acta Crystallogr*. **23**, 939944, (1967)
4. G. Blasse and A. Brill, *J. Lumin*. **3**, 109-131, (1970)
5. A. Hristea, L. Muresan, E. Indrea, M. Vasilescu and E.-J. Popovici, *SPIE (Bellingham, USA) Proceeding Series*, 781-786, (2004)
6. D. Hedden, C. Torardi and W. Zegarski, *J. Solid State Chem*. **118,** 419-421, (1995)

Acknowledgements

This research was supported by *the Romanian Ministry of Education and Research (CNCSIS Grant 1303/2004; Matnantech 31/2005).* The authors thank to the members of the Department of Materials Chemistry, The Ångström Laboratory of Uppsala University for their help in XRD and SEM measurements.

STUDIA UNIVERSITATIS BABES - BOLYAI, CHEMIA, LI, 2, 2006

Dedicated to professor Gh. Marcu at his 80th anniversary

SPECTRAL INVESTIGATIONS OF EUROPIUM ACTIVATED YTTRIUM OXIDE PHOSPHOR PREPARED BY COPRECIPITATION METHOD WITH OXALIC ACID

LAURA MURESAN[1], ELISABETH - JEANNE POPOVICI[1], AMALIA MESAROS [1,2], MARIA STEFAN[1,2], RODICA GRECU[1] AND EMIL INDREA[3]

ABSTRACT. Europium activated yttrium oxide phosphors were prepared by reagent simultaneous addition technique, using oxalic acid as precipitating reagent. The aim of the paper was to study the influence of the firing conditions on luminescent and morpho-structural properties of Y_2O_3:Eu phosphors. Thermal analysis, X-ray diffraction, SEM, FTIR and fluorescence spectroscopy were used to investigate precursor and phosphor powders. The correlation between the phosphor properties and precursor quality enabled us to select the optimal synthesis conditions.

Keywords: yttrium oxide, phosphors, luminescence; wet chemical method

INTRODUCTION

Europium activated yttrium oxide (Y_2O_3: Eu) is a well-known red emitting phosphor used for applications in displays, optoelectronic devices and fluorescent lamps [1-3]. Phosphor utilisations depend on luminescence performances and powder characteristics that are defined during the synthesis stages. Luminescence characteristics, particle morphology and size or crystalline order degree are factors that determine the use of phosphor powders in optoelectronic devices.

Conventionally, Y_2O_3: Eu powders are prepared from yttrium/europium oxide mixture, by the ceramic method that implies high firing temperature and long thermal treatment periods [4]. Mild thermal synthesis conditions could be used when oxides species are generated from precursors obtained through the wet-chemical preparation route.

The paper presents several results referring to the synthesis of fine powders of Y_2O_3: Eu phosphor from yttrium/europium oxalate precursor obtained by the wet chemical route. The co-precipitated precursor was prepared by using the reagent simultaneously addition technique –*SimAdd* developed in our previous works [5-7].

---

[1] "Raluca Ripan" Institute for Research in Chemistry, 30 Fântânele, 400294 Cluj-Napoca, Romania
[2] Faculty of Chemistry and Chemical Engineering "Babes- Bolyai" University, 11 Arany Janos, 400028, Cluj Napoca, Romania
[3] National Institute for R&D for Isotopic and Molecular Technologies, Donath 71-103,400293, Cluj-Napoca, Romania
Correspondence: ella-m@email.ro

In this purpose, europium containing yttrium oxalate based precursor was obtained under well controlled precipitation conditions from yttrium-europium nitrate and oxalic acid solutions and was converted into phosphors in different thermal treatment conditions. Spectral investigations as well as scanning electron microscopy (SEM) and thermal analysis were used for precursor and phosphors characterisation. A correlation between the preparation conditions and precursor and phosphors characteristics was established in order to improve the *SimAdd* technique for the obtaining of fine powders of europium activated yttrium oxide phosphors.

EXPERIMENTAL PART

Europium activated yttrium oxide phosphors (Y_2O_3: Eu (3 mol%)) were prepared from yttrium-europium oxalate precursor.

Yttrium-europium precursor (sample code PG26) was prepared by the wet chemical method, using the simultaneous addition (*SimAdd)* technique of reagents into a bottom solution. Equal volumes of oxalic acid (0.45M) as precipitating reagent and yttrium-europium nitrate solution (0.30M) were simultaneously added, with equal constant flow (~5.7 mL min^{-1}), into a diluted solution of oxalic acid. Precipitation was carried out at 80^0C, under continuous stirring and pH monitoring. During the precipitation stage, the pH of the bottom solution was adjusted with ammonia to 2. The precursor post-precipitation treatment consisted of 24 h aging (maturation stage), water wash and drying. Yttrium-europium oxalate precursor was fired for 2 hrs in air, at 1100°C, 1200°C and 1300°C to provide the corresponding phosphor powder, P19, P27 and P28, respectively. No flux was used for the phosphor thermal synthesis stage. The as obtained materials were water washed, dried and sieved.

Precursors and phosphors were characterised by thermal analysis-TG-DTG-DTA curves (Paulik –Erdely Derivatograf OD-102; heating rate 6º C/min), infrared absorption spectroscopy -FTIR spectra (JASKO 610 FTIR Spectrometer; KBr pellets technique), photoluminescence measurements –PL spectra (JASKO FP-6500 Spectrofluorimeter Wavel; λ_{exc}=254nm), X-ray diffraction–XRD patterns (D8Advanced Brucker Diffractometer, CuKα radiation) and Scanning Electronic Microscopy-SEM images (JEOL –JSM 5510LV Microscope; Au-coated powders) .

RESULTS AND DISCUSSION

This main aim of the study was to clarify some aspects concerning the synthesis of very fine particles of Y_2O_3: Eu phosphors by wet chemical method, using the reagent simultaneous addition technique -*SimAdd*. The precursor was prepared by co-precipitation, from yttrium-europium nitrate mixture and oxalic acid.

Mention has to be made that in precursor and phosphor samples, about 3 mole% of yttrium was replaced by europium. It is supposed that, excepting the PL properties, the isovalent substitution of Y^{3+} with small amounts of Eu^{3+} does not influence the general characteristics of precursor and phosphors so that its presence is neglected during the discussion.

For the beginning, the precursor composition was estimated on the basis of the thermal analysis. TG-DTG-DTA curves of the PG26 precursor show that the thermal decomposition proceeds in three major steps. These steps can be associated with water loss (~ 191^{0}C), decomposition of the metallic oxalate (~408^{0}C) and probable, decomposition of the metallic oxy-carbonate intermediate (~ 530^{0}C).

Assuming that the precursor is a metallic basic oxalate and taking into consideration the literature data [8], the yttrium oxide phosphor formation could be described by the following conversion path:

$$Y_2(C_2O_4)_3 \cdot xY(OH)_3 \cdot yH_2O \rightarrow Y_2(C_2O_4)_3 \cdot xY(OH)_3 \rightarrow Y_2O_2CO_3 \rightarrow Y_2O_3$$

It is well known that the thermal synthesis conditions determine the phosphor characteristics [9]. In the present study, three phosphor samples were prepared in different thermal regime, namely P19 (1100^{0}C), P27 (1200^{0}C) and P28 (1300^{0}C).

In order to correlate the precursor characteristics with the properties of the corresponding Y_2O_3: Eu phosphors, FTIR spectra and XRD spectra were registered and comparatively analysed. **Fig. 1** and **2** presents FTIR and XRD spectra for PG26 and P27 samples.

The precursor vibrational spectrum consists of some characteristic bands i.e. ν (H-O) ~3470, ν (C=O) ~1634, ν (C-O) ~1324, δ(O-C=O)+(Y-OH)~814-790. After the thermal treatment, the precursor specific FTIR bands disappear and the characteristic vibration of Y-O bond, at ~560cm^{-1} can be observed. FTIR spectra suggest the complete conversion of yttrium oxalate-based precursor into yttrium oxide phosphors.

XRD spectra illustrate that all Y_2O_3: Eu phosphor samples as well as the parent precursor consist of well-formed crystalline phases. According to the literature, the yttrium oxalate-based precursor contains mostly the crystalline phase of yttrium ammonium oxalate (PDF 221047). All Y_2O_3: Eu powders are homogeneous and well crystallized, which demonstrate the formation of Y_2O_3-Eu_2O_3 solid solutions with cubic structure (PDF411105).

The XRD measurements suggest that yttrium-based precursor contains NH_4^+ ions. One can suppose that the specific ammonium infrared vibrations, i.e. ν (N-H) and δ(N-H), are covered by those of the basic yttrium oxalate.

According to the XRD and FTIR spectra, the precursor can be formulated as: $[Y_{2-2x}(NH_4)_{2x}][(C_2O_4)_{3-3y}(OH)_{3y}] \cdot zH_2O$ where $0<x<1$; $0<y<1$.

The thermal treatment of yttrium-oxalate based precursors at 1100÷1300ºC ensures the incorporation of Eu^{3+} ions into the Y_2O_3 cubic crystalline lattice and the formation of luminescent centres.

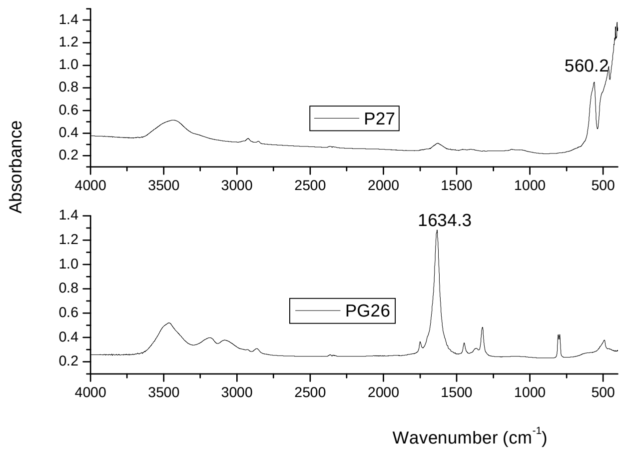

FIG. 1. FT-IR SPECTRA FOR PRECURSOR (PG26) and phosphor (P27) prepared at 1200 ºC

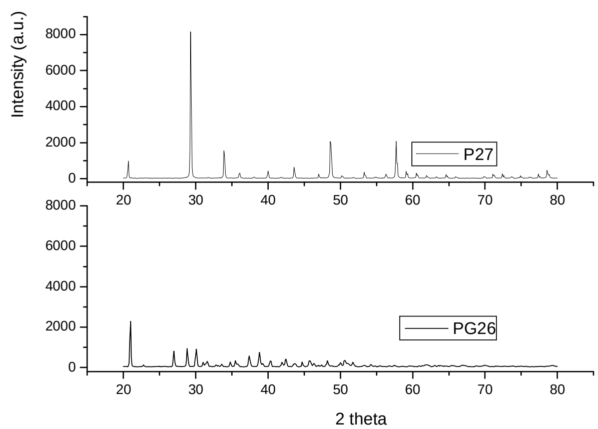

Fig. 2. XRD patterns for precursor (PG26) and phosphor (P27) prepared at 1200°C

Fig. 3 presents the emission spectra of yttrium oxide phosphor (P19) registered for different excitation radiations.

On the basis of phosphor emission spectra, the PL intensity of the main emission peak was evaluated in comparison with the standard (Kemira, I_{611nm}=100%). Under 254 nm excitation, the phosphor emits mainly in the red domain, i.e. at ~ 590 nm ($^5D_0 \rightarrow {}^7F_1$electronic transition) and ~611 nm ($^5D_0 \rightarrow {}^7F_2$

transition). The excitation radiation influences the emission intensity and even the ratio between the different emission bands.

The phosphor thermal synthesis regime determines the red emission intensity of Y_2O_3: Eu phosphors (**Fig. 4**). The emission intensity slightly increases with the firing temperature from 74.3% (P19) to 80.2% (P27) and 84.7% (P28) for 254 nm excitation and from 31.4% (P19) to 47.5% (P27) and 48.0% (P28) under 365 nm radiation excitation.

Phosphor morphology and particle size depend on the precursor characteristics and the thermal synthesis regime. The SEM images of phosphor P27 prepared at 1200^0C and of the corresponding precursor PG26 are presented in **Fig. 5**.

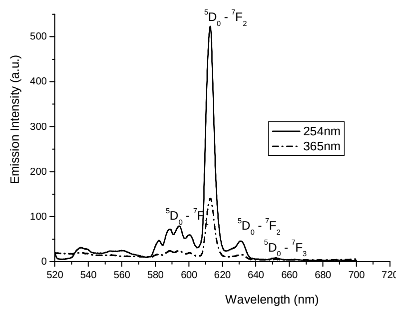

Fig. 3. Emission spectra of P19 phosphor samples

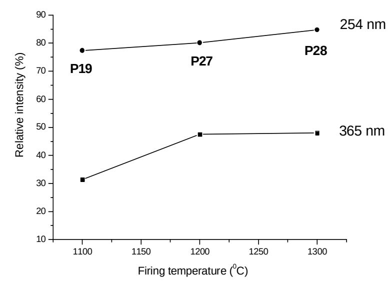

Fig. 4. Influence of synthesis temperature on the PL emission intensity

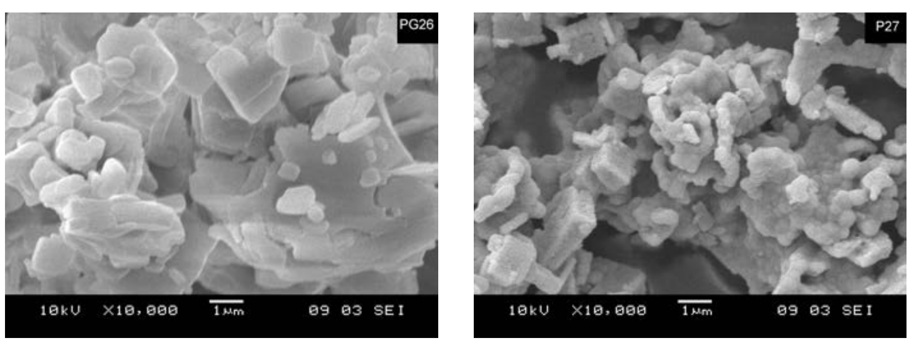

Fig. 5. SEM images of precursor (left) and phosphor (right)

Platelets like particle of precursor are converted into conglomerates, with irregular shape, of small particles. As illustrated by the SEM images, the thermal treatment performed without flux leads to a partial conversion of precursor platelets of 1 ÷ 3 µm to more or less dispersed spherical primary phosphor particles of ~0.5 µm.

The thermal treatment induces a decrease of the particle size due to the decomposition. The incomplete morphological conversion suggests that, during the phosphor thermal synthesis, some mineralising agents (fluxes) need to be added to the yttrium-based precursor.

CONCLUSIONS

The *wet chemical synthesis method*, especially the *SimAdd* technique, facilitates the control of some preparative parameters for obtaining the yttrium oxalate based-precursor for Y_2O_3: Eu powders with small particle sizes. XRD and FTIR spectral investigations suggest that the precursor is mainly a hydrated yttrium-ammonium oxalate. Additional PL and SEM measurements revealed that the firing temperature influences the luminescence characteristics and the morpho-structural properties of phosphors particles obtained by the *SimAdd* technique, from precursor prepared with oxalic acid as precipitating reagent. Further experiments are to be performed in order to improve the PL characteristics and powder morphological characteristics.

ACKNOWLEDGEMENTS

The financial support for this research was provided by the Romanian Ministry of Education and Research (MATNANECH 220/2004).

REFERENCES

1. R.P. Rao, *Solid State Comm*., **1996**, *99*, 439-443.
2. M.H. Lee, S.G. Oh, S.C.Yi, D.S.Seo, J.P.Hong, C.O.Kim, Y.K.Yoo, J.S.Yoo, *J. Electrochem.* Soc., **2000,** *147*, 3139-3142.
3. X. Jing, T. Ireland, G.Gibbons, D.J.Barber, J.Silver, A.Vecht, G.Fern, P.Trowga, D.G.Morton, *J. Electrochem.Soc.,* **1999**, 146, 4654-4658.
4. M.N. Nazarov, J.H. Khang, D.Y. Jeon, E.J. Popovici, L.Muresan, B.S.Tsukerblat, *Solid State Comm.,* **2005,** 133, 183-186.
5. A. Hristea, E.J. Popovici, L.Muresan, R.Grecu, E.Indrea, M.Voicescu, *Studia Universitatis Babes Bolyai , Seria Physica*, XLIX, **2004**, 185-188.
6. L. Muresan , E. J. Popovici, A.Hristea, M.Vasilescu, I.Silaghi-Dumitrescu, *Studia Universitatis Babes Bolyai, Seria Physica,* XLIX , **2004**,182-184.
7. E-J. Popovici**,** L. Muresan, H.Amalia, E. Indrea, M. Vasilescu, *J. Alloys. Comp*. (in press)
8. M.J.Fuller, J.Pinkstone*, J.Less.Common.Metals,* **1980**, *70,* 127-134.
9. G.Blasse, B.C.Grabmaier, „Luminescent materials", Springer Ver.,Berlin, **1994.**

STUDIA UNIVERSITATIS BABES-BOLYAI, CHEMIA, LI, 2, 2006

Dedicated to professor Gh. Marcu at his 80th anniversary

GROWTH AND CHARACTERISATION OF ZINC SULPHIDE THIN FILMS DEPOSITED ON ITO COATED GLASS

MARIA ŞTEFAN[1,2], ELISABETH-JEANNE POPOVICI [2], IOAN BALDEA[1], AMALIA MESAROS[1,2], LAURA MURESAN[2], RODICA GRECU[2]

ABSTRACT. ZnS thin films were grown onto ITO coated glass by chemical bath deposition. The multilayer technique was used in order to prepare ZnS/ITO/glass/ ZnS heterostructures with variable film thickness. Optical properties were investigated by UV-VIS absorption/reflection and fluorescence spectroscopy. The main ZnS films characteristics were correlated with the growing conditions and the annealing regime.

Key words: zinc sulphide; thin films; ITO coated glass; chemical bath deposition

1. INTRODUCTION

Zinc sulphide (ZnS) is a wide, direct band gap semiconductor with interesting optoelectronic properties. A large range of applications exists for thin films of ZnS such as n-window layers of solar cells, electroluminescent displays and other optoelectronic devices [1]. Different methods could be used for ZnS thin films preparation including sputtering, metal organic chemical vapour deposition (MOCVD), atomic layer epitaxy (ALE), pulsed laser deposition, chemical bath deposition (CBD) or electrodeposition [2,3]. Among them, CBD is a simple and inexpensive method and produces uniform, adherent and reproducible films. Moreover, CBD is a low temperature technique and can be used for ZnS deposition onto a variety of substrates.

The aim of this work is to study the influence of different CBD preparative parameters on the quality of ZnS thin films deposited onto ITO coated glass and, especially, on some of their optical characteristics, including their luminescence ability.

2. EXPERIMENTAL PART

ZnS thin films have been grown by CBD method on ITO (indium tin oxide) coated glass pieces provided by Optical Filters Ltd.(UK). The deposition of ZnS was carried out from a mixture of zinc acetate, thiourea, NH_3aqueous solution, and sodium citrate and twice distilled water. Prior the deposition, the platelets (50mm x 25mm x 1mm) were ultrasonically cleaned with acetone/ethanol mixture and dried. Moreover, all the deposition reagents were purified by some characteristic procedures. The multilayer deposition technique was used in order to prepare

[1] Faculty of Chemistry and Chemical Engineering "Babes-Bolyai" University 400028 Cluj-Napoca, Romania; marialadar@yahoo.com
[2] "Raluca Ripan" Institute for Research in Chemistry, 30 Fântânele Street, 400294 Cluj-Napoca

ZnS/ITO/glass/ZnS heterostructures with variable film thickness. The deposition temperature was 82-86ºC and pH mixture was 9.5-10.5. The details of experimental technique have been previously described [4,5]. Most of the heterostructures were obtained in a chemical bath with the standard composition: $[Zn^{2+}]$ = 0.015 M; $[C_6H_5O_7^{3-}]$ = 0.060; $[NH_3]$ = 0.300 M; [thiourea] = 0.15 M. Several samples, for luminescence investigation purpose, were prepared from chemical bath containing a smaller concentration of sodium citrate, namely 0.045 M.

The samples were washed, dried (100°C) and annealed in nitrogen (500ºC) or air (400÷550°C), using a special protecting system. In the later case, the thermal treatment was performed in special to ZnS-based mixtures containing Cu and Mn salts to generate luminescent ZnS thin films.

Zinc sulphide thin films were characterised by thickness and UV-Vis transmittance and reflectance spectra, as well as some photoluminescence investigations. Prior performing the measurements, ZnS films were partially removed with HCl (1:1) from some ZnS/ITO/glass/ZnS heterostructures to give the corresponding ZnS/ITO/glass heterostructures. Optical investigations were performed by using a UNICAM Spectrometer UV4 and photoluminescence measurements by means of a Perkin Elmer 204 Fluorescence Spectrophotometer (λ_{exc}= 365 nm). The film thickness was evaluated by the microweighing, as indicated in our previous work [6].

3. RESULTS AND DISCUSSION

ZnS/ITO/glass/ZnS heterostructures were prepared from chemical bath containing zinc acetate as zinc source, thiourea as sulphur source, aqueous solution of NH_3 as chelating and pH regulating agent, sodium citrate as chelating agent and doubly distilled water.

The chemical bath deposition process uses a controlled chemical reaction to effect the slow formation of ZnS thin films deposited onto ITO coated glass. The general chemical equation is:

$$Zn(CH_3COO)_2 + (NH_2)_2CS + 2OH^- \rightarrow ZnS + H_2CN_2 + 2H_2O + 2CH_3COO^-$$

CBD method was adapted for multilayer ZnS film formation onto ITO coated glass platelets. With this deposition technique one to five superposed ZnS layers were deposited onto ITO coated glass platelets.

In the above-mentioned conditions, adherent and homogeneous ZnS thin films were grown on both ITO coating and glass substrates to give the ZnS/ITO/glass/ZnS heterostructures. Some ZnS/ITO/glass heterostructures were obtained by the removal of ZnS films from the glass side opposite to the ITO coating

The growing parameters of the as prepared heterostructures are presented in **Table 1**. As expected, increase of zinc sulphide film thickness with the total deposition time could be noticed. The use of a high number of successively deposited layers (coatings) determines the increase of the film thickness. One can note that, the growing rate, calculated by dividing the ZnS film thickness to the total deposition time is increases with the number of coatings. According to our previous work [5,7,8], for the same deposition time, the multilayer grown film is thicker when it deposited onto the glass substrates in comparison with the film formed onto the ITO coated face of the glass platelet. Mention has to be made that, according to the manufacturer measurement, the thickness of the ITO coating is ~20 nm.

Table 1.

The growing parameters of some ZnS/ITO/glass heterostructures prepared by multilayer technique

Samples code	Total deposition time n x m*	ZnS packing density (mg/cm²)	ZnS film thickness** (nm)	ZnS film growing rate (nm/min)
ITO 3.0	0	0	0	0
ITO 3.1	1 x 60 = 60 min	0.13	33	0.55
ITO 3.2	2 x 60 = 120 min	0.33	80	0.67
ITO 3.3	3 x 60 = 180 min	0.60	150	0.83
ITO 3.4	4 x 60 = 240 min	0.80	200	0.83
ITO 3.5	5 x 60 = 300 min	1.06	260	0.87

*Where: n = number of layers, m = deposition time; ** on the ITO coated glass face

UV-Vis absorption /reflection and photoluminescence spectroscopy were used to investigate the optical properties of different ZnS/ITO/glass or ZnS/ITO/glass/ZnS heterostructures. Moreover, in order to prove the ZnS film ability to develop luminescent properties, some of the heterostructures containing relatively thick films were annealed in special ZnS-based mixtures containing copper and manganese doping ions. The photoluminescence behaviour of the as obtained copper and manganese doped ZnS/ITO/glass/ZnS heterostructures, notated ZnS:Cu,Mn /ITO/glass/ ZnS:Cu,Mn, was evaluated from the emission spectra registered under UV excitation.

The transmission spectra (**Fig.1**) of the heterostructures that contains multilayer ZnS films illustrate the high transparency of the ITO coating over the entire visible domain (over 90%). The transparency decreases parallel with the increase of the film thickness. The multiple maxima on transparency curve of some ZnS/ITO/glass heterostructures reveal a good quality of the deposited thin film (**Fig.1**).

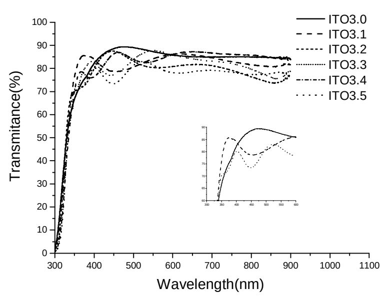

Fig. 1. Transmission spectra of some ZnS/ITO/glass heterostructures

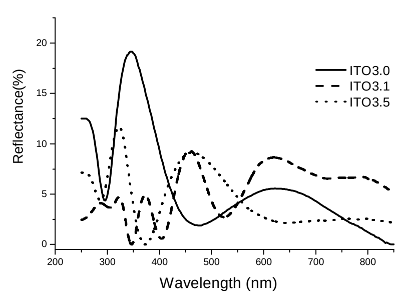

Fig. 2. Specular reflectance of ZnS films deposited onto ITO coated glass face

The reflectance spectra of ZnS/ITO/glass heterostructures were registered in order to evaluate the ZnS film optical quality (**Fig. 2**). The spectra registered at 0° incidence indicate the diffuse reflection of the films whereas the spectra obtained at 8º incidence of the visible light illustrate both the specular and diffuse reflection properties of the investigated heterostructure. The specular reflectance of some samples, evaluated as the difference between the reflection measured at 8º and 0º incidence, decreases as the number of ZnS layers increases One can note the strong specular reflection properties of the ITO coated glass. A thin film of ZnS (ITO3.1) attenuates the ITO layer reflection and shows only a weak reflection characteristic to the ZnS material. This one is clearly put in evidence for the relatively thick layers (ITO3.5).

Some of the ZnS/ITO/glass and ZnS/ITO/glass/heterostructures were treated thermally either in a nitrogen atmosphere, or in some peculiar conditions that allows the evaluation of the luminescence ability of the CBD obtained ZnS films. **Table 2** presents the thickness and the thermal treatment conditions of some heterostructures containing un-doped or copper-manganese doped ZnS thin films.

The transmittance spectra of the ZnS/ITO/glass heterostructure obtained in 300 min deposition was measured before and after the thermal treatment (**Fig.3**). It is obvious that the post-growing thermal treatment decreases the film transmittance and diminishes the film optical quality.

The emission spectra of copper-manganese doped ZnS/ITO/glass/ZnS heterostructures are depicted in **Fig. 4.** The sample prepared at 400ºC shows a very weak luminescence with relatively well evidenced emission bands situated at about 467, 524 and 560 nm. These bands are correlated with the presence of some specific emission centres associated with the self-activated SA-, Cu- and Mn-luminescence in zinc sulphide layer, respectively. The weak luminescence observed for this structure could be explained either by an incomplete incorporation of the activators into the ZnS lattice generating a small number of luminescence centres, or to a poor quality of the films deposited onto ITO substrate.

In order to verify the luminescence ability of ZnS thin films, attempts were made to incorporate Cu-Mn activators by annealing the system at 550°C. The sample obtained using this thermal synthesis regime, shows a relatively strong luminescence situated mostly into the yellow spectral region. The main emission peak is observed at 577 nm, close to the theoretical value (580 nm) originated into the Mn-centres. The higher annealing temperature is in the favour of Cu-and Mn activator incorporation.

Table 2.

Thickness and thermal treatment conditions of some ZnS containing heterostructures

Sample code	**Thickness (nm)****	**Doping and thermal treatment**	**Heterostructure**
ITO3.5TT	260	500^oC, N_2	ZnS/ITO/glass
ITO11.3	320	Cu-Mn doping, 400^oC	ZnS:Cu,Mn/ITO/glass/ZnS:Cu,Mn
ITO12.1	310	Cu-Mn doping, 550^oC	ZnS:Cu,Mn/ITO/glass/ ZnS:Cu,Mn

*where: n = number of layers, m = deposition time; ** mean value

The better yellow-orange emission observed for the heterostructure prepared at relatively high temperature reveals a good luminescence ability of zinc sulphide layer.

The luminescence performances of the ZnS/ITO/glass/ZnS heterostructures doped with copper and manganese are predominantly sensitive to the annealing regime and the doping conditions.

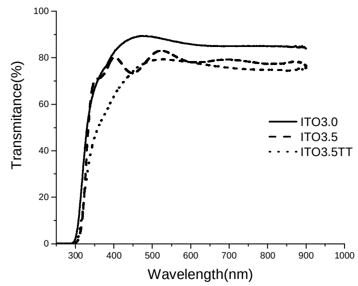

Fig. 3. Transmission spectra of some ZnS/ITO/glass samples before and after the thermal treatment

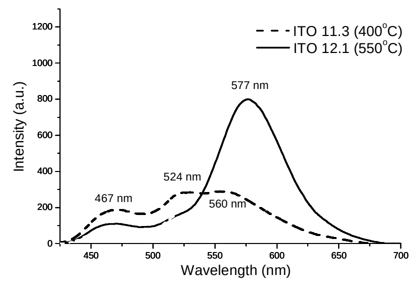

Fig. 4. Emission spectra of some ZnS: Cu, Mn films deposited onto ITO layer

4. CONCLUSIONS

The bath composition and the special CBD technique used in our experiments proved to be convenient for the deposition of adherent and homogeneous ZnS films with controllable thickness onto the ITO coated glass substrate. The growth parameters influence the optical properties of the as deposited thin films.

UV-Vis absorption /reflection investigations illustrated the quality of the as prepared ZnS/ITO/glass/ZnS heterostructures. The photo-luminescence measurements on some copper and manganese doped ZnS/ITO/glass/ZnS heterostructures proved the ability of ZnS films to develop good light emitting properties.

Acknowledgements

The authors greatly acknowledge MEC-CNCSIS for financial support of this work by Grant Td 7/52 2006

REFERENCES

1. P.O Brien, J. McAleese, J. Mater. Chem., **1998**, *8(11),* 2309-2314
2. Bayer, D. S. Boyle, P. Obrien, J. Mater. Chem., **2002**, *12*, 2940-2944
3. J. Lee, S. Lee, S. Cho, S. Chim, I. Y. Park, Y. D. Choi, Mat. Chem. Phys. **2002**, *77*, 254-260
4. M. Ladar, E.-J. Popovici, L. Pascu, R. Grecu. I.C. Popescu, E. Indrea , Studia Universitatis Babes-Bolyai , Physica, **2003**, Special Issue 2, XLVII, 469-471
5. M. Ladar, E.-J. Popovici, I. Baldea, R. Grecu, E. Indrea, Studia Universitatis Babes-Bolyai , Physica, **2004**, Special Issue 2, XLIX, 3, 157-161
6. L. Pascu, E.-J. Popovici, C. Dan, R. Grecu, E. Indrea, Proceeding of SPIE, **2001**, *4430*, 267-274;
7. R. Grecu, E.-J. Popovici, M. Ladar, L. Silaghi –Dumitrescu, E. Indrea, Studia Universitatis Babes-Bolyai , Physica, **2003**, Special Issue 2, XLVIII, 472-475
8. M. Ladar, E.-J. Popovici, I. Baldea, R. Grecu, E. Indrea, J. Alloys. Comp. (in press)

STUDIA UNIVERSITATIS BABES-BOLYAI, CHEMIA, LI, 2, 2006

Dedicated to professor Gh. Marcu at his 80th anniversary

BIS-PHENOTHIAZINYL-PHENYL-METHANE DERIVATIVES

GABRIELA CORMOS*, CASTELIA CRISTEA*, IUDIT FILIP*, IOAN A. SILBERG*

ABSTRACT. The synthesis of some *bis*-(phenothiazin-3-yl)-phenylmethane derivatives by the condensation of phenothiazine with aromatic aldehydes was investigated. The structural assignments for the new compounds were based on NMR, IR and UV-Vis spectroscopy.

INTRODUCTION:

The chemical reactivity of phenothiazine towards electrophilic substitution reactions was demonstrated in numerous examples of N- or C- substituted derivatives preparations. The transmission of the electronic effects between the two heteroatoms and the two benzene rings is very efficient and electrophilic substitution occurs easily. Rather mild electrophiles can be used to accomplish the substitution reaction in position 10 (N-alkylphenothiazines [1], N-acylphenothiazines [2]) or in positions 3 and 7 (C-halogenophenothiazines [3-5], C-nitrophenothiazines [6.] C-alkylphenothiazines [7,8]). Dyes formation by the condensation of phenothiazine with aromatic ketones (such as Michler's ketone) was also reported [9].

The paper presents the condensation reaction of phenothiazine with aromatic aldehydes in the presence of acid catalysts.

RESULTS AND DISCUSSIONS

The condensation reaction of phenothiazine **1** with aromatic aldehydes (benzaldehyde, *o*-, *m*- and *p*-nitrobenzaldehyde) in acid media was performed. The mild electrophile generated by the aldehyde in the presence of methanesulfonic acid determines the substitution of the phenothiazine ring in position 3 (activated by the electron donor effect of the nitrogen heteroatom). In boiling ethanol solvent the reaction product **4** has a low solubility and easily separates from the reaction mixture. Scheme 1 presents an overview of the chemical reactions involved.

* "Babeş-Bolyai" University, Faculty of Chemistry and Chemical Engineering, Organic Chemistry Department, Cluj-Napoca, RO- 400028, Romania

* Part I [1]

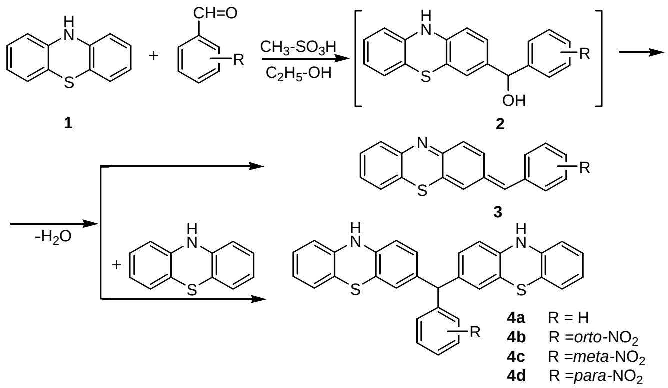

Scheme 1.

The structure assignment for compounds **4a-d** was performed by H-NMR, FTIR and UV-Vis spectroscopy.

The IR spectroscopic investigations of the reaction products showed that the alcohol intermediate **2** was not separated under the reaction conditions employed (no characteristic absorption bands due to C-O and O-H bonds stretching vibrations were recorded for the separated reaction product).

During the reaction progress, a green color appears in to the reaction mixture, possibly due to the competing elimination reaction generating the compounds **3** **(**characterized by a fully conjugated π electrons system). The compounds **3** are soluble in ethanol.

The *bis*-(phenothiazin-3yl)-phenylmethane **4a** and its nitro-substituted derivatives **4b-d** separated from the boiling reaction mixture as precipitates which were filtered. The H-NMR spectra, showed for the aliphatic proton a characteristic chemical shift situated in the range of 5.1-5.8 ppm. The most deshielded aliphatic proton appears in the structure of the *orto*-nitro-substituted derivative **4b** (δ=5.8 ppm), while the signal of the same proton in the structure **4a** is situated at 5.1 ppm. Intermediate values (5.4 ppm) were recorded for the compounds **4c-d** containing a nitro group situated in position *meta* or *para.*

EXPERIMENTAL:

The chemical reagents and the solvents were purchased from Merck (for synthesis purity)

The IR spectra were recorded on a FTIR Bruker Vector 22 spectrometer.

The UV-Vis spectra were recorded on a UNICAM Helios β spectrometer.

The H-NMR spectra were recorded on a Bruker Avance 300 MHz spectrometer.

General procedure for the condensation of phenothiazine with aromatic aldehydes.

Phenothiazine (2g, 1 mmol) was solved in ethanol (120 mL), methanesulphonic acid (0.5 mL) and an ethanolic solution of the aromatic aldehyde (0.5 mmol) were added to the clear phenothiazine solution. The reaction mixture was heated under vigorous stirring to reflux for several hours. During the reaction progress, a green color appears and a precipitate starts to accumulate.

The reaction mixture thus obtained was cooled down at room temperature, the precipitate was filtered out and then washed several times with cool ethanol. The reaction product is a grey-green powder highly insoluble in toluene, acetone and chloroform, soluble in THF.

***Bis*-(phenothiazin-3-yl)-phenylmethane 4a**

Reaction time: 12 hours, green powder , m.p. 251 ^{o}C, yield 60 %.

IR [cm^{-1}]: 3400, 3100, 1600, 1462, 1300, 803, 741, 604

UV [nm]: 248, 320.

H-RMN (300 MHz, DMSO-d_6) δ: 7.3-6.1 ppm, m 19H (phenyl and phenothiazine unit), 5.1 ppm, s, 1H (CH)

***Bis*-(phenothiazin-3-yl)-2-nitrophenylmethane 4b**

Reaction time: 40 hours, grey powder , m.p. 278 ^{o}C, yield 48%.

IR [cm^{-1}] 3400, 3100, 1514, 1339, 810, 742, 650

UV [nm]: 248, 320.

H-RMN (300 MHz, DMSO-d_6) δ: 8.1-6.6 ppm, m 18H (*o*-phenylene and phenothiazine unit, 5.8 ppm, s, 1H (CH).

***Bis*-(phenothiazin-3-yl)-3-nitrophenylmethane 4c**

Reaction time: 20 hours, brown powder, m.p. 264 ^{o}C, yield 55 %.

H-RMN (300 MHz, DMSO-d_6) δ: 8ppm, d, 2H, 7.4 m 2H, (*m*-phenylene unit), 6.1ppm, m, 14 H (phenothiazine unit), 5.3 ppm, s, 1H (CH).

***Bis*-(phenothiazin-3-yl)-4-nitrophenylmethane 4d**

Reaction time: 15 hours, grey powder , m.p. 255 ^{o}C, yield 61%.

IR: [cm^{-1}]: 3400, 3100, 1600, 1514, 1339, 809, 742, 690.

UV: 250 nm, 324 nm

H-RMN (300 MHz, DMSO-d_6) δ: 8.6 ppm s, 2H (NH), 7.34 d 2H, 8.1, d, 2H (*p*-phenylene unit), 6.6–6.9 ppm, m, 14 H (phenothiazine unit), 5.4 ppm, s, 1H (CH).

REFERENCES

1. H. Gilman, J. Eisch, *J. Am Chem. Soc*, **1955,** 77, 3862.
2. E. M. Acton, R. M. Silverstein, *J. Org. Chem,* **1959**, 24, 1487.
3. C. Bodea, M. Raileanu, *Studii Cercetari Chim. (Cluj)*, **1958**, 9, 159.
4. C. Bodea, M. Raileanu, *Ann. Chem*. **1959**, 620, 88.
5. C. Bodea, I. Silberg, *Rev. Roum. Chim*., **1964**, 9, 425.
6. C. Bodea, M. Raileanu, *Studii Cercetari Chim. (Cluj)*, **1957**, 8, 303.
7. J. S. Elliot, E. D. Edwards, A. D. Brazier, *British Pattent* 889,341, *CA* **1962**, 57, 3448b.
8. D. R. Randell, *British Pattent,* 1,036,696, *CA* **1966,** 65, 15394h.
9. R. Wizinger, S. Chatterice, *Helv. Chim. Acta*, **1952**, 35, 316.

STUDIA UNIVERSITATIS BABES - BOLYAI, CHEMIA, LI, 2, 2006

Dedicated to professor Gh. Marcu at his 80th anniversary

MOLECULAR PACKING OF SOME CAROTENOIDS IN LANGMUIR MONOLAYERS AT THE AIR/WATER INTERFACE

OSSI HOROVITZ*, MARIA TOMOAIA-COTISEL*

ABSTRACT. The characteristic molecular areas were determined from surface pressure versus molecular area isotherms of three carotenoids: β,β-carotene-4-one (echinenone, ECH), β,β-carotene-4,4'-dione (canthaxanthin, CAN) and 4,4'-diapo-ψ,ψ-carotene-4,4'-dial (APO), spread and compressed as Langmuir monolayers at the air/water interface. Quantum chemical semi-empirical SCF MO calculations (AM1 and PM3) are performed for the optimized geometries of carotenoid molecules and similar theoretical results are obtained by both methods. The characteristic surface molecular areas are discussed in terms of molecular packing in Langmuir monolayers and intermolecular interactions, respectively. The orientation of these carotenoid molecules in the Langmuir monolayers is discussed by using a rotating rigid plate model and optimized molecular geometries.

Keywords: *carotenoids, Langmuir monolayers, molecular packing, molecular structure, semi-empirical MO calculations.*

INTRODUCTION

Langmuir monolayers are obtained by spreading amphiphilic organic molecules using an appropriate solvent or a mixture of organic solvents at the air/water interface [1-3]. Generally, these monolayers are compressed up to their collapse and they are employed as model systems in studying surface phenomena, associated with various applications in science and technology [4]. In particular, carotenoids can be potential key elements for molecular electronic devices. Also, carotenoids are essential biological active molecules, which can influence or modulate the properties of cellular and subcellular structures [5, 6]. Therefore, the behavior of Langmuir monolayers of carotenoids is of interest and is investigated at the air/water interface both in pure state [7-10] and in mixtures with lipids [11-14] or electrolytes [15-18]. The obtained data show that the local ordering and molecular packing of carotenoids in Langmuir monolayers at the air/water interface depend primarily on the carotenoid molecular structure for the same aqueous phase and at similar conditions for compression rate and spreading rate.

The objective of this paper is to investigate experimentally and theoretically how the equilibrium intermolecular interactions and hydrophilic and hydrophobic forces affect the molecular packing of some carotenoids in Langmuir monolayers at the air/water interface. In the following the rotating rigid plate model previously proposed by us [19] for carotenoid molecules is reconsidered, and used to explain the molecular

* "Babes-Bolyai" University of Cluj-Napoca, Faculty of Chemistry and Chemical Engineering, Physical Chemistry Department, 400028 Cluj-Napoca, Romania

packing of the three chosen carotenoids for this study. Optimized geometries of the molecules are used, as resulted from semi-empirical MO computations. Finally, the obtained results are summarized in the conclusion section of this paper.

THE ROTATING RIGID PLATE (RRP) MODEL OF CAROTENOIDS

In order to correlate the structural and geometrical characteristics of carotenoid molecules with their surface properties as monolayers at the air-water interface, the rotating rigid-plate model of carotenoid molecules was previously proposed [19-21]. In the framework of this model, the molecule (all-*trans* isomer) is considered to be rigid (due to its delocalized π-bond system), but free rotation about the simple σ-bonds has also been taken into account, the most stable conformation being assumed. For the bond lengths and bond angles, experimental data (from X-ray analysis) have been used, when available (for canthaxanthin [22]); otherwise they have been approximated from the bond lengths and covalent radii given in chemical tables and the bond angles from the hybridization types.

The hydration of the polar headgroup of the molecule, immersed in water, was modeled by the inclusion of hydrogen-bridged water molecules. Two H_2O molecules are considered to be linked to the C=O group, thus anchored in the water phase.

The carotenoid molecule is seen as a parallelepiped; its length, *c*, is taken as the length of the chain axis (*c*'), including the hydration water molecules (see Fig.1 for canthaxanthin molecule). The length of the headgroup axis (*a*'), and also including hydration water, *a*, is the width of the molecular plate, while *b* represents its thickness – given mainly from the out-of-plane hydrogen and carbon atoms [21].

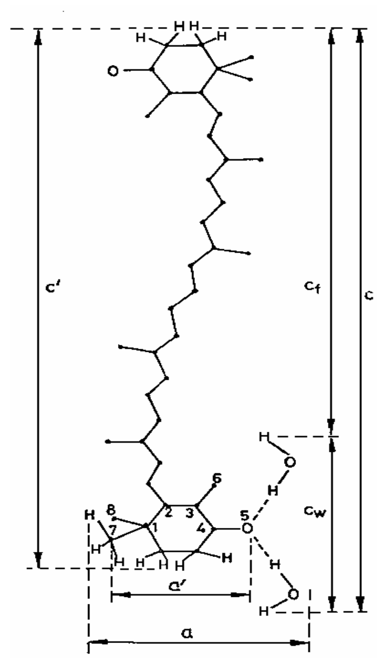

Fig.1. Rigid plate model of the canthaxanthin molecule [1]

In the estimation of the molecular areas in the monolayer at the air/water interface, arguments were given for a calculation in which the molecule is assumed to perform a free rotation about the vertical chain axis, and the resulting vertical cylinders adopt a tetragonal close packing [19, 21]. This does not necessarily imply a real rotation, but also a random orientation of the head group axis in the interface plane. Therefore, since $b < a$, the mean area occupied by a molecule in the interface layer should be $A_4 = a^2$, instead of $A_p = ab$, corresponding to a close packing of vertical rigid plates with parallel orientation.

Another estimated characteristic of the monolayer was the immersed fraction α of the molecules, defined as the ratio between the length of the part of the chain immersed in water, as determined by the hydration, c_w (Fig.1) and the total chain length, *c*:

$$\alpha = c_w/c \tag{1}$$

The free part of the chain, c_f is therefore c-c_w For echinenone and canthaxanthin, the values obtained from this model [19] were: a = 0.78 nm, b = 0.49 nm, c = 3.2 nm, c_w = 0.7 nm, α = 0.22 and A_4 = 0.61 nm^2, A_p = 0.38 nm^2.

The present paper deals with the application of the RRP model to three carotenoid pigments, namely β,β-carotene-4-one (echinenone, ECH), β,β-carotene-4,4'-dione (canthaxanthin, CAN) and 4,4'-diapo-ψ,ψ-carotene-4,4'-dial (4,4'-diapolycopenedial, APO) (Fig. 2), using their molecular structure, as resulted from semi-empirical MO calculations (AM1 and PM3).

EXPERIMENTAL PART

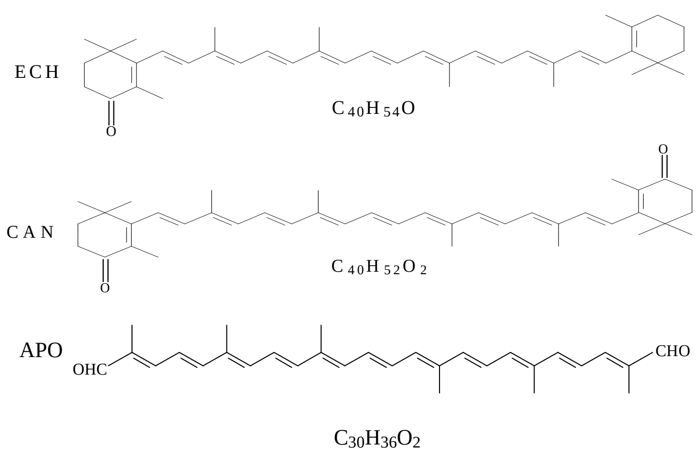

Fig.2. Molecular structure of carotenoids: β,β-carotene-4-one: ECH, β,β-carotene-4,4'-dione: CAN and 4,4'-diapo-ψ,ψ-carotene-4,4'-dial: APO.

The three natural carotenoid pigments (ECH, CAN and APO) used here were supplied by Hoffmann-La Roche and present *all-trans* configuration. The high purity spreading solvents, benzene pro-analysis or a mixture of benzene and 2-4% absolute ethanol, were purchased from Merck. Known amounts of the compounds dissolved in the spreading solvents were placed by means of a Hamilton syringe or a micropipette on the air/water interface. The water subphase was double distilled water with a resistivity of 18 Mohm cm^{-1}. Compression of the monolayer was started after about 10 minutes, allowed for solvent evaporation. Then, the spread monolayer of each carotenoid compound was compressed at a chosen rate of compression in the interval from 0.01 to 0.03 nm^2/(molecule·min), by using the Langmuir equipment KSV 5000. The reproducible compression isotherms, in terms of surface pressures versus molecular areas, were recorded at 20 ^{o}C as described elsewhere [5]. The surface pressure was measured by the Wilhelmy method within the error of ± 0.2 mN/m. The compression curves were reproducible within 0.02 – 0.04 nm^2/molecule. The results do not depend on the compression rate in the region used. Each isotherm given in this paper represents the mean of at least 10 different recordings.

COMPUTATIONAL PART

MO calculations were performed, regarding σ and π electrons, on the three carotenoids (ECH, CAN and APO) in their all-trans forms [23]. Computations were made at the restricted Hartree-Fock (RHF) level using two semi-empirical SCF MO methods: Austin Model 1, AM1 [24] and the Parametric Model number 3, PM3 [25], by means of HyperChem 7.5 software package [26]. The two methods are based on the Neglect of Differential Diatomic Overlap (NDDO) integral approximation, and differ by their parameterization. The computation options were: total charge: 0; spin multiplicity: 1 (singlet); state: lowest. The geometries of the molecules were optimized by the Polak-Ribiere (conjugate gradient) algorithm approach. The SCF convergence limit was of 0.042 kJ/mol, and RMS gradient was of $4.18 \cdot 10^9$ kJ/(m×mol).

For the optimized geometry, energetical parameters (total electronic energies, enthalpies of formation), electron distributions (charge densities and bond orders) and geometrical parameters (bond lengths, bond angles, torsion angles) were obtained [23]. Both computational methods gave quite similar results for the geometry of the molecules. The first inertial axis of the molecule is roughly going along the conjugated chain of the molecules, while the second axis is perpendicular to it in the molecular plane.

RESULTS AND DISCUSSION

The ***compression isotherms***, in terms of surface pressure (π, mN/m) versus mean molecular area (A, nm^2) curves for three carotenoids, viz. β,β-carotene-4-one (ECH), β,β-carotene-4,4'-dione (CAN) and 4,4'-diapo-ψ,ψ-carotene-

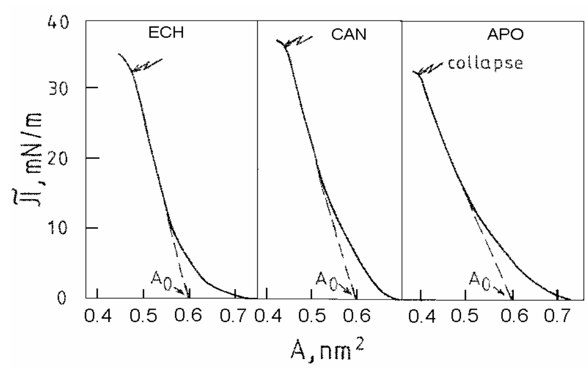

Fig.3. Compression isotherms: surface pressure versus mean molecular area for carotenoids: β,β-carotene-4-one (ECH), β,β-carotene-4,4'-dione (CAN) and 4,4'-diapo-ψ,ψ-carotene-4,4'-dial (APO) spread as monolayers at the air/water interface, at 20 °C.

4,4'-dial (APO), spread at the air/water interface, are presented in Fig. 3.

From these compression isotherms, surface properties were determined, namely: the limiting molecular area A_0 (see Fig. 3), obtained by extrapolating to π= 0 the high pressure linear portion of the compression isotherm; A_c, is the collapse area and the corresponding surface pressure noted π_c, the collapse pressure (Table 1).

Table 1.

Surface characteristics of the three carotenoids studied.

Carotenoid	π_c (mN m^{-1})	A_0 (nm^2)	A_c (nm^2)
ECH	32	0.60	0.48
CAN	36	0.60	0.44
APO	32	0.60	0.40

The ***optimized molecular geometry***, as resulted from the PM3 calculations, is visualized for the three molecules in the plane of the first two inertial axes in Fig.4.

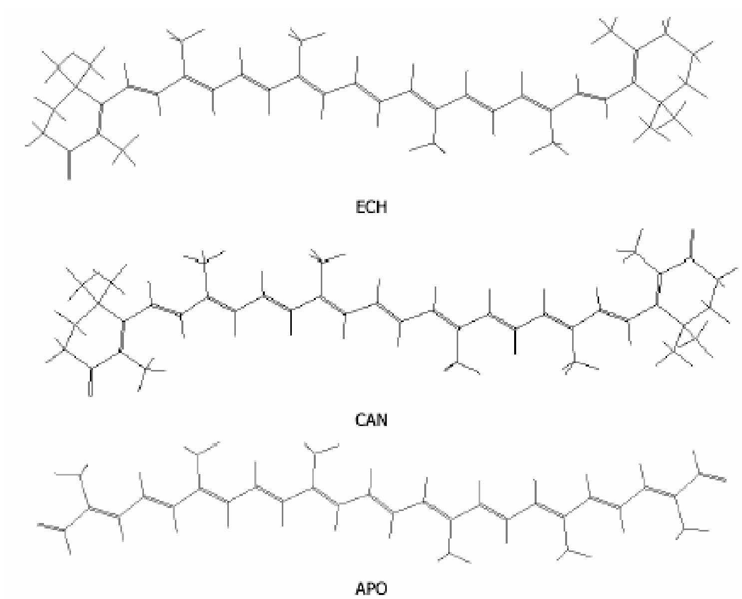

Fig. 4. Optimized geometries (PM3 calculation) for the three carotenoid molecules, represented in the plane of the first and second inertial axes.

For a discussion of the **molecular orientation and packing at the air/water interface,** on these models the length of the chain was measured, as the maximum size in the direction of the first axis: 2.93 nm (ECH), 2.94 nm (CAN), and 3.02 nm (APO). Since in these representations, distances between atomic nuclei are obtained, the covalent radii of the end atoms (H for ECH and CAN, O for APO) should be added, what gives for the lengths *c*' (Fig. 1) the values: 2.99 nm (ECH), 3.00 nm (CAN), and 3.15 nm (APO).

Following the considerations given in the earlier treatment [19], about 0.1 nm have to be added to *c*' for the lower water molecule bonded to the C=O group in ECH and CAN, thus obtaining a *c*-value of about 3.1 nm for these two molecules. As for the immersed part of these chains, given by the vertical projection of the two O····H-O bridges and of the other two O-H bonds, it was estimated to be c_w = 0.7 nm, the immersed fraction (eq. 1) being α = 0.23.

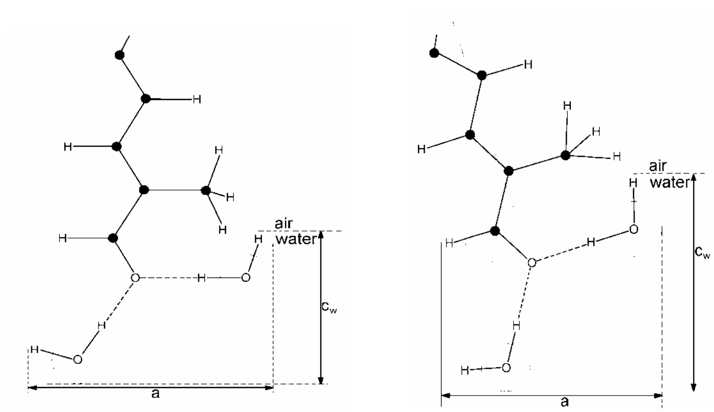

(A) **(B)**

Fig.5. The shape of the lower part of the APO-molecule and the size of its hydrated polar head group for a vertical orientation of the molecular axis – 1st inertial axis (A) and for an angle of 20° to the vertical (B)

For the APO molecule, a similar model was sketched in Figure 5A, for the lower part of the molecular chain. An angle of 60° of the C=O bond to the air-water interface was assumed, corresponding to a vertical orientation of the conjugated chain, as in earlier MO studies on this compound [27, 28]. Adding 0.23 nm for the vertical projection of the lower O····H-O bridge, we obtain for the total (hydrated) chain length *c* = 3.38 nm. As for the immersed part of the chain, besides the contribution of the lower water molecule (0.23 nm + oxygen radius), we have to consider the vertical projection of the O-H bond of the second water molecule and the H radius. This gives a c_w value of about 0.43 nm and an immersed fraction α = 0.13, less than for the other two molecules.

A previous investigation on these three carotenoid molecules [23], correlating surface properties with MO calculated quantities, viz. dipole moments, has suggested that the APO molecules should deviate from the vertical, i.e. to be inclined in order to decrease the angle of the C=O bond to the air/water interface. This orientation would allow for an increased interaction with the water molecules. The angle should be about 40°, i.e the deviation of the molecule axis from the vertical, of about 20° (Fig. 5B). For this orientation, the depth of the hydration layer, given by the two hydrogen-bonded water molecules, would be c_w = 0.56 nm and the length of the immersed part of the molecular chain about 0.6 nm. The total length of the hydrated chain is given by adding to *c'* the contribution of the lower water molecule to the hydration, about 0.29 nm, and is therefore c = 3.44 nm. The immersed fraction α becomes now 0.17. Thus the inclination allows for a better hydration of the APO molecule.

The areas occupied by the molecules in the monolayer can be estimated from the molecular volumes, *V*, calculated as QSAR properties by the HyperChem software, divided by the calculated length of the molecule *c*'. These values are given in Table 2 and are in quite good agreement with the experimental values of extrapolated molecular areas, A_o [19], obtained by extrapolating the high pressure linear portion of the surface pressure – area curves to pressure π = 0.

Table 2.

Calculated and experimental molecular areas in monolayers

Molecule	*c*' (nm)	*V* (nm^3)	*V/c'* (nm^2)	*a* (nm)	*b* (nm)	A_4 (nm^2)	A_p (nm^2)	A_o (nm^2)	A_c (nm^2)
ECH (1)	2.99	1.8334	0.613	0.74	0.56	0.548	0.414	0.60	0.48
(2)	3.10			0.87		0.757	0.487		
(3)	3.2			0.78	0.49	0.608	0.38		
CAN (1)	3.00	1.8292	0.610	0.75	0.52	0.562	0.39	0.60	0.44
(2)	3.10			0.88		0.774	0.458		
(3)	3.2			0.78	0.49	0.608	0.38		
APO (1)	3.15	1.4923	0.474	0.60	0.24	0.36	0.144	0.60	0.40
(2)	3.38			0.585		0.342	0.14		

(1) without hydration; (2) with hydration; (3) estimated in [1]

On the assumption that the dimensions of the "molecular plate", are in first approximation colinear with the inertial axes: *c* with the 1st, *a* with the 2nd and *b* with the 3rd axis, we can evaluate these dimensions. As above for *c*, from the representations of the optimized geometries of the molecules in the planes of the first and second inertial axes (Fig.4), in the plane of the first and third axes or of the second and third inertial axes (Fig. 6) the other two dimensions of the molecules, *a* and *b*, can be measured. In Table 2, these values are given as read from the diagrams with addition of the radii of the end atoms (1), and with addition of the hydration water molecules (2). The values estimated in [19] are also given (3). For the APO molecule, the value (2) was obtained from the model (Fig.5A) of the hydrated head group.

The molecular areas have been calculated from these 3 kinds of molecular dimensions:

(i) from the model of the freely rotating molecular rigid plates, with tetragonal close packing, $A_4 = a^2$;

(ii) from the model of close packing of parallel oriented rigid plates, $A_p = ab$

These values are also given in Table 1. The A_c values are the molecular areas at the collapse of the carotenoid monolayer.

The A_4 values estimated in [19] for ECH and CAN are in good agreement with the experimental A_o values. The A_4 values calculated form the values (2) are larger than the values reported in [19] (3). The explanation is that the *a*-values (3) were estimated for the head group only, while the *a*-values (2) refer to the "width" of the entire molecule, in its real geometry. The same does apply to the "thickness" *b*-values (1) and (3).

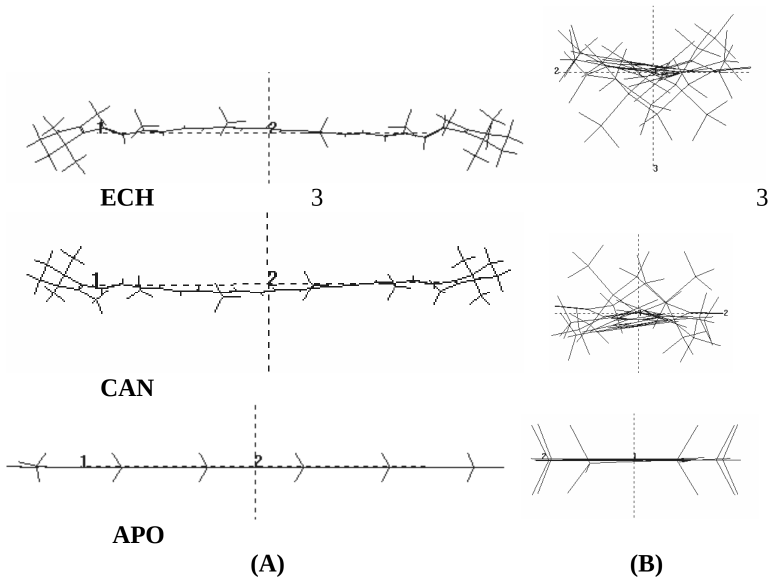

Fig.6. The carotenoid molecules, represented in the plane of the first and third inertial axes (A) and of the second and third inertial axes (B). The scales of the representations are different.

The A_p values (2), calculated from the dimensions of the hydrated ECH and CAN molecules, are in much better agreement with the molecular collapse areas than the estimated values (3); moreover, they give also the right order (ECH > CAN), while the values estimated in [19] make no difference between the two molecules. It can be assumed that near the collapse pressure, the free rotation of the molecules is hindered and the head group axes tend to assume a parallel orientation.

The APO molecule represents a different case. The lower immersed fraction for this substance brings about that higher energies are necessary to perform a vertical orientation of the chain axes. The molecules seem to keep their inclined orientation even at the collapse, due to the weak intermolecular interactions, as suggested in [23]. Therefore, the molecular areas calculated for a vertical orientation are much lower than the experimental A_o and A_c values.

CONCLUSIONS

Three carotenoid molecules, ECH, CAN, and APO, have been studied in Langmuir monolayers at the air/water interface. The surface characteristics, like limiting molecular areas, collapse areas and collapse pressures are well correlated with the carotenoid molecular structures and the molecular orientation at the air/water interface. The obtained data are explained by the interplay of the intermolecular hydrophilic and hydrophobic forces which lead to stable Langmuir monolayers, with the rotating molecules tetragonally packed in the liquid state of the monolayers (rotating rigid plate model of the carotenoid molecules). At collapse, the non-rotating carotenoid molecules are close packed in Langmuir monolayers.

Quantum chemical semi-empirical SCF MO calculations (AM1 and PM3) are performed for the optimized geometries of carotenoid molecules. From the obtained geometry of the molecules, the parameters for the rotating rigid plate model of the molecules could be estimated, in good agreement with the experimental values for the limiting molecular area A_0 and the collapse area A_c. As regards the orientation of these carotenoid molecules in the monolayer, for the echinenone and canthaxanthin molecules a perpendicular direction of the molecular axis to the air/water interface is found, while for the 4,4'-diapo-ψ,ψ-carotene-4,4'-dial (APO) molecule a deviation from the vertical is suggested.

It would be of interest to study other molecules also having the poly-ene chain attached to beta–ionone rings or to a flexible moiety like an alkyl chain.

REFERENCE

1. E. Chifu, M. Tomoaia-Cotisel**,** I. Albu, A. Mocanu, M.-I. Salajan, Cs. Racz, V.D. Pop, “Experimental Methods in Chemistry and Biophysics of Colloids and Interfaces”, *University Press,* Cluj-Napoca, 2004.
2. M.-I. Salajan, A. Mocanu, M. Tomoaia-Cotisel**,** “Progresses in Thermodynamics, Hydrodynamics and Biophysics of Thin Layers", University Press*,* Cluj-Napoca, 2004.
3. J. L. Gallani, S. Mery, Y. Galerne, D. Guillon, *J. Phys. Chem.,* B **2004**, *108*, 11627-11632.
4. L. Villalobos, Y. M. Lopez-Alvarez, B. Pastrana-Rios, G. E. Lopez, *J. Chem. Phys.,* **2005,** *122*, 104701, p.1-6
5. M. Tomoaia-Cotişel, P.J. Quinn, Chapter 10: “Biophysical Properties of Carotenoids". In: P.J.Quinn and V. Kagan (Eds.): “Subcellular Biochemistry, Vol.30: Fat-Soluble Vitamins”, Plenum Press, New York, 1998, pp. 219-242.
6. C.N. N’soukpoe-Kossi, J. Sielewiesiuk, R. M. Leblanc, R. A. Bone and J. T. Landrum, *Biochim. Biophys. Acta*, **1988**, *940*, 255-265.
7. M. Tomoaia-Cotişel, "Study on films of natural pigments and lecithins", *Ph. D. - Thesis, "Babeş-Bolyai" University of Cluj-Napoca*, **1979**, p. 178,.
8. M. Tomoaia-Cotişel, E. Chifu, *Rev. Chim. (Bucharest)*, **1981,** *32*, 1063-1069.
9. M. Tomoaia-Cotişel, E. Chifu, V. Tămaş, V. Mărculeţiu, *Rev. Roumaine Chim.*, **1980,** *25*, 175-180.
10. M. Tomoaia-Cotişel, J. Zsakó, E. Chifu, D. A. Cadenhead, *Langmuir*, **1990**, *6*, 191-197.
11. M. Tomoaia-Cotişel, E. Chifu, *J. Colloid Interface Sci.*, **1983**, *95*, 355-361.
12. M. Tomoaia-Cotişel, J. Zsakó, E. Chifu, P. J. Quinn, *Biochem. J.*, **1987**, *248*, 877-882.
13. J. Zsakó, M. Tomoaia-Cotişel, E. Chifu, *J. Colloid Interface Sci.*, **1991**, *146*, 353-362.
14. A. Shibata, Y. Kiba, N. Akati, K. Fukuzawa, H. Terada, *Chem. Phys. Lipids,* **2001,** *113*, 11-22.
15. M. Tomoaia-Cotişel, J. Zsakó, M. Sălăjan, E. Chifu, in A. Pullman, V. Vasilescu, and L. Packer (Eds.): “Water and Ions in Biological Systems”, Union of Societies for Medical Sciences, Bucharest, 1985, pp. 371-381.

16. E. Chifu, J. Zsakó, M. Tomoaia-Cotişel, M. Sălăjan, I. Albu, *J. Colloid Interface Sci*., **1986**, *112*, 241-251.
17. E. Chifu, M. Sălăjan, M. Tomoaia-Cotişel, I. Demeter-Vodnár, J. Zsakó, *Studia Univ. Babes-Bolyai, Chem*., **1987,** *32*, 50-57.
18. M. Tomoaia-Cotişel, J. Zsakó, M. Sălăjan, E. Chifu, *Rev. Roum. Morphol. Embryol. Physiol., Physiology*, **1989,** *26*, 341-347.
19. J. Zsakó, E. Chifu, M. Tomoaia-Cotişel, *Gazz. Chim. Ital.*, **1979**, *109*, 663-668.
20. J.Zsakó, V. Neagu, M.Tomoaia-Cotişel, E.Chifu, *Rev.Roum.Chim.*, **1987**, *32*, 739-748.
21. E. Chifu, M. Tomoaia-Cotişel, in "*Surfactants in Solution",* (K. L. Mittal and B. Lindman, Eds.), Vol. 2, Plenum Press, New York, 1984, pp. 1349-1364.
22. O. Isler, "Carotenoids", Birkhäuser Verlag, Basel, **1971**, p.286
23. O. Horovitz, G. Tomoaia, Cs. Racz, A. Mocanu, L.-D. Bobos, M. Tomoaia-Cotisel, *Central European Journal of Chemistry*, CEJC **2006**, *4*, 489–501.
24. M.J.S. Dewar, E.G. Zoebisch, E.F. Healy, J.J.P. Stewart, *J. Amer. Chem. Soc.*, **1985**, *107*, 3902-3909
25. J.J.P. Stewart, *J. Comput. Chem*., **1989**, *10*, 209-220
26. HyperChem7.5 Molecular Modeling System, Hypercube Inc., Gainesville, 2002
27. J. Zsako, M. Tomoaia-Cotisel, E. Chifu, in K.L. Mittal (Ed.): *Surfactants in Solution*, Vol. 9, Plenum Press, New York, 1989, pp 311-324.
28. M. Tomoaia-Cotisel, C. Racz, G. Tomoaia, C. Floare, R. Totos, L. Bobos, O. Pascu, A. Dumitru, *Studia Univ. Babes-Bolyai, Chem.*, **2005,** *50*, 39-45.

STUDIA UNIVERSITATIS BABES - BOLYAI, CHEMIA, LI, 2, 2006

Dedicated to professor Gh. Marcu at his 80th anniversary

HEMES REVISITED BY DENSITY FUNCTIONAL APPROACHES. 2. A PARADIGM FOR AXIAL LIGATION IN HEMOPROTEINS

RADU SILAGHI-DUMITRESCU*

ABSTRACT. Reported here are DFT descriptions of dioxygen reduction at the active site of cytochr]ome cd_1 nitrite reductase, an enzyme with a histidine-ligated heme active site, known to act as cytochrome oxidase. Also explored is the possibility of nitric oxide reduction by histidine-ligated hemes. The energetics of these two processes correlate well with previous findings on other hemoproteins, and allow further elaboration on the newly proposed "thiolate obstruction" theory *[Silaghi-Dumitrescu, Eur. J. Inorg. Chem. 2003, 1048]*. This theory, orthogonal if not opposed to the classical "thiolate push" dogma *[Dawson et al., J. Am. Chem. Soc. 1976, **98**, 3707]* , argues that efficient reduction of diatomics such as dioxygen and nitric oxide is more readily accomplished by histidine-ligated hemes than by thiolate– ligated hemes. Generalizing, for reductive processes involving a small diatomic as the sole substrate, neutral ligands (e.g., histidine in cytochrome oxidases and heme oxygenase, lysine in cytochrome *c* nitrite reductase) are found to always be preferable over anionic ligands. By contrast, in enzymes designed to deal with more than one substrate, anionic ligands are preferable (e.g., cysteine or tyrosine in monooxygenases), since they allow the safety switches needed to avoid uncoupling in their race against entropy.

INTRODUCTION

Proteins such as cytochrome P450 (P450), horseradish peroxidase (HRP) or hemoglobin are all known to bind and/or reduce (activate) dioxygen at their heme active sites, in the ferrous form.[1-11] The thiolate-ligated ferrous heme of P450 binds dioxygen and promotes proton-dependent O-O bond cleavage following a one-electron reduction.[1] By contrast, the ferrous histidine-ligated heme of hemoglobin only binds dioxygen in a reversible manner.[12] Hemoprotein ferric-hydroperoxo complexes decay via proton-assisted heterolytic cleavage of the O-O bond to yield water and a $[Fe=O]^{3+}$ unit (known as Compound I), where the iron is considered to be in the formal oxidation state +4 and a further oxidizing equivalent is proposed to be delocalized onto the porphyrin. Two active-site "distal" residues, a histidine and an arginine, are crucial in promoting O-O bond cleavage in the ferric-hydroperoxo complex of canonical (histidine-ligated) peroxidases. The hemoglobin active site lacks the distal arginine and is much less efficient than HRP at activating peroxide.[1-10] The heme-thiolate active site of P450 does not contain the histidine-arginine catalytic pair of HRP, yet still cleaves the O-O bond of its ferric-hydroperoxo complex

* Department of Chemistry, "Babes,-Bolyai" University, Cluj-Napoca RO-400028, Romania, and Department of Biological Sciences, University of Essex, Colchester, UK

(using water molecules as the source of protons). These differences between thiolate and histidine-ligated hemes are traditionally rationalized in terms of the thiolate ligand being able to push electron density more efficiently onto the iron-dioxygen moiety, thereby facilitating O-O bond cleavage ("the push effect").[10, 11, 13]

Notable exceptions to the thiolate/histidine rule also exist. Cytochrome oxidases, which accomplish four-electron reduction of dioxygen to water, feature histidine and not thiolate ligands.[14] Heme oxygenase, which reduces dioxygen to hydroperoxide, also features a histidine ligand.[15]

Nitric oxide reduction by thiolate-ligated heme (in cytochrome P450 nitric oxide reductase, P450nor) and by lysine-ligated heme (in cytochrome c nitrite reductase, CcNIR) may either involve two one-electron reduction steps, $[FeNO]^{3+} \rightarrow [FeNO]^{2+} \rightarrow [FeNO]^{+}$, or one two-electron reduction step, $[FeNO]^{3+} \rightarrow [FeNO]^{+}$; both mechanisms involve concomitant or subsequent protonation of the NO ligand.[16] The one-step mechanism is now generally accepted for P450nor (where subsequent addition of a second NO molecule results in generation of N_2O), whereas the two-step mechanism is active with CcNIR (where the NO ligand is subsequently further reduced to NH_3 and H_2O).[16, 17] The choice for a one-step, 2-electron mechanism in P450nor was rationalized by differences in thermodynamics: the thiolate heme-NO adduct is more electron rich and therefore a second one-electron reduction would be harder to accomplish than with a lysine-ligated heme. Indeed, this second one-electron reduction was found to be, at least in gas-phase calculations, energetically uphill with thiolate and energetically downhill with lysine. Thus, although the "thiolate push" dogma[1, 13] would link thiolate axial ligands to more facile activation of diatomics, we found the opposite to be true for nitric oxide activation ("thiolate obstruction"). Accordingly, the electrons required for nitric oxide reduction in thiolate-ligated P450nor are directly supplied by the hydride (2-electron) donor NADH, whereas in CcNIR the electrons are supplied by neighboring hemes, in a one-electron fashion.[16, 17]

The "thiolate obstruction" theory further developed upon comparing one-electron reduction of formally ferrous-dioxygen species to formally ferric-peroxo.[11, 16] There too, gas-phase reduction was thermodynamically uphill with anionic ligands (thiolate, phenoxide, imidazolate), but thermodynamically downhill with a neutral ligand (imidazole, or no ligand at all). When the same calculations were performed in a solvent of ε~4.3 rather than in gas-phase, thus mimicking an enzyme active site, the differences between histidine and anionic models were diminished to some extent, but the histidine still remained clearly more adept at favoring one-electron reduction of the ferrous-dioxygen adduct.[11] P450, which features an anionic thiolate ligand to the heme, activates dioxygen specifically for oxygen atom insertion into an organic substrate (monooxygenase chemistry). It is then desirable that dioxygen reduction only occur in the presence of substrate, to avoid the wasteful/toxic reduction of dioxygen known as uncoupling.[1] The thiolate, and anionic ligands in general, thus offers the possibility of an extra safety switch, that ensures maximum catalytic activity in systems fighting entropy (i.e., relying on the concomitant presence of more than one substrate at the active site).

Cytochrome cd_1 nitrite reductase (cd1NIR) is known to efficiently reduce dioxygen to water at its heme d_1 active site, thus acting as a soluble cytochrome oxidase.[18] The axial heme ligand in cd1NIR is a histidine. In line with our previous findings on heme *b* models, we expect one–electron reduction of the cd1NIR ferrous-dioxygen adduct to be energetically very favorable. To verify this, and to investigate the extent to which the heme d_1 may alter the properties of the ferrous-dioxygen adduct and of its reduced congeners, we report here DFT geometry optimization results on models of the cd1NIR ferrous-dioxygen, reduced ferrous-dioxygen, and ferric-hydroperoxo adducts.

Also elaborating on our "thiolate obstruction" theory, we report DFT geometry optimization results for models consisting of a histidine-ligated *b* heme coordinated by nitric oxide, in three oxidation states: Fe(III)-NO, Fe(II)-NO, and Fe(II)-NO^-; for the latter model, the two protonated states, Fe(II)-N(H)-O and Fe(II)-N-O-H are also investigated. These heme *b* models mimic the nitric oxide adducts of myoglobin, and, in addition to corroborating the "thiolate obstruction" theory, they provide insight into myoglobin's ability to perform nitric oxide reductase chemistry.

METHODS

Geometries for all models were optimized without any constraints with the UBP86 functional, which uses the gradient-corrected exchange functional proposed by Becke (1988),[19] the correlation functional by Perdew (1986),[20] and the DN** numerical basis set (comparable in size to 6-31G**) as implemented in Spartan.[21] For the SCF calculations, a fine grid was used, and the convergence criteria were set to 10^{-6} (for the root-mean square of electron density) and 10^{-8} (energy), respectively. For geometry optimization, convergence criteria were set to 0.001 au (maximum gradient criterion) and 0.0003 (maximum displacement criterion). Partial atomic charges and spin densities were derived from Mulliken population analyses.

Low-spin states (S=0, S=1/2) were assumed for all models, in line with previous experimental and theoretical findings.[11, 16, 18, 22]

RESULTS AND DISCUSSION

Table 1 and Figure 1 show geometry optimization results for cd1NIR models. Overall, the optimized geometries are consistent with crystal structure of the ferrous-dioxygen cd1NIR.

The models in Figure 1 feature a non-planar heme. This is consistent with our previous findings[11] on dioxygen/peroxo heme *b* models. Conversely, the heme was calculated to be essentially planar in the nitric oxide and nitrite adducts of cd1NIR.[18, 23] Data in Table 1 are very similar to those previously reported on equivalent heme *b* models,[11] thus suggesting that the unusual heme d_1 at the active site of cd1NIR does not alter the heme-iron-dioxygen/peroxo chemistry to any significant extent. Importantly, one-electron reduction of the formally ferrous-dioxygen species is still significantly "exothermic", confirming our "thiolate obstruction" theory. Consistent with previous findings[11] on related heme systems, $[FeO_2]^{2+}$ cd1NIR appears as a ferrous-dioxygen/ferric-superoxo hybrid. $[FeO_2]^+$ cd1NIR features one unpaired electron on the oxygen atoms and in this respect is best described as a superoxo adduct rather than peroxo. Assigning the iron in $[FeO_2]^+$ as ferrous may at this stage be tempting; however, a ferric-superoxo description (with one extra electron delocalized onto the porphyrin, and with the iron and porphyrin unpaired electrons strongly covalently coupled) is more likely.[11]

Figure 1. Geometry-optimized structures for (from left to right): formally ferrous-dioxygen ($[FeO_2]^{2+}$), ferric-peroxo ($[FeO_2]^{+}$]), and ferric-hydroperoxo ($[FeO_2H]^{2+}$) cd1NIR adducts.

Table 1.

Energies (a.u.), distances (Å), partial atomic charges and spin densities (the latter shown in parentheses) for formally ferrous-dioxygen ($[FeO_2]^{2+}$), ferric-peroxo ($[FeO_2]^{+}$]), and ferric-hydroperoxo ($[FeO_2H]^{2+}$) cd1NIR adducts.

	energy	Fe-O	O-O	Fe-N	Fe	O1	O2	OOH
$[FeO_2]^{2+}$	-2780.07420	1.78	1.28	2.11	0.48	-0.02	-0.15	-0.17
$[FeO_2]^{+}$	-2780.16461	1.90	1.31	2.15	0.46 (-0.07)	-0.13 (0.42)	-0.24 (0.52)	-0.37 (0.94)
$[FeO_2H]^{2+}$	-2780.69712	1.82	1.44	2.06	0.49 (0.56)	-0.19 (0.34)	-0.22 (0.13)	-0.07 (0.47)

Table 2 and Figure 2 show geometry optimization results for the myoglobin iron-nitric oxide adducts. These results are consistent with our previous reports on similar models with thiolate, lysine, or with no axial ligand instead of the imidazole.[16] Importantly, one-electron reduction of the formally Fe(II)-NO species is significantly "exothermic", similar to ammonia-ligated models but unlike thiolate-ligated models – in line with the "thiolate obstruction" theory.[16]

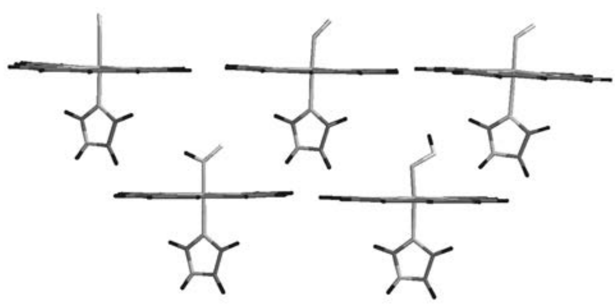

Figure 2. Optimized geometries for heme-histidine $[FeNO]^6$, $[FeNO]^7$, $[FeNO]^8$ (top row, from left to right), $[FeNHO]^8$, and $[FeNOH]^8$ adducts (bottom row, from left to right).

The $[FeNO]^6$ model features a significant amount of positive charge on the NO ligand and is thus best described as Fe^{2+}-NO^+, in line with previous assignments.[16] The $[FeNO]^7$ model features more electron density on the NO as well as a bent Fe-N-O unit, which is consistent with a Fe^{2+}-NO/Fe^{3+}-NO^- hybrid – again as previously assigned in related models.[16] The $[FeNO]^8$, $[FeNHO]^8$, and $[FeNOH]^8$ models all clearly feature an NO^- ligand, implying a ferrous center as previously assumed.[16] However, we note that, as in all other heme complexes examined to date,[11, 16, 22, 24] the bulk of the two electrons upon going from $[FeNO]^6$ to $[FeNO]^8$ is in fact not found on the NO, even though formal changes in oxidation state of the NO ligand from +1 to -1 cannot be negated. There is thus a distinction between *formal oxidation state*, which changes for NO from +1 to -1 upon going from $[FeNO]^6$ to $[FeNO]^8$, and *electron density*, which in fact varies less on the NO ligand and more on the porphyrin – even though the latter cannot be claimed to undergo any formal change in oxidation state.[22]

Table 2.

Energies (a.u.), distances (Å), partial atomic charges and spin densities (the latter shown in parentheses) for heme-histidine $[FeNO]^6$, $[FeNO]^7$, $[FeNO]^8$, $[FeNHO]^8$, and $[FeNOH]^8$ adducts.

	energy	Fe-NO	N-O	Fe-N	Fe-N-O	Fe	N	O	NO(H)
$[FeNO]^6$	-2608.96248	1.65	1.15	2.05	179	0.48	0.28	0.01	0.29
$[FeNO]^7$	-2609.16404	1.75	1.19	2.15	140	0.49 (0.57)	0.13 (0.26)	-0.13 (0.15)	0.00 (0.41)
$[FeNO]^8$	-2609.21773	1.81	1.21	2.41	123	0.51	0.02	-0.22	-0.20
$[FeNHO]^8$	-2609.76451	1.79	1.24	2.13	131	0.52	0.07	-0.24	0.04
$[FeNOH]^8$	-2609.73346	1.72	1.38	2.20	116	0.55	-0.07	-0.22	0.00

Data on the protonated models, $[FeNHO]^8$ and $[FeNOH]^8$, is particularly important, since a protonated $[FeNO]^8$ species has indeed been isolated at the histidine-ligated *b* heme of myoglobin.[25] Table 2 confirms that, as previously proposed,[25] the proton must lie on the nitrogen rather than on the oxygen atom. Second, examining partial atomic charges and bond lengths in $[FeNHO]^8$, we find all parameters to be consistent with previously described thiolate-ligated heme $[FeNHO]^8$.[16] Based on knowledge on the reactivity of this latter thiolate system,[16] the myoglobin $[FeNHO]^8$ adduct should also react with a second NO molecule, thereby generating N_2O and H_2O. Indeed, evidence for such a reaction in myoglobin was available experimentally and has to this date not been rationalized.[25] This N_2O production by myoglobin appears however to be slow and incomplete; this deficiency is likely due to three factors. Firstly, myoglobin lacks good proton donors at the active site; two protons are in fact needed to convert $[FeNHO]^8$ + NO into N_2O and H_2O. Secondly, the myoglobin heme site is relatively small and designed to bind *one*, rather than two diatomics.[12] Thirdly, myoglobin is not designed to receive electrons from biological electron-transfer agents in a rapid and efficient manner.[12] By contrast, the P450nor active site is designed to allow unrestricted contact between the NADH hydride donor to the Fe-NO adduct, and is also large enough to accommodate entry of a second NO molecule – as required for N_2O formation.[16]

CcNIR, cd1NIR and respiratory cytochrome oxidases feature additional heme groups, which are located very close to the catalytic active site and deliver electrons immediately after initial binding of the diatomic substrate (NO or O_2).[16, 17]

The energetics of the two processes examined here, dioxygen reduction by cd1NIR and nitric oxide reduction by myoglobin, correlate well with previous findings on other hemoproteins, and allow us to better elaborate on our newly proposed “thiolate obstruction” theory. This theory, orthogonal if not opposed to the classical “thiolate push” dogma, argues that efficient reduction of diatomics such as dioxygen and nitric oxide is more readily accomplished by histidine-ligated hemes than by thiolate– ligated hemes. Generalizing, for reductive processes involving a small diatomic as the sole substrate, neutral ligands (e.g., histidine in cytochrome oxidases and heme oxygenase, lysine in cytochrome c nitrite reductase) are found to always be preferable over anionic ligands. By contrast, in enzymes designed to deal with more than one substrate, anionic ligands (e.g., the cysteine or tyrosine in heme-containing monooxygenases) are preferable, since they allow the safety switches needed to avoid uncoupling in their race against entropy.

ACKNOWLEDGMENT

Dr. Ioan Silaghi-Dumitrescu is thanked for helpful discussions.

REFERENCES

1. M. Sono, M. P. Roach, E. D. Coulter and J. H. Dawson, *Chem. Rev.* **1996**, *96*, 2841-2887.
2. I. S. Isaac and J. H. Dawson, *Essays Biochem.* **1999**, *34*, 51-69.
3. H. B. Dunford in *HRP*, *Vol. II* ('Ed.'^'Eds.' M. B. Grisham), CRC Press, Boca Raton, **1991**, p.^pp. 2-17.
4. D. M. Kurtz Jr., *Essays Biochem.* **1999**, *34*, 55-80.
5. R. Davydov, T. M. Makris, V. Kofman, D. E. Werst, S. L. Sligar and B. M. Hoffman, *J. Am. Chem. Soc.* **2001**, *123*, 1403-1415.
6. R. M. Davydov, T. Yoshida, M. Ikeda-Saito and B. M. Hoffman, *J. Am. Chem. Soc.* **1999**, *121*, 10656-10657.
7. A. N. P. Hiner, E. L. Raven, R. N. F. Thorneley, G. Garcia-Canovas and J. N. Rodriguez-Lopez, *J. Inorg. Biochem.* **2002**, *91*, 27-34.
8. G. I. Berglund, G. H. Carlsson, A. T. Smith, H. Szoke, A. Henriksen and J. Hajdu, *Nature* **2002**, *417*, 463-468.
9. I. Schlichting, J. Berendzen, K. Chu, R. M. Sweet, D. Ringe, G. A. Petsko and S. G. Sligar, *Science* **2000**, *287*, 1615-1622.
10. F. Ogliaro, S. deVisser and S. Shaik, *J. Inorg. Biochem.* **2002**, *91*, 554-567.
11. R. Silaghi-Dumitrescu and I. Silaghi-Dumitrescu, *Rev. Roum. Chim.* **2004**, *3-4*, 257-268.
12. D. M. Kurtz, Jr., *Essays Biochem.* **1999**, *34*, 55-80.
13. J. H. Dawson, R. H. Holm, R. H. Trudell, G. Barth, R. E. Linder, E. Nunnernberg, C. Djerassi and S. C. Tang, *J. Am. Chem. Soc.* **1976**, *98*, 3707.
14. C. E. Cooper, N. A. Davies, M. Psychoulis, L. Canevari, T. E. Bates, M. S. Dobbie, C. S. Casley and M. A. Sharpe, *Biochim. Biophys. Acta* **2003**, *1607*.
15. P. K. Sharma, R. Kevorkiants, S. P. deVisser, D. Kumar and S. Shaik, *Angew. Chem. Int. Ed.* **2004**, *43*, 1129-1132.

16. R. Silaghi-Dumitrescu, *Eur. J. Inorg. Chem.* **2003**, 1048-1052.
17. O. Einsle, A. Messerschmidt, R. Huber, P. M. H. Kroneck and F. Neese, *J. Am. Chem. Soc.* **2002**, *124*, 11737-11745.
18. R. Silaghi-Dumitrescu, *Inorg. Chem.* **2004**, *43*, 3715-3718.
19. A. D. Becke, *Phys. Rev.* **1988**, 3098-3100.
20. J. P. Perdew, *Phys. Rev.* **1986**, *B33*, 8822-8824.
21. *Spartan 5.0, Wavefunction, Inc., 18401 Von Karman Avenue Suite 370, Irvine, CA 92612 U.S.A*.
22. R. Silaghi-Dumitrescu, *J. Biol. Inorg. Chem.* **2004**, *9*, 471-476.
23. R. Silaghi-Dumitrescu, *Rev. Chim.* **2004**, *55*, 496-498.
24. R. Silaghi-Dumitrescu, *Arch. Biochem. Biophys.* **2004**, *424*, 137-140.
25. F. Sulc, C. E. Immoos, D. Pervitsky and P. J. Farmer, *J. Am. Chem. Soc.* **2004**, *126*, 1096-1101.

Dedicated to professor Gh. Marcu at his 80th anniversary

CATALYTIC SYNTHESIS OF DIMETHYL CARBONATE FROM METHANOL AND CARBON DIOXIDE

JENŐ BÓDIS[1] AND GEORGE A. OLAH[2]

ABSTRACT. The direct synthesis of dimethyl carbonate (DMC) from carbon dioxide and methanol, or dimethyl ether, in presence of magnesium and aluminum methoxide as catalysts was studied. The reactions were performed under batch conditions with catalysts in homogeneous liquid phase of excess methanol (no other solvent was used) at different partial pressures of carbon dioxide and at different temperatures. Depending on the reaction conditions and using magnesium methoxide as catalyst, dimethyl carbonate in 2-7% yield was detected.

Keywords: Dimethyl carbonate; Carbon dioxide activation; Homogeneous catalysis; Magnesium methoxide

INTRODUCTION

The versatile chemical property of dimethyl carbonate (DMC) makes it useful as a phosgene equivalent as well as a methylating and methoxycarbonylating agent [1-3]. On the other hand, replacing hazardous compounds is one of the many goals of environmental chemistry [3].

DMC can also be used as an additive in gasoline to improve fuel combustion and reduce automotive emissions [4]. Formaldehyde emissions were also lower with DMC as octane enhancer than with MTBE.

The industrial synthesis of DMC was based on phosgene [3].

$$ClCOCl + 2\,CH_3OH \rightarrow (CH_3O)_2CO + 2\,HCl$$

In the Enichem synthesis the $CuCl/CuCl_2$ catalyzed oxidative carbonylation reaction of methanol to DMC is used [1,3,4].

$$CH_3OH + 1/2O_2 + CO \rightarrow (CH_3O)_2CO + H_2O$$

Despite the fact that the Enichem process looks very feasible, the reaction is still subject of intensive studies. Kricsfalussy *et. al.* [5] tested molten CuCl-KCl salts as catalysts, Cavinato *et. al.* [6] Pd complexes, and Delledonne *et. al.* [7] Schiff base Co

1 "Babes-Bolyai" University, "Babes-Bolyai" University, Department of Organic Chemistry, Arany János 11, 400028 Cluj, Romania,E-mail: jbodis@chem.ubbcluj.ro, Fax: 40-264-590818

2 Donald P. and Katherine B. Loker Hydrocarbon Research Institute,University of Southern California, Los Angeles, CA 90089-1661, USA

complexes. A Japanese patent [8] reports a complex catalytic system ($PdBr_2$-CuBr-KBr) in the presence of quinones and $KOOCCH_3$, with modest yields at atmospheric pressure. Relatively good space-time yields were obtained by gas phase oxidative carbonylation of methanol over ($PdCl_2$-$CuCl_2$-CH_3COOK)/activated carbon catalytic system [9]. Transition metal (Cu, Pd, Co, Rh) based catalytic systems [10] have been found to catalyze the electrochemical oxidative carbonylation of methanol.

UBE Chemical Industries [1,3,4,11] developed a pilot plant process for DMC production that uses the carbonylation of methyl nitrite over metal halides (Pd+Fe, Cu, Co, Ni or Sn) supported on active carbon.

$$CO + 2\,CH_3ONO \rightarrow (CH_3O)_2CO + 2\,NO$$

$$2\,NO + 2\,CH_3OH + \tfrac{1}{2}\,O_2 \rightarrow 2\,CH_3ONO + H_2O$$

Texaco Chemical [12-14] realized the coproduction of DMC and ethylene glycol through the transesterification of ethylene carbonate with methanol.

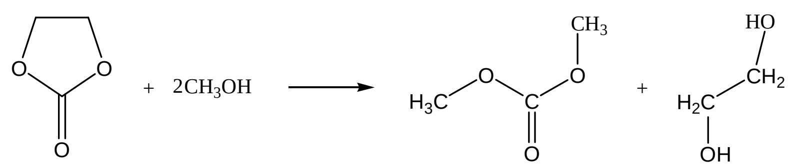

Titanium silicate molecular sieve (TS-1), exchanged with an aqueous solution of K_2CO_3 is described to be an excellent catalyst for the above transesterification reaction [15], reaching 57% yield (based on ethylene carbonate) of DMC. Some reports [16-18] claimed that by carrying out the transesterification of alkylene carbonates with methanol in presence of carbon dioxide, part of the methanol was reacting directly with CO_2 to DMC. However, the selectivity was very low and involved significant problems during separation.

The present work focuses on direct synthesis of DMC from carbon dioxide, an environmentally friendly building block, and methanol or dimethyl ether, cheap and available feedstocks of the chemical industry. Both reactions are thermodynamically unfavorable having positive ideal gas phase free energy changes (ΔG) at 100 ºC.

$$2\,CH_3OH + CO_2 \rightarrow (CH_3O)_2CO + H_2O \qquad \Delta G_{100ºC} = +12.2\ \text{kcal/mol}$$

$$CH_3OCH_3 + CO_2 \rightarrow (CH_3O)_2CO \qquad \Delta G_{100ºC} = +15.1\ \text{kcal/mol}$$

There are only few publications dealing with the reaction of carbon dioxide and methanol [19-29], and no literature report was found on the dimethyl ether reaction route. In almost all cases, the reported DMC yields were based on the amount of catalyst used. Using $Bu_2Sn(OCH_3)_2$ as catalyst [19], a 50% DMC yield was reached at 100 ºC and 5 bar CO_2 pressure after 24 hours reaction time. In the presence of thallium compounds (ethoxide, or oxide) [20], only low reaction performances were detected (*e.g.* 20 cm^3 CH_3OH resulted only 67-68 mg DMC, corresponding to 0.3% DMC yield based on used methanol). $Bu_2Sn(OBu)_2$-NaBr, $Sn(OBu)_4$-NaBr, and $Ti(OBu)_4$-NaBr systems are described as good catalysts, especially in the presence of dicyclohexylcarbodiimide as water scavenger [21-23] reaching 0.5- 2.68 % DMC yields based on methanol after 20 hours reaction time at

150 ºC and 25-60 bar. Basic catalysts (K_2CO_3, Na_2CO_3, Cs_2CO_3, K_3PO_4, and $(CH_3)_4NOH$) applied together with CH_3I as promoter [24] gave high DMC yield in reactions carried out at 100 ºC and 50 bar CO_2 pressure for 2 hours. Part of the CH_3I promoter is also consumed, making it difficult to evaluate the DMC yield based on the amount of methanol introduced into the reaction mixture. Nevertheless, in the case of K_2CO_3, DMC was obtained even in the absence of CO_2 as reactant.

Without any experimental data regarding the amount of methanol, carbon dioxide, or catalyst used, a short publication [25] claimed 30 % conversion and 99% selectivity after 12 hours reaction time by using *in situ* prepared magnesium methoxide at 180 ºC and at ~15 bar CO_2 pressure.

Results on the use of zirconia (ZrO_2) and zirconia promoted with phosphoric acid as catalysts for direct synthesis of DMC from methanol and CO_2 were also reported [26,27]. The maximum DMC yield (based on methanol) was found to be ~ 0.6% in case of zirconia and around 0.9% in case of promoted ZrO_2 catalysts.

The aim of our present contribution was to find effective catalysts or catalytic systems, and to establish the optimum reaction parameters for the direct conversion of carbon dioxide and methanol to DMC, a high scale required product both as reactant for chemical synthesis, and as gasoline octane enhancing additive.

EXPERIMENTAL

The carboxylation of methanol with carbon dioxide to dimethyl carbonate was carried out in a Parr autoclave (120 cm^3) operated at 10-150 bar and 25 - 180 ºC. Magnetic stirring at a speed of 1100 rpm was used. Weighed amount of catalysts were introduced into the autoclave. After addition of the dry methanol (usually 0.5 - 1.0 mol, Mallinkrodt, AR), the autoclave was sealed, and flushed with nitrogen or helium to remove atmospheric oxygen. The inside temperature was measured by a thermocouple. Carbon dioxide (Air Gas, research grade) was introduced in two different ways:

1.- at room temperature until ~10-55 bar total pressure and the autoclave was then placed in a thermostat bath preset to the reaction temperature.

2. - by adding carbon dioxide only after the catalyst-methanol mixture reached the desired reaction temperature. In this case the reactions had a well-defined starting time.

In the case of *in-situ* prepared methoxide catalysts, both versions were applied, but most experiments were run by introducing carbon dioxide only after the methoxide was prior formed at a higher temperature (1-2 hours at 200-210 ºC for $Mg(OCH_3)_2$ and 220-230 ºC for $Al(OCH_3)_3$). The progress of reaction in time was evaluated from the carbon dioxide consumption (added from a well-known volume reservoir keeping the working pressure in the autoclave constant). After the reaction was terminated, the autoclave was cooled to 0 ºC in a water-ice bath, and the carbon dioxide vented carefully before opening the reaction vessel.

The reactants and products were analyzed using a Hewlett Packard 5971 mass spectrometer and Varian 3300 gas chromatograph equipped with a DB 5, or HP 1 capillary columns and FID detector. When the product mixture appeared as a suspension, filtering was employed before analysis. In most cases of metal methoxide containing mixtures, distillation was applied for the separation of volatile liquid compounds (mostly DMC and methanol) from dissolved catalyst. The water content of the reaction mixture (H_2O formation is supporting the catalytic pathway of the reaction between methanol and CO_2 in presence of methoxide) was analyzed by a gas chromatograph equipped with TCD detector.

RESULTS AND DISCUSSION

The reaction of dimethyl ether with carbon dioxide was checked in different experiments realized at 20 - 180 ºC and 20 - 150 bar with catalysts such as MgO in DMF, $Pd(PPh_3)_4$ in toluene, $Cr(CO)_6$ in pyridine, and magnesium methoxide in methanol. None of these experiments provided positive results. In order to achieve the DMC synthesis from methanol and carbon dioxide, a great number of attempts were carried out at temperatures and pressures mentioned above by testing different catalysts (Et_3N, PPh_3, MgO, $Ru_3(CO)_{12}$, $Pd(PPh_3)_4$, CuPhtc, 5% Rh/C, 10% Pd/C, 5% $Pd/BaCO_3$) and catalytic systems (5% Rh/C + CuCl + KCl, 5% Rh/C + PPh_3 + CH_3I, 5% Rh/C + Et_3N, 5% Rh/C + MgO, 5% Rh/C + Et_3N + CuCl, 5% $Pd/BaCO_3$ + Et_3N, 10% Pd/C + Et_3N). However, the catalysts tested were not able to produce measurable amount of DMC. Tin compounds (SnO_2, $(CH_3)_3SnCl$) were also unsuccessful, as well.

The experimental conditions of our first successful experiments and the results obtained for the conversion of methanol to DMC upon treatment with carbon dioxide are compiled in Table 1. The magnesium methoxide catalysts were prepared *in-situ* from Mg (turnings, Mallinckrodt, AR) and absolute methanol under the depicted reaction conditions, carbon dioxide being present from the beginning. Analyses were done without any preliminary separation by injecting samples in GC, and MS respectively.

Table 1

Reaction conditions and results for the synthesis of DMC from methanol (or dimethyl ether) and carbon dioxide in the presence of magnesium methoxide catalyst prepared *in situ* from Mg and methanol at the reaction conditions.

n_{MeOH} (mol)	n_{MeOMe} (mol)	n_{Mg} (mol)	p_{CO2} (bar)	T_{react} (ºC)	p_{react} (bar)	t_{react} (h)	Y_{DMC}/MeOH (%)	Y_{DMC}/cat (%)
0.50	0.00	0.04	30	170	80	3	1.9	9.7
0.50	0.00	0.04	30	180	130	4	3.2	16.0
0.10	0.10	0.03	35	180	150	5	0.0	0.0

Y_{DMC}/MeOH: yield, molar percentage of methanol converted to DMC.
Y_{DMC}/cat: yield, molar percentage of DMC reported to the amount of catalyst.

As is shown in Table 1, only very low yields of DMC could be detected. By adding dimethyl ether, even the transformation of methanol was blocked.

In the next series of experiments (see Table 2), the magnesium methoxide was prepared in advance by stirring metallic magnesium with methanol at 200 ºC for at least 1 hour, cooling the mixture at the desired reaction temperature, than adding carbon dioxide and running the reaction at constant temperature. Analyses still were done on crude reaction mixtures.

Table 2

Reaction conditions and results for the synthesis of DMC from methanol and carbon dioxide (added only at the desired reaction temperature) in the presence of magnesium methoxide catalyst prepared previously *in-situ* from Mg and methanol at 200 ºC.

n_{MeOH} (mol)	n_{Mg} (mol)	t_{react} (h)	Y_{DMC}/MeOH (%)	Y_{DMC}/cat (%)
0.50	0.05	5	1.9	7.5
0.50	0.04	12	4.3	22.6
0.50	0.04	12	4.6	24.0

p_{CO2}= 25 bar; T_{react} = 177 ºC; p_{react} = 55 bar
Y_{DMC}/MeOH: yield, molar percentage of methanol converted to DMC.
Y_{DMC}/cat: yield, molar percentage of DMC reported to the amount of catalyst.

As shown in Table 2, the preformed catalyst led to a small increase of DMC yields, about 1%. The increased amount of magnesium didn't have a benefic effect on the reaction as part of the magnesium was found untransformed in the crude product mixture. Of course, the lower reaction time can be also a reason for the lower yield, as well.

In order to eliminate the analyses difficulties (needle blocking, reactions induced by the methoxide in the GC injector), the resulted reaction mixtures of the next experiments were separated by distillation before analysis. The yields included in Table 3 are dependent on reaction temperatures and pressures.

Table 3

Reaction conditions and results for the synthesis of DMC from methanol and carbon dioxide (12 hrs reaction time) catalyzed by magnesium methoxide preformed *in-situ* from Mg and methanol at 200 C. Carbon dioxide (p_{CO2} = 50 bar) was added to the CH_3OH-$Mg(OCH_3)_2$ mixtures at 50 ºC.

Entry	n_{MeOH} (mol)	n_{Mg} (mol)	T_{react} (ºC)	p_{react} (bar)	Y_{DMC}/MeOH (%)	Y_{DMC}/cat (%)
1	0.50	0.04	50	50	0.0	0.0
2	0.50	0.04	100	67	0.0	0.0
3	0.50	0.04	150	85	2.7	14.4
4	0.50	0.04	160	92	5.0	26.2
5	0.50	0.04	170	98	6.7	35.3
6	0.50	0.04	180	106	7.2	37.6
7*	0.50	0.04	180	140	5.5	28.2
8	1.00	0.08	170	103	6.8	35.8
9	0.50	0.02	170	103	3.7	42.9

Y_{DMC}/MeOH: yield, molar percentage of methanol converted to DMC.
Y_{DMC}/cat: yield, molar percentage of DMC reported to the amount of catalyst.
*added 50 bar CO_2 at 25 ºC.

At low temperatures (50-100 ºC), the reaction practically did not work. Increase in temperature had a positive effect on the DMC yield, the maximum yield being detected at 180 ºC. However, the variation of yields had a higher slope in the range of 150 - 170 ºC than in the temperature range of 170 - 180 ºC. The problem encountered with these experiments was, that by going up with temperature, the partial pressures of methanol and especially CO_2, are rising up. Therefore, the positive effect on the DMC yield must be attributed to both parameters, temperature and pressure together. The diminished yields obtained at high partial pressures of carbon dioxide (140 bar total pressure, Entry 7), indicates that at a certain value of the CO_2 pressure, the catalyst can be carbonated, losing its activity. A decreased amount of catalyst is leading to lower DMC yield, but to a higher catalyst related yield (Entry 9).

The content of water was measured by GC-MS analysis in the product mixture (Entry 6) and it was found to be 056 mol/l water, lower than the concentration of DMC (0.88 mol/l). It appeared to us that part of water reacts with magnesium methoxide forming CH_3OH and $Mg(OH)_2$ and deactivating the catalyst. Nevertheless, the presence of water in the product mixture is supporting our initial assumption that the reaction should be catalytic and DMC was mainly formed by insertion of CO_2 in magnesium methoxide. The resulting adduct reacts with methanol leading DMC, water and the reformed magnesium methoxide (Scheme 1).

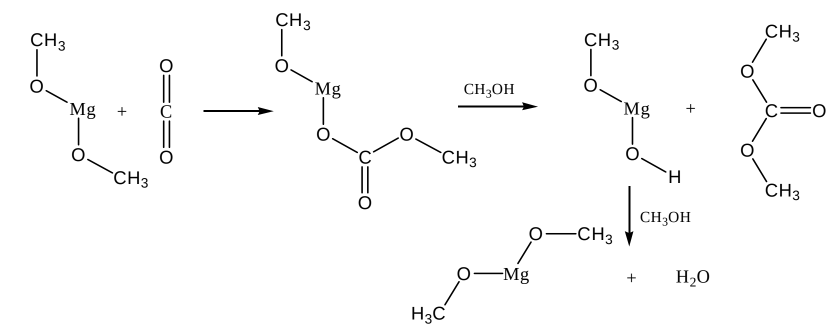

Scheme 1. Catalytic pathways during the formation of DMC from carbon dioxide and methanol in presence of magnesium methoxide.

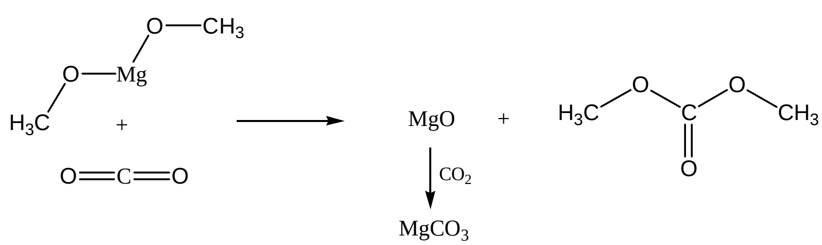

Scheme 2. Possible non-catalytic route for the formation of DMC through nonreversible reaction of magnesium methoxide with excess carbon dioxide.

However, at higher CO_2 pressures and higher temperatures (Entry 7), can be supposed another reaction route involving the $Mg(OCH_3)_2$ catalyst and CO_2, yielding DMC and $MgCO_3$ (Scheme 2). This reaction is also deactivating the catalyst and should be avoided during the DMC synthesis.

The upcoming experiments were done at different temperatures by using also preformed methoxide catalysts. CO_2 was introduced only when the methanol-magnesium methoxide mixture reached the desired reaction temperature. The reaction conditions and the obtained yields are given in Table 4.

Table 4

Reaction conditions and results for the synthesis of DMC from methanol and carbon dioxide (12 hrs reaction time) catalyzed by magnesium methoxide preformed *in-situ* from Mg or Al and methanol at 200 ºC and220 ºC respectively. Carbon dioxide (p_{CO2} = 20-25 bar) was added to the CH_3OH-methoxide mixtures only when the desired reaction temperature has been reached.

Entry	n_{MeOH} (mol)	n_M (mol)	T_{react} (ºC)	p_{react} (bar)	Y_{DMC}/MeOH (%)	Y_{DMC}/cat (%)
1	0.50	0.04	180	60	4.3	22.6
2	0.50	0.04	170	55	3.8	19.7
3	0.50	0.04	160	55	3.6	18.7
4	0.50	0.04	150	55	2.8	14.5
5*	0.50	0.04	170	55	0.4	1.7
6**	0.50	0.05	170	55	0.2	0.4

Y_{DMC}/MeOH: yield, molar percentage of methanol converted to DMC.
Y_{DMC}/cat: yield, molar percentage of DMC reported to the amount of catalyst.
*4 Å molecular sieve (Mallinckrodt) as water scavenger.
** Al as catalyst precursor.

Aluminum methoxide has also shown some activity (Entry 6). Although seen as a promising option, was not further explored in this study.

The use of a molecular sieve as water scavenger (Entry 5) had a negative effect on the reaction. Our finding is different from the almost neutral influence found for a 3Å molecular sieve on DMC formation over ZrO_2 catalyst [26], or from the positive effect of a 4Å molecular sieve revealed in case of DMC synthesis from methanol, carbon dioxide and methyl iodide mixture in presence of K_2CO_3 as catalyst [29].

At almost constant carbon dioxide partial pressures, an increase of temperature slowly increased the yields in the temperature range of 150-180 ºC (see Figure 1).

A few experiments of DMC synthesis were also realized by operating the batch pressure reactor in a continuous mode. Thus, with the help of a dip tube, a constant CO_2 flow was passed through the methoxide-methanol mixture keeping the pressure at 40–50 bar inside the autoclave, and continuously venting CO_2, DMC, CH_3OH, and water. Having the amount of distillate/time and the DMC content of the flux, we were able to evaluate the rate of DMC formation (turnover frequency, TOF = 0.08 - 0.1 mol_{DMC}/mol_{Mg}.h).

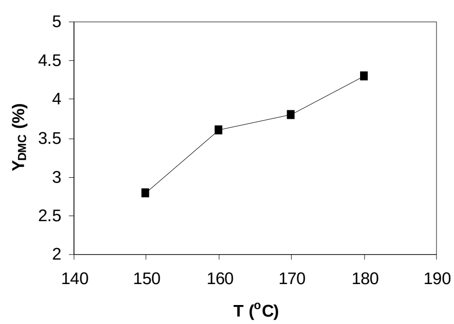

Figure 1. Effect of reaction temperature on the DMC yields under the conditions given in Table 4.

CONCLUSIONS

Magnesium methoxide looks to be a promising catalyst for the direct synthesis of dimethyl carbonate from carbon dioxide and methanol. Since the reaction can be performed in excess of methanol, there is no need for another organic solvent as reaction medium.

The catalyst is deactivated by water (a green byproduct of the reaction) and by high carbon dioxide partial pressures. Continuous operation of the process in both, homogeneous or heterogeneous reaction at optimum pressures and temperatures will be able to diminish this inconvenience in the near future.

Dimethyl ether could not be converted to dimethyl carbonate through direct reaction with carbon dioxide under the conditions investigated in this study.

ACKNOWLEDGEMENT

Financial support from the Loker Hydrocarbon Research Institute, University of Southern California, Los Angeles, is greatly appreciated.

REFERENCES

1. Y. Ono, Appl. Catal. A: Gen., 155 (1997) 133.
2. A.G. Shaikh and S.Sivaram, Chem. Rev., 96 (1996) 951.
3. M. Aresta and E. Quranta, CHEMTECH, 27 (3) (1997) 32.
4. M.A. Pacheco and C.L. Marshall, Energy & Fuels, 11 (1997) 2.
5. Z. Kricsfalussy, H. Waldmann and H.J.Traenckner, Ind. Eng. Chem. Res., 37 (1998) 865.
6. G. Cavinato and L. Toniolo, J. Organomet. Chem., 444 (1993) C65-C66.
7. D.Delledonne, F. Rivetti and U. Romano, J. Organomet. Chem., 488 (1995) C15-C19.
8. S. Yokota and H. Kojima, JP 86-55722 860313 (1987).
9. W. Yanji, Z. Xinqiang, Y. Baoguo, Z. Bingchang and C.Jinsheng, Appl. Catal. A: Gen., 171 (1998) 255.
10. G. Filardo, A. Galia, F. Rivetti, O. Scialdone and G. Silvestri, Electrochim. Acta, 42 (13-14) (1997) 1961.
11. T. Matsuzaki, T. Shinamura, Y. Toriyahara and Y. Yamasaki, Eur. Patent Appl. EP 565 076, (1993).
12. J.F Knifton, US Patent 4,661,609 (1987).
13. R.G. Duranleau, E.C.Y. Nieh and J.F. Knifton, US Patent 4,691,041 (1986).
14. J.F Knifton, R.G. Duranleau, J. Mol. Catal., 67 (1991) 389.
15. T. Tatsumi, Y. Watanabe and K.A. Koyamo, Chem. Commun., (1996) 2281.
16. H.J. Buysch, H. Krimm and H. Rudolph, DE 77-2748718 771029 (1979).
17. M.J. Green, WO 84-GB82 840315 (1984).
18. H. Zhu, L.B. Chen and Y.Y. Jiang, Chin. Chem. Lett., 6 (12) (1995) 1029.
19. N. Yamazaki, S. Nakahama and K.Endo, JP 77-68310 770609 (1979).
20. A. Yoshisato and T. Hagiwara, JP 92-336091 921216 (1994).
21. J. Kizlink, Coll. Czech. Chem. Commun., 58 (1993) 1399.
22. J. Kizlink and I. Pastucha, Coll. Czech. Chem. Commun., 59 (1994) 2116.
23. J. Kizlink and I. Pastucha, Coll. Czech. Chem. Commun., 60 (1995) 687.
24. S. Fang and K. Fujimoto, Appl. Catal. A: Gen., 142 (1996) L1-L3.
25. J. Qi, L. Qihe and H. Zhongtao,Cuihua Xuebao, 17 (2) (1996) 91.
26. K. Tomishige, T. Sakaihori, Y. Ikoda and K. Fujimoto, Catal. Lett., 58 (1999) 225.
27. K. Tomishige, Y. Ikoda, T. Sakaihori and K. Fujimoto, J. Catal., 192 (2000) 355.
28. Y. Ikoda, T. Sakaihori, K. Tomishige and K. Fujimoto, Catal. Lett., 66 (2000) 59.
29. Z. Hou, B. Han, Z. Liu, T. Jiang and G. Yang, Green Chemistry, 4 (2002) 467.

Dedicated to professor Gh. Marcu at his 80th anniversary

REMOVAL OF SOME HEAVY METAL IONS FROM SYNTHETIC WASTEWATERS USING NATURAL ZEOLITES. A COMPARATIVE STUDY

MARIA STANCA[a], ANDRADA MĂICĂNEANU[*,a], SILVIA BURCĂ[a], HOREA BEDELEAN[b]

ABSTRACT. This paper presents some results obtained for removal of lead (II), zinc(II) and iron (II) ions from wastewaters by ionic exchange on natural zeolites from Transilvania. We used zeolitic (clinoptilolitic) volcanic tuffs from Măcicaş (M), Pâglişa (P) and Cepari Vultureni (CV) areas (Cluj county). The experiments were conducted in a batch reactor (static regime) and in a fixed bed column (dynamic regime). The efficiency of removal is high for all the natural zeolites and ions considered. A pretreatment of the zeolite with Na^+ solutions increased the efficiency of the ionic exchange process.

KEY WORDS: Natural zeolites, clinoptilolite, wastewaters, lead, zinc, iron, ionic exchange.

1. INTRODUCTION

It is well known that 70% of the Earth's surface is covered by water, which follows a cycle driven by the absorption of energy from the Sun (evaporation-condensation-precipitation-infiltration to ground water). During this cycle, in which human activities play an important role, water pollution occurs. Heavy metal ions pollution is considered to be of high risk, due to the toxic effect upon the living organisms. Cadmium, chromium, cobalt, copper, lead, mercury, nickel and zinc are considered to have high toxicity, while iron and manganese are considered non toxic but with aesthetic effect. Copper and zinc ions are linked to some processes that take place in human body, but if their concentration is too large can become toxic.[1] Other heavy metal ions are highly toxic al low concentrations and can accumulate in the human body leading to different diseases.

Heavy metal ions in water come from natural and anthropogenic sources. Natural sources include rock weathering, soil erosion or dissolution of water-soluble salts. Usually metal ions introduced in water by natural sources are in small quantities and they not have any adverse effects on humans or other living organisms. Anthropogenic sources include municipal wastewater treatment plants, mining, industry (chemical, metallurgic, leather and textile, petroleum refining) corrosion and electroplating. If these wastewaters are not properly treated, heavy metal ions can be transported as

[*] Corresponding author; e-mail: andrada@chem.ubbcluj.ro

[a] Department of Chemical Technology, "Babeş-Bolyai" University, 11 Arany Janos st., RO - 400028 Cluj-Napoca

[b] *Department of Geology, "Babeş-Bolyai" University, Cluj-Napoca,1 Mihail Kogălniceanu st., RO - 400084 Cluj-Napoca*

dissolved species, can be adsorbed on sediments, volatilize in atmosphere and finally can be taken up by organisms causing deleterious effects.[1,2]

Pollutants removal from wastewaters and water disposal in nature or recycling in the economic circuit is one of the main strategies applied to avoid environmental pollution.

Heavy metal ions removal from wastewaters can be realized using methods like: extraction, reduction, precipitation, electrochemical processes, adsorption or ionic exchange,[2-6] each of them with advantages and disadvantages. The main disadvantage in most of the cases is the high cost of the process.

Adsorption and ionic exchange processes are widely applied to remove heavy metal ions from wastewaters due to their high efficiency even for small concentration of metal. In recent years many researchers oriented their efforts to improve existing materials[7-12] and processes (e.g. use of fluidised bed to remove copper on ionic exchange resin)[13,14] or to find inexpensive materials that can be used as adsorbents or ionic exchangers. In the second category are included natural materials and natural wastes. There were investigated many natural zeolites and clays: Mexican clinoptilolite,[15] Croatian clinoptilolite,[16] American clinoptilolite,[17] montmorillonite,[18-22] scolecite (Brazilian natural zeolite),[23,24] phillipsite (Jordanian zeolite),[25] vermiculite,[26] erionite, chabazite, mordenite,[17] kaolinite,[27,28] dolomite,[29] smectite and hectorite (magnesian smectite),[30-32] gibbsite,[33] sepiolite,[34] micas, illites[35-37] and bentonites.[34-42] Other studies were oriented on the investigation of adsorptive properties of some natural materials and wastes such as apple residues,[43] grape stalk wastes,[44] crab shell particles,[45,46] rice bran,[47] coffee grounds,[48] tree leaves,[49] ash particles derived from palm oil wastes,[50] peanut shell,[51] sheep manure wastes[52,53] or algae and microalgae.[54-56]

In this work we used zeolitic (clinoptilolitic) volcanic tuffs from Măcicaş, Pâglişa and Cepari Vultureni areas (Cluj county) to remove lead, zinc and iron from synthetic wastewaters. The deposits of volcanic tuffs from these areas are very important, from the environmental point of view, due to their clinoptilollite content, which is between 70 and 90% of rock mass. Volcanic tuff samples were collected from two stratigraphical horizons, those from the higher level are marked with "1" and they have a microporous structure, while those from the lower level are marked "2" and they have a mediumporous structure. Physico-chemical and mineralogical characterisation of all the zeolitic volcanic tuffs used in this study will make the object of another paper.

2. EXPERIMENTAL

Adsorptive and ionic exchange properties of natural zeolites are determined by the structure of their crystalline network, which determine the channel system and also by the negative charge excess due to $[AlO_4]^{5-}$ tetrahedrons compensated by mono- or divalent cations (eg. Na^+, K^+, Ca^{2+}, Mg^{2+}). These counter ions are mobile and can be total or partial exchanged during ionic exchange processes. Heavy metal ions removal was realised on zeolitic volcanic tuff modified by treatment with 1M HCl (Z-H form) and 1M NaCl + NaOH pH = 10 (Z-Na form). There were used two granulations, 0.63-1.0 mm and 0.2-0.4 mm of the zeolitic volcanic tuff. The stages involved in the zeolite preparation are as follows: crushing, grinding, size separation, washing with distilled water, drying at 105°C for 6 hours, treatment with 1M HCl in a stirring reactor with a zeolite acid solution ratio of 1:10, washing with distilled water to pH = 7 and finally drying at 105°C for 6 hours. At the end of this sequence we obtained the zeolite in -H form (Z-H). Also, during the treatment with HCl, zeolite channels are cleaned and pores opened. To bring the zeolite in -Na form which proved to be more efficient in the ionic exchange process,[17] the zeolite is subjected subsequently to an alkaline treatment with strong Na^+ solution (1M NaCl solution brought to pH = 10 with a 1M NaOH solution) according to equation (1). After the alkaline treatment the zeolite samples are washed again with distilled water to pH = 7 and dried for 6 hours at 105°C.

$$\text{Z-H} + \text{NaCl} \rightleftharpoons \text{Z-Na} + \text{HCl} \quad (1)$$

There were used monocomponent synthetic solutions containing Zn^{2+}, Pb^{2+} or Fe^{2+} ions, prepared from $ZnSO_4 \cdot 7H_2O$, $(CH_3OO)_2Pb \cdot 3H_2O$ and $FeSO_4 \cdot 7H_2O$ respectively, all analytical purity reagents. Concentrations of the solutions used in this study were selected accordingly to their toxicity and the maximum admissible concentrations in surface and drinking water.[57,58] Determination of heavy metal ions in solution was realised using a Jenway spectrophotometer. Iron was determined as total iron. Experiments were carried out without any modification of the pH for the synthetic solutions.

The ionic exchange process was realised in a batch reactor in static regime using 10 g zeolitic volcanic tuff and 100 ml metal ions solution (zeolite:solution = 1:10). Synthetic wastewater samples were taken every 24 hours until the equilibrium was reached. We also worked on a fixed bed column (d_i = 15 mm) containing 5 g zeolite, with a flow rate of 0,055 ml/s (for all experiments) when samples were collected every 100 ml until the zeolite was exhausted (dynamic regime). The ionic exchange reactions are as follows:

$$\text{2Z-Na} + Zn^{2+} \rightleftharpoons Z_2\text{-Zn} + 2Na^+ \quad (2)$$

$$\text{2Z-Na} + Pb^{2+} \rightleftharpoons Z_2\text{-Pb} + 2Na^+ \quad (3)$$

$$\text{2Z-Na} + Fe^{2+} \rightleftharpoons Z_2\text{-Fe} + 2Na^+ \quad (4)$$

Zeolitic volcanic tuffs used in our study were labelled considering the stratigraphical horizon and their origin as follows: Măcicaş area – M1 and M2, Pâglişa area – P1 and P2 and Cepari Vultureni area – CV.

The ionic exchange efficiencies, η, in %, were calculated with equation (5), considering the final concentration as follows: (a) in static regime – after the equilibrium was reached and (b) in dynamic regime – after 100 ml of synthetic wastewater passed the zeolitic volcanic tuff column bed.

$$\eta = \frac{C_i - C_f}{C_i} \cdot 100 \quad (5)$$

where

C_i is the initial concentration, in mg/L

C_f is the final concentration, in mg/L.

3. RESULTS AND DISCUSSIONS

3.1. Influence of the chemical treatment on the ionic exchange capacity in dynamic regime.

The influence of the chemical treatment over the ionic exchange capacity was studied on the P1 sample brought in P1-H and P1-Na forms. The experiments were carried out in a column filled with 5 g zeolite with granulation of 0.2-0.4 mm and a synthetic solution containing Zn^{2+} ions, concentration 136.64 mg/L. Our results indicated that the efficiency of the ionic exchange process is almost twice as large in case of the -Na form modified zeolite (figure 1) – 42.03% for P1-H and 76.13% for P1-Na. This result is in agreement with conclusions of some previous studies performed on clinoptilolitic type natural zeolites.[17,59,60] In case of the treatment with NaCl solutions,[17,60] experimental results indicate that natural zeolites improve significantly their ion exchange capacity. Also H^+ radius is 2.08 Å, while Na^+ radius is only 0.95 Å, which will increase diffusion rate through the zeolite channels. If a NaOH treatment was applied,[59] an increase of the crystallinity degree was observed (explained by the amorphous phase reduction), which will improve zeolite exchange properties.

3.2. Comparison between the ionic exchange efficiencies of the zeolitic volcanic tuffs in static regime.

We studied the ionic exchange for zinc (237.58 mg/L) and lead (5.38 mg/L) ions using M1-Na, M2-Na, P1-Na, P2-Na and CV-Na samples with a granulation of 0.63-1.0 mm. Variation of heavy metal ions concentration in time and the ionic exchange efficiency for all the zeolitic volcanic tuffs are presented in figures 2 and 3 for zinc and figures 4 and 5 for lead. The ionic exchange reactions took place for both ions and all zeolitic volcanic tuffs considered (Zn^{2+} and Pb^{2+} concentrations in water decrease), therefore the zeolites under study are considered to be active in the ionic exchange reactions. In case of zinc, the efficiency of the ionic exchange process was higher than 96% for all samples considered.

The equilibrium in case of lead ion was reached more rapidly by comparison to zinc ion, which indicates a favourable kinetic for Pb^{2+} ion. Experimental ionic exchange studies performed on natural zeolites containing as a main component clinoptilolite and multicomponent heavy metal ions solutions showed that Pb ion is in the top of the selectivity sequences (Pb>Cu>Cd>Zn>Cr>Co>Ni).[61-63] In case of lead, ionic exchange efficiencies were over 93% with the exception of M1-Na microporous zeolitic volcanic tuff sample, where the efficiency is only 71.18%. This result can be correlated with the Pb^{2+} ionic radius (1.2 Å), which we assume that is too large by comparison with the pore diameter (microporous sample). After a comparison of ion exchange efficiencies for al the zeolitic volcanic tuffs and each ion, we can conclude that for the CV-Na zeolitic sample were obtained the best results in both cases. Also P1-Na zeolitic sample, in case of lead, and M1-Na zeolitic sample, in case of zinc, showed similar efficiencies for the process under study.

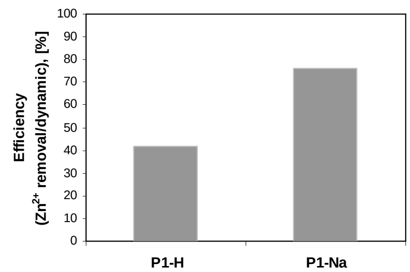

Figure 1. *Ionic exchange efficiency for zinc removal on P1 zeolitic volcanic tuff subjected to acid (P1-H) and acid-alkaline treatment (P1-Na)*

3.3. Comparison between the ionic exchange efficiencies of the zeolitic volcanic tuffs in dynamic regime.

In this part of the work we studied the ionic exchange process in dynamic regime, in a fixed bed column, for Zn^{2+} and Fe^{2+} on M1-Na, P1-Na and CV-Na zeolitic volcanic tuffs. We used each time a 5 g zeolitic sample with granulation of 0.2-0.4 mm and solutions with different concentrations. In case of zinc we studied the influence of concentration over the efficiency of the ionic exchange process using solutions containing 136.64 mg Zn^{2+}/L and 59 mg Zn^{2+}/L, while for iron we considered solutions with 22.93 mg Fe^{2+}/L and 10 mg Fe^{2+}/L. Preliminary tests performed with zeolitic volcanic tuff with granulation 0.63-1.0 mm and higher concentrations for heavy metal ions gave unsatisfactory results, probably due to diffusional limitations.

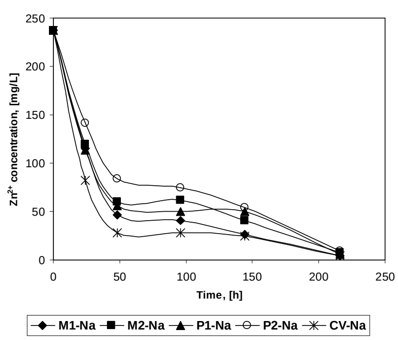

Figure 2. *Comparison between variations of Zn^{2+} concentration (in the synthetic wastewater) in time for all zeolitic volcanic tuffs studied, in -Na form and static regime.*

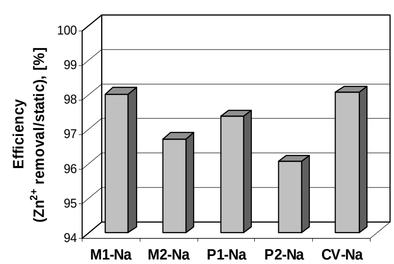

Figure 3. *Ionic exchange efficiency for zinc removal in static regime on all zeolitic volcanic tuffs studied.*

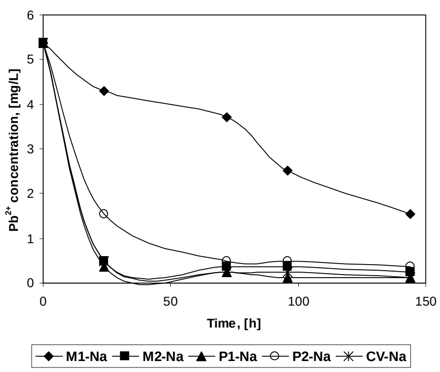

Figure 4. *Comparison between variations of Pb^{2+} concentration (in the synthetic wastewater) in time for all zeolitic volcanic tuffs studied, in -Na form and static regime.*

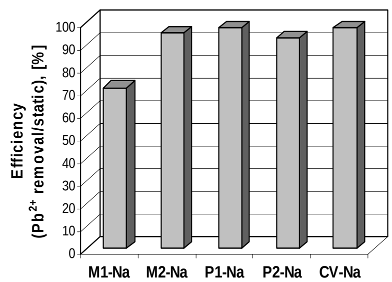

Figure 5. *Ionic exchange efficiency for lead removal in static regime on all zeolitic volcanic tuffs studied.*

For removal of zinc in dynamic regime, were considered M1-Na, P1-Na and CV-Na zeolitic volcanic tuffs, which proved to have higher ionic exchange efficiencies in the static regime study. Results are presented in figures 6 and 7. We found out that in this case, the zeolitic volcanic tuff from Pâglişa area (P1-Na) presents a higher ionic exchange capacity, at the beginning of the process. This might be due to the pores distribution in the P1 sample, which has a surface area smaller than M1 sample, therefore pores are more accessible for the ionic exchange process. In case of P1-Na sample, we also investigated the ionic exchange for a second solution, diluted approximately at half. The efficiency of the ionic exchange process was calculated to be 81.57%, while for the first solution the efficiency was 76.13% after first 100 ml of synthetic wastewater passed the column bed. Also, the wastewater volume that can be processed, before the zeolite exhaustion, increased from 400 ml for the concentrated solution to 1000 ml for the diluted solution.

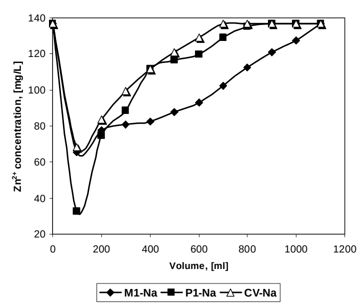

Figure 6. *Comparison between variations of Zn^{2+} concentration (in the synthetic wastewater) with the efluent volume for M1-Na, P1-Na and CV-Na zeolitic samples in dynamic regime.*

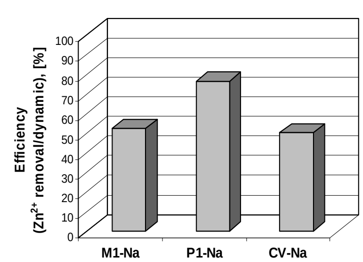

Figure 7. *Ionic exchange efficiency for zinc removal in dynamic regime on M1-Na, P1-Na and CV-Na zeolitic samples*

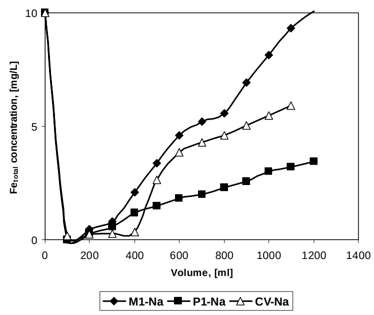

Figure 8. *Comparison between variations of Fe_{total} concentration (in the synthetic wastewater) with the effluent volume for M1-Na, P1-Na and CV-Na zeolitic samples in dynamic regime.*

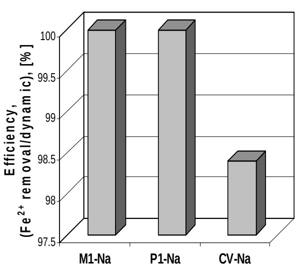

Figure 9. *Ionic exchange efficiency for iron removal in dynamic regime on M1-Na, P1-Na and CV-Na zeolitic samples*

The same zeolitic volcanic tuffs were used to study the removal of iron from synthetic wastewaters (initial solution 10 mg Fe^{2+}/L). Results are presented in figures 8 and 9. All zeolitic samples demonstrated high efficiencies for iron removal. Iron was completely removed after first 100 ml of synthetic wastewater passed the zeolitic bed for M1-Na and P1-Na zeolitic samples, while for CV-Na zeolitic sample an efficiency of 98.4% was calculated.

We also carried out tests on P1-Na zeolitic sample using a second, more concentrated solution (figure 10). We observed that for the concentrated solution the exhaustion of the zeolite sample took place after we processed 900 ml wastewater. In case of the diluted solution after 1200 ml, when we stopped the experiment, the residual concentration of iron in solution was only 3.43 ml Fe_{total}/L (the ionic exchange process takes place until the initial concentration of iron is reached after the solution passed the zeolitic volcanic tuff bed, as a consequence of the ionic exchanger exhaustion). During the experiment we observed that $Fe(OH)_3$ brown precipitate started to build up on top of the zeolite sample, leading to an increase of the pressure drop, which modifies the hydraulic regime across the column.

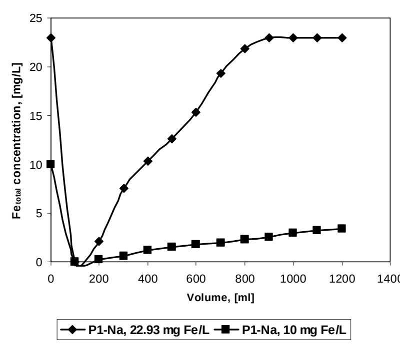

Figure 10. *Comparison between variations of Fe_{total} concentration (in the synthetic wastewater) with the effluent volume for P1-Na zeolitic sample in dynamic regime for two concentrations of iron solutions.*

4. CONCLUSIONS

(1) All zeolite samples considered can be used in wastewaters treatment to remove lead, zinc and iron.

(2) Our results indicated that the efficiency of the ionic exchange process is almost twice as large in case of the -Na form modified zeolite by comparison with the –H form.

(3) In static regime the most efficient samples were CV-Na and M1-Na for zinc removal and CV-Na and P1-Na for lead removal.

(4) The equilibrium in case of lead ion (static regime) was reached more rapidly by comparison to zinc ion, which indicates a favourable kinetic for Pb^{2+} ion.

(5) In case of dynamic regime for zinc removal, the most efficient sample was P1-Na. Also the ionic exchange process was more efficient and column exhaustion took place after a larger volume of wastewater was processed when solution concentration is lower.

(6) The iron was removed completely after 100 ml wastewater passed on M1-Na and P1-Na samples and the life of the zeolite was extended when diluted solution was used.

(7) After the heavy metal ions removal from wastewaters, the zeolites samples in metal ion form (Z-Me^{n+}) can be regenerated and reused in the same process with metals recovery[2] and as catalysts in flue gas treatment to remove NO_x[64] or in Fenton type processes to remove organic pollutants from wastewater.[65]

(8) Further studies will consider multicomponent synthetic solutions and wastewaters collected from industrial effluents.

ACKNOWLEDGMENT

This material is based upon work supported by CNCSIS grant 1745.

REFERENCES

1. J.R. Garbarino, H.C. Hayes, D.A. Roth, R.C. Antweiler, T.I. Brinton and H.E. Taylor; R.H. Meade (ed.), *Contaminants in the Mississippi River*, U.S. GEOLOGICAL SURVEY CIRCULAR 1133**,** Reston, Virginia, 1995**.**
2. M. Macoveanu, D. Bîlbă, N. Bîlbă, M. Gavrilescu and G. Şoreanu, *Procese de schimb ionic în protecția mediului*, Matrixrom, Bucharest, 2002.
3. G. Neagu, *Depoluarea solurilor şi apelor subterane*, Casa Cărții de Ştiință, Cluj-Napoca, 1997.
4. D. Baciu, *Tehnici, utilaje şi tehnologii de depoluare a apelor reziduale*, Matrixrom, Bucharest, 2001.
5. O. Ianculescu, Gh. Ionescu and R. Racovițeanu, *Epurarea apelor uzate*, Matrixrom, Bucharest, 2001.
6. S.A. Mirbagheri and S.N. Hosseini, *Desalination*, **2004**, *171*, 85-93.
7. J. Rivera-Utrilla and M. Sánchez-Polo, *Water Res.*, **2003**, *37*, 3335-3340.
8. M. Amara and H. Kerdjoudj, *Desalination*, **2004**, *168*, 195-200.
9. H. Kaşgöz, S. Özgümüş and M. Orbay, *Polymer*, **2003**, *44*, 1785-1793.

10. E. Bae, S. Chah and J. Yi, *J. Colloid Interface Sci.*, **2000**, *230*, 367-376.
11. J.S. Kim and J. Yi, *J. Chem. Technol. Biotechnol.,* **1999**, *74*, 544-550.
12. G. Chamoulaud and D. Bélanger, *J. Colloid Interface Sci.*, **2005**, *281*, 179-187.
13. M.A. Zarraa, *Chem. Eng. Technol.*, **1992**, *15*, 21-25.
14. J. Yang and A. Renken, *Chem. Eng. Technol.*, **2000**, *23*, 1007-1012.
15. M. Vaca Mier, R. López Callejas, R. Gehr, B.E. Jiménez Cisneros and P.J.J. Alvarez, *Water Res.*, **2001**, *35*, 373-378.
16. J. Perić, M. Trgo and N. Vukojević Medvidović, *Water Res.*, **2004**, *38*, 1893-1899.
17. K.D. Mondale, R.M. Carland and F.F. Aplan, *Minerals Eng.*, **1995**, *8*, 535-548.
18. C. Cooper, J-Q. Jiang and S. Ouki, *J. Chem. Technol. Biotechnol.,* **2002**, *77*, 546-551.
19. O. Altin, O.H. Ozbelge and T. Dogu, *J. Chem. Technol. Biotechnol.,* **1999**, *74*, 1131-1138.
20. O. Altin, O.H. Ozbelge and T. Dogu, *J. Chem. Technol. Biotechnol.,* **1999**, *74*, 1139-1144.
21. M. Auboiroux, P. Baillif, J-C. Touray and F. Bergaya, *Comptes Rendues de l'Académie des Sciences – Series IIA – Earth and Planetary Science*, **1998**, *327*, 727-730.
22. A.M.L. Kraepiel, K. Keller and F.M.M. Morel, *J. Colloid Interface Sci.*, **1999**, *210*, 43-54.
23. R.S. Jimenez and S.M. Carvalho, *Quim. Nova*, **2004**, *27*, 734-738.
24. S.T. Bosso and J. Enzweiler, *Water Res.*, **2002**, *36*, 4795-4800.
25. A.A-H. Ali and R. El-Bishtawi, *J. Chem. Technol. Biotechnol.,* **1999**, *69*, 27-34.
26. M.G. da Fonseca, M.M. de Oliveira, L.N.H. Arakaki, J.G.P. Espinola and C. Airoldi, *J. Colloid Interface Sci.*, **2005**, article in press, corrected proof.
27. A. Melnitchenko, J.G. Thompson, C. Volzone and J. Ortiga, *Appl. Clay Sci.*, **2000**, *17*, 35-53.
28. I. Heidmann, I. Christl, C. Leu and R. Kretzschmar, *J. Colloid Interface Sci.*, **2005**, *282*, 270-282.
29. P.V. Brady, H.W. Papenguth and J.W. Kelly, *Appl. Geochem.*, **1999**, *14*, 569-579.
30. G. Kamei, C. Oda, S. Mitsui, M. Shibata and T. Shinozaki, *Eng. Geology*, **1999**, *54*, 15-20.
31. M.L. Shegel, A. Manceau, D. Chateigner and L. Charlet, *J. Colloid Interface Sci.*, **1999**, *215*, 140-158.
32. M.L. Shegel, L. Charlet and A. Manceau, *J. Colloid Interface Sci.*, **1999**, *220*, 392-405.
33. R. Weerasooriya, H.J. Tobschall, H.K.D.K. Wijesekara, E.K.I.A.U.K. Arachchige and K.A.*S*. Pathirathne, *Chemosphere*, **2003**, *51*, 1001-1013.
34. A. García-Sánchez, A. Alastuey and X. Querol, *Sci. Total Environ.*, **1999**, *242*, 179-188.
35. S. Grier and W.D. Johns, *Appl. Clay Sci.*, **2000**, *16*, 289-299.
36. C. Poinssot, B. Baeyens and M.H. Bradbury, *Geochim. Cosmochim. Acta*, **1999**, *63*, 3217-3227.
37. J. Echeverría, J. Indurain, E. Churio and J. Garrido, *Colloids Surf. A*, **2003**, *218*, 175-187.
38. J. Bors, S. Dultz and B. Riebe, *Appl. Clay Sci.*, **2000**, *16*, 1-13.
39. Y. Tachi, T. Shibutani, H. Sato and M. Yui, *J. Contam.Hydrol.*, **2001**, *47*, 171-186.
40. E. González Pradaa, M. Villafranca Sánchez, F. Cantón Cruz, M. Socias Viciana and M. Fernández Pérez, *J. Chem. Technol. Biotechnol.,* **1994**, *59*, 289-295.
41. T.E. Eriksen, M. Jansson and M. Molera, *Eng. Geology*, **1999**, *54*, 231-236.
42. T. Missana, M. García-Gutiérrez and Ú. Alonso, *Appl. Clay Sci.*, **2004**, *26*, 137-150.
43. S.H. Lee, C.H. Jung, H. Chung, M.Y. Lee and J-W. Yang, *Proc. Biochem.*, **1998**, *33*, 205-211.

44. I. Villaescusa, N. Fiol, M. Martínez, N. Miralles, J. Poch and J. Serarols, *Water Res.*, **2004**, *38*, 992-1002.
45. M-Y. Lee, K-J. Hong, T. Kajiuchi and J-W. Yang, *J. Chem. Technol. Biotechnol.,* **2004**, *79*, 1388-1394.
46. D.S. Kim, *Bioresour. Technol.*, **2003**, *87*, 355-357.
47. S.F. Montanher, E.A. Oliveira and M.C. Rollemberg, *J. Hazard.Mater.*, **2005**, *117*, 207-211.
48. T. Tokimoto, N. Kawasaki, T. Nakamura, J. Akutagawa and S. Taneda, *J. Colloid Interface Sci.*, **2005**, *281*, 56-61.
49. L. Hu, A. Adeyiga, T. Greer, E. Miamee and A. Adeyiga, *Chem. Eng. Comm.*, **2002**, *189*, 1587-1597.
50. K.H. Chu, M.A. Hashim, *J. Chem. Technol. Biotechnol.,* **2002**, *77*, 685-693.
51. W. Wafwoyo, C.W. Seo and W.E. Marshall, *J. Chem. Technol. Biotechnol.,* **1999**, *74*, 1117-1121.
52. F.A.A. Al-Rub, M. Kandah and N. Al-Dabaybeh, *Eng. Life Sci.*, **2002**, *2*, 111-116.
53. M. Kandah, F.A. Abu Al-Rub and N. Al-Dabaibeh, *Life Sci.*, **2002**, *2*, 237-243.
54. S. Schiewer and M.H. Wong, *Chemosphere*, **2000**, *41*, 271-282.
55. E. Sandau, P. Sandau, O. Pulz and M. Zimmermann, *Acta Biotechnol.*, **1996**, *16*, 103-119.
56. O. Raize, Y. Argaman and S. Yannai, *Biotechnol. Bioeng.*, **2004**, *87*, 451-458.
57. Ordin 161/2006 pentru aprobarea Normativului privind clasificarea calității apelor de suprafață în vederea stabilirii stării ecologice a corpurilor de apă.
58. Lege privind calitatea apei potabile 458/8.07.2002.
59. A. Iovi, G. Burtică and R. Pode, *Chem. Bull. Tech. Univ. (Timişoara)*, **1993**, *52*, 29-37.
60. C. Cobzaru, S. Oprea, T. Hulea, V. Hulea and E. Dumitriu, *Rev. Chim. (Bucureşti)*, **2002**, *53*, 674-677.
61. S.K. Ouki and M. Kavannagh, *Waste Management Res.*, **1997**, *15*, 383-394.
62. M.V. Mier, R.L. Callejas, R. Gehr, B.E.J. Cisneros and P.J.J. Alvarez, *Water Res.*, **2000**, *35*, 373-378.
63. E. Erdem, N. Karapinar and R. Donat, *J. Colloid Interface Sci.*, **2004**, *280*, 309-314.
64. R.M. Heck and R.J. Farrauto, *Catalytic Air Pollution Control*, 2nd edition, Wiley-Interscience, New-York, **2002**.
65. M. Stanca, N. Dulămiță and S. Burcă, *Environment & Progress*, **2004**, *2*, 289-292.

Dedicated to professor Gh. Marcu at his 80th anniversary

SPECTROSCOPIC AND MAGNETIC INVESTIGATIONS OF THE CHROMIUM(III) TUNGSTOARSENATE

DAN RUSU*

ABSTRACT. The sandwich-type tungstoarsenate complex $Na_6[Cr_4(H_2O)_2\}(AsW_9O_{34})_2]$. $18H_2O$ (**Cr^{III}AsW$_9$**) was synthesized and investigated by elemental analysis, thermogravimetry, FT-IR, UV-VIS, EPR spectroscopy and magnetic susceptibility methods. The results suggest a sandwich-type structure in which two of the $[AsW_9O_{34}]^{9-}$ trilacunary Keggin fragments are connected by a Cr_4O_{16} group of four coplanar CrO_6 octahedra sharing edges.

The aim of this study consists in establishing the modifications that Cr^{III} ions make in the trivacant Keggin units, in determination of the local symmetry around the chromium ions and the identification of the nature of the chromium-chromium interactions.

Keywords: polyoxometalates, heteropolyoxometalates, chromium(III), tungstoarsenates

Introduction

Scientific interest in polyoxometalates is increasing worldwide, due to the enormous variety of structures of these compounds, often with unusual properties, rendering them useful candidates in medicinal applications and other fields such as nanomaterials, catalysis and magnetochemistry [1-4]. Although the mechanism of formation of polyoxometalates is commonly described as self-assembly, it is not well understood. In spite of this drawback, the synthesis of new compounds can be based on a rational synthetic approach and efficient control of the reaction path.

Lacunary polyoxometalates are usually synthesized from precursor ions by loss of one or more MO_6 octahedra [1, 5]. These lacunary polyoxometalates show an increased reactivity for metal ions and organometallic fragments, leading to the formation of a broad variety of complexes, in which the heteropolyanion framework remains unchanged. Taking into account the coordination requirements and the size of a given transition metal ion, the geometry of the reaction product can often be predicted.

Although polyoxometalate complexes of the trilacunary $[PW_9O_{34}]^{9-}$ with metal cations and organometallic fragments have been extensively investigated, there are relatively few papers concerning $[AsW_9O_{34}]^{9-}$ analogs [6-9].

Herein the synthesis and characterization of trilacunary $[AsW_9O_{34}]^{9-}$(**AsW$_9$**) and $Na_6[Cr_4(H_2O)_2\}(AsW_9O_{34})_2]\cdot 18H_2O$ (**CrAsW$_9$**) are reported. The complex was investigated using chemical and thermal analysis, UV-VIS, FT-IR and EPR spectra,

* Physical Chemistry Department, University of Medicine and Pharmacy, 400023 Cluj-Napoca, Romania.

as well as magnetic susceptibility measurements. The results suggest a sandwich-type structure similar to that reported by Knoth *et al.* [10], in which two of the **AsW_9** units are connected by a belt of four chromium atoms (Fig. 1).

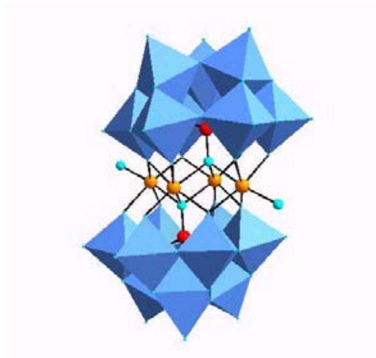

Fig. 1. Proposed structure of the $Na_6[Cr_4(H_2O)_2\}(AsW_9O_{34})_2]\cdot 18H_2O$ polyoxometalate complex.

Experimental

1. Methods

Tungsten, chromium, sodium and arsenicum were determined by atomic absorption. The water content was determined on the basis of thermal analysis performed using a METTLER-TGA/SDTA 851^{e}STAR^{e}Software derivatograph. FT-IR spectra were recorded on a Jasco FT/IR 610 spectrophotometer in the 4000–400 cm^{-1} range, using KBr pellets. Electronic spectra in the visible range were performed in aqueous solutions on an ATI Unicam-UV-Visible spectrophotometer with Vision Software V 3.20. EPR spectra on powdered solids have been recorded at room temperature and 80 K at *ca.* 9.6 GHz (X-band) using a Bruker ESP 380 spectrometer. The magnetic susceptibility measurements were performed using a Faraday type balance in the temperature range of 77–273 K.

2. Materials

Reagent grade chemicals were used and all syntheses and studies were carried out in distilled water.

The sodium salt of the polyoxometalate ligand, $Na_8H[AsW_9O_{34}]$ (**AsW_9**) was prepared following the procedure described previously in the literature [11].

Synthesis of $Na_6[Cr_4(OH_2)_2(AsW_9O_{34})_2]\cdot 18H_2O$ $CrCl_3\cdot 6H_2O$ (1.34 g, 3.094 mmol) was dissolved in water (10 ml) and added dropwise, while stirring, to a boiling aqueous solution (50 ml) of $Na_8H[AsW_9O_{34}]\cdot 11H_2O$ (5.5 g, 2.070 mmol). The slightly turbid final solution was boiled for 2h, its pH adjusted between 4.5 and 5.0 with 6M HCl, and filtered under suction. The filtrate was heated at 80°C, while stirring, until half of the volume remained. It was then cooled to room temperature. A few days later a green precipitate appeared. It was recrystallized from hot water, at pH= 6.0-6.5 and dried under vacuum over P_2O_5. The yield was 2.3 g (60%). Anal. Calc. for $H_{40}As_2Cr_4Na_6O_{88}W_{18}$ (5776.95): As 2.80; Cr 4.00; Na 2.60; W 63.10. Found: As 2.85; Cr 3.96; Na 2.63; W 63.04. IR (polyoxometalate region, cm^{-1}): 955, 890, 839, 795, 734, 517, 472, 440.

Results and Discussions

The reaction of Cr^{III} with $\mathbf{AsW_9}$ in water can be described by equation. (1). Isolation of the products as sodium salts and recrystallization from hot water, resulted in relatively good yields of the $\mathbf{Cr^{III}AsW_9}$ complexes.

$$4Cr^{3+} + 2[AsW_9O_{34}]^{9-} + 2H_2O \quad \rightarrow \quad [Cr_4(OH_2)_2(AsW_9O_{34})_2]^{6-} \qquad (1)$$

Elemental analysis of the final products are consistent with the suggested formula for $\mathbf{Cr^{III}AsW_9}$.

Thermal study behavior of the new chromium (III) tungstoarsenate reveals that complex contain 18 crystallization water molecules and two coordination water molecules. For $\mathbf{Cr^{III}AsW_9}$, two endothermic processes were observed between 120 and 260 °C (Fig. 2). These processes were assigned to water loss. The TG curves showed that the last process, corresponding to coordination water molecule loss, was the slowest. The exothermal process, appearing around 480°C on the DTA curve of complex, was assigned to the decomposition of polyoxometalate [12]. On the basis of these thermogravimetric studies, it can be thus concluded that $\mathbf{Cr^{III}AsW_9}$ are thermally stable up to 480°C.

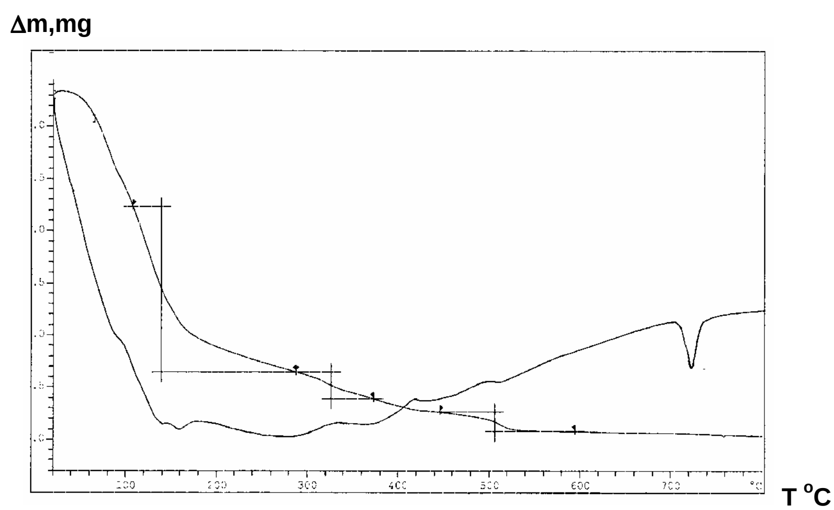

Fig. 2. Thermogravimetric and thermodifferential curves of $Cr^{III}AsW_9$.

Electronic Spectra

It have been registered the electronic UV and VIS spectra on aqueous solutions of the sodium salts of the polyoxometalates complex $Cr^{III}AsW_9$ and have been compared with this of the ligand AsW_9.

The UV electronic spectra (Fig. 3) are characteristic to the polyoxometalates and similar to the ligand. [13,14] The higher energy band (ν_1) at ~ 50000 cm^{-1}, due to the $d\pi$-$p\pi$ proper transitions from the W=O_t (O_t -terminal oxygen atom) bonds, insignificantly shifted in the complex, compared to the ligand, which can been associated with the lack of involvement of the terminal oxigen atoms in the coordination of the cations of transitional metals.

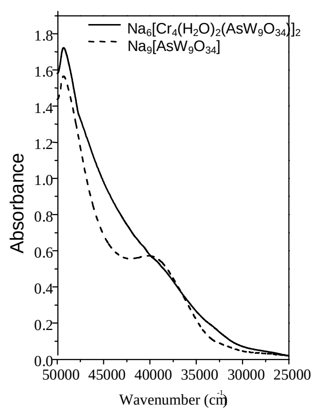

Fig. 3. UV spectra of the sodium salts of $Cr^{III}AsW_9$ (solid) and AsW_9 (dotted) obtained in $5x10^{-5}$ mol·l^{-1} aqueous solution.

The lower energy band (ν_2) at ~ 39000 cm^{-1}, due to the dπ-pπ-dπ electronic transitions from the tricentric W-$O_{c,e}$-W ($O_{c,e}$–bridging oxygens between two WO_6 octahedra sharing corner or edge respectively), bonds, with an expected absorbtion maximum in 40000-38000 cm^{-1} range, in Cr^{III} complex spectrum, apearing as to shoulders in the spectrum, is due to the decrease of the symmetry as well as to the distorsion of the WO_6 octahedra through complexation, which influences the electronic transfer from these bonds. [15]

Information about the local environment of Cr(III) ions has been obtained by means of d-d transitions from the visible electronic spectrum performed in aqueous solution. Two bands of the chromium complexes, at 16770 cm^{-1} and 21200 cm^{-1} are assigned to $^4A_{2g}$(F)→ $^4T_{2g}$(F) (ν_1) and $^4A_{2g}$(F)→ $^4T_{2g}$(F) (ν_2) transitions. The third band ($^4A_{2g}$(F)→ $^4T_{1g}$(P)) expected in the UV domain is obscured by the change-transfer and ligand-specific bands.

The first broad and unsplit band (ν_1) yields the $10D_q$ parameter, while the second (ν_2) is also broad and asymmetric. This can be explained by a small distortion from the ideal octahedral symmetry, because of the Jahn-Teller effect, spin-orbit coupling and the mixing of neighboring quartet-doublet states ($^4T_{1g}$ and $^2T_{2g}$ or $^2A_{1g}$).

The position of the third band and the spectral parameters were calculated by the method proposed by Lever [16], using a value of 400 cm^{-1} for the interelectronic repulsion constant. The obtained values are: $D_q/B = 4.2$, $\nu_3/B = 88.6$, $\beta = 0.388$, $\nu_3 = 35286$ cm^{-1}. The latter band (ν_3), assigned to a forbidden transition of two electrons, should have low intensity [17].

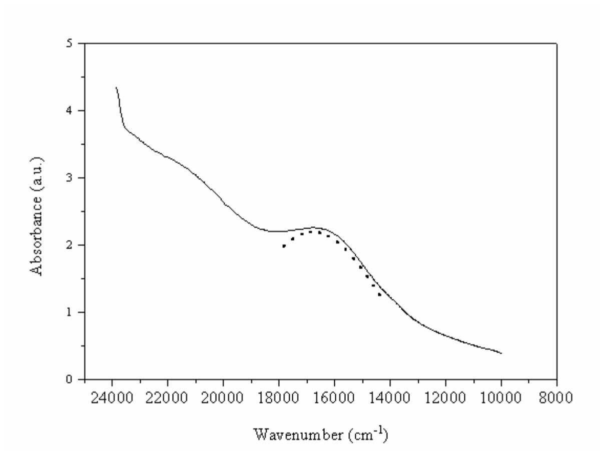

Fig.4. The visible electronic spectrum of the $Cr^{III}AsW_9$ complex in $5x10^{-3}$ mol·l^{-1} aqueous solution. The Gaussian components are represented with dashed lines.

Vibrational Spectra

All antisymmetric frequencies bonds involving tungsten ions are shifted towards higher or lower frequencies (1–18 cm^{-1}) in the complex spectrum compared to the ligand spectrum (Table 1).

The relative small shift of the ν_{asym}W-O_t vibration band from 945 cm^{-1} in the ligand spectrum to 950 cm^{-1} in complex spectrum is due to the fact that the terminal O_t atoms at the lacunary surface are not involved in the coordination of Cr^{III} ions [18]. The vibration frequencies of the As-O_i (O_i -internal oxygen atom) bonds are not observed at ~820 cm^{-1} overlaps that of W-O_b-W (O_b – bridging oxygen atom) bonds. [18] Two vibration bands of tricentric W-O_c-W bonds of the corner sharing WO_6 octahedra appear in spectrum of the ligand at 878 and 843 cm^{-1}, respectively, and in complex spectrum at 890 and 839 cm^{-1}, respectively, suggesting the nonequivalence of the W-O_c-W bonds when linking octahedra from the equatorial and polar regions of the trilacunary fragments [18].

Two vibration bands of tricentric W-O_e-W bonds of the edge-sharing WO_6 octahedra appear in the ligand spectrum at 795 and 752 cm^{-1}, respectively, suggesting that two nonequivalent bonds of this type are present. The complex spectrum shows two bands at 796 and 734 cm^{-1} too. [19]

TABEL 1.

FT-IR Data of the $Cr^{III}AsW_9$ complex and the AsW_9 ligand

Vibration band	ν (cm^{-1})	
	AsW_9	Cr^{III} AsW_9
ν_{as}W-O_t	945	950
$\nu_{as}AsO_i$+ν_{as}W-O_c-W	878	890
ν_{as}W-O_c-W	843	839
ν_{as}W-O_e-W	795	795

	752	734

Magnetic measurements

The temperature dependence of the reciprocal molar susceptibility $1/\chi_m$ for the Cr^{III}–AsW_9 complex in the 77–273 K temperature range is presented in Fig. 5.

The effective magnetic moment obtained from the magnetic susceptibility data in the 77 – 273 K temperature range is μ_{eff} = 10.66 μ_B. The value of Curie-Weiss temperature θ = -6.1 K, indicates the presence of antiferromagnetic coupling between the Cr^{III} ions.

These measurements, together with the informations obtained from EPR spectroscopy, leaded to the establishment of intra- and intermolecular metal-metal interactions .

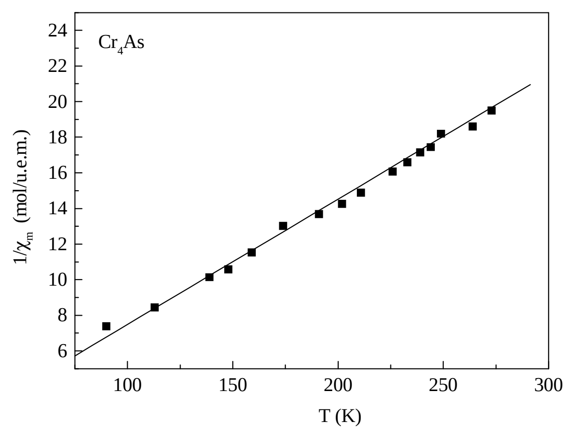

Fig. 5. Variation of reciprocal molar susceptibility of the $Cr^{III}AsW_9$ complex with respect to temperature. Solid line represents the best fit of the experimental data with a Curie-Weiss behavior.

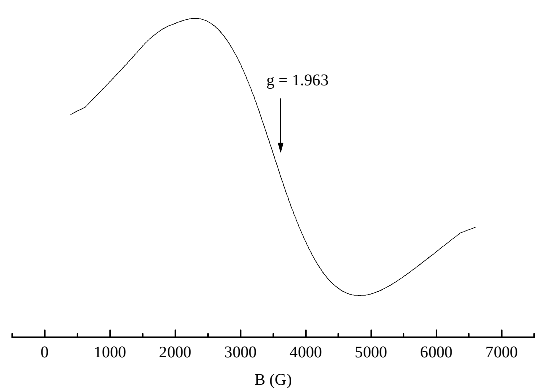

Fig. 6. EPR Spectrum of the $Cr^{III}AsW_9$

EPR Spectrum

The polycrystalline EPR spectrum of the Cr complex obtained at 80 K contains a single large ≈ 2495 G pseudo-isotropic signal centered at g=1.963. The line width of the signal indicates the presence of the coupling between the chromium ions; the almost isotropic shape of this is due to an O_h symmetry around the chromium (III) ions. The shape of this signal is not modified at 293 K. By raising the temperature, the line width of signal decreases, which indicates the presence of small Cr(III)-Cr(III) super-exchange interactions (Fig. 6). [20]

Conclusions

The results of the performed investigations revealed that the chromium complex of the AsW_9 trilacunary polyoxometalate was prepared. A sandwich-type structure, similar to the structure of the other complexes reported by Knoth *et. al*., [10] (Fig. 1) is inferred from the experimental results. The coordination of the chromium (III) ions in the lacunary region of the Keggin units results from the shift of the $\nu_{asym}(W–O_{c,e}–W)$ stretching frequencies in the FT-IR spectrum of the complex compared to the ligand spectrum.

Every metal ion is surrounded by six oxygen atoms in a distorted O_h symmetry and has a $d_{x^2-y^2}$ orbital as ground state. The almost isotropic shape form of the signal from EPR spectrum registered on the $Cr^{III}AsW_9$ is due to an O_h symmetry around the Cr^{III}.

The magnetic susceptibility measurements in the 77–273 K temperature range have indicated the presence of antiferromagnetically coupled Cr^{III} ions.

REFERENCES

1. M.T. Pope, „*Heteropoly and Isopoly Oxometalates"*, Springer-Verlag: Berlin, **1983**.
2. M.T. Pope and A. Müller (Eds.), „*Polyoxometalates: From Platonic solid to Anti-RetroViral Activity"*; Kluwer Academic Publishers: Dordrecht, **1994**.
3. C.L. Hill, *Chem. Rev.***1998,** *98*, 1.
4. M.T. Pope and A. Müller (Eds.), „*Polyoxometalate Chemistry: From Topology Via Self-Assembly to Applications";* Kluwer: Dordrecht, **2001**.
5. G. Marcu and M. Rusu, „*Chimia polioxometalatilor"*, Ed. Tehnică, Bucureşti, **1997.**
6. H.T. Evans, Jr., C. Tourné, G. Tourné and T.J.R. Weakley, *J. Chem. Soc., Dalton Trans.* **1986**, 2699.
7. T.J.R. Weakley, *Acta Crystallogr., Sect. C*, **1997,** *53* IUC9700025.
8. L.H. Bi, R.D. Huang, J. Peng, E.B. Wang, Y.H. Wang and C.W. Hu*, J. Chem. Soc*., *Dalton Trans*. **2001,** 121.
9. D.R. Rusu, Ph. D. Thesis, Babeş-Bolyai Univ. Cluj-Napoca, **2002**.
10. J. Domaille and W.H. Knoth, P.R.L. Harlow, *Inorg. Chem*. **1986,** *25*, 1577.
11. R. Massart, R. Contant, J.M. Fruchart, J.P. Ciabrini and M. Fournier, *Inorg. Chem*. **1977,** *16,* 2916.

12. E. A. Nikitina and N.A. Tsvetov, *Zh. Neorgan. Khim.* **1962,** *7*, 325.
13. H. So, M.T. Pope, *Inorg. Chem.* **1972**, *11* (6), 1441.
14. G. M., Varga, Papaconstantinou, E., Pope, M. T., *Inorg. Chem.*, **1970**, *9*, 662.
15. C. R. Mayer, R. Thouvenot, *J. Chem. Soc., Dalton Trans.* **1998**, 7.
A. B. P. Lever, *J. Chem. Educ.*, **1968**, *45*, 711.
16. B. P. Lever, *Inorganic Electronic Spectroscopy*, Elsevier, New York, 2nd edn., **1984.**
17. R. Contant, M. Abbesi, J. Canny, M. Richet, B. Keita, A. Belhouari, L. Nadjo, *Eur. J. Inorg. Chem.* **2000**, *3*, 566.
18. C. J. Gómez-Garcia, C. Giménez-Saiz, S. Triki, E. Coronado, P. Le Magueres, L. Ouahab, L. Ducasse, C. Sourisseau, P. Delhaes, *Inorg. Chem.* **1995**, *34*, 4139.
19. R. Sessoli, D. Gatteschi, A. Caneschi, M. A. Novak, *Nature*, **1993**, *365*, 141.

STUDIA UNIVERSITATIS BABES - BOLYAI, CHEMIA, LI, 2, 2006

Dedicated to professor Gh. Marcu at his 80th anniversary

THE INFLUENCE OF ADHESIVE ON COMPOSITE MATERIALS BONDED JOINTS ASSEMBLIES

O. NEMEŞ[1*], F. LACHAUD[2], A. MOJTABI[3], V. SOPORAN[1], O. TĂTARU[1]

ABSTRACT. The paper presents a theoretical calculation model of plane assemblies joined with adhesive, based on an energy method. After the determination of the cinematically acceptable field of stresses, according to the applied load, a variational calculus on the expression of elastic potential energy leads to the complete expression of the stress field in the whole assembly. A first parametric analysis (geometrical and physical parameters) is carried out on a double-lap plane assembly and makes it possible to deduce the optimal length and thickness of the adhesive. For the assembly, the total force-displacement behavior is well defined. Thus the analytical model makes it possible to determine the rigidity of the assembly and to obtain a simple formulation very rapidly which gives the total behavior of the assembly.

Keywords: Stress Analysis, Bonded joints, Numerical modeling

INTRODUCTION

The increase in use of adhesive bonded joints is due to the many advantages of this method compared to the traditional methods. This assembling method distributes the stresses over the whole joining surface and removes the concentrations of stresses to the boundary of holes generated by bolting or riveting assemblies. The mechanical performance of an adhesive bonded joint is related to the distribution of the stresses in the adhesive layer. Consequently it is essential to know this distribution, which, because of its complexity, makes prediction of fractures difficult. From the first works of Volkersen (1938) when only a distribution of the shear stress in the adhesive joint was taken into account to the more recent studies by finite elements, many formulations have made it possible to define the field of stresses in such assemblies better and better.

Since the first work of Volkersen until the more recent studies by finite elements many formulations allowed to better define the stress field in such assemblies. Among those, we can mention in principal the works due to:

[*] e-mail: ovidiu.nemes@sim.utcluj.ro
[1] Technical University of Cluj-Napoca
[2] ENSICA Toulouse
[3] “Paul Sabatier” University Toulouse

- Goland and Reissner (1944) – dealing with the description of the peeling stress. They showed that the effects of flexion create additional stresses which are superimposed on shear stresses,
- Hart-Smith (1973) - studied the elastoplastic behavior of the joint of adhesive and took into account the effects of temperature,
- Renton and Vinson (1977) have checked certain results by experimental way.

One should mention also the theoretical work of Oljado and Eidinoff (1978), or those due to Bigwood (1989), and Allman (1977),

Following Goland and Reissner (1944), Volkersen (1965) introduced into his new analysis the normal stress "stress of shearing" (peeling stress) which is variable in the thickness of the adhesive layer. This assumption enabled him to build a stress field observing the boundary conditions of the assembly. However, due to the complexity and difficulty of its implementation, this analytical formulation is not easily applicable.

Gilibert and Rigolot (1979 – 1991) propose, based on the method of the asymptotic developments connected in the vicinity of the ends, an analytical formulation of the stress field over the entire covering length. If this formulation constitutes a clear improvement of the modeling of the field of the constraints on the level of the ends and represents experimental reality better, it is however not valid near the free edges.

Other more recent studies, due to Liyong (1994) present an analytical formulation making it possible to calculate the mechanical strength of the double-lap joints by taking into account the effects of temperature; however the author disregards the stress distribution and calculates only the joint shearing deformation energy.

Adams and Peppiatt (1974), in their finite element analysis, circumvented this difficulty by studying a joint modified by the addition of a regularizing part. However even this study is not satisfactory on the level of the ends.

Tsai and Oplinger (1998) develop the existing traditional solutions by the inclusion of shearing strains, neglected until there. The solutions obtained ensure a better forecast of the distribution and intensity of the shear stress.

Mortensen and Thomsen (2002) developed the approach for the analysis and the design of the joints adhesive bonded. They held into account the influence of the interface effects between the adherents and they modeled the adhesive layer by assimilating it to a spring.

Nemeş (2004) use a technique based on the minimization of the potential energy. The first stage consists in building a statically acceptable stress field, i.e. verifying the boundary conditions and the equilibrium equations. Then, the potential energy generated by such a stress field is calculated. In the third stage, the potential energy is minimized in order to determine the stress distributions. As we have just seen, the analytical formulations and the finite element analysis provide a stress field satisfying for the median part of the joints. On the other hand, these two approaches provide results that do not satisfy the boundary conditions imposed at the ends of covering. However it is in the vicinity of these ends that one observes the majority of the phenomena of degradation (non-linear behavior, damage, cracking, even fracture). The analytical study that follows gives a first solution of the field of the constraints respecting the whole of these conditions.

RESULTS AND DISCUSSION

THEORETICAL MODEL

All work has encountered difficulties in modeling the stress field in the vicinity of the ends of the joint. The method used to obtain the optimal field for this type of assembly consists of:

- Construction of a statically acceptable field,
- Calculation of the potential energy associated with the stress field,
- Minimization of this energy by a variational method,
- Resolution of the differential equation obtained.

Definitions and hypothesis. Let us consider a plane joining with double covering (Figure 1) whose supports are maintained stuck by a marked elastic adhesive of the index ©.

The whole joining is in balance under the action of a tensile load. The two adherents are subjected to the same load of F/2 traction following axis X, the median plate it being subjected to an opposite load of intensity F. Considering the geometrical symmetries of the problem, our analysis will be limited to the study of the higher half of the assembly represented Figure **2**.

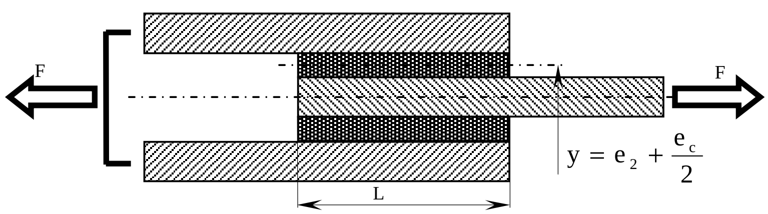

Figure 1. Double-lap adhesive assembly

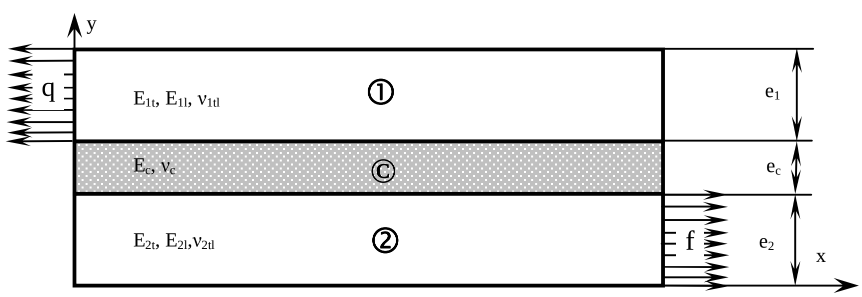

Figure 2. Geometrical and material definition of the double-lap joint

Where:

- **E_c, ν_c,** Young's modulus and Poisson's ratio of the adhesive ©,
- **E_{tl}, E_{ll}, ν_{tll}**, longitudinal, transverse modulus and Poisson's ratio of the inner tube,

- **E_{2t}, E_{2l}, v_{tl2}**, longitudinal, transverse modulus and Poisson's ratio of the external tube,
- **e_c**, adhesive © thickness,
- **e_1, e_2,** adherents ① and ② thickness,
- **L**, joining length,
- **f** and **q**, tensile stresses following x axis, on the adherents.

The constraints in various materials will be located by the index (i), where i = ①, © or ②. We are in the case of plane constraints and we will adopt the following assumptions:

- the state of plane stresses: $\tau_{zx}^{(i)} = \tau_{zy}^{(i)} = \sigma_{zz}^{(i)} = 0$
- the $\sigma_{xx}^{(i)}$, $\tau_{xy}^{(i)}$ et $\sigma_{yy}^{(i)}$ stresses are independent of z variable
- the $\sigma_{xx}^{(1)}$ et $\sigma_{xx}^{(2)}$ stresses are function only of x variable
- the normal stress in the adhesive will be considered null: $\sigma_{xx}^{(c)} = 0$

The stress field is thus reduced to:

- adherent ①: $\sigma_{xx}^{(1)}(x)$, $\tau_{xy}^{(1)}(x,y)$, $\sigma_{yy}^{(1)}(x,y)$,
- adhesive ©: $\tau_{xy}^{(c)}(x)$, $\sigma_{yy}^{(c)}(x,y)$,
- adherent ②: $\sigma_{xx}^{(2)}(x)$, $\tau_{xy}^{(2)}(x,y)$, $\sigma_{yy}^{(2)}(x,y)$.

The stress field definition. We build a statically acceptable stress field by respecting the preceding assumptions. i.e. checking the local equilibrium equations, the boundary conditions as well as the conditions of continuity to the interfaces with the adhesive. We write the balance of the forces which act on the whole of joining by carrying out a fictitious cut of the assembly following y axis.

The stress components for each three component must satisfy the equilibrium equations, the conditions of continuity of the vector forced with the crossing of the interfaces as well as the boundary conditions in x = 0, X = L, y = 0 and $y = (e_1 + e_2 + e_c)$. Starting from equilibrium equations, in order to determine the various component the of the stress vectors, we must write the boundary conditions as well as the conditions of continuity of the stress vectors with the interfaces.

On the free edges, the normal stress on the surface and shear stresses are null (equal with zero value). With the crossing of the interfaces, these same stresses must be continuous. The nullity of the shear stress for y = 0 is due to the symmetry of the problem. All these conditions were gathered below:

- For x = 0: $\sigma_{xx}^{(1)} = q$, $\sigma_{xx}^{(2)} = 0$, $\tau_{xy}^{(1)} = 0$, $\tau_{xy}^{(2)} = 0$
- For x = L: $\sigma_{xx}^{(1)} = 0$, $\sigma_{xx}^{(2)} = f$, $\tau_{xy}^{(1)} = 0$, $\tau_{xy}^{(2)} = 0$
- For y = 0: $\tau_{xy}^{(2)} = 0$
- For $y = e_2$: $\tau_{xy}^{(2)} = \tau_{xy}^{(c)}$, $\sigma_{yy}^{(2)} = \sigma_{yy}^{(c)}$
- For $y = e_2 + e_c$: $\tau_{xy}^{(1)} = \tau_{xy}^{(c)}$, $\sigma_{yy}^{(1)} = \sigma_{yy}^{(c)}$
- For $y = e_1 + e_c + e_2$: $\tau_{xy}^{(1)} = 0$, $\sigma_{yy}^{(1)} = 0$

The stress field is thus reduced to the following components:

$$\tau_{xy}^{(1)}(x,y) = \left[\left(e_1 + e_2 + e_c\right) - y\right]\frac{d\sigma_{xx}^{(1)}}{dx},$$

$$\sigma_{yy}^{(1)}(x,y) = \frac{1}{2}\left[y - \left(e_1 + e_2 + e_c\right)\right]^2 \frac{d^2\sigma_{xx}^{(1)}}{dx^2}$$

$$\tau_{xy}^{(c)}(x) = e_1 \frac{d\sigma_{xx}^{(1)}}{dx},$$

$$\sigma_{yy}^{(c)}(x,y) = e_1\left[\left(\frac{e_1}{2} + e_2 + e_c\right) - y\right]\frac{d^2\sigma_{xx}^{(1)}}{dx^2}, \qquad (1)$$

$$\sigma_{xx}^{(2)}(x) = f - \frac{e_1}{e_2}\sigma_{xx}^{(1)}$$

$$\tau_{xy}^{(2)}(x,y) = \frac{e_1}{e_2}\, y\, \frac{d\sigma_{xx}^{(1)}}{dx},$$

$$\sigma_{yy}^{(2)}(x,y) = \frac{e_1}{2}\left[\left(e_1 + e_2 + 2e_c\right) - \frac{y^2}{e_2}\right]\frac{d^2\sigma_{xx}^{(1)}}{dx^2}$$

Deformation energy calculation. In the defined stress field, the only unknown factor is the expression of the normal stress $\sigma_{xx}^{(1)}$, expression which we will determine using the principle of minimum of complementary energy. The potential energy associated with the statically acceptable field previously given is written for a joining length 1 and width unit on axis z:

After integration following y, for the potential energy was obtained the following form:

$$\xi_P = \underbrace{\int_0^L \left[A\sigma_{xx}^{(1)^2} + B\sigma_{xx}^{(1)}\frac{d^2\sigma_{xx}^{(1)}}{dx^2} + C\left(\frac{d\sigma_{xx}^{(1)}}{dx}\right)^2 + D\sigma_{xx}^{(1)} + E\left(\frac{d^2\sigma_{xx}^{(1)}}{dx^2}\right)^2 + F\frac{d^2\sigma_{xx}^{(1)}}{dx^2} + K\right]dx}_{\Gamma} \qquad (2)$$

the constants A, B, C, D, E, F and K depend on the geometrical and material characteristics of the three components as well as the applied loading. The expressions of these various constants according to the geometrical and physical characteristics of the assembly are given by the following equations.

By applying to the functional ξ_P a variational calculus and by using the boundary conditions which one also writes in the form:

$$\sigma_{xx}^{(1)}(x=0)=q=\frac{e_2}{e_1}f\ ,\ \frac{d\sigma_{xx}^{(1)}}{dx}(x=0)=0\ ,\ \sigma_{xx}^{(1)}(x=L)=0\ ,\ \frac{d\sigma_{xx}^{(1)}}{dx}(x=L)=0 \tag{3}$$

we obtain that the energy is minimal when the stress function $\sigma_{xx}^{(1)}(x)$ is solution of the following differential equation:

$$E\frac{d^4\sigma_{xx}^{(1)}(x)}{dx^4}+(B-C)\frac{d^2\sigma_{xx}^{(1)}(x)}{dx^2}+A\sigma_{xx}^{(1)}(x)+\frac{D}{2}=0 \tag{4}$$

Parametric study of the adhesive bonded joints

Stress distribution. Figure 3 shows the stress distributions in the adhesive for the analyzed configurations. These data show that the peeling stresses are more important than shear stresses. This observation joined the remarks of Volkersen (1965), Gilibert and Rigolot (1985) who also argument that the peeling stress are most important. We notice that: for σ_{yy}, the maximum values are obtained on the free edges (z = 0, z = L). These values are much localized at the edges; however, the maximum constraint σ_{yymax} is obtained in compression, for τ_{xy}, we raises two peaks of stresses located at equal distance of the two free edges. The peaks do not have the same intensity because of the difference of rigidities of the two stuck adherents.

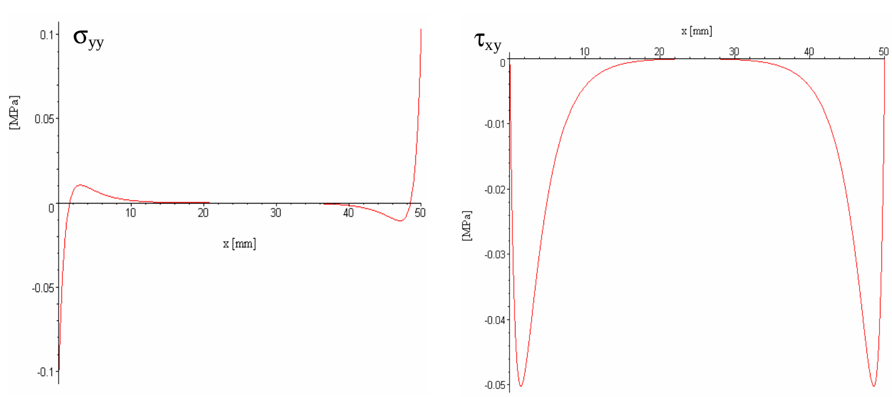

a) b)

Figure 3. Distribution of the stresses in the adhesive of a VE ±45°-AV 119-VE ±45° assembly for F = 1 N/mm. a) the peeling stress (σ_{yy}), b) the shear stress (τ_{xy}).

Based on previous analysis of distributions we can note that the peeling stress are more important than the shear stresses thus the use of a criterion of rupture of the adhesive bonded joint must take into account not only the stress shear τ_{xy} but also the peeling stress σ_{yy}.

Parametric study

Covering length influence. Figure 4 shows the influence of covering length on the distribution and the intensity of shear stresses. The fact of increasing the length of joining beyond a certain value does not have any influence on the maximum stresses in the adhesive. Indeed, for the assembly with double covering there is an optimal length of covering beyond which the added length is not under load. By increasing gradually the covering length we observed:

- the reduction of the values of the shear stress in the middle of the joint,
- the displacement of the stress peaks towards the free edges.

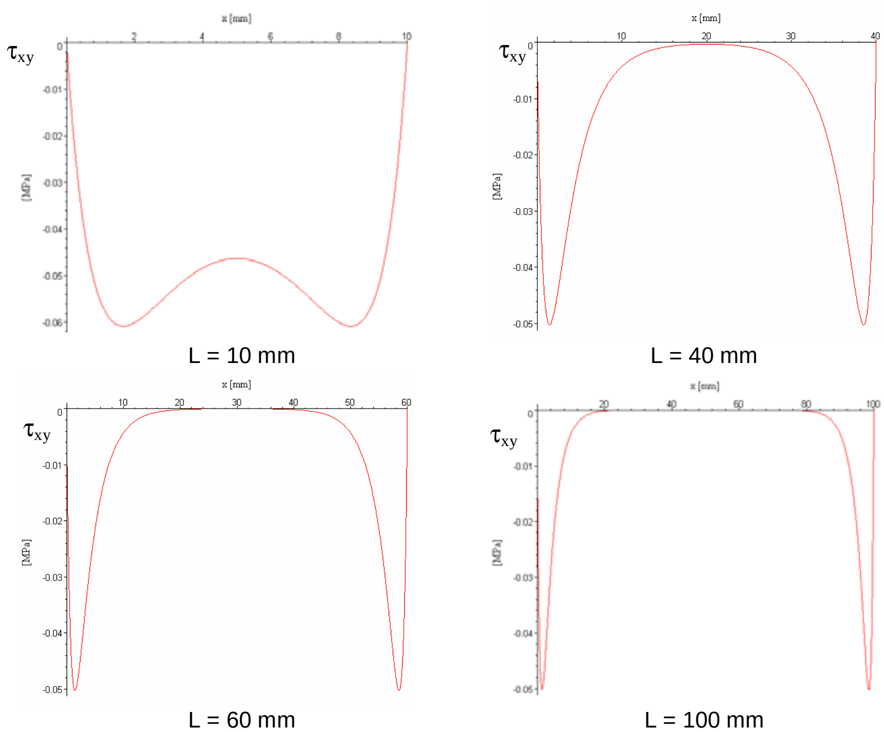

Figure 4. Variation of τ_{xy} in the adhesive according to the covering length (L = 10÷100 mm) and F = 1 N/mm, for a VE ±45°-AV 119-VE ±45° assembly.

Influence of rigidities. Figure 5 represents the influence of the elastic module of the adhesive on the shear stress in the adhesive. The maximum peaks will increase slightly when the elastic module grows.

The influence of relative rigidity, between the two stuck substrates, is illustrated in Figure 6.

We can notice that the maximum peaks on the two edges are not equaled any more if ratio E_2/E_1 is different from 1.

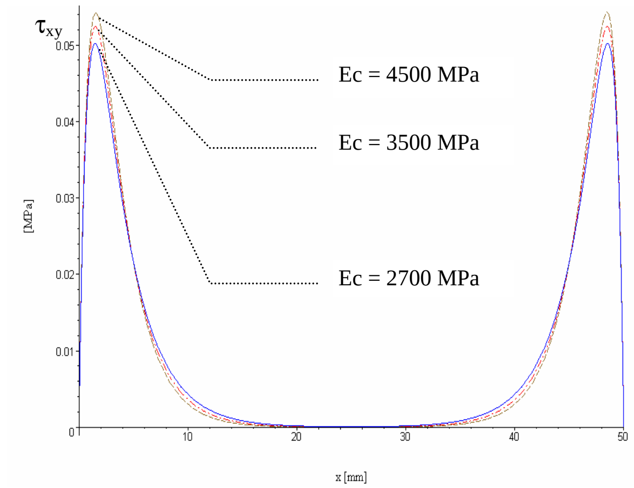

Figure 5. Variation of the shear stress ($-\tau_{xy}$) in the adhesive according to the elastic module of the adhesive.

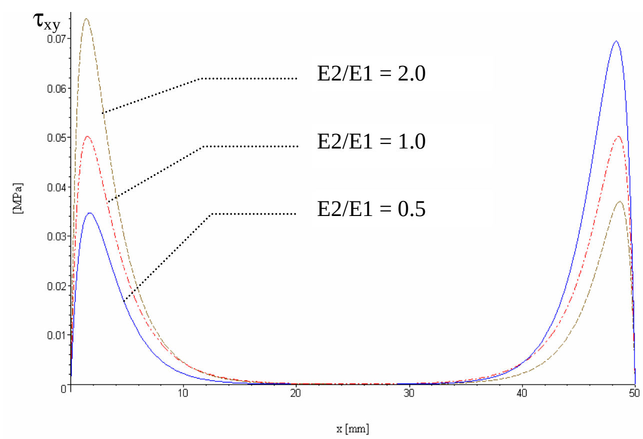

Figure 6. Variation of the shear stress ($-\tau_{xy}$) according to relative rigidity.

Influence of adhesive thickness. Figures 7 - 8 show the influence of adhesive thickness. When the adhesive thickness increases the maximum stresses in the adhesive decrease and the distribution (shear and peeling stress) tends to be uniform over the entire covering length, except in the vicinity of the free edges.

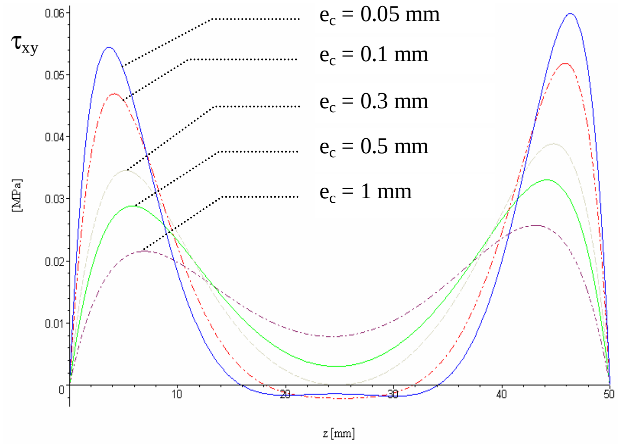

Figure 7. Variation of the shear stress ($-\tau_{xy}$) according to the adhesive thickness.

At the same time, for the peeling stresses, we can also note a considerable reduction in the maximum values to the level of the free edges.

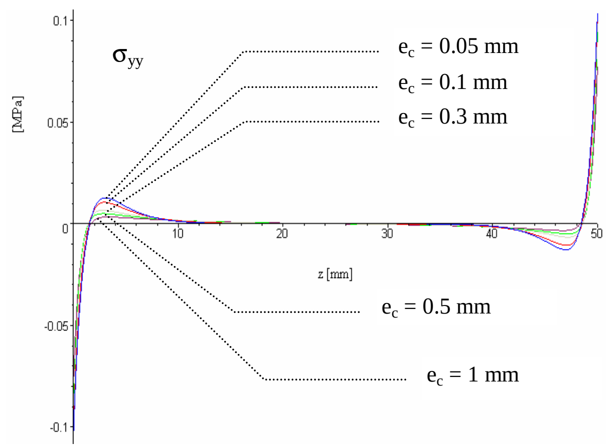

Figure 8. Variation of the peeling stress (σ_{yy}) according to the adhesive thickness.

CONCLUSIONS

The present data point the followings:

- the maximum values of σ_{yy} are obtained on the free edges and the maximum values are localized at the edges,
- concerning τ_{xy}, we found two peaks of stresses located at equal distance of the two free edges,
- the peeling stresses are more important than shear stresses,

- there is an optimal length beyond which the maximum stress do not evolve any more,
- the intensities of the peaks are influenced by the rigidities difference of the two adherents, the maximum peaks increase slightly when the elastic module grows,
- the shear stress in the adhesive increases with the increase in the relative rigidity of the adherents,
- more the thickness of adhesive is increased, more the values of the stresses decrease on the level of the free edges and the distribution tends to being uniform.

REFERENCES

1. Adams, R.D., Peppiat, N.A., *Journal of Strain Analysis*, **1974**, *9*, 185-196.
2. Allman, D.J., *Journal of Mechanical Applied Mathematics*, **1977**, *30*, 415-436.
3. Bigwood, D.A., Crocombe, A.D., *International Journal of Adhesion & Adhesives*, **1989**, *9*, 229-242.
4. Gilibert, Y., Rigolot, A., *Matériaux et Constructions*, **1985**, *18*, 363-387.
5. Gilibert, Y., Rigolot, A., *Mécanique des solides*, **1979**, *288*, 287-290.
6. Gilibert, Y., *Matériaux et techniques*, **1991**, 5-16.
7. Goland, M., Buffalo, N.Y., Reissner, E., *Journal of Applied Mechanics*, **1944**, *66*, A17-A27.
8. Hart-Smith, L.J., Douglas Aircraft Co., *NASA-CR-112236*, **1973**.
9. Liyong Tong, *International Journal of Solids Structures*, **1994**, *31*, 2919-2931.
10. Mortensen, F., Thomsen, O.T., *Composite Structures*, **2002**, *56*, 165-174.
11. Mortensen, F., Thomsen, O.T., *Composite Science and Technology*, **2002**, *62*, 1011-1031.
12. Nemeş, O., *Contribution à l'étude des assemblages collés cylindriques et plans*, PhD. Thesis, INSA Toulouse, France, **2004**.
13. Ojalvo, I.U., Eidinoff, H.L., Bond *AIAA Journal*, **1978**, *16*, 204-211.
14. Renton, W.J., Vinson, J.K., *Journal of Applied Mechanics*, **1977**, 101-106.
15. Tsai, M.Y, Oplinger, D.W., Morton, J., *Int. J. Solid Structures*, **1998**, *35*, 1163-1185.
16. Volkersen O., Die *Luftfahrtforschung*, **1938**, *15*, 41-47.
17. Volkersen, O., Recherché *Construction métallique*, **1965**, *4*, 3-13.

STUDIA UNIVERSITATIS BABES-BOLYAI, CHEMIA, LI, 2, 2006

Dedicated to professor Gh. Marcu at his 80th anniversary

MODELING AND SIMULATION OF THE AMMONIA ABSORPTION PROCESS IN SODIUM CHLORIDE SOLUTION USING CHEMCAD

CALIN CORMOS*, ANA-MARIA CORMOS*, SERBAN AGACHI*

ABSTRACT. In this paper the mathematical modeling and the simulation results for ammonia absorption in sodium chloride solution (brine) have been presented. The ammoniacal brine is used to obtain sodium bicarbonate and sodium carbonate in soda ash plants (according to the Solvay process).

The ammonia absorption process is performed in the absorption columns sequence. Because the absorption process is an exothermic process, the absorption columns are provided with cooling systems.

Modeling and simulation of the ammonia absorption in sodium chloride solution were done using ChemCAD software package. The evolutions of the process parameters were studied during the absorption process. The model and the simulation results proved to be a reliable tool for analyzing the absorption processes and can be used to improve the real plant operation.

1. INTRODUCTION

Sodium carbonate is a common inorganic industrial chemical, also known as soda ash (Na_2CO_3). The synthesis process of soda ash (sodium carbonate) using Solvay process is done starting from sodium chloride, limestone, coke and ammonia as raw materials [1, 2].

The natural sodium chloride solution (brine) is extracted from soil and purified (removal of solid impurities by filtration and removal of calcium and magnesium ions by precipitation). Into the purified sodium chloride solution, ammonia is absorbed (the recovered ammonia from the residual liquid phase is used). After ammonia absorption, the solution is carbonated with gaseous carbon dioxide coming from two main sources: thermal decomposition of the limestone and sodium bicarbonate calcination process. After carbonation of ammoniacal brine, a suspension of sodium bicarbonate results. Sodium bicarbonate is filtered and the residual liquid phase is treated with calcium hydroxide solution (slaked lime) in order to recover the ammonia

* *Babes – Bolyai University, Faculty of Chemistry and Chemical Engineering, 11 Arany Janos Street, RO-400028, Cluj – Napoca, Romania, Tel: +40264593833, Fax: +40264590818, E-mail: cormos@chem.ubbcluj.ro, cani@chem.ubbcluj.ro, sagachi@chem.ubbcluj.ro*

from ammonium salts (ammonium chloride, carbonate, bicarbonate etc.). Sodium bicarbonate resulted after filtration is washed, dried and calcined in order to obtain sodium carbonate (soda ash).

2. MODELING AND SIMULATION OF THE PROCESS

The ammonia absorption process is done using an absorption columns sequence. Because the absorption process is exothermic the columns are provided with cooling systems. The ammonia absorption process is presented in figure 1 [1,2].

The purified brine is distributed in the ammonia recovering column I *2* and in ammonia recovering column III *4*. The sodium chlorine solution (brine) rich in ammonia passes in the ammonia recovering column II *3*, and into the first absorber *6*. In the absorbers *6* and *7*, the brine flows in counter-current with cold gas from distillation (the gas from distillation are cooled at 55-60^oC, in the refrigerator *8*). During the ammonia absorption process, the temperature increases and reaches 60-63^oC to the bottom of the absorption column *6*. The ammonia concentration in the first absorber is 15-20 DN. In the second absorber *7*, the temperature is kept constant in the interval of 60-65^oC, by cooling. The ammoniacal brine from the second absorber *7* (with concentration 100-106 DN/20 ammonia and 30-35 DN/20 carbon dioxide) is cooled at 30-35^oC, in the refrigerator *9* and collected in the ammoniacal brine tank 10 in order to be send to carbonation process. The condensed phase is collected in tank *11* and sent to ammonia distillation. The outlet gas from the first absorber *6* contains 9-17% ammonia and 55-60% carbon dioxide. The ammonia from the outlet gas of the absorber *6* is absorbed in the recovering column *3*, and the rich carbon dioxide gas passes to the calciner gas collector.

The main ionic reactions of the ammonia absorption in sodium chloride solution (brine) are presented below [2]. Most of the authors agreed to the following description of the ionic reactions that take place during the absorption process:

$$H_2O \leftrightarrows H^+ + OH^- \quad (1)$$

$$CO_2 + H_2O \leftrightarrows HCO_3^- + H^+ \quad (2)$$

$$HCO_3^- \leftrightarrows CO_3^{2-} + H^+ \quad (3)$$

$$NH_3 + H_2O \leftrightarrows NH_4^+ + OH^- \quad (4)$$

$$NH_3 + HCO_3^- \leftrightarrows NH_2COO^- + H_2O \quad (5)$$

$$NaCl \leftrightarrows Na^+ + Cl^- \quad (6)$$

$$NH_4OH \leftrightarrows NH_4^+ + OH^- \quad (7)$$

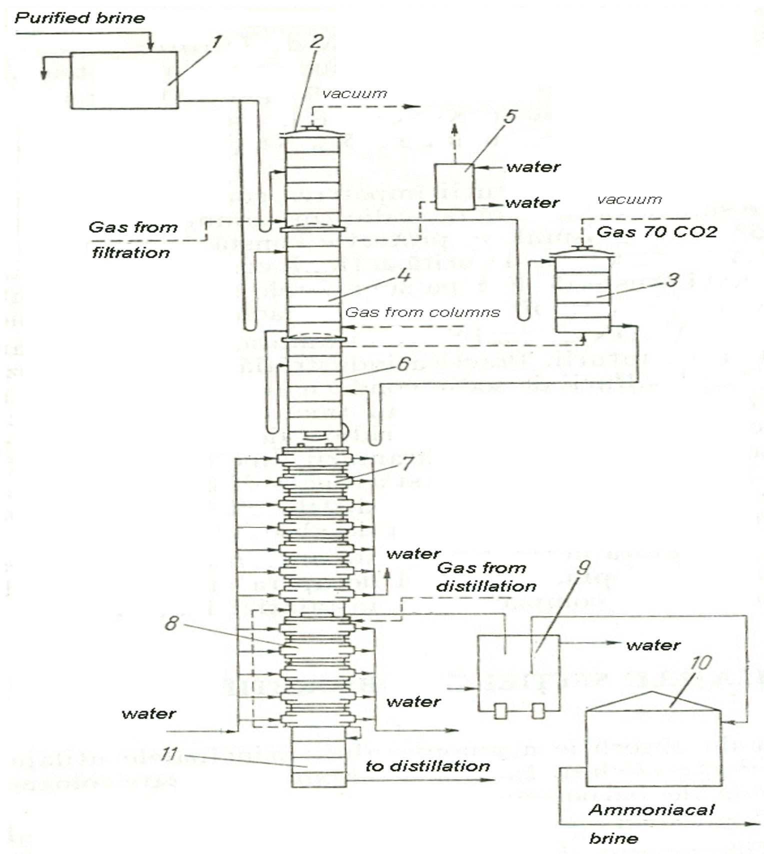

Figure 1. Ammonia absorption process [1]
1 - purified brine tank, 2 – ammonia recovering column I (from the filtration gas), 3- ammonia recovering column II (from absorption stage), 4- ammonia recovering column III (from the carbonation column gas), 5 – gas cleaner, 6 – ammonia absorber I, 7- ammonia absorber II, 8 – refrigerator of the distillation gas, 9 – refrigerator of the ammoniacal brine, 10- ammoniacal brine tank, 11- condensed tank

The parameters used for modeling and simulation of the ammonia absorption process in sodium chloride solution (brine) are presented in the tables 1, 2 and 3.

Table 1.

The properties of the inlet gaseous streams

Parameter	Measuring Unit	Gas coming from sodium bicarbonate filtration process	Gas coming from carbonation columns	Gas coming from ammonia distillation process
Temperature	[^oC]	25	50	60
Pressure	[bar]	0.5	1	0.9
CO_2	[mole %]	3.20	5.36	14.33
CO	[mole %]	0	1.00	0.03
O_2	[mole %]	18.42	1.50	0.05
N_2	[mole %]	73.68	68.52	0.33
H_2O	[mole %]	3.50	5.33	14.42
NH_3	[mole %]	1.20	18.28	70.83
Flow	[kg/h]	850	1016	1136.15

Table 2.

The properties of the inlet liquid stream (purified brine)

Parameter	Measuring Unit	Value
Temperature	[^oC]	20
Pressure	[bar]	1
NaCl	[weight %]	24,63
H_2O	[weight %]	75.47
Flow	[kg/h]	10600

Table 3.

Parameters of the absorption columns

Parameter	No. of stage	Feed tray for liquid stream	Feed tray for gas stream	Cooling duty
First absorber	6	1,4	6	0
Second absorber	6	1	6	$1* 100^7$ J/h
Ammonia recovering column I	4	1	4	0
Ammonia recovering column II	6	1	6	0
Ammonia recovering column III	6	1	6	0

The modeling and simulation of the ammonia absorption process were done using ChemCAD (version 5.1.3) software package. The electrolyte package was used as thermodynamic option for simulation of the ammonia absorption process [4,5].

The main window of the application developed for ammonia absorption process is presented in the figure 2.

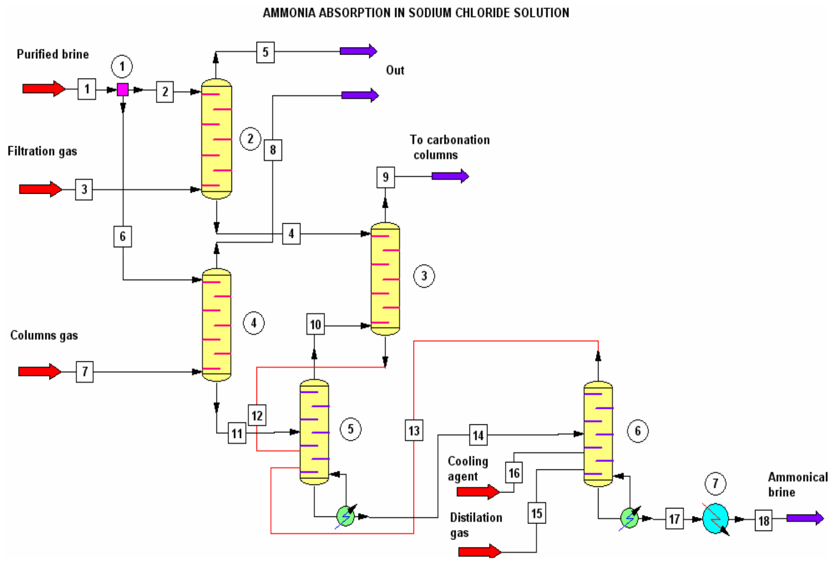

Figure 2. Simulation of the ammonia absorption process using ChemCAD

3. RESULTS AND DISCUSSIONS

The simulation results of ammonia absorption process in brine (sodium chloride solution) using ChemCAD, are presented below.

The properties of output gaseous streams resulted from the simulation in case of the recovering columns and absorber columns are presented in table 4 and 5.

Tabel 4.

The properties of the gaseous streams leaving the ammonia recovering columns

Parameter	Measuring Unit	Gas from ammonia recovering column I	Gas from ammonia recovering column III	Gas from ammonia recovering column II
Temperature	[^{o}C]	20	20	26
Pressure	[bar]	1	1	1
CO_2	[mole %]	2.2	0	49.45
CO	[mole %]	0	1.38	2.85
O_2	[mole %]	19.17	2.07	6.67
N_2	[mole %]	76.77	94.7	38.07
H_2O	[mole %]	1.86	1.85	2.9
NH_3	[mole %]	0	0	0
Flow	[kg/h]	820	775	80

Tabel 5.

The properties of the gaseous streams leaving the ammonia absorbers

Parameter	Measuring Unit	First absorber	Second absorber
Temperature	[^{o}C]	39	36
Pressure	[bar]	1	1
CO_2	[mole %]	0.16	0.12
CO	[mole %]	5.58	7.82
O_2	[mole %]	8.11	14.83
N_2	[mole %]	79.11	71.57
H_2O	[mole %]	5.57	4.70
NH_3	[mole %]	1.47	0.95
Flow	[kg/h]	8.2	8.6

The ammoniacal brine resulted in the absorption process has the following properties: temperature 62^{o}C, pressure 1 bar, flow 12000 kg/h, and composition (mass %): 64.88 % water, 15 % ammonia, 5.34 % NH_4OH, 3.11 % NH_2COO^-, 8.52 % Na^+, 1.39 % CO_3^{-2}, 0.56 % HCO_3^-, 1.93 % NH_4^+, 13.14 % Cl^-.

In the sequence of absorption columns, the temperature variations are: for the ammonia recovering column I the change is of 20-26^{o}C, for the ammonia recovering column III is of 20-39.5^{o}C, for the ammonia recovering column II the temperature is constant, for the first ammonia absorber is of 36-39^{o}C and for the second ammonia absorber is of 30-60 ^{o}C.

The variations of the temperature for the ammonia recovering columns are presented in the figures 3 and 4.

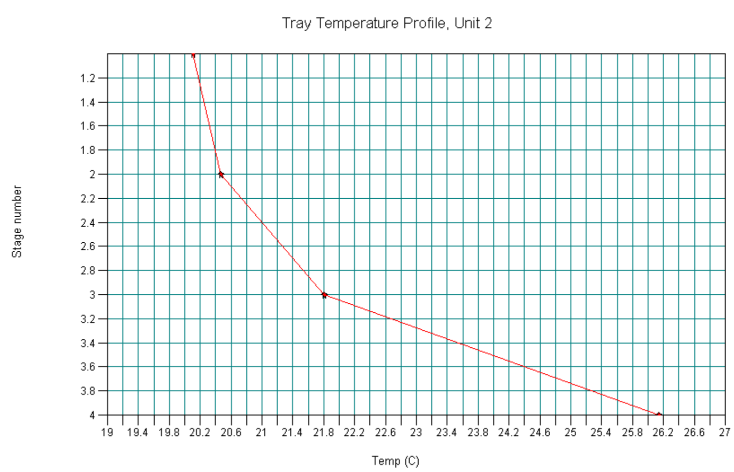

Figure 3. Variation of the temperature in the ammonia recovering column I

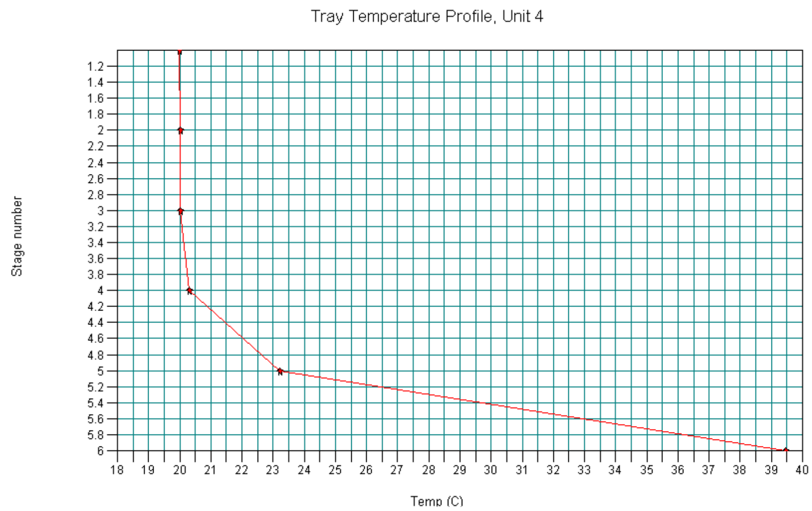

Figure 4. Variation of the temperature in of the ammonia recovering column III

The simulation results presented above were compared with data collected from real plant operation. The operation data collected from a real plant are presented in the table 6 [1, 2, 3].

Tabel 6.

The properties of the gaseous streams leaving the ammonia recovering columns (data collected from a real plant operation)

Parameter	Measuring Unit	Ammonia recovering column I	Ammonia recovering column III	Ammonia recovering column II
Temperature	[^{o}C]	-	-	25-30
CO_2	[mole %]	1.3	3.2	69.7
H_2O	[mole %]	1.8	3.2	5.1
NH_3	[mole %]	0.06	0.19	0.06
Inert	[mole %]	96.9	93.4	25.2

From the comparison of the simulation and real plant data, one can observe a close similarity between simulation results and experimental data. This fact validates the application developed for simulation the process and proves the utility of the model in analyzing and optimization of the real plant operation.

4. CONCLUSIONS

Modeling and simulation of the ammonia absorption process in sodium chloride solution (brine) was done using ChemCAD software package (version 5.1.3).

The evolutions of the process parameters (liquid and gaseous flows, composition of the streams, temperatures) were studied during the carbonation process. The simulation results were compared with real plant operation data in order to validate the application developed for the absorption process.

The mathematical model and the simulation results proved to be a reliable tool for analyzing and optimizing the real plant operation of the ammonia absorption in sodium chloride solution used in soda ash manufacturing process according to the Solvay technology.

REFERENCES

1. Filipescu L., Tehnologia produselor sodice si clorosodice, vol. 1, Editura Tehnica, Bucuresti, 1983, page 88 – 120
2. Calistru C., Leonte C., Tehnologia substantelor anorganice, Editura Didactica si Pedagogica, Bucuresti, 1972
3. Cormos C.C.,.Cormos A.M, Agachi S., Modeling and simulation of carbonation process of ammoniacal brine solution in soda ash plant, Revista de Chimie, 57(2), 2006, pp 130-137
4. Cormos C.C., Cormos A.M, Agachi S, Modeling and simulation ammonia recovery process in soda as plant, Revista de Chimie, 56(11), 2005, pp 581-587
5. Cormos C., Modelarea matematica si simularea sintezei pantotenatului de calciu racemic, Teza de doctorat, Cluj – Napoca, 2004

În cel de al LI-lea an (2006) *STUDIA UNIVERSITATIS BABEŞ-BOLYAI* apare în următoarele serii:

matematică (trimestrial)
informatică (semestrial)
fizică (trimestrial)
chimie (semestrial)
geologie (trimestrial)
geografie (semestrial)
biologie (semestrial)
filosofie (semestrial)
sociologie (semestrial)
politică (anual)
efemeride (semestrial)
studii europene (trei apariții pe an)
dramatica (semestrial)
business (semestrial)
psihologie-pedagogie (anual)
ştiințe economice (semestrial)
ştiințe juridice (trimestrial)
istorie (trei apariții pe an)
filologie (trimestrial)
teologie ortodoxă (semestrial)
teologie catolică (trei apariții pe an)
teologie greco-catolică - Oradea (semestrial)
teologie catolică - Latina (anual)
teologie reformată (semestrial)
educație fizică (semestrial)

In the LI-th year of its publication (2006) *STUDIA UNIVERSITATIS BABEŞ-BOLYAI* is issued in the following series:

mathematics (quarterly)
computer science (semesterily)
physics (quarterly)
chemistry (semesterily)
geology (quarterly)
geography (semesterily)
biology (semesterily)
philosophy (semesterily)
sociology (semesterily)
politics (yearly)
ephemerides (semesterily)
European studies (three issues / year)
business (semesterily)
dramatica (semestrial)
psychology - pedagogy (yearly)
economic sciences (semesterily)
juridical sciences (quarterly)
history (three issues / year)
philology (quarterly)
orthodox theology (semesterily)
catholic theology (three issues / year)
greek-catholic theology - Varadiensis (semesterily)
catholic theology - Latina (yearly)
reformed theology (semesterily)
physical training (semesterily)

Dans sa LI-ème année (2006) *STUDIA UNIVERSITATIS BABEŞ-BOLYAI* paraît dans les séries suivantes:

mathématiques (trimestriellement)
informatiques (semestriellement)
physique (trimestriellement)
chimie (semestriellement)
géologie (trimestriellement)
géographie (semestriellement)
biologie (semestriellement)
philosophie (semestriellement)
sociologie (semestriellement)
politique (annuellement)
éphémérides (semestriellement)
études européennes (trois apparitions / année)
dramatica (semestrial)
affaires (semestriellement)
psychologie - pédagogie (annuellement)
études économiques (semestriellement)
études juridiques (trimestriellement)
histoire (trois apparitions / année)
philologie (trimestriellement)
théologie orthodoxe (semestriellement)
théologie catholique (trois apparitions / année)
théologie greco-catholique - Varadiensis (semestriellement)
théologie catholique - Latina (annuellement)
théologie réformée - (semestriellement)
éducation physique (semestriellement)

web: http://www.studia.ubbcluj.ro   e-mail: office@studia.ubbcluj.ro